

Copyright © 2001, by the author(s).
All rights reserved.

Permission to make digital or hard copies of all or part of this work for personal or classroom use is granted without fee provided that copies are not made or distributed for profit or commercial advantage and that copies bear this notice and the full citation on the first page. To copy otherwise, to republish, to post on servers or to redistribute to lists, requires prior specific permission.

**ELECTROMAGNETIC SIMULATION
AND MODELING WITH APPLICATIONS
IN LITHOGRAPHY**

by

Thomas Vincent Pistor

Memorandum No. UCB/ERL M01/19

1 May 2001

**ELECTROMAGNETIC SIMULATION
AND MODELING WITH APPLICATIONS
IN LITHOGRAPHY**

by

Thomas Vincent Pistor

Memorandum No. UCB/ERL M01/19

1 May 2001

ELECTRONICS RESEARCH LABORATORY

College of Engineering
University of California, Berkeley
94720

Electromagnetic Simulation and Modeling with Applications in Lithography

by

Thomas Vincent Pistor

B.A.Sc. (University of Waterloo, Canada) 1995

M.A.Sc. (University of California at Berkeley) 1997

A dissertation submitted in partial satisfaction of the requirements for the degree of

Doctor of Philosophy

in

**Electrical Engineering
and Computer Sciences**

in the

GRADUATE DIVISION

of the

UNIVERSITY of CALIFORNIA, BERKELEY

Committee in charge:

Professor Andrew R. Neureuther, Chair

Professor Jeffrey Bokor

Professor Panayotis Papadopoulos

Spring 2001

Electromagnetic Simulation and Modeling with Applications in Lithography

Copyright © 2001

by

Thomas Vincent Pistor

All rights reserved

Abstract

Electromagnetic Simulation and Modeling with Applications in Lithography

by

Thomas Vincent Pistor

Doctor of Philosophy in Electrical Engineering

University of California at Berkeley

Professor Andrew R. Neureuther, Chair

This thesis is concerned with methods for calculating scattered fields and aerial images in photolithography. Several improvements to the Finite-Difference Time-Domain code TEMPEST are documented and a vector formulation of optical imaging is presented. The implementation of this theory is then used to study mask effects in EUV lithography, phase defects in alternating phase shift masks and several other lithography-related applications.

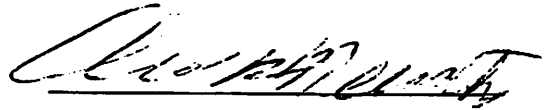
The numerics of TEMPEST including the updating equations, domain excitation, convergence checking, and boundary conditions are reviewed. The Fourier Boundary Condition that operates on the Fourier components of the electromagnetic field is introduced and shown to be useful as an efficient and accurate model for the EUV multilayer mirror. An overview and performance analysis of the re-parallelization of TEMPEST for running across a Network of Workstations (NOW) is presented.

A vector model for an optical imaging system that can accommodate the highly oblique plane waves existing in high numerical aperture imaging or inspection is developed. Mathematical models for photomasks are presented and organized by their level of complexity.

A study of EUVL masks is undertaken where the effects of absorber thickness, side wall angle, corner rounding, angle of incidence and substrate defects are investigated. Key observations include a degradation of mask depth of focus due to off-axis imaging, a dependence of CD on absorber feature thickness due to interference, and the ability of a shallow mirror defect to interact strongly with a mask feature.

Phase defects in alternating phase shift masks are investigated from both printability and inspectability points-of-view. Isotropic wet etching was seen to decrease defect printability. Defects with a pre-wet-etch size larger than 200nm were seen to cause greater than 10% CD variation. In simulation studies of defect inspectability annular illumination was observed to yield stronger normalized difference signal than circular illumination.

The breadth of uses for TEMPEST in lithography is demonstrated by overviewing simulations of pinholes, alignment marks, aberration monitors, reflective notching, and two-dimensional phase shift mask topographies.



Professor A.R. Neureuther

Committee Chairman

***Dedicated to my poor mom and dad
who think I'm coming home now.***

Acknowledgments

Professor Neureuther has been nothing but a constant source of inspiration, enthusiasm, knowledge, kindness, encouragement and ideas. I wish to express my most sincere thanks to him.

Other professors who have assisted me and to whom I owe thanks include Professors Bokor and Oldham in the EECS department, Professor Papadopoulos in the Mechanical Engineering department and Professor Cangelaris at the University of Illinois at Urbana-Champaign.

This research was supported by a U.C. Regents Fellowship, SRC contract 96-LC-460, the SRC Graduate Fellowship Program, DARPA grant MDA972-97-1-0010 and Lawrence Livermore National Labs.

Students and friends who have helped me along the way include Bob Socha, Kostas Adam, Alberto Salleo and Alfred Wong. I would also like to thank my good friend Romolo Magarelli, his wife Mary and the Barbieri's in Toronto for their support during the most difficult times of my graduate career.

And finally, there is my wonderful family. Rob and Laurie, my brother and sister, my grandparents Aldo and Louise, and all my cousins, aunts and uncles have been there for me the whole way. My parents, Anita and Tino, have taught me "everything" and have supported me always. Thank you.

CHAPTER 1. Introduction.....	1
1.1. Electromagnetic Simulation and Modeling in Lithography.....	1
1.1.1. The need for Electromagnetic Simulation and Modeling in Lithography	1
1.2. Background and History of FDTD and TEMPEST	2
1.2.1. The FDTD method and the Yee equations	3
1.2.2. Convergence Checking	8
1.2.3. Domain Excitation	9
1.2.4. TEMPEST Algorithm	11
1.3. Optical Imaging Models and Aerial Image Calculation.....	11
1.4. This Thesis	14
1.4.1. Academic Contributions	14
1.4.1.1. Fourier Boundary Condition.....	14
1.4.1.2. Imaging System Formulation	15
1.4.2. Improvements to TEMPEST.....	15
1.4.2.1. PML boundary condition.....	15
1.4.2.2. Parallelization	16
1.4.3. Simulation Studies	16
1.4.3.1. EUV	16
1.4.3.2. Alternating Phase Shift Mask Defects.....	16
1.4.3.3. Overview of Various Lithography-Related Simulations.....	16
 CHAPTER 2. Boundary Conditions for the Finite-Difference Time-Domain	
Method	17
2.1. Introduction	17
2.2. Perfect Conductor Boundary Condition	18
2.3. Periodic and Symmetric Boundary Conditions.....	18
2.4. Material Boundary Conditions	24
2.5. Absorbing Boundary Conditions.....	24
2.6. Fourier Boundary Condition	30
2.6.1. Implementation	32
2.6.2. Performance	33
2.6.3. Fourier Boundary Condition used as an Absorbing Boundary Condition	
(FABC)	34
2.6.4. Other Uses of the FBC.....	37
2.7. Summary	37
 CHAPTER 3. Parallelizing the Finite Difference Time Domain Algorithm ...	40
3.1. Introduction	40
3.2. Technique	40
3.3. Performance.....	42
3.4. Summary	43

CHAPTER 4. Imaging System Modeling.....	45
4.1. Introduction	45
4.1.1. The Imaging System Model.....	47
4.2. Source and Illumination Optic	48
4.2.1. Discretization of the Source.....	50
4.3. The Object	51
4.4. Projection Optic.....	54
4.5. Film Stack Effects	57
4.6. The Imaging Equations	58
4.7. Photomask Models and Scattering Coefficient Calculation.....	59
4.7.1. Approximating the Scattering Coefficients for a Nearby Plane Wave..	60
4.7.2. Mask Models.....	66
4.7.2.1. Thin, scalar, constant scattering coefficient model	68
4.7.2.2. Thick, vector, constant scattering coefficient model.....	72
4.7.2.3. Thick, vector non-constant scattering coefficient model	80
4.7.3. Choosing the Appropriate Mask Model.....	85
4.8. Discussion	86
CHAPTER 5. Simulation of Extreme Ultraviolet Lithography.....	88
5.1. Introduction	88
5.2. Mask Feature Simulations.....	91
5.2.1. 1D pattern, 2D TEMPEST Domain.....	92
5.2.1.1. Line/Space Pattern - 2D Topography	93
5.2.1.2. Near Field Intensity and Aerial Image	94
5.2.1.3. CD and position vs. Angle-Of-Incidence (AOI)	95
5.2.1.4. Absorber Material Thickness	95
5.2.1.5. Absorber side wall angle	98
5.2.2. 2D pattern, 3D TEMPEST Domain.....	99
5.2.2.1. Square Features, 3D Topography.....	99
5.2.2.2. The near field.....	100
5.2.2.3. Interior vs. Exterior Topographies	101
5.2.2.4. Corner rounding on an Exterior Post.....	102
5.2.2.5. Arbitrary Mask Pattern at two Angles of Incidence.....	102
5.3. Defect Simulations	103
5.3.1. Constant Width, Varying Height	108
5.3.2. Constant Heights, Varying Widths	109
5.3.3. Point Defect Interaction with Line Feature.....	110
5.4. Summary and Discussion	110
CHAPTER 6. Phase Shift Mask Inspection.....	113
6.1. Introduction	113
6.2. Inspection System Overview and Theory	113
6.2.1. A Proposed Model for Scanning Beam Optical Microscopy.....	115
6.3. A Simulation Study of Defect Printability and Inspection.....	117

6.3.1.	Topography	117
6.3.2.	Printability.....	117
6.3.3.	Inspection.....	120
6.4.	Conclusions and Discussion.....	125
CHAPTER 7. Other Simulations related to Lithography		129
7.1.	Pinholes for EUV Point Diffraction Interferometry.....	129
7.2.	Alignment Mark Simulation.....	129
7.3.	The Aberration Ring Test.....	132
7.4.	Reflective Notching.....	137
7.5.	Phase Shift Mask Topography Effects	138
7.6.	Conclusions	140
CHAPTER 8. Conclusions.....		143
8.1.	Theory	143
8.2.	The Applications	144
8.2.1.	EUVL.....	144
8.2.2.	Phase Shifting Masks: Defect Printability and Inspection.....	145
8.2.3.	Other uses of simulation in lithography.....	145
8.3.	Future	146
CHAPTER A. Plane Waves		147
A.1.	Uniform Plane Waves in Free Space.....	147
A.2.	K-Space Representation of Plane Waves	151
CHAPTER B. TE and TM Plane Wave Decomposition of the Discretized Electric Field.....		153
B.1.	Decomposition of the Continuous Electric Field	153
B.2.	Decomposition of the Discretized Electric Field	155
CHAPTER C. Plane Wave Translation in K-Space		158

1 Introduction

1.1. Electromagnetic Simulation and Modeling in Lithography

Lithographers are interested in the formation of a light pattern inside a thin layer of photoresist atop a silicon wafer. This light pattern is referred to as the “aerial image”. To form this aerial image, a light source, a photomask and a complex imaging system are needed. “Electromagnetic Simulation and Modeling” refers to the calculation of this aerial image and of other electromagnetic fields relevant to its formation.

More specifically, “Electromagnetic Simulation” refers to the computer *simulation* of the propagation of an electromagnetic field and “Modeling” refers to the formulation and application of mathematical descriptions of the various objects that participate in the formation of the aerial image.

A primary goal of this thesis is to describe methods to calculate the aerial image and various other electromagnetic fields relevant to lithography and the formation of the aerial image. To do so, mathematical models are derived for the various objects involved. All objects involved in the formation of the aerial image are ultimately described by the Maxwell equations. Some objects, such as phase shift masks, require a direct solution of the Maxwell equations in order to be modeled, while other objects, such as the projection optic in a stepper/scanner can be described by much higher level equations, such as the equations of Fourier optics.

1.1.1. The need for Electromagnetic Simulation and Modeling in Lithography

There are several reasons why simulation and modeling are important in lithography:

1. **Non-existence of hardware.** Researchers are often interested in how a future device might perform. For example, in extreme ultraviolet lithography, researchers have been using computer simulation to predict how masks and optics will perform for a 0.25 NA tool that is still under construction[82].

2. **Machine Time is Limited and/or Expensive.** Even though a machine (such as a stepper or scanner or inspection tool) may exist, the cost of using it may be quite high. A stepper that is being used to print microprocessors in a production situation can produce thousands of dollars worth of product in minutes. It is rather expensive to take the tool out of production for research experiments.

3. **Measurability and Understanding.** Simulation provides the lithographer with a much higher degree of measurability. Intermediate field values such as the near field intensity or scattered orders at the entrance pupil of the projection optic or even the latent aerial image are available with simulation and can be measured. In experiment, only final resist profiles that have the combined effects of all optical systems and resist development mixed together can be measured.

4. **Time-to-market.** It is, quite simply, faster to calculate aerial images than to design and build a mask, go into the microfab and print/measure aerial images. Time-to-market is extremely important in the fast-paced semiconductor industry.

5. **Gedanken experiments.** Simulation allows lithographers to run experiments that are impossible to run in practice. Adam[4], for example, investigated the scattering from phase well corners and the cross coupling of energy between phase wells by separating the scattered fields from adjacent phase wells.

1.2. Background and History of FDTD and TEMPEST

The computer program TEMPEST is an implementation of the Finite-Difference Time-Domain (FDTD) algorithm introduced by Yee[98] as a method for solving the Maxwell equations. TEMPEST was first implemented in two dimensions by Guerrieri[39] and Gamelin[31][32] on a massively parallel supercomputer architecture and used to study scattering from wafer topography, gratings, reflective notching and alignment.

Wong[88] extended the code to three dimensions and re-implemented a version to run on single processor workstations. Wong also developed a novel absorbing boundary condition, techniques for modeling dispersive materials and used the code to research phase shifting mask structures.

Nguyen[58][59] used TEMPEST to study Extreme Ultraviolet Lithography (EUVL) mask topography effects (absorber features and multilayer mirror defects) in two dimensions. Socha[71][73][74] formulated a computationally efficient method for analyzing topography scattering with vector polarized partially coherent spatial illumination and implemented in TEMPEST-PCD and used it to study wafer and mask inspection and reflective notching.

Pistor[62] implemented Berenger's Perfectly Matched Layers (PML) boundary conditions[10] and re-parallelized the code for running on a Network Of Workstations (NOW)[6]. Pistor[63] also introduced the Fourier Boundary Condition (FBC) as an efficient way to model the multilayer mirrors used in Extreme Ultraviolet Lithography (EUVL). Pistor conducted various 3D simulations of EUV mask features and multilayer mirror defects[64][65][66].

Adam has used TEMPEST to study OPC[2] and phase defects[3] and to develop new methods for fast and accurate simulations of alternating phase shift masks of large arbitrary two-dimensional patterns[4]. Deng[23] continues to use TEMPEST to investigate EUVL multilayer mirror defects and alignment issues in imprint lithography[24].

1.2.1. The FDTD method and the Yee equations

The continuous form of the Maxwell equations for linear, isotropic, non-magnetic, non-dispersive materials are written:

Equation 1-1.
$$\nabla \times \vec{E} = -\frac{\partial \vec{B}}{\partial t}$$

Equation 1-2.
$$\nabla \times \vec{H} = \frac{\partial \vec{D}}{\partial t} + \vec{J}_e$$

Equation 1-3.
$$\nabla \cdot \vec{D} = \rho$$

Equation 1-4.
$$\nabla \cdot \vec{B} = 0$$

where \vec{J}_e is the electric current density, \vec{E} and \vec{H} are the electric and magnetic field strengths respectively, \vec{D} and \vec{B} are the electric and magnetic flux densities respectively and ρ is the electric charge density.

The following two constitutive relations and current relation also apply:

Equation 1-5.
$$\vec{B} = \mu(\vec{r})\vec{H}$$

Equation 1-6.
$$\vec{D} = \epsilon(\vec{r})\vec{E}$$

Equation 1-7.
$$\vec{J}_e = \sigma(\vec{r})\vec{E}$$

It is assumed that the materials involved are time invariant but the material properties may, however, be spatially varying.

A numerical scheme for solving the Maxwell equations, first used by Yee [98] is used by TEMPEST. This scheme, here forth referred to as “the Yee algorithm” involves the replacement of both temporal and spatial derivatives by finite differences. The time axis uses a “leapfrog” technique whereby the E fields are calculated at integer time steps (i.e. $n=0,1,2,3,\dots$) and the H fields are calculated at integer-plus-one-half time steps (i.e. $n=0.5,1.5,2.5,\dots$). (see Figure 1-1). For the spatial discretization, the Yee algorithm and TEMPEST use a staggered grid where each of the six field components E_x, E_y, E_z, H_x, H_y and H_z reside at different positions within a region of space called the Yee cell. A 2x2x2 cluster of Yee cells is illustrated in Figure 1-2.

The application of the abovementioned temporal and spatial discretization schemes leads to the following set of “updating equations”[78][89] for the Yee algorithm:

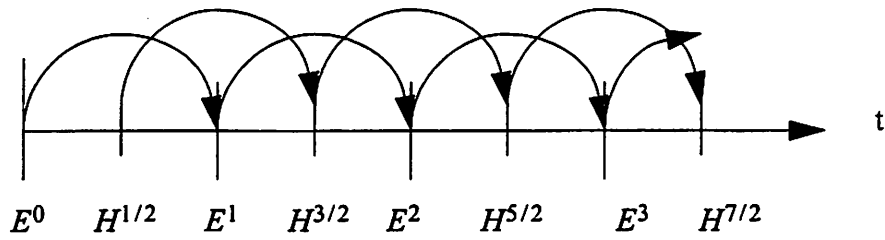


Figure 1-1. The "Leapfrog" temporal discretization scheme

Time E and H fields are calculated at discrete points in time - the E field at the integer time steps and the H fields at integer-plus-one-half time steps.

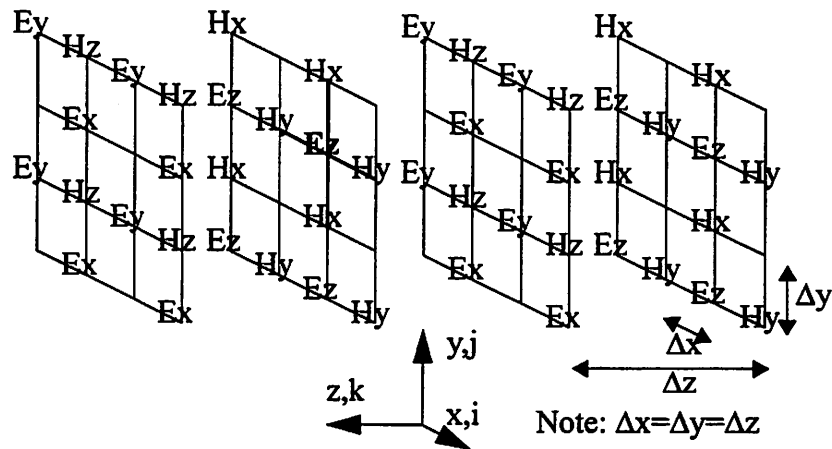


Figure 1-2. Staggered Grid Arrangement of the Field Components

Note that each field component is surrounded by precisely those components needed to calculate the curl component (of its dual field) required by its updating equation.

Equation 1-8.

$$\begin{aligned}
E_x^{n+1}\left[i+\frac{1}{2}, j, k+\frac{1}{2}\right] &= \alpha\left(E_x^n\left[i+\frac{1}{2}, j, k+\frac{1}{2}\right]\right) + \backslash \\
&\quad \beta\left(H_y^{n+\frac{1}{2}}\left[i+\frac{1}{2}, j, k\right]-H_y^{n+\frac{1}{2}}\left[i+\frac{1}{2}, j, k+1\right]+H_z^{n+\frac{1}{2}}\left[i+\frac{1}{2}, j+\frac{1}{2}, k+\frac{1}{2}\right]-H_z^{n+\frac{1}{2}}\left[i+\frac{1}{2}, j-\frac{1}{2}, k+\frac{1}{2}\right]\right) \\
E_y^{n+1}\left[i, j+\frac{1}{2}, k+\frac{1}{2}\right] &= \alpha\left(E_y^n\left[i, j+\frac{1}{2}, k+\frac{1}{2}\right]\right) + \backslash \quad (6 \text{ flops}) \\
&\quad \beta\left(H_z^{n+\frac{1}{2}}\left[i-\frac{1}{2}, j+\frac{1}{2}, k+\frac{1}{2}\right]-H_z^{n+\frac{1}{2}}\left[i+\frac{1}{2}, j+\frac{1}{2}, k+\frac{1}{2}\right]+H_x^{n+\frac{1}{2}}\left[i, j+\frac{1}{2}, k+1\right]-H_x^{n+\frac{1}{2}}\left[i, j+\frac{1}{2}, k\right]\right) \\
E_z^{n+1}[i, j, k] &= \alpha\left(E_z^n[i, j, k]\right) + \backslash \quad (6 \text{ flops}) \\
&\quad \beta\left(H_x^{n+\frac{1}{2}}\left[i, j-\frac{1}{2}, k\right]-H_x^{n+\frac{1}{2}}\left[i, j+\frac{1}{2}, k\right]+H_y^{n+\frac{1}{2}}\left[i+\frac{1}{2}, j, k\right]-H_y^{n+\frac{1}{2}}\left[i-\frac{1}{2}, j, k\right]\right) \quad (6 \text{ flops})
\end{aligned}$$

Equation 1-9.

$$\begin{aligned}
H_x^{n+\frac{1}{2}}\left[i, j+\frac{1}{2}, k\right] &= H_x^n\left[i, j+\frac{1}{2}, k\right] + \backslash \\
&\quad \Gamma\left(E_y^n\left[i+1, j+\frac{1}{2}, k-\frac{1}{2}\right]-E_y^n\left[i, j+\frac{1}{2}, k+\frac{1}{2}\right]+E_z^n[i, j+1, k]-E_z^n[i, j, k]\right) \quad (5 \text{ flops}) \\
H_y^{n+\frac{1}{2}}\left[i+\frac{1}{2}, j, k\right] &= H_y^n\left[i+\frac{1}{2}, j, k\right] + \backslash \\
&\quad \Gamma\left(E_z^n[i, j, k]-E_z^n[i+1, j, k]+E_x^n\left[i+\frac{1}{2}, j, k+\frac{1}{2}\right]-E_x^n\left[i+\frac{1}{2}, j, k-\frac{1}{2}\right]\right) \quad (5 \text{ flops}) \\
H_z^{n+\frac{1}{2}}\left[i+\frac{1}{2}, j+\frac{1}{2}, k+\frac{1}{2}\right] &= H_z^{n-\frac{1}{2}}\left[i+\frac{1}{2}, j+\frac{1}{2}, k+\frac{1}{2}\right] + \backslash \\
&\quad \Gamma\left(E_x^n\left[i+\frac{1}{2}, j, k+\frac{1}{2}\right]-E_x^n\left[i+\frac{1}{2}, j+1, k+\frac{1}{2}\right]+E_y^n\left[i+1, j+\frac{1}{2}, k+\frac{1}{2}\right]-E_y^n\left[i, j+\frac{1}{2}, k+\frac{1}{2}\right]\right) \quad (5 \text{ flops})
\end{aligned}$$

where

$$\begin{aligned}
\alpha &= \frac{2\varepsilon - \sigma\Delta t}{2\varepsilon + \sigma\Delta t} \\
\beta &= \frac{\Delta t}{\Delta x} \cdot \frac{2}{2\varepsilon + \sigma\Delta t} \\
\Gamma &= -\frac{\Delta t}{\mu\Delta x}
\end{aligned}$$

Equation 1-10.

The outlined scheme is shown to be stable (i.e. the solution doesn't blow up) in [90] for situations where $|Re(n_{complex})| \geq |Im(n_{complex})|$, $n_{complex}$ being the complex refractive index of the material¹. When this criterion is not met, for example in many metals at visi-

ble, infrared and ultraviolet wavelengths, a different set of updating equations involving a secondary field component, \vec{D} , is used[92]:

$$D_x^{n+1}\left[i+\frac{1}{2}, j, k+\frac{1}{2}\right] = C_1 D_x^n\left[i+\frac{1}{2}, j, k+\frac{1}{2}\right] + C_2 E_x^n\left[i+\frac{1}{2}, j, k+\frac{1}{2}\right] \quad (4 \text{ flops})$$

$$D_y^{n+1}\left[i, j+\frac{1}{2}, k+\frac{1}{2}\right] = C_1 D_y^n\left[i, j+\frac{1}{2}, k+\frac{1}{2}\right] + C_2 E_y^n\left[i, j+\frac{1}{2}, k+\frac{1}{2}\right] \quad (4 \text{ flops})$$

Equation 1-11. $D_z^{n+1}[i, j, k] = C_1 D_z^n[i, j, k] + C_2 E_z^n[i, j, k] \quad (4 \text{ flops})$

Equation 1-12.

$$E_x^{n+1}\left[i+\frac{1}{2}, j, k+\frac{1}{2}\right] = C_3\left(E_x^n\left[i+\frac{1}{2}, j, k+\frac{1}{2}\right] + D_x^{n+1}\left[i+\frac{1}{2}, j, k+\frac{1}{2}\right]\right) + C_4\left(H_y^{n+\frac{1}{2}}\left[i+\frac{1}{2}, j, k\right] - H_y^{n+\frac{1}{2}}\left[i+\frac{1}{2}, j, k+1\right] + H_z^{n+\frac{1}{2}}\left[i+\frac{1}{2}, j+\frac{1}{2}, k+\frac{1}{2}\right] - H_z^{n+\frac{1}{2}}\left[i+\frac{1}{2}, j-\frac{1}{2}, k+\frac{1}{2}\right]\right) \quad (7 \text{ flops})$$

$$E_y^{n+1}\left[i, j+\frac{1}{2}, k+\frac{1}{2}\right] = C_3\left(E_y^n\left[i, j+\frac{1}{2}, k+\frac{1}{2}\right] + D_y^{n+1}\left[i, j+\frac{1}{2}, k+\frac{1}{2}\right]\right) + C_4\left(H_z^{n+\frac{1}{2}}\left[i-\frac{1}{2}, j+\frac{1}{2}, k+\frac{1}{2}\right] - H_z^{n+\frac{1}{2}}\left[i+\frac{1}{2}, j+\frac{1}{2}, k+\frac{1}{2}\right] + H_x^{n+\frac{1}{2}}\left[i, j+\frac{1}{2}, k+1\right] - H_x^{n+\frac{1}{2}}\left[i, j+\frac{1}{2}, k\right]\right) \quad (7 \text{ flops})$$

$$E_z^{n+1}[i, j, k] = C_3\left(E_z^n[i, j, k] + D_z^{n+1}[i, j, k]\right) + C_4\left(H_x^{n+\frac{1}{2}}\left[i, j-\frac{1}{2}, k\right] - H_x^{n+\frac{1}{2}}\left[i, j+\frac{1}{2}, k\right] + H_y^{n+\frac{1}{2}}\left[i+\frac{1}{2}, j, k\right] - H_y^{n+\frac{1}{2}}\left[i-\frac{1}{2}, j, k\right]\right) \quad (7 \text{ flops})$$

where,

$$1. \quad n_{\text{complex}} = n - jk = \sqrt{\epsilon_r + \frac{\sigma}{j\omega\epsilon_0}}$$

If $\epsilon_r \geq 1$	If $\epsilon_r < 1$
$\omega_0 = \frac{\epsilon_0(\epsilon_r - 1)\omega^2}{\sigma}$	$\omega_0 = \frac{\sigma}{\epsilon_0(1 - \epsilon_r)}$
$C_1 = e^{-\omega_0\Delta t}$	$C_1 = e^{-\omega_0\Delta t}$
$C_2 = (\epsilon_r - 1)\left(1 + \frac{\omega^2}{\omega_0^2}\right)(1 - C_1)^2$	$C_2 = (\epsilon_r - 1)\left(1 + \frac{\omega^2}{\omega_0^2}\right)(1 - C_1)^2$
$C_3 = \frac{1}{1 + (\epsilon_r - 1)\left(1 + \frac{\omega^2}{\omega_0^2}\right)(1 - C_1)}$	$C_3 = \frac{1}{1 + (1 - \epsilon_r)\left(1 + \frac{\omega^2}{\omega_0^2}\right)(\omega_0\Delta t - (1 - C_1))}$
$C_4 = \frac{C_3\Delta t}{\epsilon_0\Delta x}$	$C_4 = \frac{C_3\Delta t}{\epsilon_0\Delta x}$

1.2.2. Convergence Checking

The goal of convergence checking is to determine whether or not the fields have reached steady state. This is done by comparing the fields at two points in time separated by one cycle ($1/f$ seconds). If they are equal (by some specified criterion) then the fields are assumed to have reached steady state. Once in steady state, no further changes to the fields are expected.

TEMPEST uses a cubic grid of test points (spaced five nodes apart in x, y and z) for the convergence checking. The electric field amplitude is calculated at each of these test points and compared to its value one cycle prior. The relative error is calculated for each test point:

Equation 1-13.
$$pterr = \frac{\vec{E}_{amp}(cT) - \vec{E}_{amp}((c-1)T)}{\vec{E}_{amp}(cT) + \vec{E}_{amp}((c-1)T)},$$

unless the denominator is deemed extremely small in which case the test point is not considered. The error at each point is compared to mre , the maximum relative error (usually set to 0.1) and quantized to a zero or one:

Equation 1-14.
$$PTERR = \begin{cases} 0, & pterr \leq mre \\ 1, & pterr > mre \end{cases}$$

The quantized error, $PTERR$ is summed for all test points to yield the total error:

Equation 1-15.

$$TOTERR = \sum_{testpoints} PTERR$$

In TEMPEST 5.0, the fields are said to have converged if $TOTERR = 0$ for three consecutive cycles.

1.2.3. Domain Excitation

The FDTD updating equations, as written in Equation 1-8 through Equation 1-12 do not introduce energy to the simulation domain. At time step zero, the electric and magnetic fields are zero throughout the domain and will remain so for all subsequent time steps unless energy is introduced. This introduction of energy is called “exciting the domain”.

In lithography simulation, the energy introduced into the simulation domain is in the form of a time-harmonic propagating field - a plane wave (or perhaps a group of plane waves). TEMPEST excites the domain with a plane wave by introducing current source terms into the Maxwell equations¹:

Equation 1-16.

$$\nabla \times \vec{E} = -\frac{\partial \vec{B}}{\partial t} + \vec{J}_{s,m}(x, y, z, t)$$

Equation 1-17.

$$\nabla \times \vec{H} = \frac{\partial \vec{D}}{\partial t} + \vec{J}_{s,e}(x, y, z, t)$$

For a monochromatic plane wave excitation emanating unidirectionally from the plane $z = z_{exc}$, with the phase front normal \vec{k} , the source terms are set to:

Equation 1-18.

$$\vec{J}_{s,m}(x, y, z, t) = Re\{\vec{A}_m e^{j(\omega t - k_x x - k_y y)}\} \delta(z - z_0)$$

Equation 1-19.

$$\vec{J}_{s,e}(x, y, z, t) = Re\{\vec{A}_e e^{j(\omega t - k_x x - k_y y)}\} \delta(z - z_0)$$

The magnitude, phase, sign of the z -component of the k -vector, and polarization of the plane wave is set by the complex vector coefficients \vec{A}_m and \vec{A}_e .

Consider the integral form of the Maxwell curl equations:

1. For simplicity, the region of space where the current terms are non zero is assumed to be lossless (i.e. $\sigma = 0$).

Equation 1-20.
$$\oint_C \vec{E} \cdot d\vec{l} = \int_A \left(-\frac{\partial \vec{B}}{\partial t} + \vec{J}_{s,m} \right) dA$$

Equation 1-21.
$$\oint_C \vec{H} \cdot d\vec{l} = \int_A \left(\frac{\partial \vec{D}}{\partial t} + \vec{J}_{s,e} \right) dA$$

Where the area A is a rectangular region in the zx-plane with perimeter the contour C as shown in Figure 1-3. For Δx sufficiently small, and in the limit $\Delta z \rightarrow 0$, Equation 1-20 becomes

$$\oint_C \vec{E} \cdot d\vec{l} \cong \Delta x E_{2,x} - \Delta x E_{1,x} = \Delta x K_{m,y}$$

$$\Rightarrow E_{2,x} - E_{1,x} = K_{m,y}$$

Equation 1-22.

where the existence of a surface current $K_{m,y}$ has been admitted, but the existence of infinite flux density is not (hence the area integral over $\frac{\partial \vec{D}}{\partial t}$ disappears).

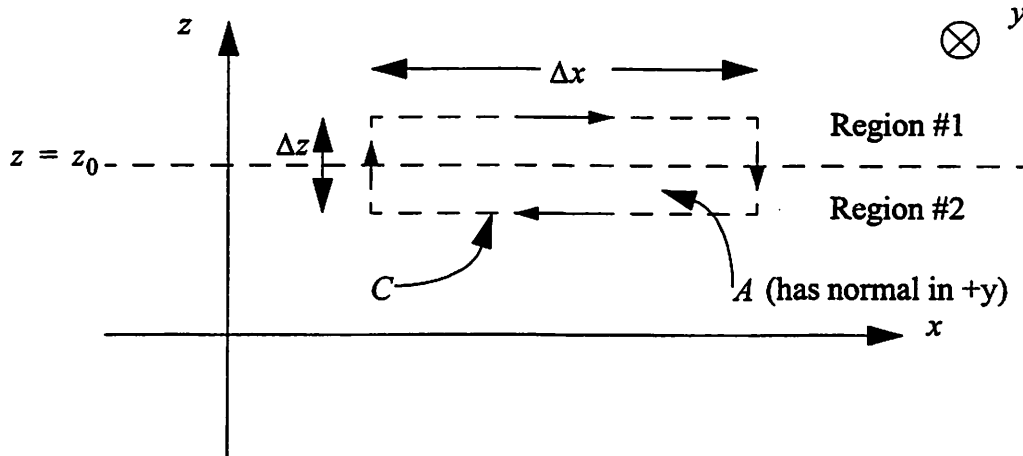


Figure 1-3. Determining the source currents for domain excitation

Similarly,

Equation 1-23.
$$E_{2,y} - E_{1,y} = -K_{m,x}$$

Equation 1-24.
$$H_{2,x} - H_{1,x} = K_{e,y}$$

Equation 1-25.
$$H_{2,y} - H_{1,y} = -K_{e,x}$$

At this point, setting the condition that the fields are zero in Region #1 leads to the relation between the current sources and the excited field:

Equation 1-26.
$$K_{m,y} = E_{2,x}$$

Equation 1-27.
$$K_{m,x} = -E_{2,y}$$

Equation 1-28.
$$K_{e,y} = H_{2,x}$$

Equation 1-29.
$$K_{e,x} = -H_{2,y}$$

Thus, with knowledge of the x and y components of the electric and magnetic fields, the surface current source terms are known. The Yee updating equations can be modified to include these source terms.

1.2.4. TEMPEST Algorithm

The TEMPEST algorithm is outlined in Figure 1-4.

1.3. Optical Imaging Models and Aerial Image Calculation

An “imaging system” in this thesis refers to the machines lithographers use to projection print images onto the wafer (“steppers” and/or “scanners”) or to the machines used to inspect either the wafers or the mask (“inspection systems”). Rather than directly solving the Maxwell equations to model the many optical elements present in an imaging system (lenses, apertures, mirrors etc.), the science of optics[15][35] is applied.

One notable implementation of the equations of optics, specifically the Hopkins formulation[42], is SPLAT[83], a program written at UCB by Flanner [30] and used by Neureuther to investigate defect interactions with features[56] and optical proximity effects[29]. Toh[83] added aberration capabilities to SPLAT and used it to investigate the effects of lens aberrations in lithography. Yeung[100] extended the Hopkins theory to include high numerical aperture effects and thin-film interference effects.

Because SPLAT is based on the Hopkins theory of partially coherent imaging[42] which uses transmission cross-coefficients (TCCs) to calculate the image intensity pattern, it assumes that the mask can be modeled by a scalar transmission function and that the scattering coefficients (or “diffraction efficiencies”) are independent of angle of incidence.

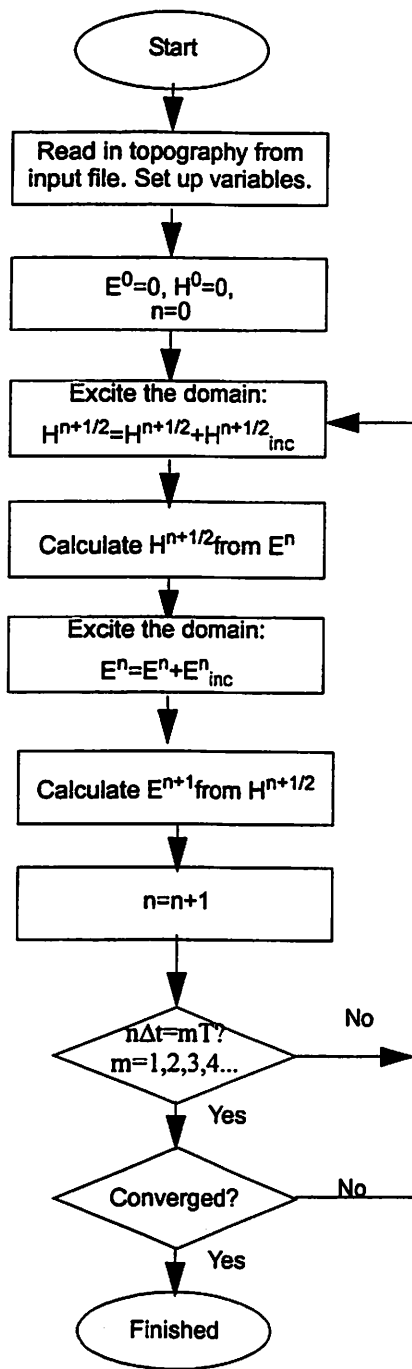


Figure 1-4. The TEMPEST Algorithm

Program flow with convergence checking. Note that convergence is checked only at time steps which correspond to the beginning of a wave cycle.

This assumption breaks down for high numerical aperture imaging and in inspection where highly oblique incidences are present. A vector-based theory that allows for the possibility of non-constant scattering coefficients is needed.

This thesis addresses the need for a vector based formulation of the optics and a linking of this vector-based formulation to the output of TEMPEST (Chapter 4). The position of the imaging system model in the overall scheme of aerial image calculation is illustrated in Figure 1-5. The imaging system model must take into account important optical parameters such as numerical aperture, partial coherence, magnification, defocus, aberrations and the specifics of the illumination.

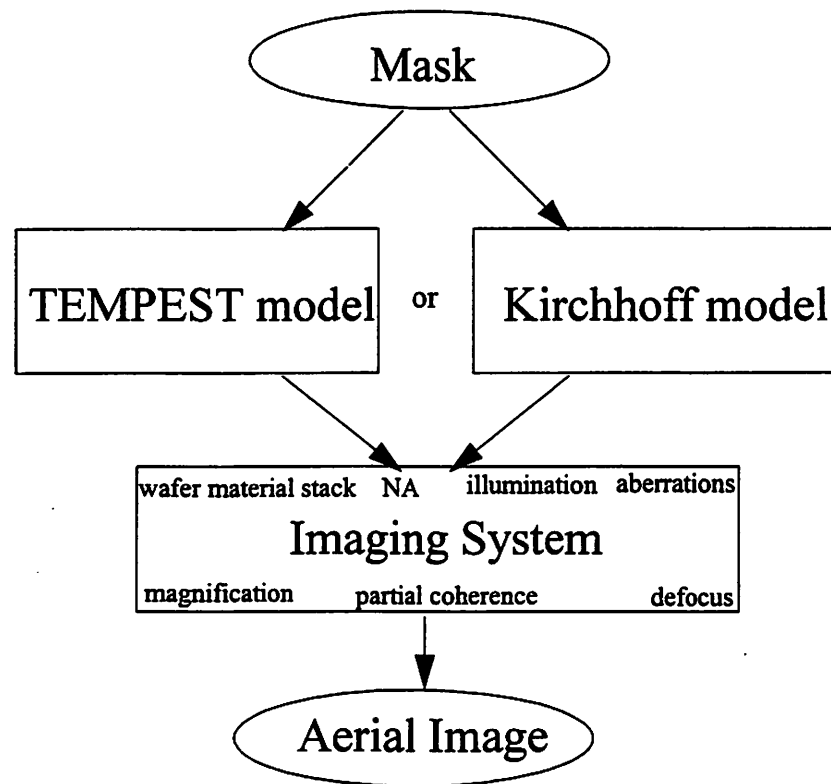


Figure 1-5. Overview of Aerial Image Calculation

The photomask can be modeled rigorously with TEMPEST or approximated using the Kirchhoff approximation (thin mask, described by transmission function). The imaging system model must interface with the mask model(s) and form the aerial image taking into account various optical parameters.

1.4. This Thesis

This thesis documents the many extensions to TEMPEST made over the past six years (since 1995). These improvements have enabled the simulation of many lithography-related phenomena including three-dimensional simulation of EUV masks and aerial image calculation for mask inspection systems.

The research described in this thesis is classified into three categories: academic contributions, improvements to TEMPEST and simulation studies. Due to breadth of topics discussed, topic-specific background is spread throughout the thesis and usually occurs in the beginnings of the chapters.

1.4.1. Academic Contributions

Two major academic contributions are described in this thesis. By the word “academic” it is meant that these contributions are novel and have not been researched in the context of electromagnetic simulation and lithography.

1.4.1.1. Fourier Boundary Condition

The growing interest in Extreme Ultraviolet Lithography (EUVL) has spurred on the need to simulate the scattering from the patterned multilayer mirror structures that serve as reflective photomasks for the soft x-ray wavelengths. These multilayer mirror structures are large relative to the wavelength of soft x-rays and thus require prohibitive amounts of computer memory to program into a FDTD simulator.

The Fourier Boundary Condition (FBC) is an alternative to programming the entire multilayer mirror structure into TEMPEST. It is a boundary condition that operates in the spatial frequency domain (i.e. it operates on the individual plane wave components of the propagating field) and can be programmed to yield any arbitrary reflectivity for the various plane wave angles of incidence. By programming the FBC with the reflective characteristics of an EUV multilayer mirror, tremendous memory savings can be achieved since the entire mirror structure does not have to be programmed into the FDTD grid.

1.4.1.2. Imaging System Formulation

Chapter 4 addresses the need for a fully three-dimensional, vector link between rigorous mask simulation and the optics of an advanced imaging system. Chapter 4 describes a model for an imaging system in which all components (the illumination, the object, the projection optic and the film stack at the wafer) are considered as operators on plane waves. The illumination is considered as a source of plane waves. The mask, a scatterer of plane waves, taking each input plane wave and scattering it into many output plane waves. The projection optic and the thin-film stack at the wafer are combined into a plane wave operator that take a single plane wave as input and yield a single plane wave as an output.

The details of mask models (how they scatter plane waves) is then investigated. Several mask models are presented along with a discussion of the range of applicability and the approximations made in each case.

A model for scanning optical microscopy commonly used in inspection systems is also proposed in Chapter 6.

1.4.2. Improvements to TEMPEST

The TEMPEST code has undergone several revisions in recent years. These are important contributions to but not academic, meaning that the theory behind these improvements has been developed and documented by other researches. The improvements made are nevertheless very important and crucial to the usefulness of electromagnetic simulation in photolithography.

1.4.2.1. PML boundary condition

For a long time, a lack of a good absorbing boundary condition has plagued the FDTD method as artificial reflections from the FDTD grid boundary would interfere with the true solution. In 1994, Berenger published a paper[10] on a new type of boundary condition which he named "Perfectly Matched Layers" or PML. The boundary condition is essentially a non-physical material with the special property that it absorbs electromagnetic radiation without reflection for all frequencies and angles of incidence. This new boundary condition was implemented into TEMPEST and is explained in Chapter 2.

1.4.2.2. Parallelization

The EUV simulations, because of the small wavelength and large feature sizes can require large simulation domains (perhaps several gigabytes). With current day technology (PC's and Workstations) it is impractical to simulate such large domains (not enough addressable memory and processors are too slow). Parallelization is a solution that allows many processors to operate on the problem simultaneously (Chapter 3).

1.4.3. Simulation Studies

The last three chapters of this thesis are dedicated to simulation results.

1.4.3.1. EUV

Chapter 5 presents several results concerning mask feature parameters such as absorber thickness and side wall angle and results concerning multilayer mirror defect printability. The Fourier Boundary Condition technique introduced in Chapter 2 and the parallel processing improvements presented in Chapter 3 were used for efficiency.

1.4.3.2. Alternating Phase Shift Mask Defects

Chapter 6 presents a simulation study of the printability and inspectability of phase defects in alternating phase shift masks. Aerial images for both printing and inspection scenarios are calculated. Due to the high angles of incidence present in mask inspection, the aerial images for inspection cases were calculated with the non-constant scattering coefficient mask model discussed in Chapter 4.

1.4.3.3. Overview of Various Lithography-Related Simulations

Outlines for the simulation of pinholes for EUV interferometry, wafer alignment marks, aberration monitor topography, reflective notching and two-dimensional phase shift mask topographical parameters are given.

2 Boundary Conditions for the Finite-Difference Time-Domain Method

2.1. Introduction

The Maxwell equations, being a system of second order partial differential equations, require boundary conditions in order for a unique solution to exist. This is true whether the fields are being solved in the continuous domain or in a discretized domain.

From a numerical algorithm point of view, the Yee equations (Equation 1-8 through Equation 1-12) update each cell's field values with equations involving neighboring cells. The cells at the edges of the (finite) simulation domain will be missing some of their neighbors and so either replacement cell must be used or a different set of updating equations must be used for the boundary cells.

This chapter begins by introducing the simplest boundary condition, the perfect conductor boundary condition. Periodic and symmetric boundary conditions are then discussed. These boundary conditions use other, judiciously chosen, cells as replacements for the missing cells. This has the effect of making the simulated topography infinitely long and periodic in the directions where the boundary conditions are applied. This is useful to lithographers since periodic mask topographies are common.

In many situations, the simulation domain may be lined with a material that absorbs energy to a degree sufficient to consider the fields at the boundary to be negligible. In these situations, it will not matter which boundary conditions are used at the edge of the simulation domain since any unphysical reflections will also be negligible. Such a situation is called a "material" boundary condition (MBC), since it involves the existence of some absorbing material. Although technically not a boundary condition, MBC's find use in situations

where highly reflective substrates are present such as mask inspection and reflective notching simulations.

A particularly useful subclass of the MBC is the Perfectly Matched Layers (PML) boundary condition invented by Berenger in 1994[10]. This boundary condition is quite good at absorbing outbound radiation without reflection.

Finally, a novel boundary condition called the “Fourier Boundary Condition” (FBC) is introduced. It operates on the Fourier components (plane waves) of electromagnetic fields and can be programmed to yield an arbitrary reflectivity versus angle-of-incidence. The FBC finds its main use in modeling multilayer mirrors used in Extreme Ultraviolet Lithography (Chapter 5), but other uses are also discussed.

2.2. Perfect Conductor Boundary Condition

The perfect conductor boundary condition is perhaps the easiest boundary condition to implement. The electric field simply gets set to zero inside the boundary cells. This can be seen from Equation 1-8 and Equation 1-10 letting $\sigma \rightarrow \infty$. If the electric field is initialized to zero at the beginning of the simulation, it can simply be not updated and thus remain zero throughout the simulation.

Although this boundary condition is easy to apply, it is not very useful by itself since lithographers are rarely interested in simulating topographies inside perfectly conducting boxes. It is useful when used to terminate the grid in conjunction with a material boundary condition such as PML.

2.3. Periodic and Symmetric Boundary Conditions

Another simple way to terminate the FDTD grid is to find some other cells within the domain to use in place of the missing nearest neighbors. Consider a cell on the most positive x face, $[N_x - 1, j, k]$ which is missing one of its nearest neighbors (the missing neighbor is the cell that would reside at $[N_x, j, k]$). There are three logical choices for the missing neighbor replacement:

a) use the cell at $[0, j, k]$ as the missing neighbor

b) use the cell at $[N_x - 2, j, k]$ (i.e. the cell uses is one existing neighbor in the x-direction as both neighbors)

c) use the cell at $[N_x - 1, j, k]$ (i.e. the cell uses itself as the missing neighbor)

These three options are illustrated in Figure 2-1. Choice (a) will lead to a simulated topography that is periodic in the directions which the boundary condition is applied and is referred to as a Periodic Boundary Condition (PBC). Choices (b) and (c), lead to topographies that have mirror symmetry, and are useful for saving computer resources because only half of a symmetric topography needs to be programmed and simulated.

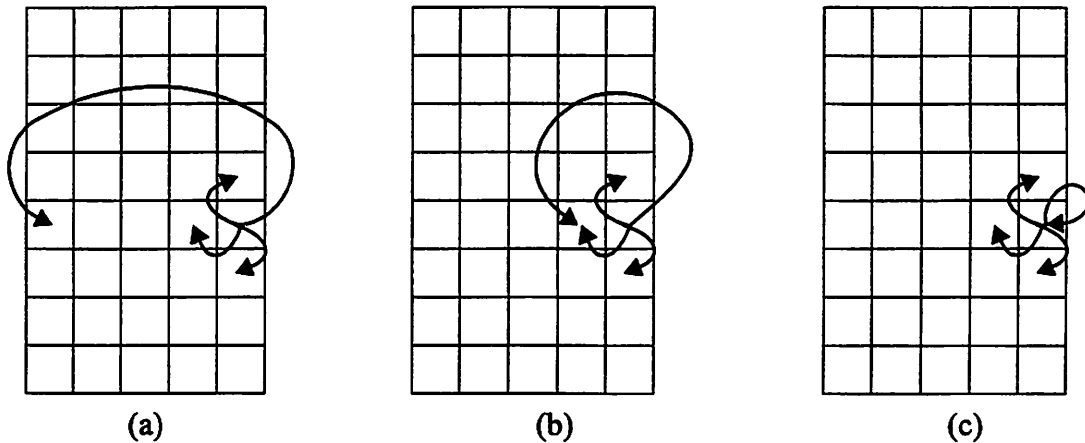


Figure 2-1. Replacement Possibilities for the Missing Nearest Neighbor Cell

a) Using the cell at the opposite end of the domain will lead to a periodic boundary condition. b) Using the existing neighbor will lead to a symmetric boundary condition. c) Using the cell it itself as its nearest missing neighbor will also lead to a symmetric boundary condition.

In lithography, it is common to have periodic mask structures such as a line/space pattern or an array of contact holes. The PBC is useful when applied in two directions (the x and y directions) but is rarely used in three dimensions (this would be a 3D array of objects - not usually occurring). The third dimension (the z-direction) usually applies another type of boundary condition such as a material boundary condition.

The effects of applying the periodic boundary condition are detailed in Figure 2-2 for a 2D topography and in Figure 2-3 for a 3D topography. When simulating photomasks, a 1D mask pattern, such as a line/space pattern, requires a 2D simulation domain and a 2D mask pattern, such as an array of contact holes requires a 3D simulation domain. A 2D simulation domain is simply a 3D simulation domain with one cell in the y-direction¹ and represents a topography that is uniform in the y-direction. 2D simulation domains are much smaller than 3D simulation domains and thus run many times faster (seconds rather than hours). All simulations in this thesis have periodic boundary conditions applied in the x and y directions.

The application of PBC's to the x and y directions of the simulation domain will have implications on the allowed plane wave excitations. Because the both the topography and the field values are “wrapped around”, both are periodic. Of course only one period of the topography and fields is tracked inside the computer, but, nevertheless, the electric and magnetic field components are periodic in the x and y directions. The general expression for the electric field for a propagating plane wave is:

Equation 2-1.
$$\vec{E}(x, y, z, t) = \vec{A}e^{j(\omega t - k_x x - k_y y - k_z z)}$$

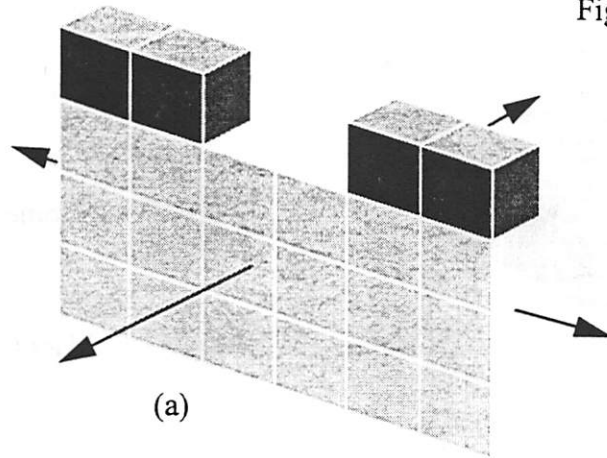
where $\vec{k} = (k_x, k_y, k_z)$ is the wave vector (units of radians/length) that indicates the wavelength and direction of propagation, ω is the radian frequency (units of radians/time) and \vec{A} is a complex vector indicating the polarization direction of the electric field and its magnitude and phase. Consider the electric field at the particular plane $z = 0$ and at the particular time $t = 0$. The field is a function of x and y only:

Equation 2-2.
$$\vec{E}(x, y) = \vec{A}e^{-j(k_x x + k_y y)}$$

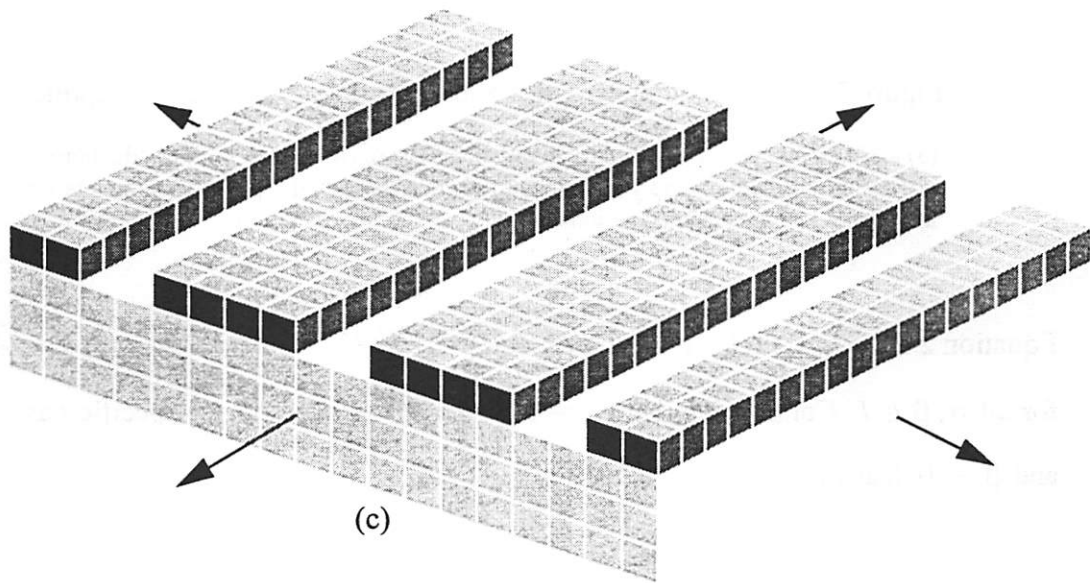
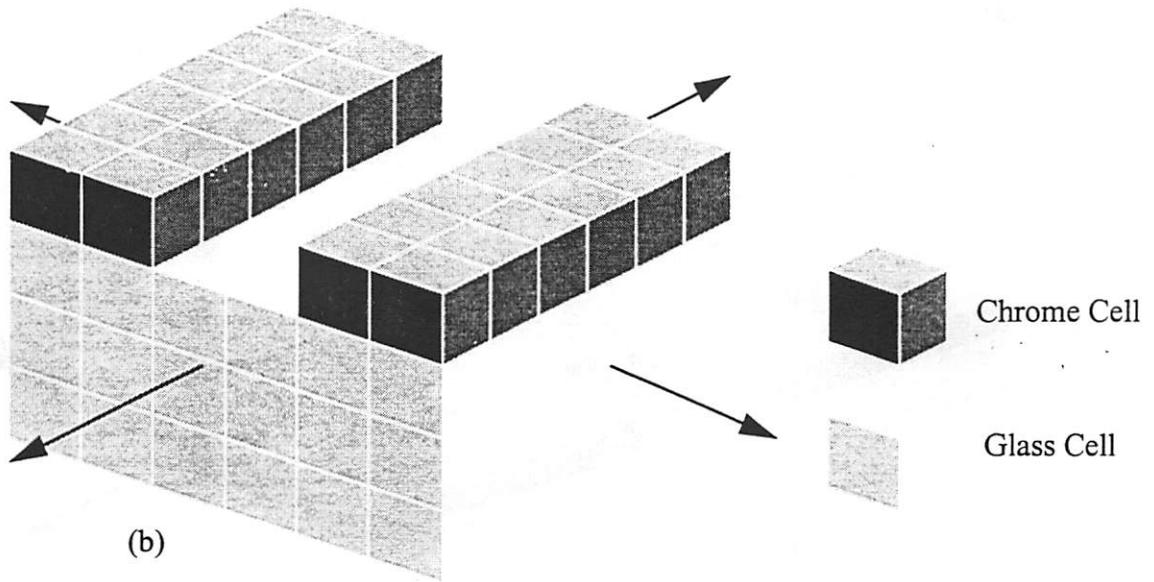
If the simulation domain has x and y dimensions of L_x and L_y respectively, and if periodic boundary conditions are applied, then the field of Equation 2-2 must be periodic in x and y with period L_x and L_y respectively, and therefore:

1. TEMPEST uses the y-direction as the only direction where only one cell is allowed. This is an arbitrary choice.

Figure 2-2. 2D Topography with Periodic Boundary Conditions Applied



(a) a 2D topography is really a 3D topography, but with only 1 cell in the y-dimension. (b) Applying periodic boundary conditions in the y-direction repeats the domain infinitely in the y-direction, thus "extruding" the topography in the y-direction. (c) Finally, applying periodic boundary conditions in the x-direction repeats the extruded domain in the x-direction.



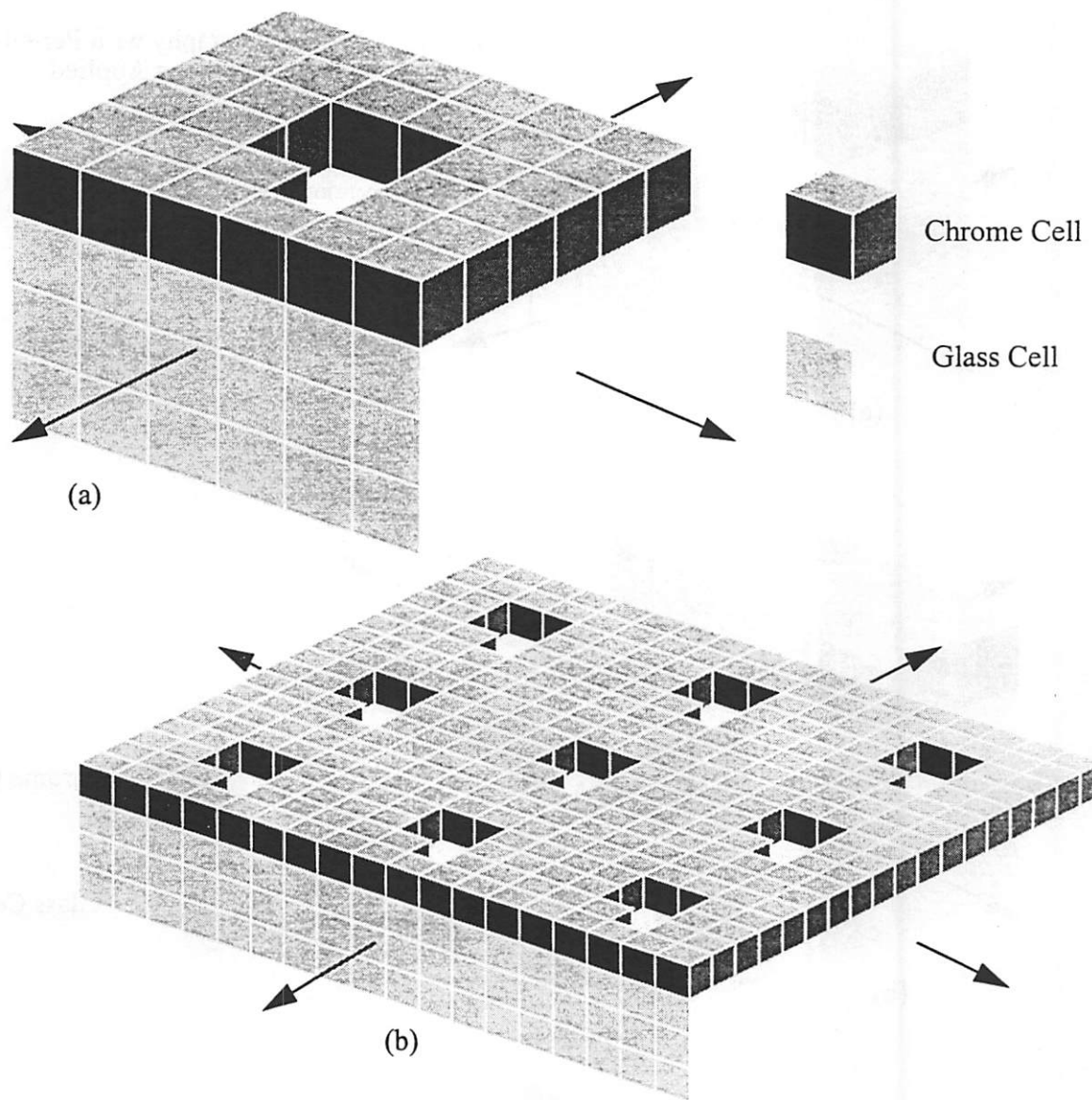


Figure 2-3. 2D Topography with Periodic Boundary Conditions Applied

(a) a 3D topography is required for simulating a 2D mask pattern. (b) Periodic boundary conditions in the x and y directions imply that the actual topography simulated in an infinite two dimensional periodic array.

$$\text{Equation 2-3. } \vec{E}(x + \alpha L_x, y + \beta L_y) = \vec{A} e^{-j(k_x(x + \alpha L_x) + k_y(y + \beta L_y))} = \vec{E}(x, y) = \vec{A} e^{-j(k_x x + k_y y)}$$

for all $\alpha, \beta \in I$. Considering that $e^a = e^{a + 2\pi m}$ for $m \in I$ and the specific case $\alpha = 1$ and $\beta = 0$ leads to:

$$\begin{aligned}
k_x(x + L_x) + k_y(y) &= k_x x + k_y y + 2\pi m \\
\Rightarrow k_x L_x &= 2\pi m \\
\Rightarrow k_x &= \frac{2\pi m}{L_x}
\end{aligned}$$

Equation 2-4.

A similar argument leads to

$$\text{Equation 2-5.} \quad k_y = \frac{2\pi n}{L_y}, \quad n \in I$$

Thus, PBC's imply that the k-vector for a propagating plane wave inside the simulation domain is limited to a discrete set of values determined by the condition of periodicity in the simulation domain with dimensions L_x by L_y . This means that only certain angles of incidence are allowed by the simulation domain.¹

The allowed k-vectors are best visualized using the k-space representation of plane waves (see Appendix A) and is done so in Figure 2-4.

The angle of plane wave propagation can written:

$$\text{Equation 2-6.} \quad \theta = \text{asin}\left(\frac{\sqrt{k^2 - k_x^2 - k_y^2}}{k}\right)$$

and

$$\text{Equation 2-7.} \quad \phi = \text{atan}\left(\frac{k_y}{k_x}\right)$$

where θ is the angle the direction of plane wave propagation makes with the z-axis and ϕ is the azimuthal angle.

1. The condition $\vec{E}(x + \alpha L_x, y + \beta L_y) = \vec{E}(x, y)$, $\alpha, \beta \in I$, is overly strict. If a complex field formulation of the Yee equations is used, then a less restrictive periodic equation can be applied: $\vec{E}(x + \alpha L_x, y + \beta L_y) = e^{j(\alpha\gamma + \beta\delta)} \vec{E}(x, y)$, $\gamma, \delta \in R$, $\alpha, \beta \in I$. This would allow fields that are periodic up to a phase factor to exist inside the simulation domain. The time-averaged field intensity, of course, by periodic symmetry is restricted to being a truly periodic real function.

TEMPEST does not implement a complex formulation of the Yee algorithm (to reduce memory requirements) and, although it is theoretically possible, it is difficult to extract the complex fields in an efficient manner and so the more restrictive condition is adhered to.

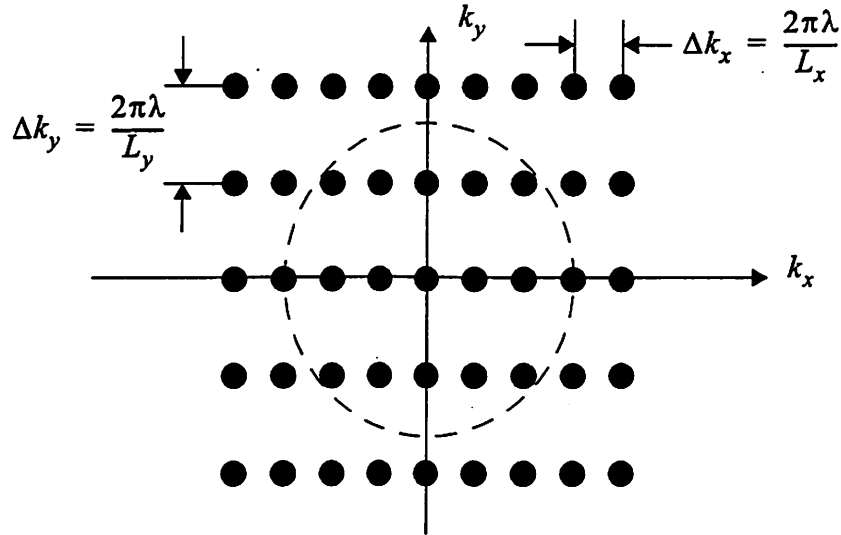


Figure 2-4. Plane Waves Allowed by Periodic Boundary Conditions in Two Dimensions

2.4. Material Boundary Conditions

Often, a simulated topography lies on top of a substrate with a reflective and/or highly absorbing material. This can be useful for truncating the FDTD grid in one direction. If the reflective and/or highly absorbing substrate is thick enough to sufficiently attenuate any wave before reaching the domain boundary, then the fields will be very small at the domain boundary and the simple perfect conductor boundary condition could be applied. This ideal is illustrated in Figure 2-5. Technically, this is not really a new boundary condition, rather it is just the perfect conductor boundary condition applied in a situation where the reflections produced are negligible.

2.5. Absorbing Boundary Conditions

An absorbing boundary condition is a boundary condition that absorbs electromagnetic radiation exiting the simulation domain without producing reflections. This effectively “extends” the simulation domain to infinity in the direction normal to the side of the simulation domain that has the boundary condition applied.

In this thesis, the absorbing boundary conditions are applied to the top and bottom of the simulation domain effectively extending the material at the top of the domain upwards to $z = \infty$ and the material at the bottom of the domain downwards towards $z = -\infty$. Con-

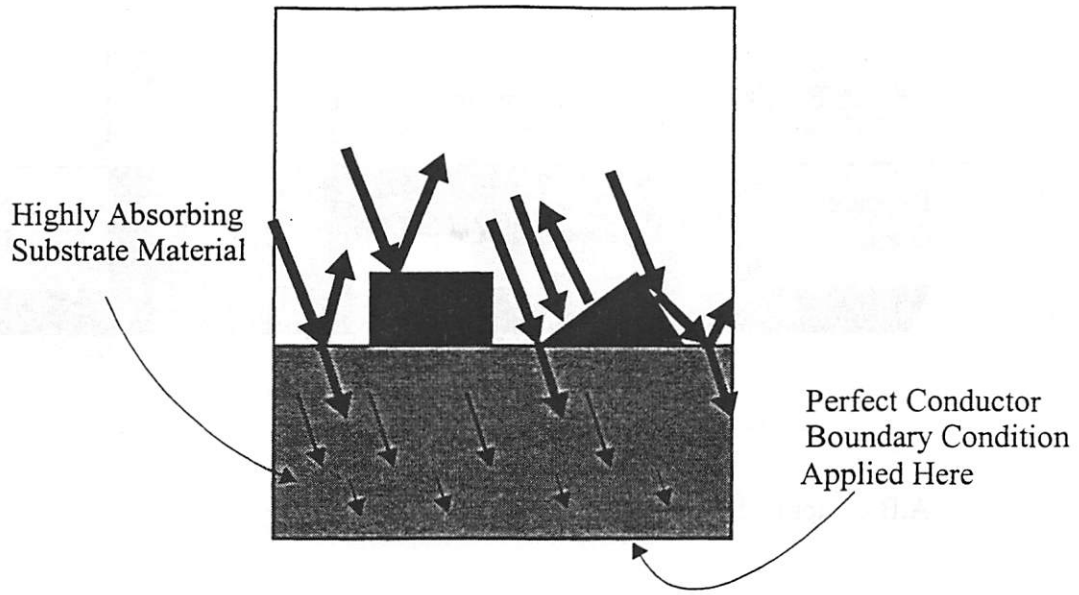


Figure 2-5. The Material Boundary Condition

The field is attenuated by the substrate material enough so that any reflection of the perfect conductor boundary condition at the bottom of the domain is negligible.

consider the simulation of typical photomask shown in Figure 2-6. The combination of periodic boundary conditions in the x and y directions and the absorbing boundary condition in the z direction implies a simulated topography that is infinite in extent, period in the x and y directions with a infinite half space of glass in the upper side and an infinite half-space of air on the lower side.

Several schemes for implementing absorbing boundary conditions have been developed [55][40][51][91], but all exhibited mediocre reflection performance until Berenger, in 1994, invented the first truly useful absorbing boundary condition which he named “Perfectly Matched Layers” here forth referred to as “PML”[10][33][102].

The PML boundary condition is a material boundary condition with the special condition that the material is chosen in such a way as to absorb outgoing fields without producing any reflections. As with the general material boundary condition, the idea is to have thickness of the material enough to sufficiently attenuate the field effecting the use of the perfect conductor boundary condition at the true boundary of the simulation domain.

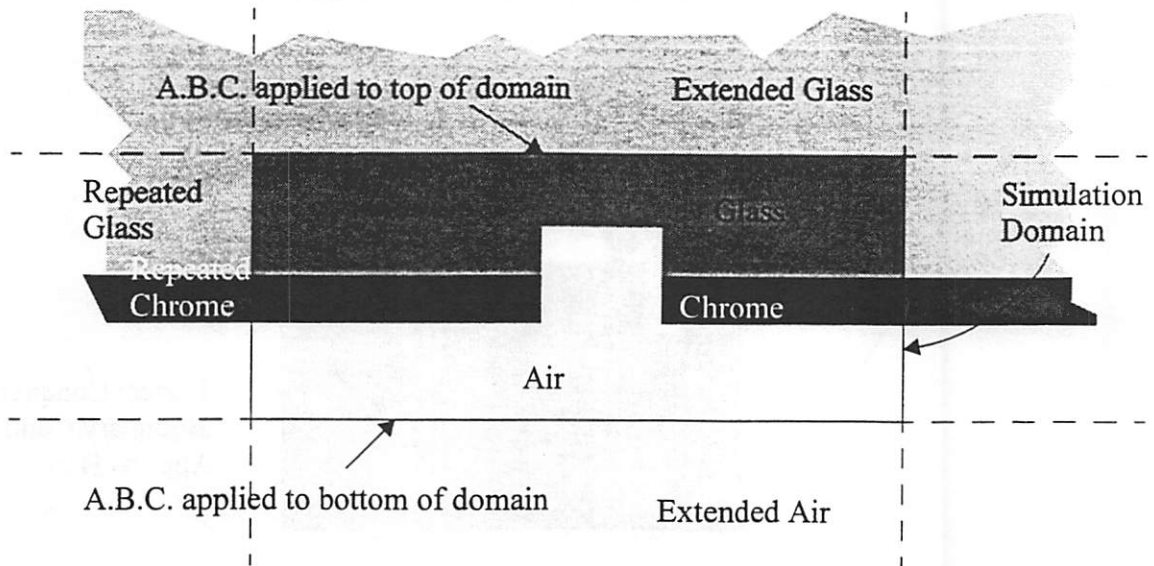


Figure 2-6. Absorbing Boundary Conditions Applied to the Top and Bottom of the Domain

Periodic boundary conditions repeat the domain topography in the x direction while absorbing boundary conditions at the top and bottom of the domain extend the (repeated) topography upwards and downwards.

There is no choice of a physically real material that is reflectionless. To find a material that is reflectionless, one needs to look beyond physically realizable materials to magnetic current conducting, anisotropic materials that can not exist physically (due to lack of magnetic charge, current and conductivity) but can exist inside a computer simulation. The Maxwell curl equations, and the constitutive relations, generalized for magnetic conductivity and anisotropy are written:

Equation 2-8.
$$\nabla \times \vec{E} = -\frac{\partial \vec{B}}{\partial t} + \vec{J}_m$$

Equation 2-9.
$$\nabla \times \vec{H} = \frac{\partial \vec{D}}{\partial t} + \vec{J}_e$$

Equation 2-10.
$$\vec{D} = \begin{bmatrix} \epsilon_x & 0 & 0 \\ 0 & \epsilon_y & 0 \\ 0 & 0 & \epsilon_z \end{bmatrix} \vec{E}$$

Equation 2-11.

$$\vec{B} = \begin{bmatrix} \mu_x & 0 & 0 \\ 0 & \mu_y & 0 \\ 0 & 0 & \mu_z \end{bmatrix} \vec{H}$$

Equation 2-12.

$$\vec{J}_e = \begin{bmatrix} \sigma_{e,x} & 0 & 0 \\ 0 & \sigma_{e,y} & 0 \\ 0 & 0 & \sigma_{e,z} \end{bmatrix} \vec{E}$$

Equation 2-13.

$$\vec{J}_m = \begin{bmatrix} \sigma_{m,x} & 0 & 0 \\ 0 & \sigma_{m,y} & 0 \\ 0 & 0 & \sigma_{m,z} \end{bmatrix} \vec{E}$$

where subscripts e and m are now used to differentiate between electric and magnetic current and conductivity.

Fourier transforming the curl and constitutive equations and switching to the usual complex phasor notation for the fields gives:

Equation 2-14.

$$\nabla \times \vec{E}(\omega) = -j\omega \vec{B}(\omega) + \vec{J}_m(\omega)$$

Equation 2-15.

$$\nabla \times \vec{H}(\omega) = j\omega \vec{D}(\omega) + \vec{J}_e(\omega)$$

Equation 2-16.

$$\vec{D}(\omega) = \epsilon_0 \epsilon_r(\omega) \vec{E}(\omega)$$

Equation 2-17.

$$\vec{B}(\omega) = \mu_0 \mu_r(\omega) \vec{H}(\omega)$$

Equation 2-18.

$$\vec{J}_e(\omega) = \underline{\sigma}_e(\omega) \vec{E}(\omega)$$

Equation 2-19.

$$\vec{J}_m(\omega) = \underline{\sigma}_m(\omega) \vec{H}(\omega)$$

Substituting the constitutive equations into the curl equations gives:

$$\text{Equation 2-20. } \nabla \times \vec{E}(\omega) = -j\omega \mu_0 \left(\underline{\mu}_r(\omega) - \frac{\underline{\sigma}_m(\omega)}{j\omega \mu_0} \right) \vec{H}(\omega) = -j\omega \mu_0 \underline{\mu}_{\text{complex}}(\omega) \vec{H}(\omega)$$

and

$$\text{Equation 2-21. } \nabla \times \tilde{H}(\omega) = j\omega \epsilon_0 \left(\epsilon_r(\omega) + \frac{\sigma_e(\omega)}{j\omega \epsilon_0} \right) \tilde{E}(\omega) = j\omega \epsilon_0 \epsilon_{complex}(\omega) \tilde{E}(\omega),$$

where the following complex permeability and permittivity tensors have been introduced:

$$\begin{aligned} \underline{\mu}_{complex}(\omega) &= \underline{\mu}_r(\omega) - \frac{\underline{\sigma}_m(\omega)}{j\omega \mu_0} \\ \underline{\epsilon}_{complex}(\omega) &= \underline{\epsilon}_r(\omega) + \frac{\underline{\sigma}_e(\omega)}{j\omega \epsilon_0} \end{aligned}$$

Equation 2-22.

In the frequency domain, the effects of conductivity and permittivity (or permeability) are lumped together. Thus, any material is described by two complex, second-order, diagonal tensors $\underline{\mu}_{complex}(\omega)$ and $\underline{\epsilon}_{complex}(\omega)$.

Berenger deduced $\underline{\mu}_{complex}(\omega)$ and $\underline{\epsilon}_{complex}(\omega)$ by solving the plane wave reflection problem[49] (Figure 2-7) where the reflected wave's amplitude is set to zero and the material properties are solved for. This led to[33]:

$$\text{Equation 2-23. } \underline{\epsilon}_{complex,B}(\omega) = \underline{\epsilon}_{complex,A}(\omega) \begin{bmatrix} \kappa + \frac{\sigma}{j\omega \epsilon_0} & 0 & 0 \\ 0 & \kappa + \frac{\sigma}{j\omega \epsilon_0} & 0 \\ 0 & 0 & \left(\kappa + \frac{\sigma}{j\omega \epsilon_0} \right)^{-1} \end{bmatrix}$$

and

$$\text{Equation 2-24. } \underline{\mu}_{complex,B}(\omega) = \underline{\mu}_{complex,A}(\omega) \begin{bmatrix} \kappa + \frac{\sigma}{j\omega \epsilon_0} & 0 & 0 \\ 0 & \kappa + \frac{\sigma}{j\omega \epsilon_0} & 0 \\ 0 & 0 & \left(\kappa + \frac{\sigma}{j\omega \epsilon_0} \right)^{-1} \end{bmatrix}$$

where

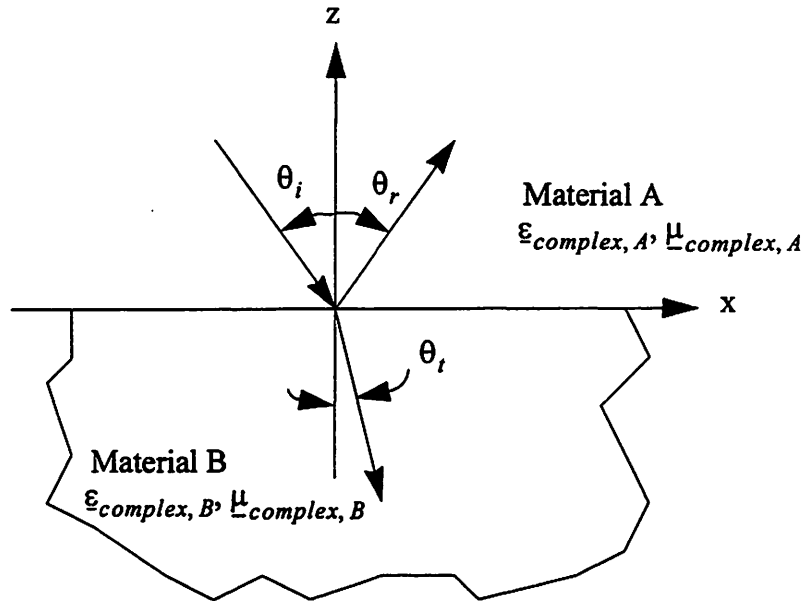


Figure 2-7. Set-up for the Plane Wave Reflection Problem

This is the setup for the standard reflection of plane waves problem. The phase matching condition at $z=0$ will force $\theta_r = \theta_i$ (angle of incidence equals angle of reflection) while other boundary conditions on the electric and magnetic fields will determine the θ_t (direction of transmitted wave) and the magnitude of both the reflected and transmitted waves relative to that of the incident wave. For PML, instead of solving for the reflection coefficient in terms of material properties, the reflection coefficient is set to zero and the material properties are solved for.

$$\epsilon_{complex,A}(\omega) = \epsilon_0 \left(\epsilon_r + \frac{\sigma_e}{j\omega\epsilon_0} \right)$$

Equation 2-25.

$$\mu_{complex,A}(\omega) = \mu_0 \mu_r$$

are the material constants for Material A. The attenuation of the transmitted wave in Material B is controlled by the κ and σ parameters.

The PML theory thus far works in the continuous domain but not in the discretized domain. Berenger[10] noted that an abrupt change in $\epsilon_{complex}$ or $\mu_{complex}$ in a finite difference scheme will produce reflections. For this reason, the κ and σ parameters (which provide the attenuation) must start at 1 and 0 respectively at the interface between the PML and the adjacent material, and then be slowly “ramped up” from cell to cell as the depth into the PML material increases to provide the attenuation. In [33] it was determined that a quartic

variation in these parameters was optimal. The application of the PML (in one direction - specifically, the z-direction) is illustrated in Figure 2-8.

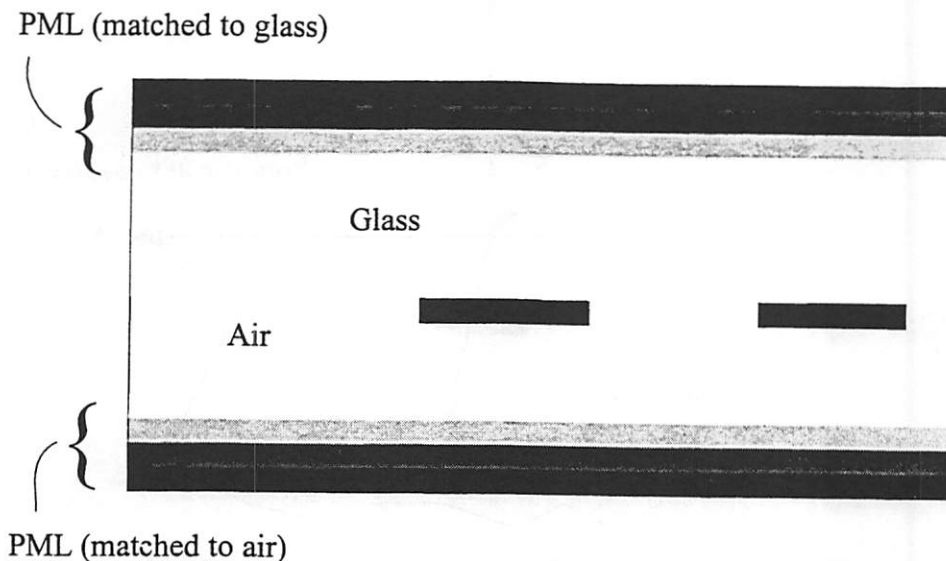


Figure 2-8. A 2D FDTD domain with PML at the top and at the bottom

A typical phase shift mask topography is illustrated. The PML at the top is matched to the glass and the PML at the bottom is matched to the air. The conductivity is “ramped” up from layer to layer to eliminate numerical reflections.

The TEMPEST implementation of PML requires the material at the top and bottom of the domain to be homogeneous (i.e. the PML can be matched to only one material). Typically 8 cells of PML are sufficient for eliminating reflections in lithography simulation. The backside of the PML can be terminated with the perfect conductor boundary condition or even a period boundary condition (applied in the z direction) if PML exists at both the top and the bottom of the simulation domain.

2.6. Fourier Boundary Condition

The motivation for the development of the Fourier Boundary Condition was provided by the multilayer mirror substrate used for the mask in Extreme Ultraviolet Lithography (EUVL) (Chapter 5). This multilayer mirror typically has 80 or more alternating thin-film layers of silicon and molybdenum and is patterned with an absorbing material (chromium for example) to create a reflective photomask. The multilayer mirror by itself is a one-

dimensional topography and is uniform in two dimensions. The total thickness of the typically 80 layers is approximately 20 wavelengths. Programming such a structure (20 wavelengths in one dimension) into a FDTD grid, such as that used by TEMPEST, would require vast amounts of memory. Coupled with the fact that an analytical solution for the mirror reflectivity exists, a more efficient way to model the multilayer mirror was sought. The Fourier Boundary Condition (FBC) was developed and implemented into TEMPEST for this reason.

The idea behind the FBC is to decompose the electromagnetic field into plane wave components (using Fourier transform theory), to then apply an appropriate reflection coefficient to each plane wave component, and finally, to generate a reflected wave for each plane wave component. This approach can also be considered as an “equivalent dependent source” approach.

The construction of the FBC is outlined in Figure 2-9. The top half of the simulation

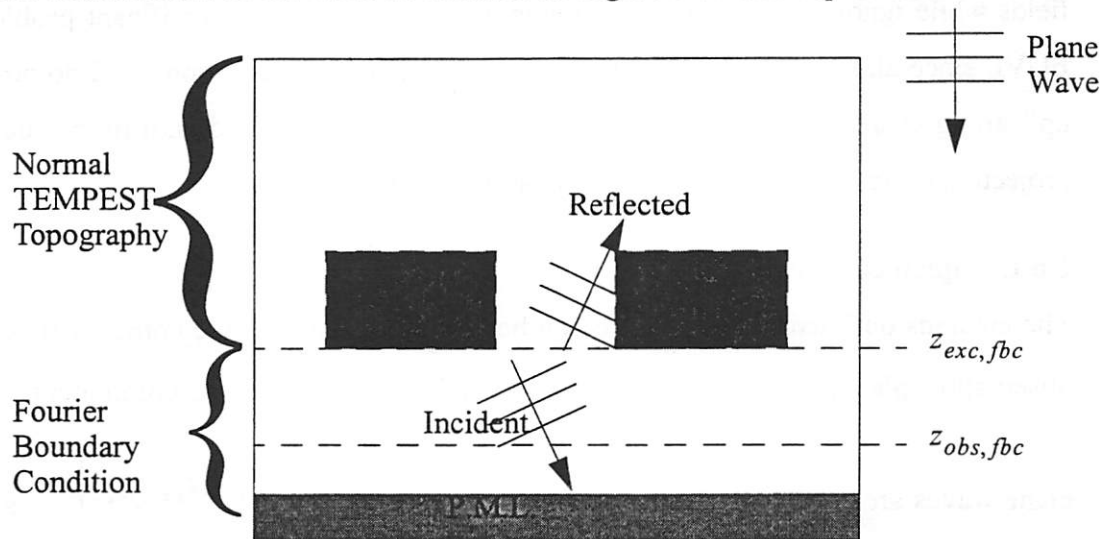


Figure 2-9. Components of the Fourier Boundary Condition

The incident field passes by the topography and is observed at the observation plane at $z = z_{obs, fbc}$. The incident field passes on down to the P.M.L. boundary condition where it is absorbed without reflection. Reflected waves for each incident plane wave are generated at the excitation plane at $z = z_{exc, fbc}$

domain is normal TEMPEST topography. The FBC exists from the plane $z = z_{exc, fbc}$ downward. The incident field passes by the topography and is observed at the observation

plane at $z = z_{obs, fbc}$. The incident field continues beyond the observation plane on down to the PML boundary condition where it is absorbed without reflection. The observed field at the observation plane is decomposed into plane wave components. A reflection coefficient for each of these incident plane waves is used to generate a new plane wave that emanates upward from the excitation plane $z = z_{exc, fbc}$. This new, upward travelling plane wave takes the place of the reflected plane wave.

The Fourier Boundary Condition is useful because it allows arbitrary reflection coefficients to be applied individually to each incoming plane wave component. When applied to a multilayer mirror, the plane wave reflection coefficients can be calculated analytically (using thin film theory [19]) and the FBC can be programmed to mimic the reflectivity of the mirror.

The FBC considers only the propagating plane wave components of the electromagnetic fields while ignoring the evanescent components. This is not a significant problem for EUVL since all materials have indices of refraction very close to unity and do not “kick up” strong evanescent fields. Additionally, the evanescent fields do not propagate to the projection optic and play no direct role in aerial image formation.

2.6.1. Implementation

The methods outlined in Appendix B can be used to decompose the complex field at the observation plane, $E(x, y, z_{obs, fbc})$, into its polarized plane wave components. These

plane waves are written in the two-element vector form, $\begin{bmatrix} A_{TE, mn}(z_{exc, fbc}) \\ A_{TM, mn}(z_{exc, fbc}) \end{bmatrix}_{k_{mn}}$, and are

indexed by the integers m and n . After decomposing the field, the next step is to “backward propagate” the plane waves to the plane where the FBC is acting, specifically, the excitation plane $z = z_{exc, fbc}$:

$$\text{Equation 2-26. } \begin{bmatrix} A_{TE, mn}(z_{exc, fbc}) \\ A_{TM, mn}(z_{exc, fbc}) \end{bmatrix}_{k_{mn}} = e^{j(-k_{mn,z}(z_{exc, fbc} - z_{obs, fbc}))} \begin{bmatrix} A_{TE, mn}(z_{obs, fbc}) \\ A_{TM, mn}(z_{obs, fbc}) \end{bmatrix}_{k_{mn}}$$

At this point, the reflection coefficients are applied to the waves and the reflected waves are written:

$$\text{Equation 2-27.} \quad \begin{bmatrix} R_{TE, mn} \\ R_{TM, mn} \end{bmatrix}_{k_{mn}} = \begin{bmatrix} r_{TE}(\theta_{mn}) A_{TE, mn}(z_{obs, fbc}) \\ r_{TM}(\theta_{mn}) A_{TM, mn}(z_{obs, fbc}) \end{bmatrix}_{k_{mn}}$$

These reflected waves are unidirectionally excited (by method of Chapter 1) upwards, in the direction opposite to the incident field.

The finite space between the bottom of the topography (which coincides with the excitation plane $z = z_{exc, fbc}$) and the PML material should be large enough to allow the evanescent fields kicked up by the topography to die away. The observation plane is situated between the PML and the excitation plane and should be located nearer to the PML again to avoid evanescent fields kicked up by the topography.

2.6.2. Performance

The FBC was implemented in the TEMPEST program mainly for the simulation EUVL mask scattering. Therefore, a good test of the FBC is to measure its performance (accuracy, speed and memory required) for a multilayer mirror scenario. Figure 2-10 shows the reflectivity (power) versus angle of incidence for a typical EUVL multilayer mirror. Reflectivity curves were generated in three ways: i) thin-film stack theory was used to calculate the theoretical reflectivity ii) the entire forty-bilayer mirror was programmed into the FDTD grid in TEMPEST (a “brute force” method), and iii) the FBC reflectivity was set to the theoretical reflectivity of the multilayer mirror. The reflectivity calculated by the “brute force” method was found to track the theoretical reflectivity relatively well for small angles, but deviated quite significantly for angles above 10 degrees. The FBC reflectivity matched the theoretical reflectivity to within 1% for the eight angles of incidence measured up to 36 degrees.

The memory required the 3D simulation of a typical EUV mask is illustrated in Figure 2-11. The use of the FBC is seen to save a tremendous amount of memory, especially for large features (large simulation domains). The 3D simulation of a 100nm feature would require more than 20 GBytes using the brute force method while using the FBC to model

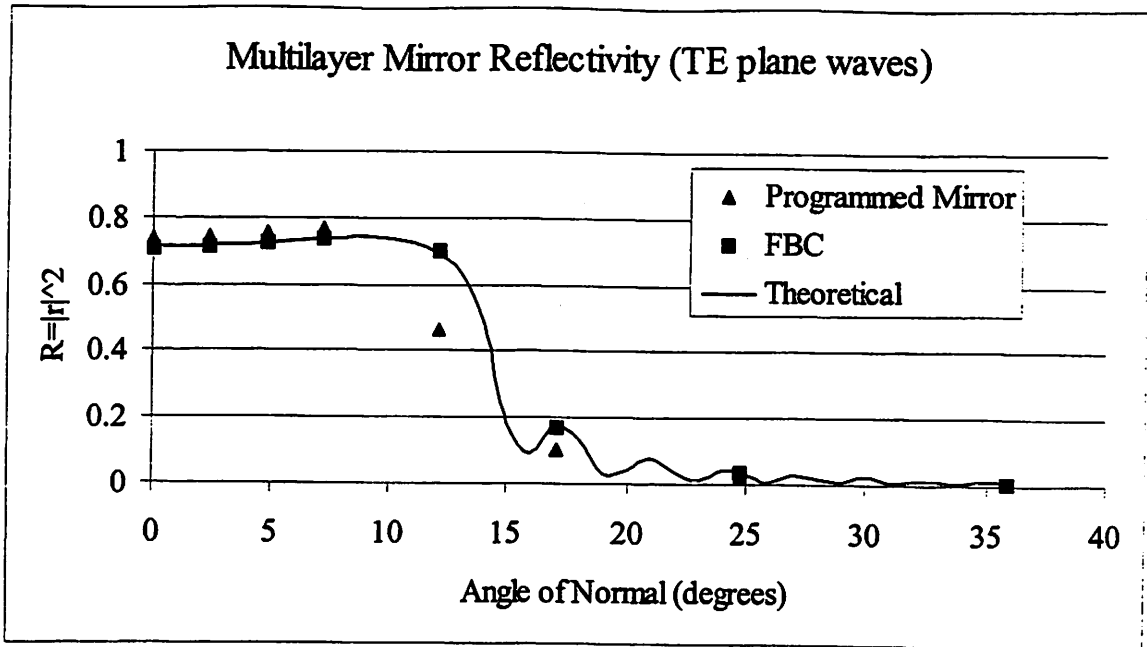


Figure 2-10. Multilayer Mirror Reflectivity (TE plane waves)

Both the “brute-force” programming of the multilayer mirror into the F.D.T.D. grid and the F.B.C. version do reasonably well in reproducing the theoretical reflectivity curve. The F.B.C. version, however, runs quicker and uses about one twentieth the

the mirror reduces the memory required to less than 4 Gbytes - an achievable memory requirement for the current-day technology.

The simulation time is dominated by FDTD updating equations and not by the Fourier operation used in the FBC. Thus, the simulation time curves will look similar to the memory required curves of Figure 2-11. A typical simulation time for a 100nm feature is 10 to 12 hours (assuming FBC is used, 16 200MHz PentiumPro processors working in parallel - see Chapter 3). Smaller features (30nm to 50nm CD) can run on desktop systems with 256MBytes in less than two hours when the FBC is used.

2.6.3. Fourier Boundary Condition used as an Absorbing Boundary Condition (FABC)

The Fourier Boundary Condition described thus far has been used to generate reflected waves for the purpose of simulating the reflections generated by some one dimensional topography (such as a multilayer mirror). A simple rearrangement of the excitation plane and the observation plane make the FBC useful in another respect - as an absorbing bound-

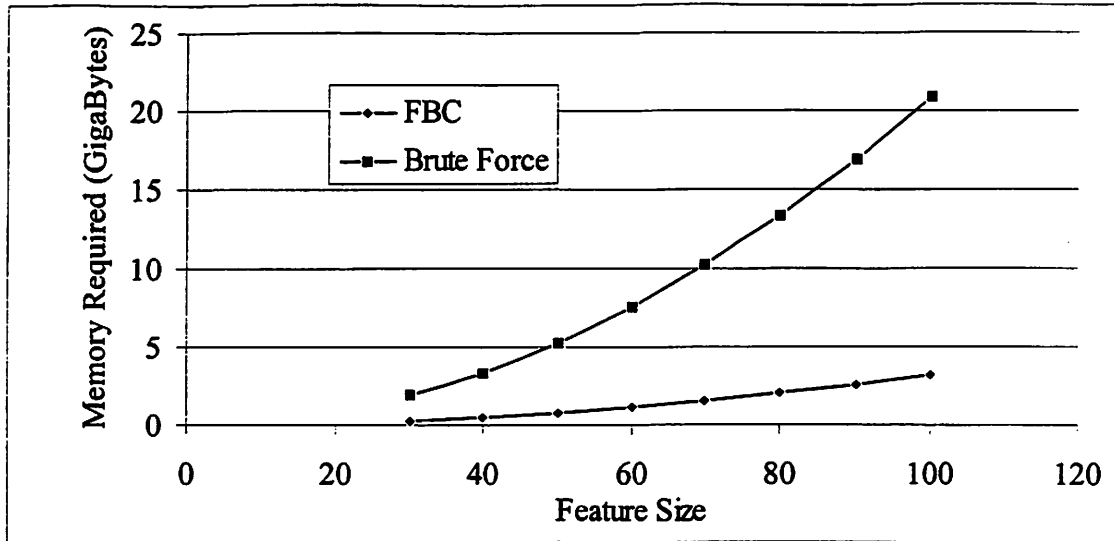


Figure 2-11. Memory Required for 3D EUV Mask Simulation

Using the FBC to model the multilayer mirror requires considerably less memory than does programming the entire mirror into the simulation domain. The simulation domain is assumed to be twice the feature size in the x and y directions, assumes 100nm thick aluminum absorber, $\lambda=13.4\text{nm}$, 4X mask size, and a 40 bilayer multilayer mirror.

ary condition. Suppose the positions of the excitation plane and the observation plane were interchanged. Additionally, suppose that the excitation plane generated plane waves not in the “reflected” direction (up), but in the “transmitted” direction (down) - (see Figure 2-12). The incident field will be decomposed into its component plane waves, and for each of these plane waves, a “transmitted” wave will be generated at the excitation plane. This time however, the excited wave will be travelling in the exact same direction of propagation as the incident wave. The two waves will add coherently. It is possible to program the transmitted wave to have the exact amplitude as the incident wave, but with a π phase shift to exactly cancel the incident wave. This cancellation will occur for all incident plane waves and so the field will be zero below the excitation plane. Since the field is zero below the excitation plane, any sort of boundary condition can be used (i.e. the perfect conductor boundary condition). The FBC, in this manner, forms a useful absorbing boundary condition. This ABC is referred to as the FABC

Of course, the PML already discussed above is an excellent absorbing boundary condition. The advantage of the FABC as compared to the PML is that it uses less memory and will

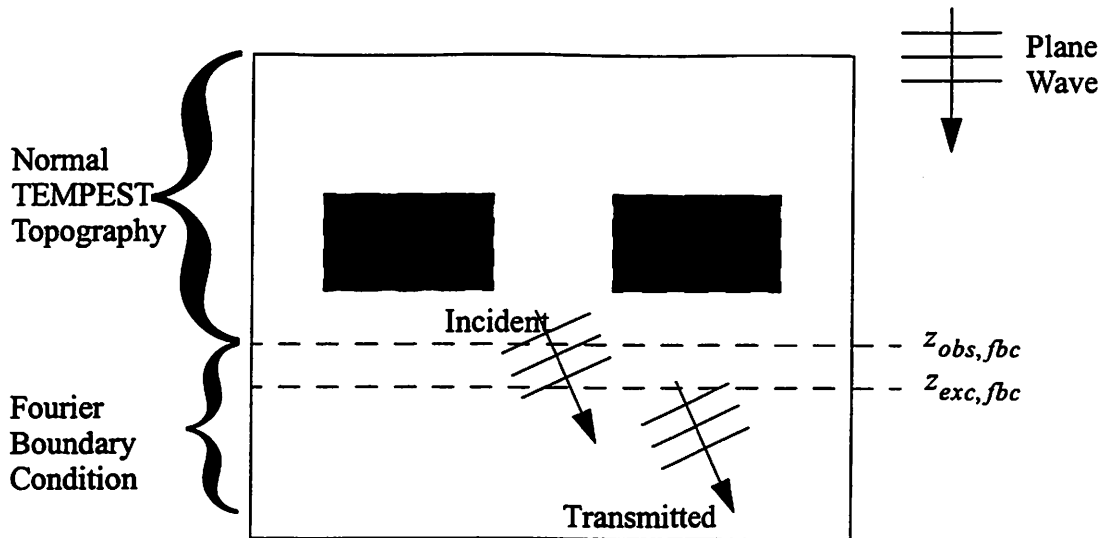


Figure 2-12. The Fourier Boundary Condition as an Absorbing Boundary Condition

The incident field passes by the topography and is observed at the observation plane at $z = z_{obs, fbc}$. A transmitted wave that exactly cancels the incident wave is generated at the excitation plane. The field below the excitation plane is zero and so no boundary condition need be applied.

run faster. The disadvantage is that it only works for monochromatic light and will likely not perform well for high angles of incidence.

The performance of the FABC is shown in Figure 2-13 where the reflectivity (power reflected) is plotted as a function of angle of incidence.

The FABC concept can be extended to surfaces other than planar surfaces. Consider a spherical region of space inside which the isolated topography to be simulated exists. Assuming homogeneous free space exists at the boundary of the sphere, a new boundary condition could be devised in analogy to the FABC. The field at some spherical surface $r = r_{obs}$ is observed and decomposed into spherical harmonics[44] (rather than plane waves). A second excitation sphere $r = r_{exc}$ outside the observation sphere could be used to generate outward propagating spherical harmonics that exactly cancel those observed at the observation plane. This scheme could be used for simulating truly isolated topographies. In fact this entire spherical domain could exist inside a rectangular (and periodic) simulation domain such as that used in TEMPEST. The usual plane wave excitation could be used provided the observation surface is programmed to ignore it. Again the advantage

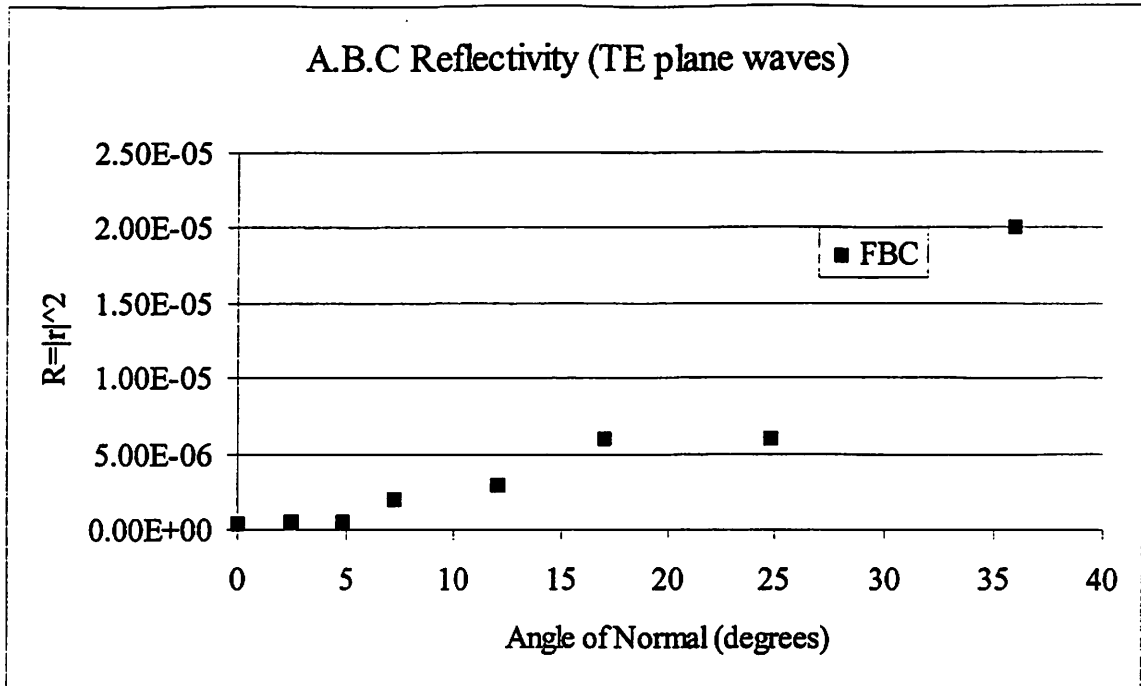


Figure 2-13. F.A.B.C. Reflectivity for TE Plane Waves

of this scheme over the PML is that it may possibly use fewer cells and run slightly faster provided the spherical harmonic decomposition isn't too intensive.

2.6.4. Other Uses of the FBC

Because any type of reflection/transmission coefficients can be applied to the FBC, many possible uses come about. For example, it could be used as a polarization filter (simply set the transmission of the TE waves to unity and the TM waves to zero). It could be used as an aperture (or spatial filter), or even as a 1X aberrated lens. Any operation in Fourier space could be applied.

2.7. Summary

The FDTD simulation domain must somehow be terminated with numerical boundary conditions. Various boundary conditions have been outlined and discussed.

Periodic and symmetric boundary conditions are typically applied in the horizontal directions and make the simulated topography periodic and infinite in length. Periodic boundary

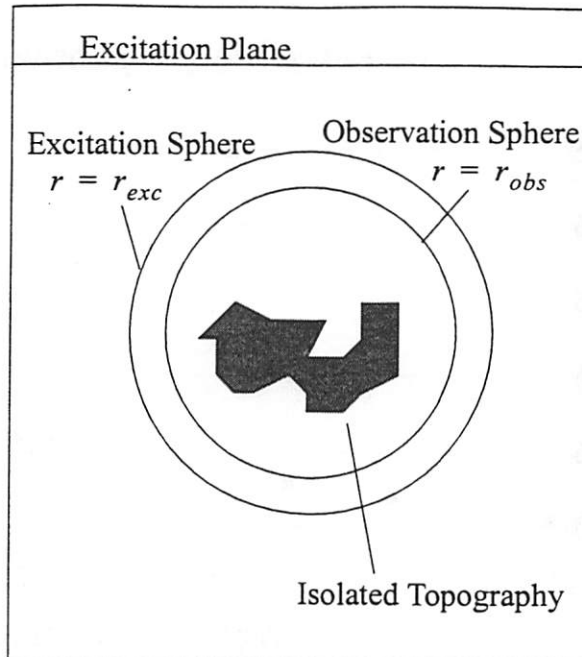


Figure 2-14. A scheme for extending the FABC to 3D

conditions, as implemented in TEMPEST, restrict the set of plane waves that are allowed to exist inside the simulation domain to those which have the same periodicity as the topography.

Material boundary conditions are simply the existence of a material at the boundary of the simulation domain with thickness and absorption sufficient to attenuate the outbound energy to a negligible level effecting the use of perfect conductor boundary conditions to terminate the grid.

Perfectly Matched Layers (PML) is an example of a material boundary condition where the material is especially chosen in such a way that no reflections are generated. This makes PML an excellent absorbing boundary condition that is typically applied to the top and bottom of a simulation domain to “extend” the domain upwards and downwards to infinity.

The Fourier Boundary Condition (FBC) was developed as an efficient model for an EUVL multilayer mirror. It operates on the Fourier components (plane) waves of the incident field and can be programmed to yield an arbitrary reflectivity versus angle-of-incidence. The FBC was demonstrated to be both an accurate and efficient model for a multilayer mirror.

The FBC can also be useful as an absorbing boundary condition as it can be set up to detect outgoing waves and eliminate them by annihilation with an annihilating wave with equal magnitude but opposite phase.

3 Parallelizing the Finite Difference Time Domain Algorithm

3.1. Introduction

The Finite Difference Time Domain Electromagnetic Simulation program TEMPEST was originally written to run on a parallel processor architecture [31][32][39]. In fact, the “MP” in “TEMPEST” stands for “massively parallel”. In 1995, as workstation memories began to exceed 100MByte, it became feasible to run TEMPEST simulations on desktop computers and Wong ported the TEMPEST code to a single processor architecture [96]. Since that time, it was found that the single processor version of TEMPEST and the current-day computational ability of workstations is insufficient for the newly-emerging EUV lithography simulations (see Chapter 5). Ironically, the code has been ported back to a parallel architecture - this time, not for a single multiprocessor supercomputer, but rather a Network of Workstations (also known as NOW) [6].

This chapter presents an overview of the (re)parallelization of the TEMPEST code and presents some performance results of the parallelized code.

3.2. Technique

The finite difference time domain algorithm first proposed by Yee[98] is easily parallelizable because each cell’s updating equations (See Chapter 1) involve only the six nearest neighbor cells. Matrix methods, such as the Finite Element Method, involve inverting a matrix - an operation that is not as easily parallelizable.

The parallelization of the algorithm involves breaking the simulation domain up into simulation subdomains (see Figure 3-1). Because, by TEMPEST convention, excitation planes are always xy-planes, the domain is divided only in the z-direction. This avoids breaking

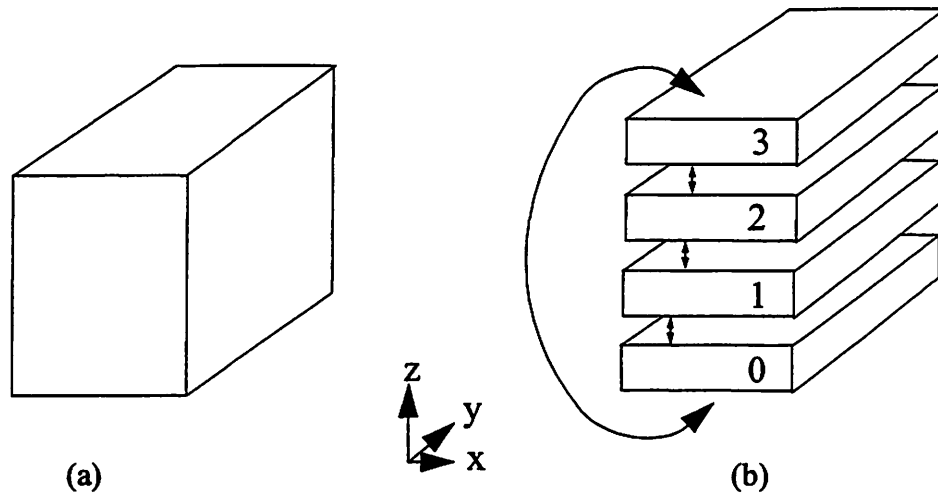


Figure 3-1. Breaking up the Simulation Domain for Parallel Calculation

The unbroken simulation domain (figure (a)) is divided with xy-cut-planes into simulation subdomains (figure (b)).

up excitation planes or output planes where Fourier Transform operations are performed. Not breaking the domain in the x and y directions also has the advantage that because of periodic boundary conditions, each subdomain is connected with itself in the x and y directions meaning no communications overhead for vertical faces.

Each processor in a multiprocessor system will execute the FDTD updating equations within its own simulation subdomain. Information at the upper and lower boundaries of each subdomain is passed between neighboring subdomains. Periodic boundary conditions are applied, as usual, in the x and y directions. The top of the upper domain “wraps” around to the bottom of the lower domain (effectively creating a periodic boundary condition also in the z-direction), although typically the Perfectly Matched Layers boundary condition (see Chapter 2) is used at the top and the bottom of the simulation domain.

The coding of the communication between subdomains is accomplished with The Message Passing Interface (MPI)[52], a protocol of routines that allow multiple processes to communicate across an inhomogeneous network of workstations.

3.3. Performance

Given that the total number of mathematical operations required for electromagnetic simulation is independent of how the simulation domain is divided, the best possible improvement obtainable with parallelization would be linear with the number of processors. Unfortunately, the added overhead of the communication of the boundary cell information limits the speed-up factor to being sub-linear. Obviously the best performance will be obtained when the amount of information to be communicated between subdomains is minimized and when communication speed is high.

The performance of parallel TEMPEST was assessed through several simulation experiments on different numbers of processors and with different groupings of the subdomains on different multiprocessor boxes. Figure 3-2 graphs the speed-up factor versus the number of processors. All simulations were run on SUN UltraSPARC II "boxes". Each box had multiple processors. The ideal speed-up factor curve is linear and equal to the number of processors. The "1 Box w/2 procs." curve is the performance of a box with only two processors. The "1 Box w/8 procs." is for a box with eight processors in it. Its speed-up curve closely tracks the ideal linear curve up until the number of processes exceeds eight (the number of processors in the box). The "Grouped 3 Boxes w/8 procs" curve is for the case when the processes are evenly divided between three boxes, and the neighboring processes are grouped to together (i.e. if 12 process simulation then processes 0,1,2 and 3 are run on box #1, processes 4,5,6 and 7 on box #2 and processes 8,9,10 and 11 on box #3) - minimizing the communication overhead. This curve has a considerably lower slope compared to the same-box curves due to the slower communication rate across the network between boxes. Finally, to grasp the importance of grouping nearby subdomains on the same box, a worse-case assignment was investigated where neighboring subdomains were located on different boxes meaning that all communications were across the network and none were within any box. The curve "Alt. 3 Boxes w/8 procs." shows that the performance of this scheme drastically degrades beyond six processes with a maximum speed-up factor of approximately 2.5.

Another factor affecting performance is load balancing. Since all subdomains must update together at the same time, the entire simulation will be limited by the slowest subdomain

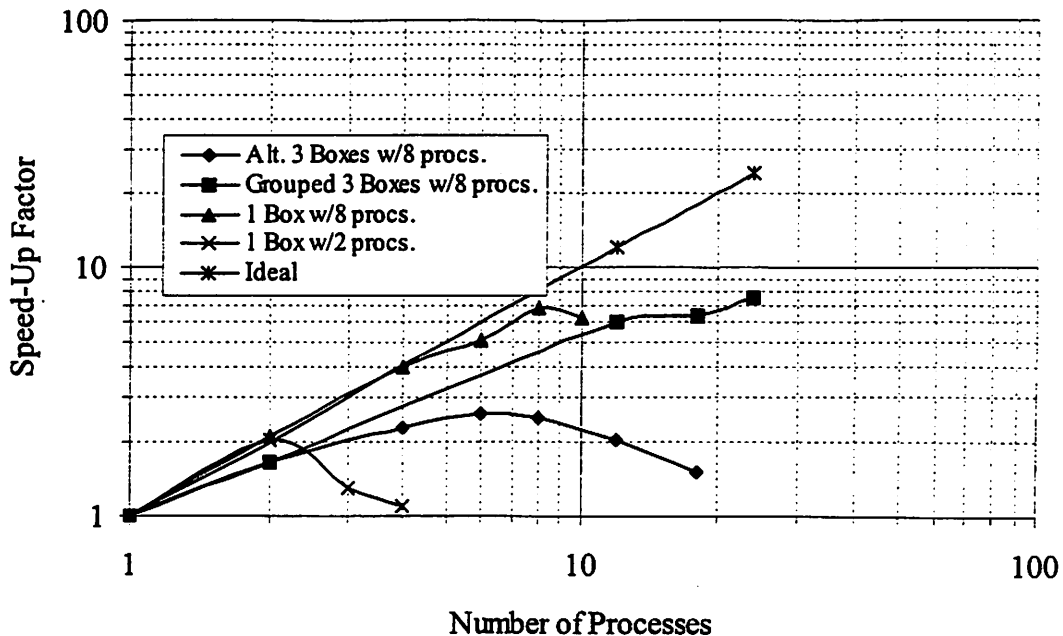


Figure 3-2. Performance of Parallel TEMPEST

and therefore, to maximize performance, the load (as measured in FLOPS) should be evenly distributed amongst the subdomains. The load of a particular subdomain depends on what updating equations the cells inside the domain use, which in turn depends on what kinds of materials present inside the subdomain. The following table lists the various types of materials (categorized by their updating equation type) along with the memory and FLOPS required per cell.

Material Type/ Updating equation	Memory required assuming single precision floating point numbers (bytes/cell)	FLOPs required/cell
Yee	25	33
Dispersive	37	48
PML	49	66

Table 3-1. Computational Resource Requirements for Various Materials

3.4. Summary

A parallelized version of TEMPEST using the Message Passing Interface to run across a Network of Workstations (NOW) was developed and benchmarked. It was observed that

the performance depended strongly on the inter-process communications overhead. The performance across several processors in the same box approximated the ideal linear speed-up curve, while the performance when all communications were over a network showed a maximum speed-up factor of only 2.5 for 6 processes.

One conclusion that can be drawn is that it is far better to buy one large box with N processors than to buy N boxes with one single processor each. However, often it is the memory requirements, and not the speed requirements that determine when parallel processing is needed and what architecture is required. Further discussion of these issues occurs in a book by Taflove.[79]

4 Imaging System Modeling

4.1. Introduction

Often, it is not the fields in the immediate vicinity of the mask topography, but rather an image formed by an imaging system at a remote image plane that is of primary interest to lithographers. This image, sometimes called the “aerial image” can be the intensity pattern in a thin layer of photoresist on a silicon wafer or perhaps the intensity pattern produced on a CCD camera or the retina of the human eye.

A modern, complex optical imaging system can have several lens, polarizer, aperture, and mirror components and is usually very large in relation to the wavelength of light. Thus it is not practical to simulate the imaging system with the FDTD method and TEMPEST. However, the science of optics can be applied to the imaging system components for modeling purposes.

The Hopkins theory of partially coherent imaging[41][42] is commonly used to calculate aerial images in lithography. One computer program, SPLAT, is based on Hopkins’ theory and has been used for aerial image calculation in lithography for several years[83][2].

To print or inspect smaller features, optics designers build optics with higher numerical apertures. For numerical apertures exceeding 0.5 to 0.6, the paraxial approximations made in scalar imaging theory are invalid and theory has been extended by Cole et al.[21][22] who removed the paraxial ray approximation in the projection optic model. This led to the “Radiometric Correction Factor” that extended the usefulness of the projection optic model to numerical apertures in the range 0.6 to 0.7.

But even with the radiometric correction factor, the scalar theory is deficient for high numerical aperture lithography ($NA \geq 0.6$) due to the differences in the way TE and TM plane waves behave, especially at the image plane where highly oblique plane waves exist. Yeung[100] realized that a vector formulation is required for high NA imaging inside thin film stacks and generalized the Hopkins' formula for vector fields. But he then points out that, upon entering the photoresist, the plane waves bend towards the normal reducing their degree of obliquity, and reverts back to a scalar theory which he claims is "sufficient for the practical simulation of aerial images in planar thin-film structures for numerical apertures at least as high as 0.6."

This thesis introduces the removal of yet one more approximation that is valid only when the plane waves incident to the mask are nearly normal. The Hopkins theory - even the extended vector theory developed by Yeung - still relies on the assumption that the object (photomask) can be represented as a two-dimensional transmission function that is independent from the angle of incidence and thus assumes constant diffraction efficiencies (later on referred to as "scattering coefficients"). This assumption of constant diffraction efficiencies is usually valid for angles of incidence less than 20 or 30 degrees[68][93] but is often invalid for large angles of incidence such as those occurring during mask inspection.

The Hopkins imaging equations can not be used when diffraction efficiencies depend on angle of incidence. This thesis presents imaging equations that are not based on Hopkins' formulation, but rather on a formulation where Köhler illumination is assumed, an integration is performed across the object plane for each point on the source and the source is integrated over last. The formulation is sometimes referred to as "Source Integration" or "Abbe's Formulation"[1][72]. The imaging system model represents each component of the system as an operator on plane waves. A full-vector formulation is maintained from the source, to the object, to the projection optic and down into the film stack at the wafer.

An overview the imaging system model is given in section 4.1.1. Sections 4.2 to 4.5 are devoted to detailing the models for each component in the imaging system. Then all components are linked together in section 4.6 and the imaging equations are presented. The

exact details of the mask model are deferred until section 4.7 where three different mask models are presented followed by a discussion of when the use of each model is appropriate.

4.1.1. The Imaging System Model

In this thesis, the “imaging system” consists of two optics - the illumination optic and the projection optic (see Figure 4-1). The illumination optic is responsible for modifying the light emitted from a source (usually a laser or a mercury arc-lamp) to create an electromagnetic field with the coherence properties and angular spectrum appropriate to illuminate the object (photomask). The object scatters this “incident field” presented by the illumination optic into the “scattered field”. The projection optic (sometimes called the “camera”) takes the scattered field and passes it (via numerous optical components) to the “image plane” (the wafer or a CCD camera etc.). Finally, if the image is being formed inside some material, such as a layer of photoresist on a silicon wafer, then diffraction and refraction will again affect the aerial image and can be modeled by applying either thin film stack theory or rigorous electromagnetic simulation.

The basis of the imaging system model comes from Fourier Optics [35] where the electromagnetic fields are considered as superpositions of plane waves. Each component in the imaging system can be regarded as an operator on plane waves as illustrated in Figure 4-2. In (a), the source and condenser optics emit plane waves, each plane wave travelling in a different direction and mutually coherent from the others. The object (photomask) takes each single plane wave generated by the source and condenser, and scatters it into many plane waves as depicted in figure (b). The projection optic, (c), operates on each plane wave output from the object yielding an output plane wave with the same direction (but possibly with different magnitude and phase). The film stack at the wafer, (d), like the projection optic yields a plane wave with the same direction of propagation as its input and thus it is possible to combine the effects of the projection optic and the thin-film stack at the wafer into a single “equivalent transfer function”.

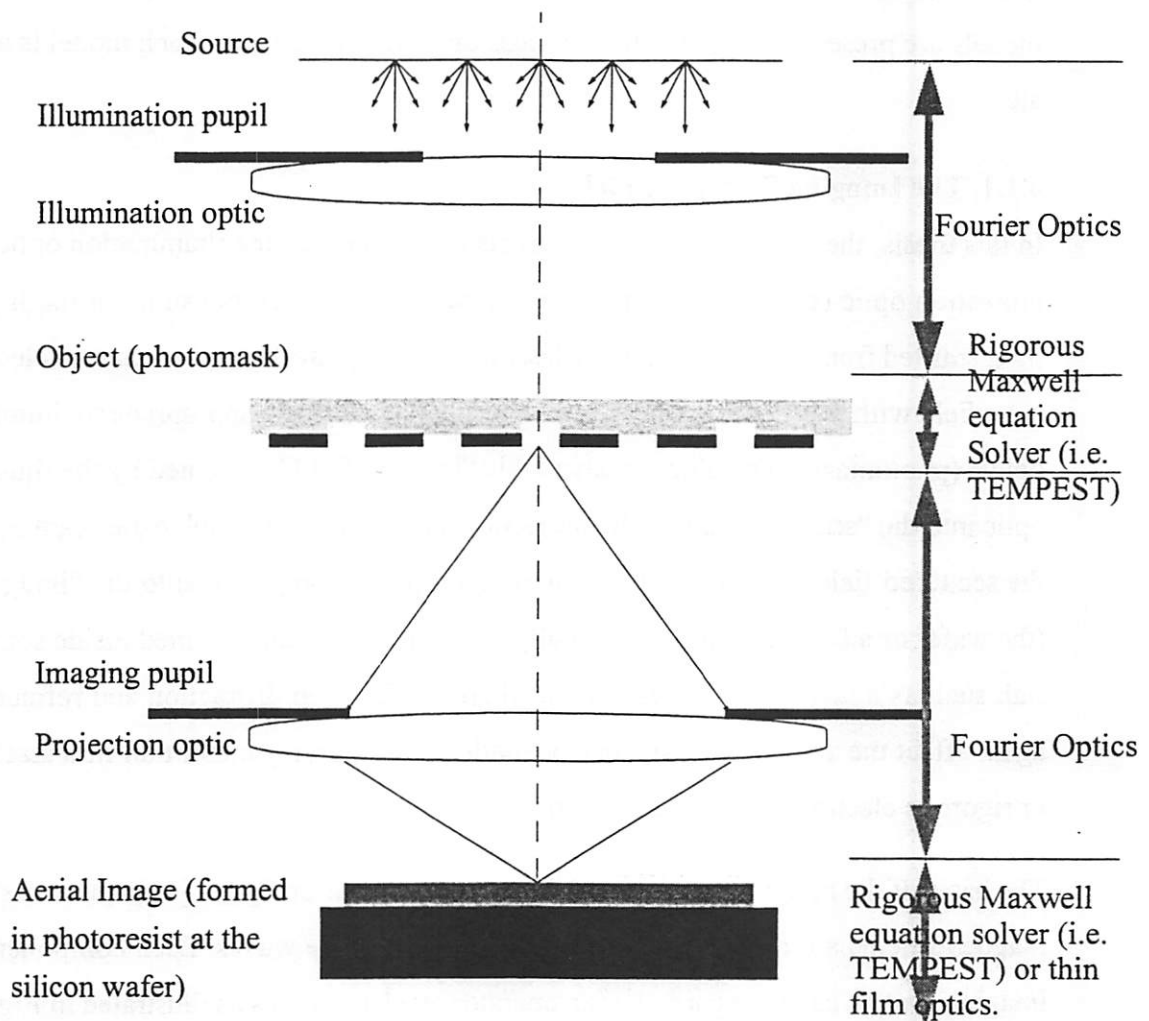


Figure 4-1. A Simplified Model for an Imaging System

The science of Fourier Optics is applied to model the source, illumination optic and projection optic. Rigorous ElectroMagnetic Simulation (REMS) may be required to model the object (photomask). The formation of the aerial image inside a film stack at the image plane may be model either by REMS or by thin-film-stack theory.

4.2. Source and Illumination Optic

The purpose of the illumination optic (sometimes also called the “condenser”) is to direct light emitted from the source (typically a mercury arc lamp, a laser or perhaps a synchrotron) in such a way so as to illuminate the object with the appropriate degree of uniformity and coherence properties. Illumination optics are usually classified as being either “critical” or “Köhler”. [16]. With critical illumination, an extended source is imaged onto the object and thus any nonuniformities in the brightness of the extended source will be trans-

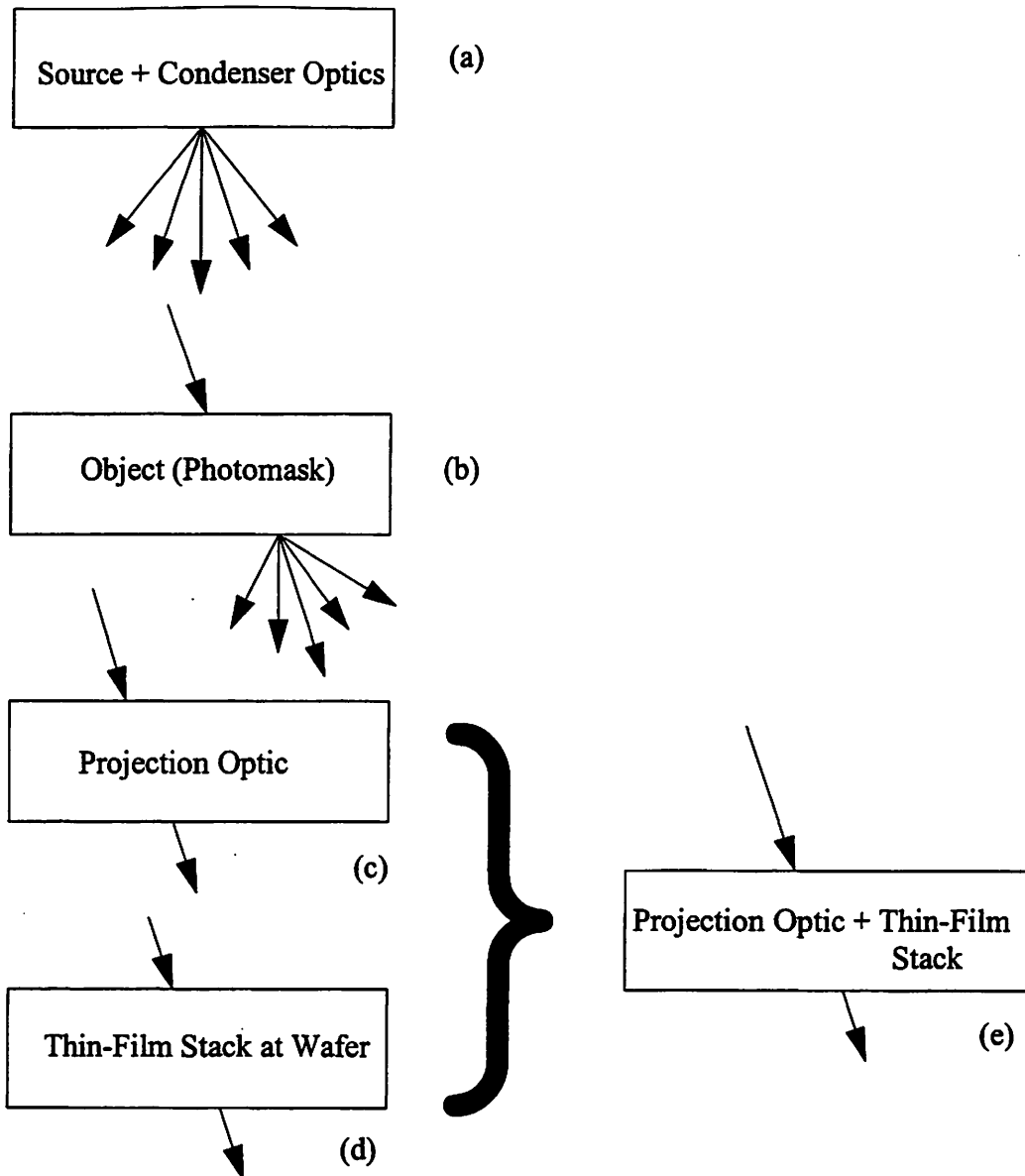


Figure 4-2. Plane Wave Representation of Imaging System Components

Each component of the imaging system can be visualized as some sort of operation on plane waves. In this figure, plane waves are represented by arrows indicating their directions of propagation.

ferred to the illumination of the object. With Köhler illumination however, the field presented to the object is the Fourier transform of field emitted by the source and so irregularities in the brightness distribution on the source will not cause irregularities in the intensity of the illuminating field. For this reason, only Köhler illumination is further considered in this thesis.

With Köhler illumination, a point on an extended source will image to a plane wave at the object. Different points on the source will correspond to different plane waves (with different directions of propagation) at the mask. If points on the source are assumed to radiate independently (i.e. incoherently), then the illuminating plane waves with different angles of incidence will be incoherent relative to each other. It is also assumed that plane waves with the same direction of propagation, but with orthogonal polarizations are also mutually incoherent.

For the imaging system model discussed in this thesis, the source and illumination are together regarded as source of mutually incoherent plane waves. The set of plane waves presented to the mask can be visualized in k-space. Four illumination schemes used in lithography are circular, annular[60], quadrupole and quasar[20] and are illustrated in Figure 4-3.

4.2.1. Discretization of the Source

In a real imaging system, the source will occupy some continuous region of space and thus contain an infinite number of radiating points, and therefore present an infinite number of incoherent plane waves to the object (photomask). In some situations, such as when the source is circular and uniform, it is possible to perform an integration which accounts for all plane waves generated by the source (for example the van Cittert-Zernike theorem[17]), but often it is necessary to numerically evaluate this integral by approximating it with a summation over a set of “source integration points”. Source discretization involves choosing a finite subset of the plane waves that sufficiently represent the source. An example of source discretization is illustrated in Figure 4-4 where the set of an infinity of plane waves is replaced by a finite set of plane waves evenly distributed throughout the illuminated region of k-space. The number of source integration points necessary can be determined by requiring the mutual intensity at the image due to continuous and discretized sources to agree within some pre-determined amount. This problem has been worked out by Socha[72] for the case of circular illumination where it was determined that:

$$n_{2D} = \frac{\pi}{4} \left(N_s \frac{2\sigma NA w}{\lambda} \right)^2 \quad \text{Eq. 4-1.}$$

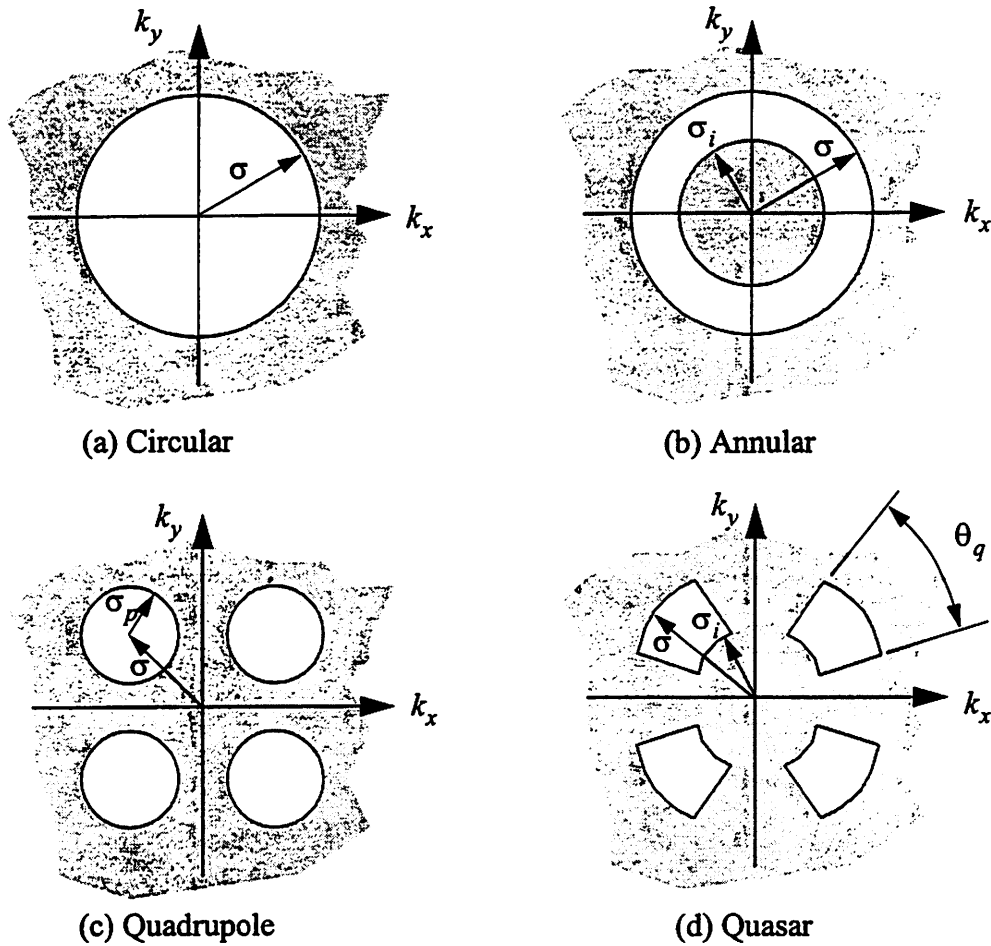


Figure 4-3. Common Illumination Schemes used in Photolithography

where w is the length of the (assumed square) mask period and N_s is an oversampling factor that is typically chosen to be 4.

4.3. The Object

In a semiconductor printing tool (steppers and scanners) or inspection system, the “object” is a photomask. The mask scatters the incident field into what is called the “scattered” field. The scattered field could be a “transmitted” field as in the case of printing, or a “reflected” field as in the case of some types of inspection systems. As discussed in section 4.2, the source and illumination optic illuminate the object with a mutually incoherent set of plane waves. By superposition (the linearity of the Maxwell equations), the mask’s effect on the total incident field can be understood by considering its effect on each individual plane wave component of the incident field.

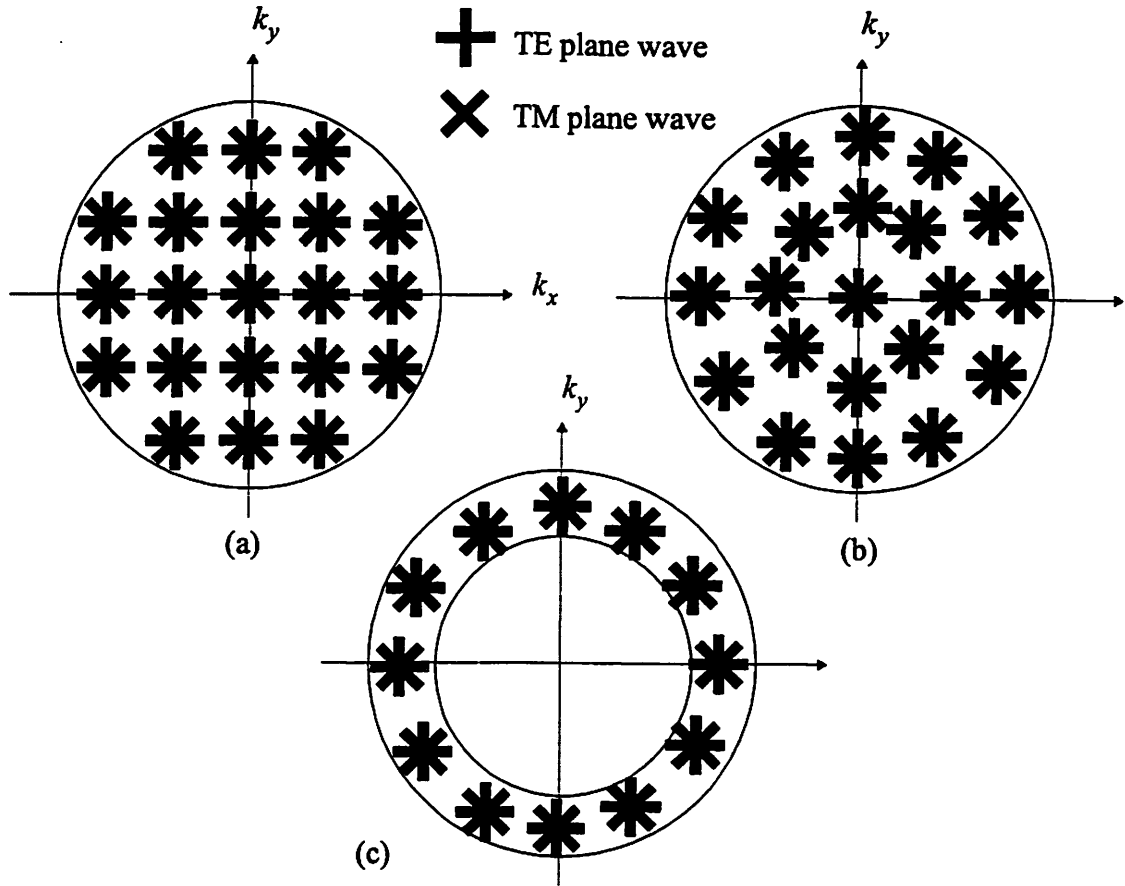


Figure 4-4. Source Discretization

(a) A circular source discretized with a Cartesian distribution of points. (b) A circular source discretized with a radial distribution of points. (c) An annular source discretized with a radial distribution of points.

Due to the difficulty in implementing absorbing boundary conditions in the horizontal directions and the simplicity of implementing periodic boundary conditions, only bi-periodic objects (photomasks) are considered in this thesis. Isolated topographies can be approximated by using large periods.

If the object is a bi-periodic structure in the x and y directions, the intensity of the scattered field will also have the same symmetry. The complex field inside the simulation domain will take the form $E(x, y, z) = u(x, y, z)e^{j(k_x L_x + k_y L_y)}$ where $u(x, y, z)$ is a periodic function with the same periodicity as the simulation domain. (arguments similar to those used by Bloch[12] for electrons in periodic potentials can be used to arrive at these conclusions.) Thus the scattered field can be fully described by a finite and discrete set of Fourier com-

ponents. Those Fourier components that are propagating plane waves (i.e. not evanescent waves) are sometimes called the “diffracted orders”. The magnitude and phase of each diffracted order in relation to the magnitude and phase of the incident plane wave is represented by a single complex number called the “scattering coefficient”. The set of scattering coefficients corresponding to the set of diffracted orders will be referred to as “the scattering coefficients”.

Scattering coefficients are denoted as $SC_{p, mn}(w_{in})$, where $w_{in} = \begin{bmatrix} A_{in, TE} \\ A_{in, TM} \end{bmatrix} \vec{k}_{in}$ is the input

plane wave with unity electric field magnitude (see Appendix A for plane wave notation). The finite set of scattering coefficients is indexed by the polarization $p \in \{TE, TM\}$ and the integers m and n which, for consideration of only the propagating plane waves¹, take on the following values:

$$-1 < \frac{\frac{2\pi m}{L_x} - k_{in, x}}{k} < 1, m \in I \quad \text{Eq. 4-2.}$$

$$-1 < \frac{\frac{2\pi n}{L_y} - k_{in, y}}{k} < 1, n \in I, \quad \text{Eq. 4-3.}$$

where L_x and L_y are the periods of the bi-periodic mask in the x and y directions respectively.

The propagating component of the scattered field, for a single incident plane wave w_i , in the case of a bi-periodic mask, is thus:

$$F_{scat}(w_i) = \sum_{m, n} \begin{bmatrix} SC_{TE, mn}(w_i) \\ SC_{TM, mn}(w_i) \end{bmatrix} \vec{k}_{scat, mn, i} \quad \text{Eq. 4-4.}$$

1. In input plane wave will in general scatter into both propagating plane waves and non-propagating (evanescent plane) waves. Only the propagating plane waves are collected by the projection optic.

This superposition of plane waves propagates on to the projection optic and subsequently to the image (wafer).

All the details of the object have capsulated into the scattering coefficients. A detailed explanation of scattering coefficient calculation is deferred until section 4.7.

4.4. Projection Optic

The role of the projection optic in the imaging system is to direct the plane waves scattered from the object (photomask) in such a way as to form a scaled image of the object at the image plane. An ideal projection optic would form a perfect image of the object at the image plane, but the finite wavelength of the light, and diffraction prevent the projection optic from perfectly reproducing the object's pattern.

It is desirable have a mathematical model for the projection optic so that aerial images can be calculated from the scattered field as described above. A useful model for the projection optic must account for demagnification (M), numerical aperture (NA), pupil plane configuration and non-idealities such as aberrations and defocus (d). Fourier optics has provided a relatively simple and useful mathematical model for the projection optic that can be expressed as a convolution of the scalar field at the object ($U_o(u, v)$) with a point spread function ($h(u, v)$) that is equal to the Fourier transform of the imaging pupil: (following Goodman[37])

$$U_i(u, v) = h(u, v) \otimes U_o(u, v) \quad \text{Eq. 4-5.}$$

where

$$U_g(u, v) = \frac{1}{|M|} U_o\left(\frac{u}{M}, \frac{v}{M}\right) \quad \text{Eq. 4-6.}$$

is the geometrical-optics prediction of the image and

$$h(u, v) = \int_{-\infty}^{\infty} \int_{-\infty}^{\infty} P(\lambda z_2 \tilde{x}, \lambda z_2 \tilde{y}) \exp[-j2\pi(u\tilde{x} + v\tilde{y})] d\tilde{x} d\tilde{y} \quad \text{Eq. 4-7.}$$

However, these equations assume a scalar theory and operate on fields in the spatial domain, not on plane waves.

It is not difficult to cast these equations into the required plane wave operator form. For a given purely TE or purely TM input plane wave there will correspond a single output plane wave of the same polarization whose k-vector is related to the input plane wave's k-vector by the following equations:

$$k_{out,x} = Mk_{in,x} \quad \text{Eq. 4-8.}$$

$$k_{out,y} = Mk_{in,y} \quad \text{Eq. 4-9.}$$

$$k_{out,z} = \pm \text{sgn}(k_{in,z}) \sqrt{k^2 - k_{out,x}^2 - k_{out,y}^2} \quad \text{Eq. 4-10.}$$

where M is the optical demagnification (i.e. $M=4$ for a 4X reduction system) and the sign for $k_{out,z}$ is chosen depending on whether the projection optic is a transmission or reflection optic.

The amplitude transfer function is closely related to the Fourier transform of the point spread function (Equation 4-7) and thus equal to a scaled pupil function[18]. This amplitude transfer function is the basis of the plane wave operator. It is augmented by other factors that account for defocus, aberrations and high NA correction:

$$h_p(\vec{k}_{out}) = P_p(k_{out,xy})D(k_{out,xy}^2)R(k_{out,xy}^2)A_p(k_{out,x}, k_{out,y}) \quad \text{Eq. 4-11.}$$

where the four factors are, in order, i) the pupil function, the defocus function, the radiometric correction function and the aberrations function. To accommodate possible differences with respect to polarization, the pupil function and aberrations function are subscripted by p the polarization.

Typically, the pupil function is a circular function which admits all plane waves within a radius $\frac{1}{kNA}$ in k-space:

$$P(k_{out,xy}) = \text{circ}\left(\frac{k_{out,xy}}{NA \cdot k}\right). \quad \text{Eq. 4-12.}$$

However, just as different pupils can be used for illumination (see Figure 4-3), different pupil functions can be used for imaging. For example, in a scheme called “dark-field imaging”, an annular pupil function is used, rather than a circular pupil function.

The image plane defocus factor, $D(k_{out,xy}^2)$ accounts for image (wafer) defocus. In this definition, the image is assumed to be formed in air and not inside photoresist. $D(k_{out,xy}^2)$ is expressed as[50]:

$$D(k_{out,xy}^2) = e^{-\frac{2\pi d}{\lambda} \left(1 - \sqrt{1 - \frac{k_{out,xy}^2}{k^2}}\right)} \quad \text{Eq. 4-13.}$$

where d is the amount of defocus.

The radiometric correction factor $R(k_{out,xy}^2)$ is a consequence of an extension of scalar diffraction theory for imaging in a projection lens where the paraxial approximation is not made[21]. The radiometric correction factor takes the following form:

$$R(k_{out,xy}^2) = \left(\frac{1 - \frac{k_{out,xy}^2}{M^2 k^2}}{1 - \frac{k_{out,xy}^2}{k^2}} \right)^{1/4}, \quad \text{Eq. 4-14.}$$

where again, M is the optical reduction of the projection optic.

The final term in the amplitude transfer function accounts for the optical aberrations (imperfections in the lens polishing). The aberrations are described as a wavefront deviation that is usually expressed in polar coordinates and by an expansion in the Zernike polynomials $W_n(r, \alpha)$:

$$A_p(k_{out,x}, k_{out,y}) = \sum_{n=1}^{37} Z_{p,n} W_n\left(\frac{k_{out,xy}}{NA \cdot k}, \text{atan}\left(\frac{k_{out,y}}{k_{out,x}}\right)\right) \quad \text{Eq. 4-15.}$$

The function $A_p(k_{out,x}, k_{out,y})$ is subscripted by the polarization p to allow different aberrations to be applied to the TE and TM polarizations separately.

The amplitude transfer function as expressed in Equation 4-11 is a function of k-vector for the plane wave at the exit pupil. As an operator on plane waves the projection optic can be expressed:

$$\tilde{h}(w) = \tilde{h} \left(\begin{matrix} A_{TE} \\ A_{TM} \end{matrix} \right)_{\vec{k}} = \begin{bmatrix} A_{TE} h_{TE}(k_x, k_y) \\ A_{TM} h_{TM}(k_x, k_y) \end{bmatrix}_{\vec{k}_{out}} \quad \text{Eq. 4-16.}$$

where the output plane wave has the k-vector \vec{k}_{out} .

4.5. Film Stack Effects

The imaging system model developed thus far assumes the formation of the aerial image in air at the image plane. When printing circuitry on a silicon wafer however, lithographers are more interested in the image intensity inside a thin layer of photoresist on top of a silicon substrate (see Figure 4-5). Especially for high NA imaging systems, there is consid-

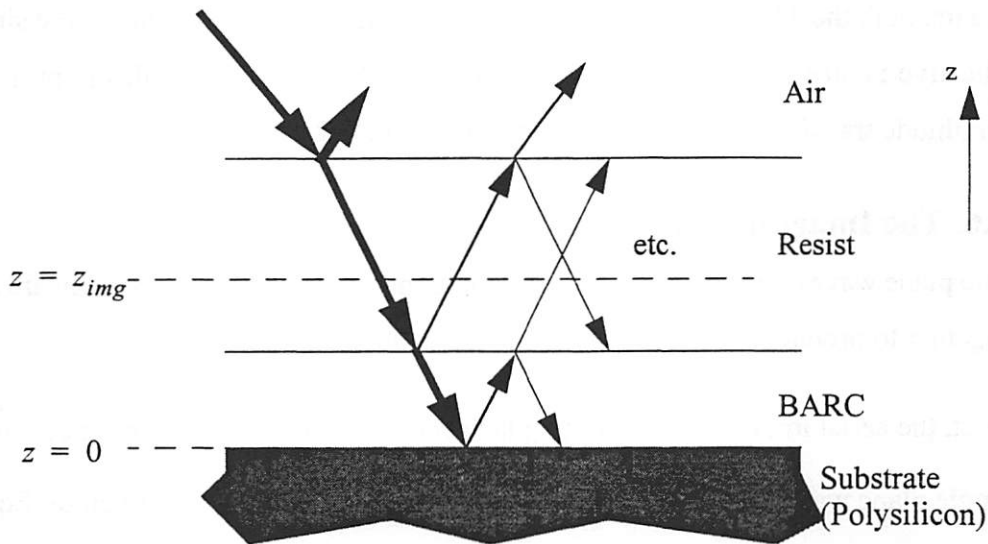


Figure 4-5. Imaging inside a thin-film stack

The incident plane wave is multiply reflected and transmitted by the layers of the thin-film stack. The x and y components of the k-vector for all waves remain constant.

erable difference between aerial images formed inside a thin layer of photoresist and those form in air. This is mainly due to the bending of the waves towards the normal as they enter the photoresist and the standing wave created by reflection from the bottom surface of the resist.

To model the aerial image formation inside the film stack researchers (Flagello[28] and Yeung[100]) used thin film optics theory to integrate a correction factor into the projection optic's amplitude transfer function that could account for the multiple reflections between layers in the film stack.

Boundary conditions for planar material interfaces force the xy-plane projections of k-vectors for the reflected and transmitted waves to remain constant and thus, for any particular height, z , the final field will be an infinite sum of plane waves having the same spatial frequency. The theory of thin-film optics[11] can be used to find the thin-film stack multiplication factor $f_p(k_{xy}, z)$ that can be appended to the amplitude transfer function as follows:

$$\tilde{h}(\tilde{w}) = \tilde{h} \left(\begin{bmatrix} A_{TE} \\ A_{TM} \end{bmatrix} \right) = \begin{bmatrix} A_{TE} h_{TE}(k_x, k_y) f_{TE}(k_{xy}, z) \\ A_{TM} h_{TM}(k_x, k_y) f_{TM}(k_{xy}, z) \end{bmatrix}_{\tilde{k}_{out}} \quad \text{Eq. 4-17.}$$

Again, both the TE and TM polarizations are handled separately. Due to the simple multiplicative nature of the stack effect factor, it can be combined with the projection optic amplitude transfer function as illustrated in Figure 4-2.

4.6. The Imaging Equations

The plane wave operator models for the components of the imaging system are now linked together to produce the complete imaging equations.

First, the aerial image due to a single plane wave (\tilde{w}_i) from the source is considered. This single plane wave scatters from the object into the field $F_{scat}(\tilde{w}_i)$ given by Equation 4-4. The scattered field is transformed by the projection optic (that may or may not have the thin-film stack effects incorporated) into the image component

$$F_{img}(\tilde{w}_i) = h(F_{scat}(\tilde{w}_i)). \quad \text{Eq. 4-18.}$$

$F_{img}(\tilde{w}_i)$ is the field at the image plane (specified as a superposition of plane waves) due to the single plane wave \tilde{w}_i emitted from the source. At this point it is necessary to convert from a superposition of plane waves notation to an electric field notation. Using the equations of Appendix A,

$$\vec{E}_{img, i}(x, y) = \operatorname{Re} \left\{ \sum_{m, n} e^{j(-k_{img, mn, i, x}x - k_{img, mn, i, y}y)} M_{\vec{k}_{img, mn, i}} h \left(\begin{bmatrix} SC_{TE, mn}(\vec{w}_i) \\ SC_{TM, mn}(\vec{w}_i) \end{bmatrix}_{\vec{k}_{scat, mn, i}} \right) \right\} \quad \text{Eq. 4-19.}$$

where $M_{\vec{k}}$ is a 3 by 2 matrix that transforms from the polarization component basis to the Cartesian coordinate basis, specified in Appendix A as:

$$M_{\vec{k}} = \begin{bmatrix} \frac{k_y}{k_{xy}} & \frac{k_z k_x}{k k_{xy}} \\ \frac{k_x}{k_{xy}} & \frac{k_z k_y}{k k_{xy}} \\ 0 & -\frac{k_{xy}}{k} \end{bmatrix}. \quad \text{Eq. 4-20.}$$

The intensity of this electric field, (still due to the single plane wave \vec{w}_i from the source) is then written as

$$I_{img, i}(x, y) = \frac{1}{2} |\vec{E}_{img, i}(x, y)|^2. \quad \text{Eq. 4-21.}$$

Each plane wave emitted from the source will have a corresponding image. Because Köhler illumination is assumed, the individual plane waves emitted from the source are assumed incoherent from one another and therefore the (time averaged) intensities of the images from the individual source plane waves are added to form the final aerial image:

$$I_{img}(x, y) = \sum_i \frac{1}{2} |\vec{E}_{img, i}(x, y)|^2 \quad \text{Eq. 4-22.}$$

4.7. Photomask Models and Scattering Coefficient Calculation

Until this point, the object or photomask has been treated as a “black box” that takes an “incident” plane wave and scatters it into many “scattered” plane waves. The relation between the magnitudes and phases of the scattered waves and the incident wave are described by a set of complex numbers called the “scattering coefficients”.

This section describes how the scattering coefficients are calculated and how the different calculation techniques form the various photomask models.

4.7.1. Approximating the Scattering Coefficients for a Nearby Plane Wave

The mask model as described by Equation 4-4 requires a knowledge of the scattered plane waves for each possible incident plane wave. It is often too computationally expensive to calculate the scattering coefficients for each plane wave emitted from the source and so some approximations must be made.

Incident plane waves that are near to each other in k-space (direction of propagation) are likely to scatter in a same way. This is observed by Wong [93] and also in Figure 4-6 which shows the scattered orders for a typical phase shift mask topography at 0 and 10 degree incidences. The fact that the scattered order magnitudes hardly change from 0 to 10 degree incidences suggest that it may not be necessary to calculate scattering coefficients for all plane waves within some neighborhood in k-space and that scattering coefficients for a single incident plane wave within that neighborhood could be used to approximate those throughout the neighborhood. This idea is illustrated in Figure 4-7.

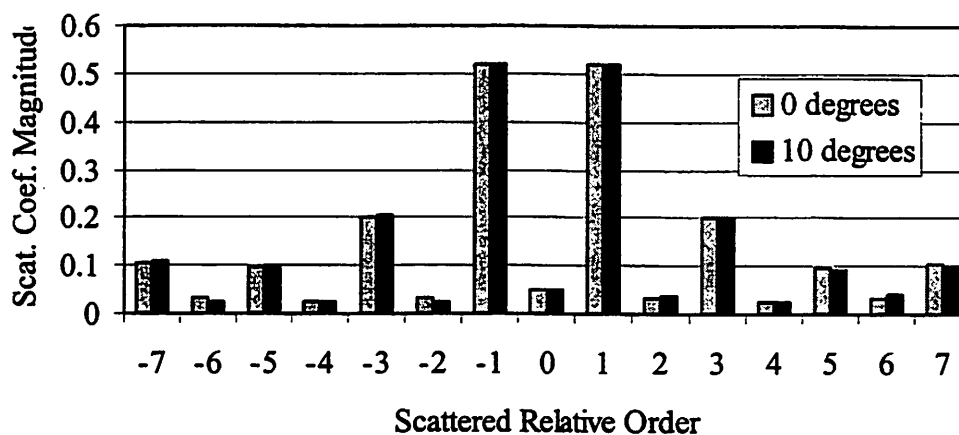


Figure 4-6. Scattered orders are approximately equal for nearby incident plane waves

The scattering coefficient magnitude is plotted for a 0.18 μ m, 1:1 phase shift mask with 248nm TE-polarized incident plane waves.

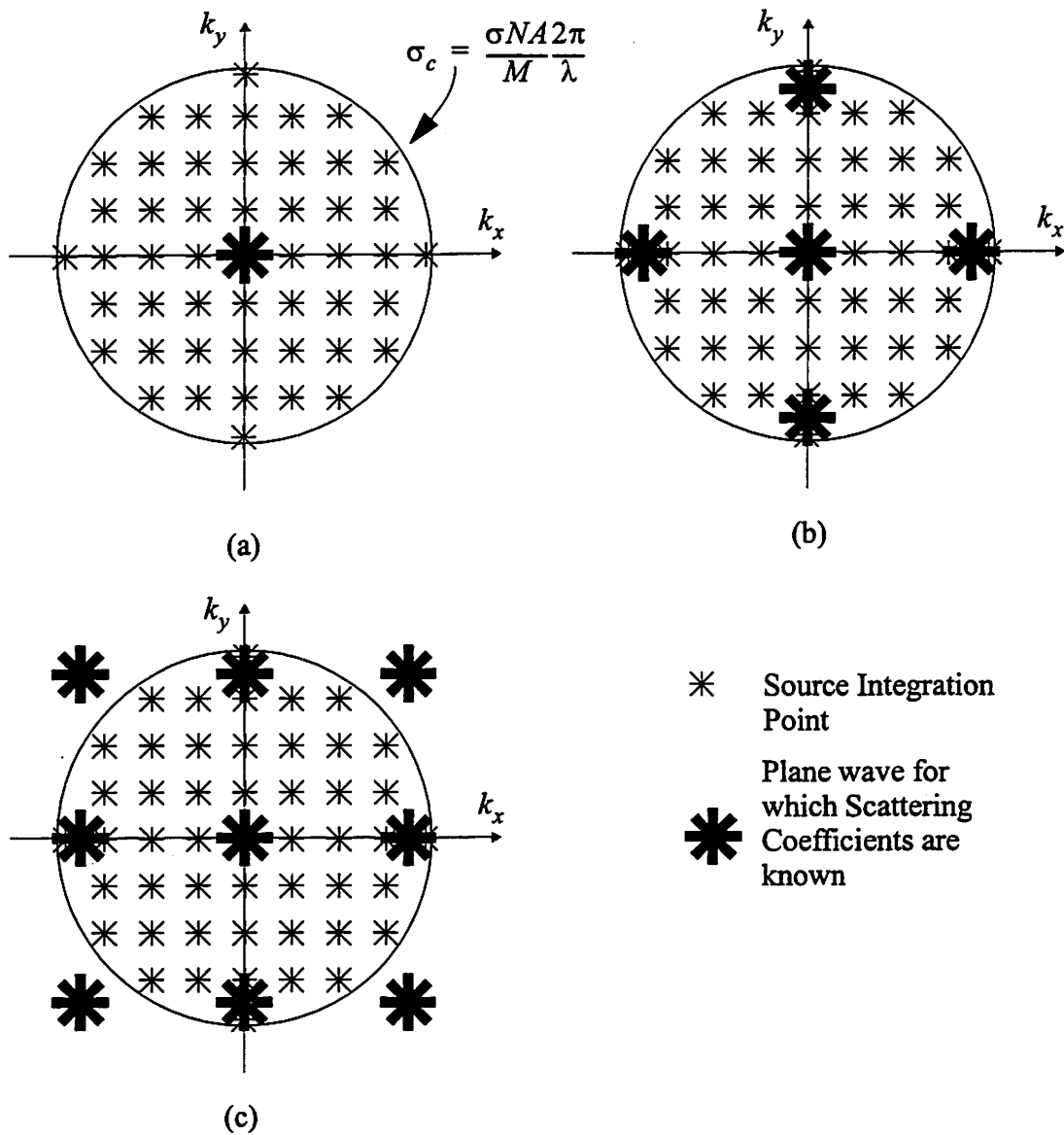


Figure 4-7. Scattering coefficients are known for only a small number of plane waves incident on the mask

In (a), scattering coefficients are known only for the normally incident TE and TM plane waves. Scattering coefficients for all other source integration points will be approximated by these known scattering coefficients. In (b), the scattering coefficients are known for normally incident TE and TM waves and also for 4 locations (both TE and TM) on the pupil extremity. Some sort of interpolation scheme must be used. In (c), 4 additional locations for which scattering coefficients are known are added, this time they are not inside the illumination pupil, but can still be used to approximate scattering coefficients for nearby angles of incidence.

A method for approximating scattering coefficients in a neighborhood surrounding a point in k-space where scattering coefficients are exactly known is outlined.

Problem:

Given the scattering coefficients, $SC_{p, mn}(w_{ref})$, for a single incident “reference”

plane wave $w_{ref} = \begin{bmatrix} A_{ref, TE} \\ A_{ref, TM} \end{bmatrix}_{\vec{k}_{ref}}$ (either calculated using TEMPEST or by some

other means), approximate the scattering coefficients for a nearby incident plane

wave $w = \begin{bmatrix} A_{TE} \\ A_{TM} \end{bmatrix}_{\vec{k}}$.

Solution:

First, it must be understood that the given set of scattering coefficients only contains information about how the reference plane wave scatters. It contains no information whatsoever regarding how the plane wave with the same direction of propagation, but with opposite polarization scatters. For example, if a TEMPEST simulation is run with a reference plane wave that is normally incident and x-polarized, no information is obtained regarding how a normally incident y-polarized plane wave scatters.

Keeping the abovementioned fact in mind, the first step in estimating the scattering coefficients for the input plane wave w is to determine what component of this input plane wave has the same polarization as the reference plane wave. This is done by translating the input plane wave’s direction of propagation to the direction of propagation of the reference plane wave. (See Appendix C for plane wave translation). The translated wave is

$$w_2 = \begin{bmatrix} A_{2, TE} \\ A_{2, TM} \end{bmatrix}_{\vec{k}_{ref}} = \text{translate}(w, \vec{k}_{ref}) \quad \text{Eq. 4-23.}$$

The magnitude of the projection of this translated plane wave onto the reference wave is taken:

$$c = \frac{\tilde{w}_2 \bullet \tilde{w}_{ref}}{|\tilde{w}_{ref}|}. \quad \text{Eq. 4-24.}$$

c , is a complex number that represents the “projection” of the input wave onto the reference wave. It’s magnitude represents how much information the known set of scattering coefficients contains regarding how the input wave w scatters. This can be better understood by considering the following example:

Example

Assume that scattering coefficients are known for the wave $\tilde{w}_{ref} = \begin{bmatrix} 1 \\ 0 \end{bmatrix}_{(0,0)}$ (normally incident TE wave that has electric field in the y-direction). Consider the following five cases (see Figure 4-8) for the input wave w :

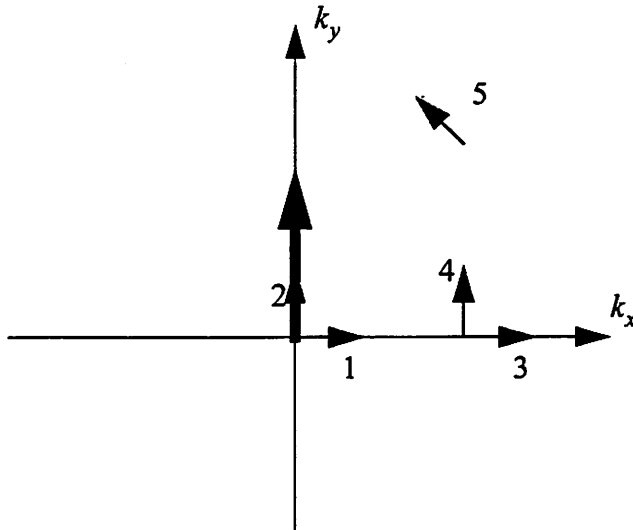


Figure 4-8. Five different cases for the input plane wave w

Case 1: $\underset{\sim}{w} = \begin{bmatrix} 1 \\ 0 \end{bmatrix}_{(0,0)}$. A normally incident TE wave, the same as the reference

wave. $|c| = 1$ meaning the known scattering coefficients contain all information how this wave scatters.

Case 2: $\underset{\sim}{w} = \begin{bmatrix} 0 \\ 1 \end{bmatrix}_{(0,0)}$. A normally incident TM wave. $|c| = 0$ meaning the known

scattering coefficients contain no information about how this wave scatters.

Case 3: $\underset{\sim}{w} = \begin{bmatrix} 0 \\ 1 \end{bmatrix}_{(k,0)}$. A TM plane wave obliquely incident from the +x direction.

$|c| = 0$ meaning the known scattering coefficients contain no information about how this wave scatters.

Case 4: $\underset{\sim}{w} = \begin{bmatrix} 1 \\ 0 \end{bmatrix}_{(k,0)}$. A TE plane wave obliquely incident from the +x direction.

$|c| = 1$ meaning the known scattering coefficients contain all information about how this wave scatters.

Case 5: $\underset{\sim}{w} = \begin{bmatrix} 1 \\ 0 \end{bmatrix}_{(k,k)}$. A TE plane wave obliquely incident from a direction that is

not on one of the Cartesian axes. $|c| = \sqrt{\frac{1}{2}}$ which means that the known scattering coefficients contain some information about how this wave scatters. The remainder of the information about how this wave scatters would be contained in the set of scattering coefficients for normally incident TM wave.

(End of Example)

The approximation for the (+m,+n)th scattered order for w is made from the (+m,+n)th scattered order for the reference wave $\underset{\sim}{w}_{ref}$. The (known) (+m,+n)th

scattered order for the reference wave is denoted by $w_{ref, scat, mn}$ and is expressed as¹

$$w_{ref, scat, mn} = \begin{bmatrix} SC_{TE, mn}(w_{ref}) \\ SC_{TM, mn}(w_{ref}) \end{bmatrix} \left(k_{ref,x} + \frac{2\pi m}{L_x}, k_{ref,y} + \frac{2\pi n}{L_y} \right) \quad \text{Eq. 4-25.}$$

The approximated (+m,+n)th scattered order for w is then set to be the translation of $w_{ref, scat, mn}$ to the appropriate k-space location with the added projection factor c :

$$\begin{aligned} w_{scat, mn} &= \begin{bmatrix} SC_{TE, mn}(w) \\ SC_{TM, mn}(w) \end{bmatrix} \left(w_{k_x} + \frac{2\pi m}{L_x}, w_{k_y} + \frac{2\pi n}{L_y} \right) \\ &= c \cdot \text{translate} \left(w_{ref, scat, mn}, \left(k_x + \frac{2\pi m}{L_x}, k_y + \frac{2\pi n}{L_y} \right) \right) \end{aligned} \quad \text{Eq. 4-26.}$$

The approximated scattering coefficients $SC_{p, mn}$ are defined implicitly by Equation 4-26.

(End of Solution)

In the above development, a formula for approximating scattering coefficients for a general incident wave with a *single* known set of scattering coefficients was derived. Now, the question as to how can an approximation be made when *multiple* sets of scattering coefficients are known for various incident waves is addressed.

Let the set of ordered pairs $K = (k_{x, q}, k_{y, q})$, indexed by the integer q , be the locations in k-space of the plane waves for which scattering coefficients are known. Let the set of plane waves $w_{sim, p, q} \in \{TE, TM\}$ be the TE and TM plane waves corresponding to the ordered pairs in K . (i.e. for each ordered pair there is a corresponding TE and TM plane wave for which the scattering coefficients are known.) The known scattered waves are then

1. It is noted that the scattered wave, in general, will not have the same polarization as the incident wave.

$$\underline{w}_{sim, pq, scat, mn} = \begin{bmatrix} SC_{TE, mn}(\underline{w}_{sim, p, q}) \\ SC_{TM, mn}(\underline{w}_{sim, p, q}) \end{bmatrix} \Big|_{k_{scat, mn}} \quad \text{Eq. 4-27.}$$

The (+m,+n)th scattered wave for incident wave \underline{w}_i can be approximated from a particular plane wave of the set $\underline{w}_{sim, p, q}$ using Equation 4-26:

$$\begin{aligned} \underline{w}_{scat, pq, mn} &= \begin{bmatrix} SC_{TE, mn}(\underline{w}_i) \\ SC_{TM, mn}(\underline{w}_i) \end{bmatrix} \left(k_{x,i} + \frac{2\pi m}{L_x}, k_{y,i} + \frac{2\pi n}{L_y} \right) \\ &\cong c_{pq} \cdot \text{translate} \left(\underline{w}_{sim, pq, scat, mn}, \left(k_{x,i} + \frac{2\pi m}{L_x}, k_{y,i} + \frac{2\pi n}{L_y} \right) \right) \end{aligned} \quad \text{Eq. 4-28.}$$

This approximation is made for each wave for which the scattering coefficients are known (i.e. for each p and q). Finally, a weighted average is performed over all the known sets of scattering coefficients (i.e. over p and q) to give the (+m,+n)th scattered wave for the input wave \underline{w}_i :

$$\underline{w}_{scat, mn} = \frac{1}{W_{tot}} \sum_q \sum_p w_{pq} \underline{w}_{scat, pq, mn} \quad \text{Eq. 4-29.}$$

where the weighting coefficients are w_{pq} and the total weight:

$$W_{tot} = \sum_q \sum_p w_{pq} \quad \text{Eq. 4-30.}$$

The idea behind the weightings is that for a particular input wave, the approximation made from scattering coefficients derived from waves close to the input wave will be made more important (receive a higher weighting) than scattering coefficients derived from waves farther away for the input wave. This is illustrated in Figure 4-9. The details of the weighting assignment will be discussed in a later section.

4.7.2. Mask Models

Just as photomasks in lithography have various degrees of complexity, so do photomask models. Simple photomasks, typically have simple models, while more complicated pho-

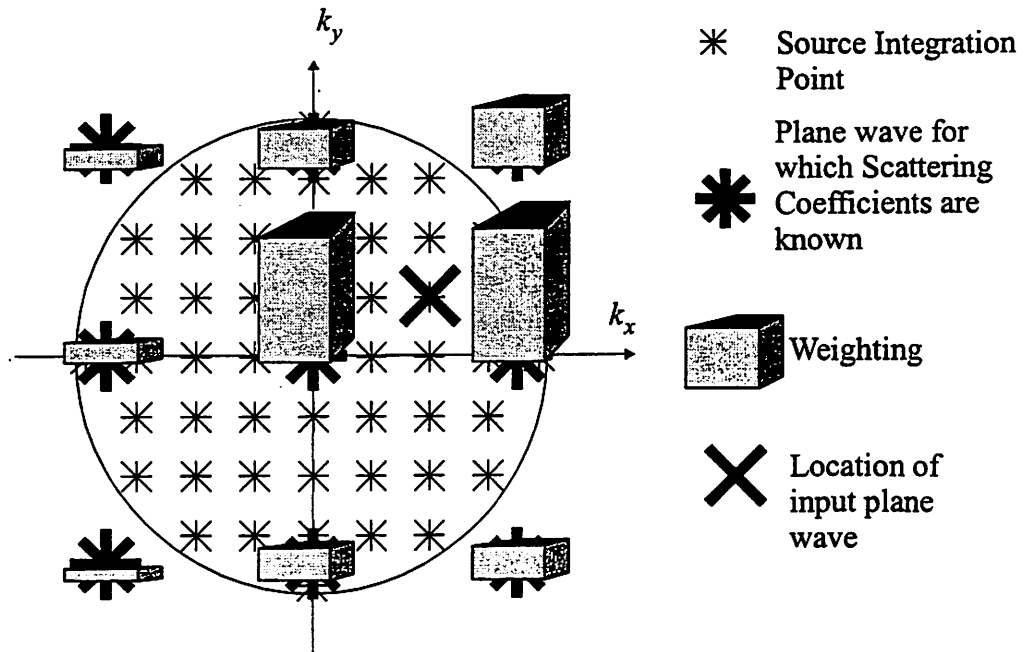


Figure 4-9. Assigning Weightings to the Sets of Scattering Coefficients

Scattering coefficients derived from plane waves close to the input plane wave are weighted more heavily.

tomasks, such as phase shift masks must use more complicated models. Three mask models will be introduced. These mask models differ from each other in two ways:

- i) the number and location in k -space of plane waves for which scattering coefficients are calculated
- ii) the method used to calculate these scattering coefficients

Alternatively, the photomask models can be classified using the following three criteria:

- i) Whether rigorous electromagnetic simulation is necessary to calculate the scattering coefficients (whether the mask is “thick” or “thin”)
- ii) whether polarization is important (i.e. there is coupling between the scalar field components and/or differently polarized plane waves with the same direction scatter differently from the mask.)
- iii) whether the scattering coefficients depend on the angle of incidence

4.7.2.1. Thin, scalar, constant scattering coefficient model

The most simple model for the mask, takes the mathematical form of a simple scalar transmission function that has a direct and simple relationship with the pattern of chrome and glass on the photomask:

$$E_{out}(x, y, z_{obj}) = t(x, y)E_{in}(x, y, z_{obj}) \quad \text{Eq. 4-31.}$$

E_{in} is the scalar electric field just before scattering from the mask, while E_{out} is scalar electric field after scattering from the mask. Consider a typical chrome on glass binary mask, if the chrome is thin (in relation to the wavelength of light), and if the pattern has features with large horizontal dimensions (in relation to the wavelength), then edge effects (diffraction) are insignificant and the transmission function model and Kirchhoff boundary conditions[36] can be used. The transmission through the regions where there is no chrome is assumed to be perfect, while the transmission in the regions where there is chrome can be considered as zero. Thus, for a thin mask, where the horizontal dimensions of the mask pattern features are large, the scattering by the mask can be modeled by a simple transmission function and furthermore, the transmission function is simply the chrome pattern (i.e. the transmission is zero where there is chrome and unity where there is no chrome). This concept is illustrated in. Figure 4-10(a).

This simple transmission function model can also be applied to more complicated masks, such as alternating and attenuating phase shifting masks. Figure 4-10(b) shows how the complex transmission function can model the 180 degree phase shifted line on an alternating phase shifting mask.

The mask model framework requires the scattering coefficients for particular input plane waves. Equation 4-31 will be used to determine scattering coefficients for the normally incident TE and TM waves. Consider the two-dimensional Fourier transform of Equation 4-31, assuming that $t(x, y)$ is a periodic function in x and y and using a plane wave input ($E_{in}(x, y, z_{obj}) = A_{in}e^{j(k_{x1}x + k_{y1}y + k_z z_{obj})}$) with spatial frequency (k_{x1}, k_{y1})

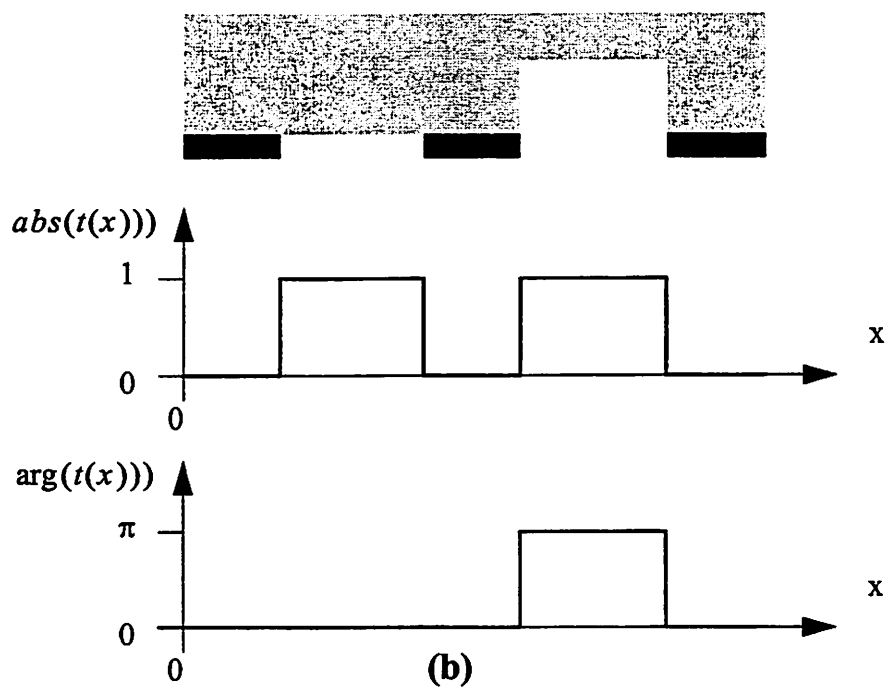
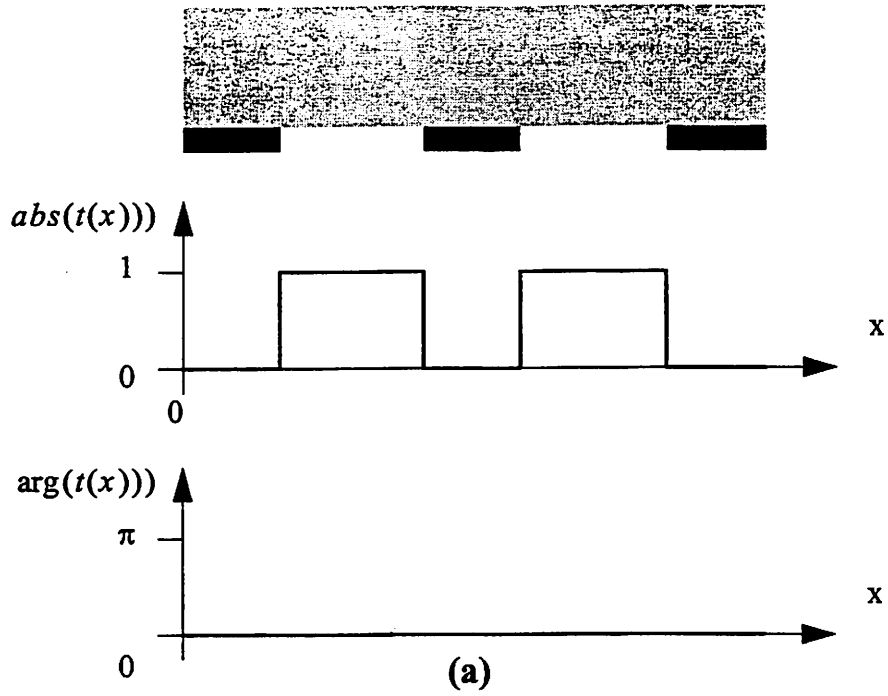


Figure 4-10. Modeling Chrome-on-Glass and Alternating Phase Shift Masks with the Thin-Film Scalar, C.S.C.A. Model

a) A simple chrome-on-glass mask has no phase shifters. The transmission function is a real binary function. b) A phase shifting mask has a complex transmission function that can have more than two values (0, 1 and -1 in this case).

$$\begin{aligned}
E_{out}(k_x, k_y, z_{obj}) &= \sum_{m,n} t_{mn} \delta\left(k_x - \frac{2\pi m}{L_x}, k_y - \frac{2\pi n}{L_x}\right) \otimes A_{in} \delta(k_x - k_{x1}, k_y - k_{y1}) \\
&= A_{in} \sum_{m,n} t_{mn} \delta\left((k_x - k_{x1}) - \frac{2\pi m}{L_x}, (k_y - k_{y1}) - \frac{2\pi n}{L_x}\right)
\end{aligned}
\tag{Eq. 4-32}$$

The scattered field is seen to be a summation of plane waves with t_{mn} as the coefficients. (a delta function in k-space is a plane wave). These t_{mn} coefficients are directly related to the scattering coefficients, but before calculating the scattering coefficients from the t_{mn} , an important point concerning polarization must be discussed.

Equation 4-31 is a scalar equation. It can not be applied to all three electric field components since the three electric field components are not independent (see Appendix A). The scattering coefficients, on the other hand, apply to polarized plane waves where all three components of the electric field are known. A method is needed to apply the scalar information contained in Equation 4-31 to the calculation of the scattering coefficients. This mask model requires scattering coefficients for two plane waves (the normally incident TE and the normally incident TM). The normally incident TE wave has the electric field polarized completely in the y-direction, while the normally incident TM wave has the electric field polarized completely in the x-direction (by convention). Equation 4-31 will therefore be applied twice - once to the y-component for the TE wave and a second time to the x-component for the TM wave.

For the normally incident TE wave:

$$\begin{aligned}
E_{x, in}(x, y, z_{obj}) &= 0 \\
E_{y, in}(x, y, z_{obj}) &= 1 \\
E_{z, in}(x, y, z_{obj}) &= 0
\end{aligned}
\tag{Eq. 4-33}$$

And the scattered waves are calculated by applying Equation 4-31 to the x and y components of the electric field.

$$E_{x, out}(x, y, z_{obj}) = 0 \tag{Eq. 4-34}$$

$$E_{y, out}(x, y, z_{obj}) = t(x, y)E_{y, in}(x, y, z_{obj}) \quad \text{Eq. 4-35.}$$

and from Equation 4-32,

$$E_{x, mn} = 0 \quad \text{Eq. 4-36.}$$

$$E_{y, mn} = t_{-m, -n} \quad \text{Eq. 4-37.}$$

Knowing the x and y components of the electric field for a plane wave, the equations of Appendix A can be used to convert the plane wave to its polar form:

$$\begin{aligned} \begin{bmatrix} A_{TE} \\ A_{TM} \end{bmatrix}_{\tilde{k}_{mn}} &= [M]_{\tilde{k}_{mn}}^{-1} \begin{bmatrix} E_{x, mn} \\ E_{y, mn} \end{bmatrix} \\ &= [M]_{\tilde{k}_{mn}}^{-1} \begin{bmatrix} 0 \\ t_{-m, -n} \end{bmatrix} \\ &= t_{-m, -n} [M]_{\tilde{k}_{mn}}^{-1} \begin{bmatrix} 0 \\ 1 \end{bmatrix} \end{aligned} \quad \text{Eq. 4-38.}$$

And thus the scattering coefficients for the normally incident TE wave are written:

$$\begin{bmatrix} SC_{TE, mn} \left(\begin{bmatrix} 1 \\ 0 \end{bmatrix}_{(0,0)} \right) \\ SC_{TM, mn} \left(\begin{bmatrix} 1 \\ 0 \end{bmatrix}_{(0,0)} \right) \end{bmatrix} = t_{-m, -n} M_{\tilde{k}}^{-1} \begin{bmatrix} 0 \\ 1 \end{bmatrix} \quad \text{Eq. 4-39.}$$

Similarly, the scattering coefficients for the normally incident TM wave are written:

$$\begin{bmatrix} SC_{TE, mn} \left(\begin{bmatrix} 0 \\ 1 \end{bmatrix}_{(0,0)} \right) \\ SC_{TM, mn} \left(\begin{bmatrix} 0 \\ 1 \end{bmatrix}_{(0,0)} \right) \end{bmatrix} = t_{-m, -n} M_{\tilde{k}}^{-1} \begin{bmatrix} 1 \\ 0 \end{bmatrix} \quad \text{Eq. 4-40.}$$

This mask model is a scalar mask model (as opposed to a “vector” model) because no coupling between cartesian components of the electric fields is introduced by Equation 4-31.

The TE and the TM waves scatter in the same way as evidenced by Equation 4-39 and Equation 4-40. Furthermore, Equation 4-31 also implies that the scattering coefficients remain the same for different plane waves. To see this consider the two-dimensional spatial Fourier transform of Equation 4-31 given in Equation 4-32. The scattered field is a summation of plane waves with t_{mn} as the coefficients and therefore t_{mn} are also the scattering coefficients. Clearly, for different input plane waves (different k_{x1} and k_{y1}), the scattered field remains a summation of plane waves with t_{mn} as the coefficients and thus Equation 4-31 implies constant scattering coefficients. The effect of changing the input plane wave is to simply shift the positions of the scattered plane waves in k-space.

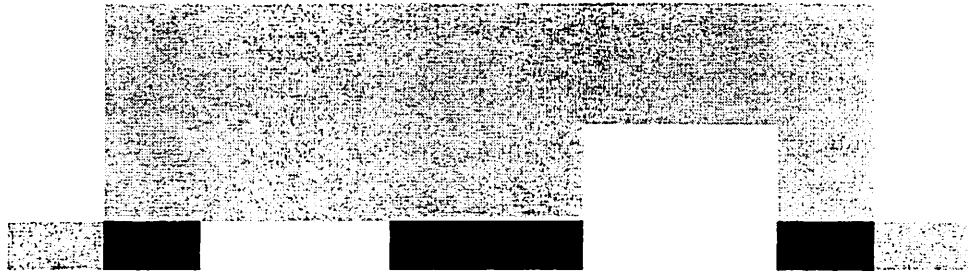
Because this mask model assumes constant scattering coefficients, there is no need to use Equation 4-31 to calculate scattering coefficients for any other plane waves - no more information will be obtained. Thus, this model knows the scattering coefficients for two plane waves, the normally incident TE and TM plane waves, a situation illustrated in Figure 4-7 (a) and scattering coefficients for all other incident plane waves are approximated using Equation 4-28 with $p \in \{TE, TM\}$ and q indexing over only a single value (corresponding to $(k_x, k_y) = (0, 0)$), and the weightings $w_{pq} = 1$.

This mask model is essentially the same as that used by the Hopkins' formulation of imaging[41][42]. The Kirchhoff boundary conditions[36] are used and a simple transmission function with a transmission pattern identical to the chrome pattern is assumed and used for both the TE and TM waves. The model is scalar in that no coupling between field components is assumed.

4.7.2.2. Thick, vector, constant scattering coefficient model

The thin, scalar, constant scattering coefficient model described above is accurate so long as the actual mask transmission function is well approximated by the ideal uniform transmission function as shown in Figure 4-10. This approximation is good so long as the aspect ratios (feature height/feature width) of the mask features are small. Feature aspect ratio increases as the horizontal dimensions of the feature get smaller (the C.D. of the feature

shrinks) and/or as the heights of the features (in the vertical or z-direction) grows. Phase shifting masks have features with higher aspect ratios than do simple chrome on glass masks. As feature aspect ratio increases, scattering from the feature edges and corners, which is neglected by the previous mask model, becomes important and can no longer be neglected. Figure 4-11 shows how the rigorously calculated transmission of the mask dif-



Mask Transmission Magnitude for Various Pitches
(1:1 Line/Space, 4X Phase Shift Mask, $\lambda=193\text{nm}$)

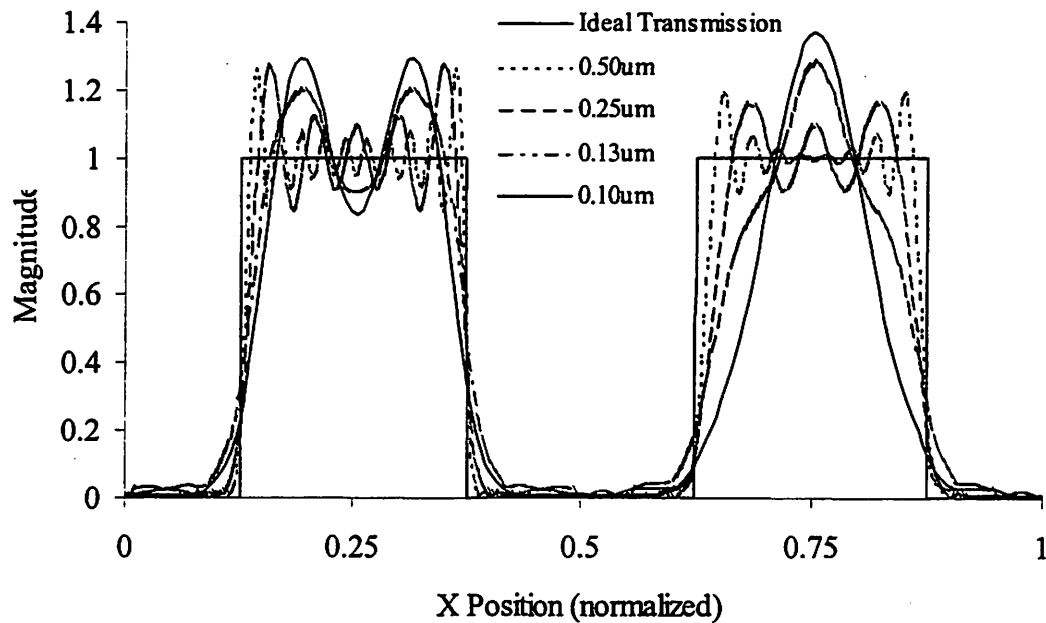


Figure 4-11. Mask transmission magnitude for various C.D.'s.

The thin mask approximation breaks down as the mask horizontal dimensions shrink, especially for the phase shifted line. Note how the transmission for the 0.50um C.D. case closely resembles that of the thin mask (ideal transmission), while the transmission for the 0.10um C.D. pattern is quite different from the ideal transmission.

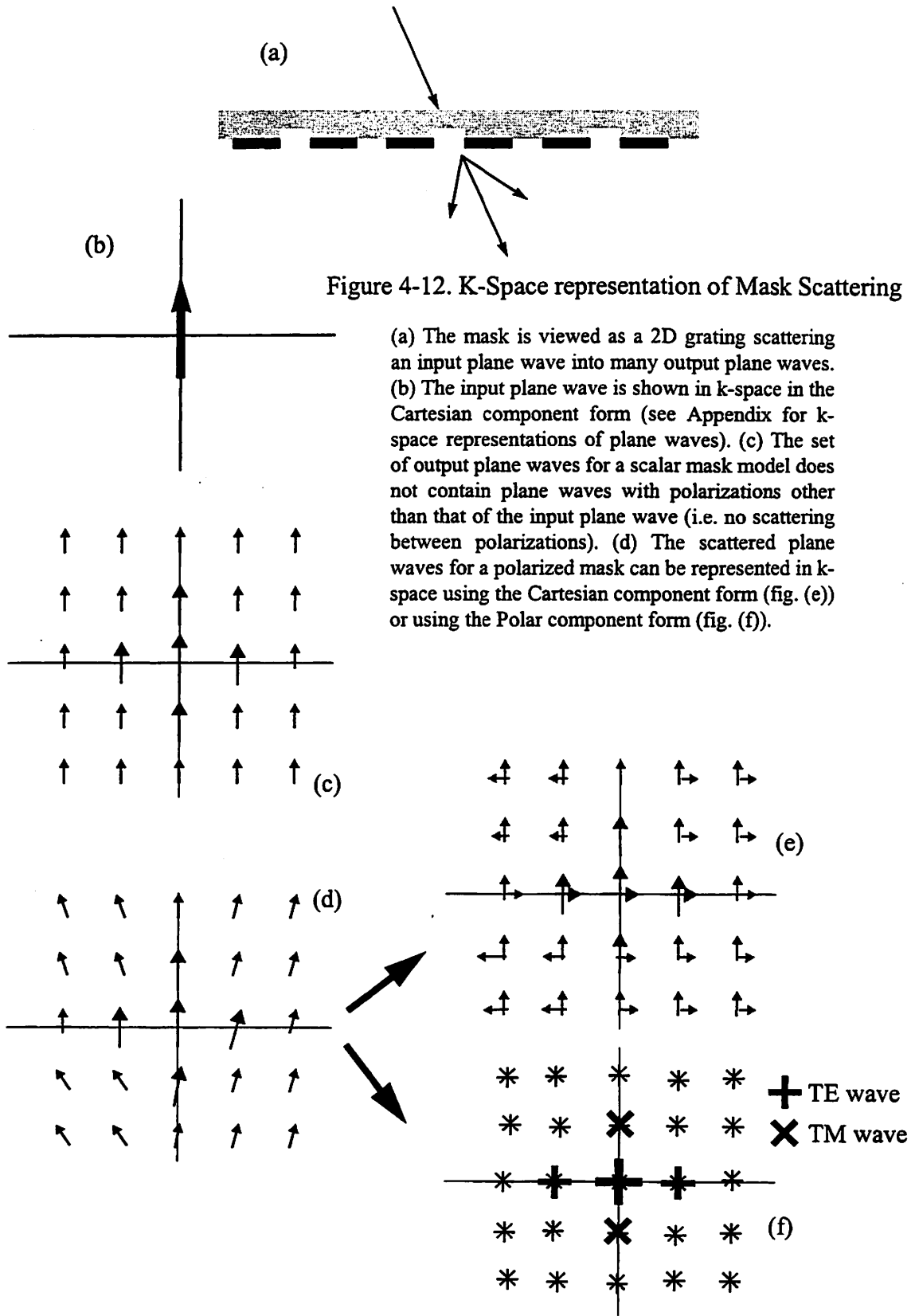
fers from the ideal transmission by comparing the magnitude of the electric field just below the mask with the ideal mask transmission assumed in the thin mask approximation.

As Figure 4-11 suggests, a more complicated transmission function must be used to capture the edge effects not considered in the thin mask model. This model, the “Thick, scalar, constant scattering coefficient model” is similar to the “Thin, scalar, constant scattering coefficient model” except that TEMPEST is used to calculate that transmission function (and thus the scattering coefficients) rather than just assuming a simple perfect transmission function as in Figure 4-10.

The thin, scalar model in the previous section is also lacking in other important respects - it does not account for scattering from one electric field polarization direction into another (Figure 4-12), nor for differences in how differently polarized waves scatter. Figure 4-13 shows how a small phase shifted contact hole can scatter light with one polarization into other polarizations. The incident field is completely polarized in the y-direction while the output field has electric field components in the x and z directions. Note that most of the energy remains in the y-component, but considerable energy is scattered into the other components.

To account for polarization effects, scattering coefficients are calculated for both polarizations at normal incidence which is in contrast to the previous model where the same transmission function (set of scattering coefficients) is used for both polarizations.

Extracting a transmission function from a rigorous electromagnetic simulation has several mathematical steps. First, the mask topography is programmed into TEMPEST, and the scattering of a single, purely TE or purely TM wave, originating from the “excitation plane”, is simulated. The scattered electric field is observed at the “observation plane” and is subsequently decomposed into plane wave components via the method of Appendix B. Both the excited plane wave and the scattered plane waves are propagated to the “object plane”. The “object plane” is, conceptually, a plane where a fictitious “equivalent thin mask” resides. This “equivalent thin mask” has a transmission function equivalent to the scattering effect of the real (thick) mask. See Figure 4-14 for an illustration of the various planes involved. The mathematical details now follow.



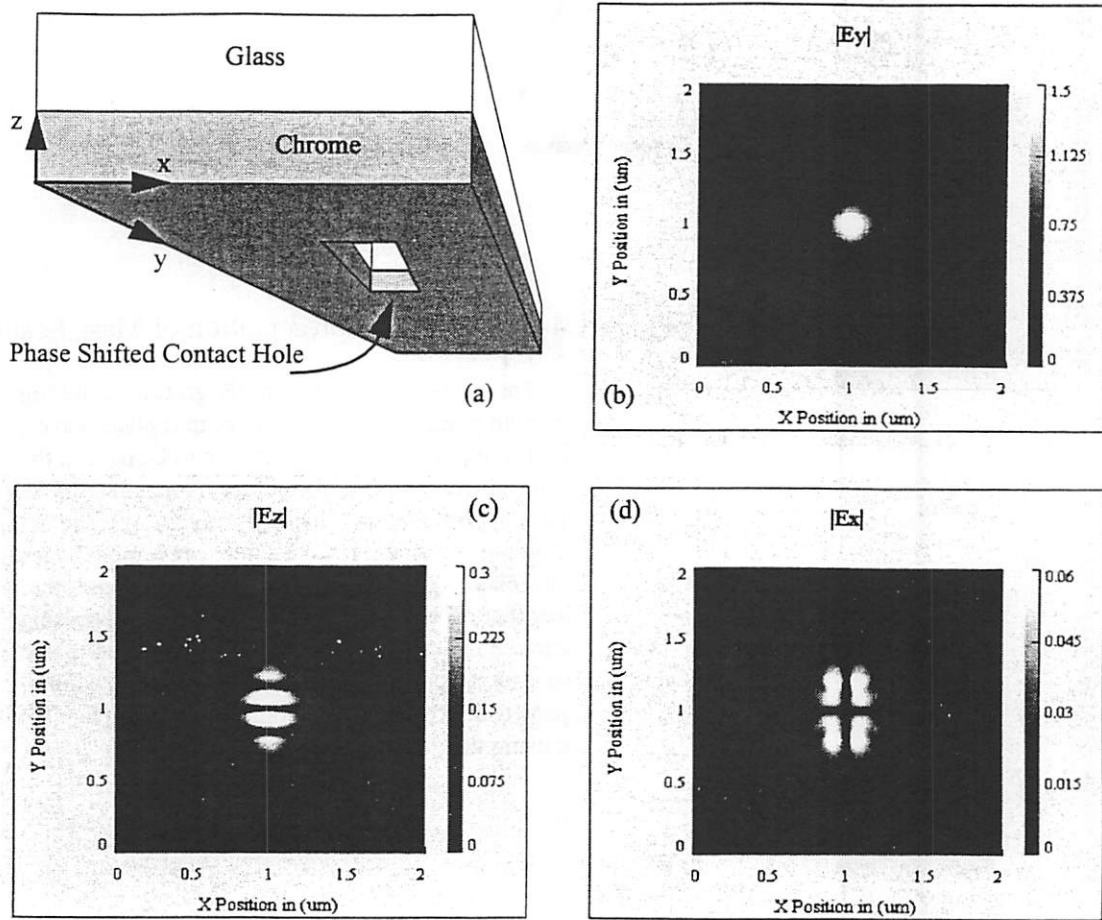


Figure 4-13. Polarization Scattering by a Three Dimensional Topography

- (a) The scattering topography is a 100nm, 180 degree phase shifted contact. The incident plane wave is from above with the electric field polarized in the y-direction
- (b) Most of the energy remains in the y-component of the electric field, but some scatters into the z and x components as shown in figures (c) and (d).

The excited (or “incident”) plane wave w_{sim} originates at the excitation plane. It is typically either a purely TE or purely TM wave. i.e.

$$w_{sim} = \begin{bmatrix} A_{sim} \\ 0 \end{bmatrix} \left(\frac{2\pi m_0}{L_x}, \frac{2\pi n_0}{L_y} \right) \text{ OR } w_{sim} = \begin{bmatrix} 0 \\ A_{sim} \end{bmatrix} \left(\frac{2\pi m_0}{L_x}, \frac{2\pi n_0}{L_y} \right) \quad \text{Eq. 4-41.}$$

The electric field is observed at the observation plane. This is the scattered field and is decomposed into a set of propagating plane wave components (see Appendix B):

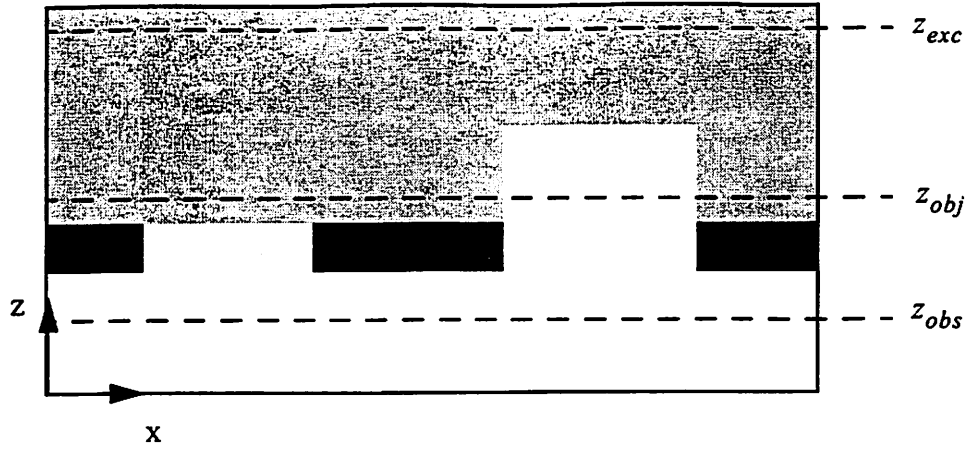


Figure 4-14. The Excitation, Observation and Object Planes used in the Calculation of the Mask Transmission Function

The incident field is excited, unidirectionally downward from the “excitation plane” ($z = z_{exc}$). The complex electric field is observed at the “observation plane” ($z = z_{obs}$), and the scattering coefficients are calculated for a “equivalent thin mask” which exists at the “object plane” ($z = z_{obj}$).

$$\begin{bmatrix} \underline{A}_{TE, mn} \\ \underline{A}_{TM, mn} \end{bmatrix}_{\underline{k}_{scat, mn}} = \Delta x \Delta y [\underline{M}]_{\underline{k}_{mn}}^{-1} \begin{bmatrix} e^{j\left(\frac{2\pi m}{L_x} r_{ex, x} \Delta x + \frac{2\pi n}{L_y} r_{ex, y} \Delta y\right)} \underline{E}_x[-m, -n] \\ e^{j\left(\frac{2\pi m}{L_x} r_{ey, x} \Delta x + \frac{2\pi n}{L_y} r_{ey, y} \Delta y\right)} \underline{E}_y[-m, -n] \end{bmatrix} \quad \text{Eq. 4-42.}$$

where $\underline{k}_{mn} = \left(\frac{2\pi(m_0 + m)}{L_x}, \frac{2\pi(n_0 + n)}{L_y} \right)$ is the direction of propagation of the $(+m, +n)^{\text{th}}$ scattered order. The plane wave coefficients $\underline{A}_{TE, mn}$, and $\underline{A}_{TM, mn}$, however, are not the scattering coefficients for the equivalent thin mask residing at the “object plane” because they have the wrong phase relationship with the input wave w_{sim} . Once the differences in location of the three planes are compensated for by propagating the waves to the object plane (see Figure 4-15), the scattering coefficients for w_{sim} are yielded:

$$\begin{bmatrix} SC_{TE, mn}(w_{sim}) \\ SC_{TM, mn}(w_{sim}) \end{bmatrix}_{k_{scat, mn}} = \frac{\begin{pmatrix} A_{TE, mn} \\ A_{TM, mn} \end{pmatrix}_{k_{scat, mn}} e^{-jk_{scat, mn, z}(z_{obj} - z_{obs})}}{A_{sim} e^{-jk_{sim, z}(z_{obj} - z_{exc})}} \quad \text{Eq. 4-43.}$$

where $k_{scat, mn, z}$ is the z-component of the k-vector for the scattered orders and $k_{sim, z}$ is the z-component of the k-vector for the input wave w_{sim} .

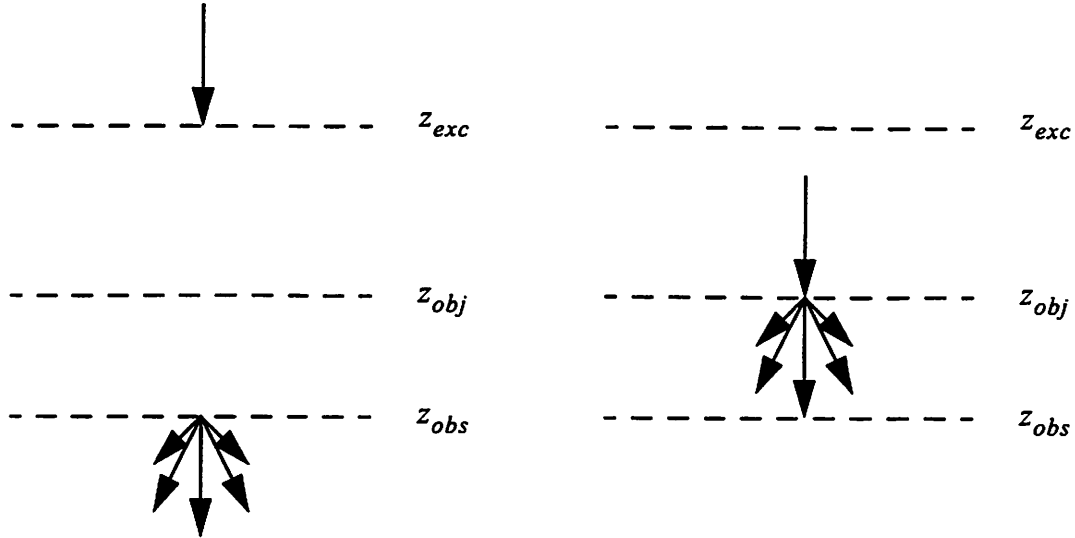


Figure 4-15. Generating an Equivalent Thin Mask

The plane wave at the excitation plane must be forward propagated to the object plane and the plane waves at the observation plane must be backward propagated to the object plane in order to obtain the scattering coefficients for the equivalent thin mask located at the object plane.

Like the previous model, the scattering coefficients are known only for the normally incident TE and TM waves. Scattering coefficients for all other incident plane waves are approximated using Equation 4-28 with $p \in \{TE, TM\}$ and q indexing over only a single value (corresponding to $(k_x, k_y) = (0, 0)$), and with the weightings $w_{pq} = 1$.

For lithographers, the differences between the thin and thick models is best quantified by observing and comparing aerial images. Figure 4-16 and Figure 4-17 graph the difference in measured line width (CD) for a single, isolated mask feature with 193nm lithography. Figure 4-16 indicates that the accuracy of the thin mask approximation begins to degrade

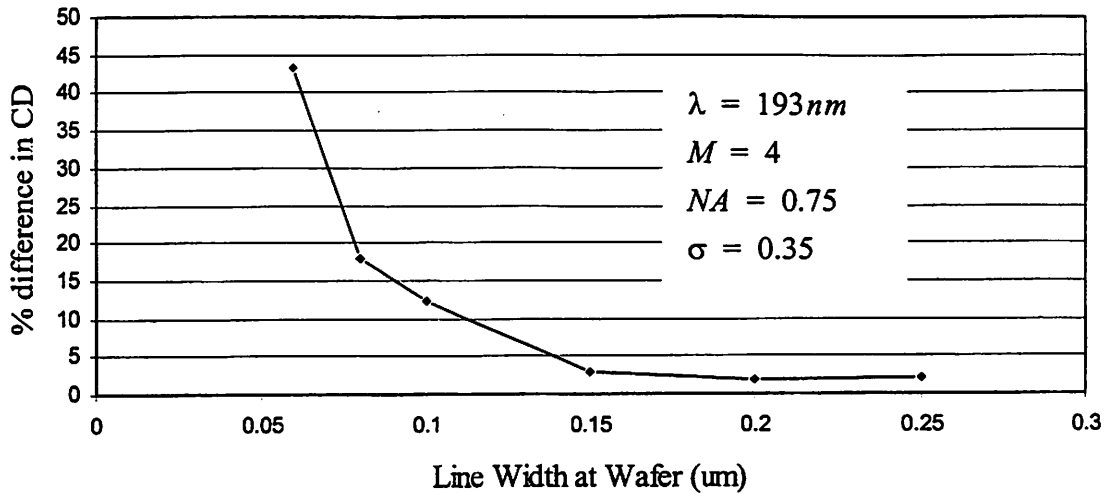
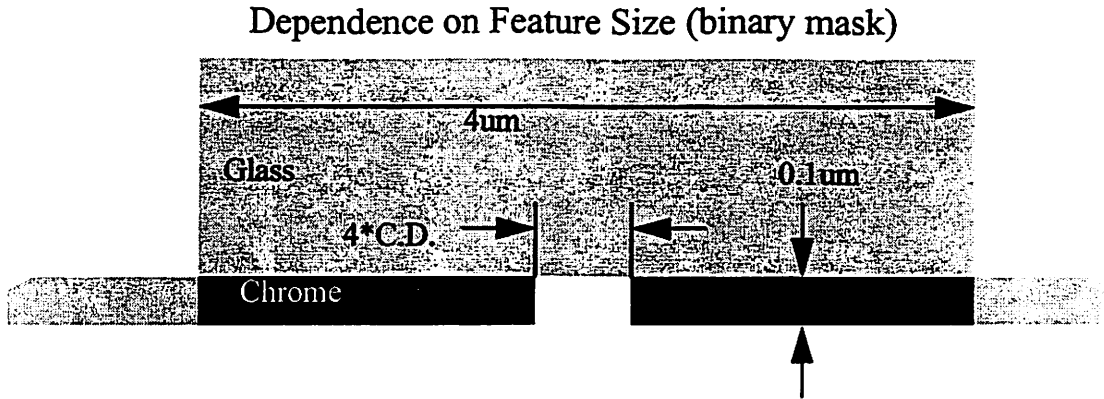


Figure 4-16. Thin mask Approximation Error vs. Feature Size for Simple Chrome on Glass line with 193nm Lithography

As the width of the opening in the chrome shrinks, scattering from the edges becomes more significant in proportion to the energy that transmits through the opening.

for C.D. less than 0.15um. Figure 4-17 indicates that for phase shifting masks, the situation is even worse because of the higher aspect ratio of the phase shifted features.

Figure 4-18 shows how aerial images for a typical alternating phase shift mask topography differ when calculated with thin, scalar and the thick, vector models. Clearly rigorous electromagnetic simulation is required for alternating phase shift mask topographies.

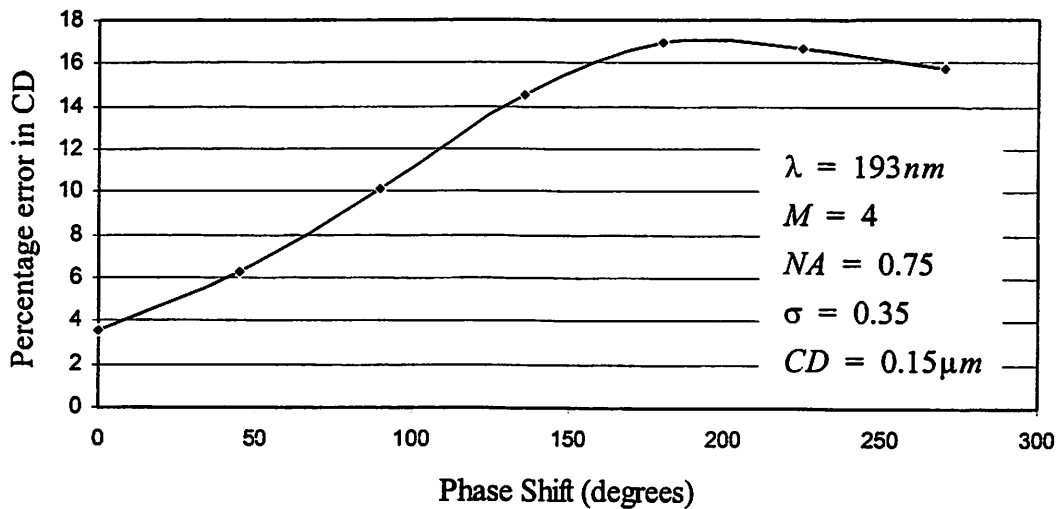
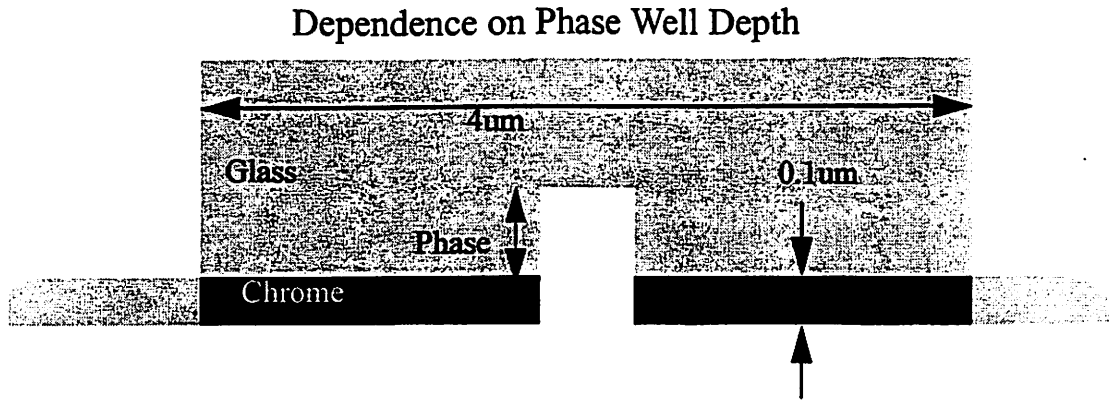


Figure 4-17. Thin mask Approximation Error vs. Phase Well Depth for 0.15 μm lines with 193nm lithography

As the depth of the phase shifter deepens, the accuracy of the perfect transmission model degrades. Phase shifters must be modeled rigorously.

4.7.2.3. Thick, vector non-constant scattering coefficient model

The final level of mask model complexity involves removing the assumption of constant scattering coefficients. This model, like the previous model, uses rigorous electromagnetic simulation to calculate scattering coefficients for certain plane waves. But, in this model, scattering coefficients are calculated for plane wave other than normally incident. Figure 4-7 (b) and (c) are two examples of different distributions of plane waves at multiple angles for which scattering coefficients are calculated with TEMPEST.

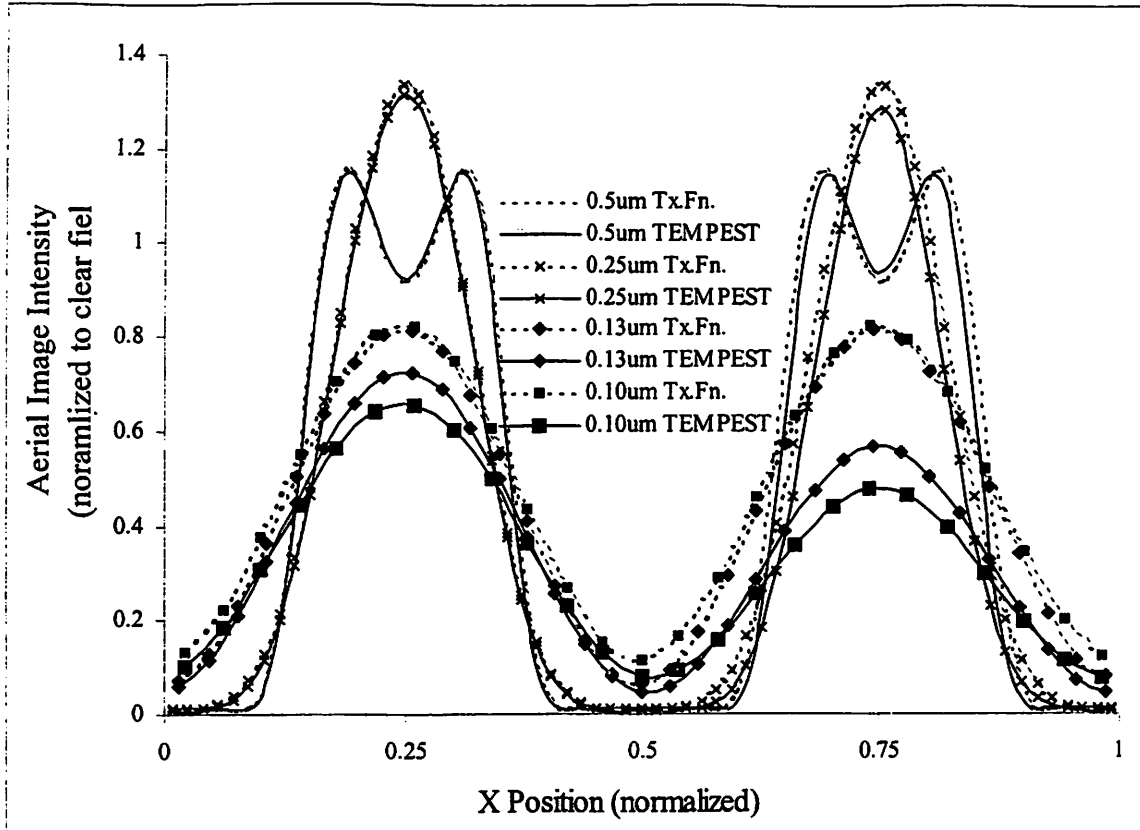


Figure 4-18. Aerial Image Intensity for Alt. PSM at Various CD's

The simulation parameters used: (1:1 Line/Space, 4X PSM, $\lambda=193\text{nm}$, $\text{NA}=0.75$, $\sigma=0.35$). Dramatic differences between the thin, scalar, mask model and the thick vector model are observed for features smaller than $0.25\mu\text{m}$. The unshifted line is on the left and the shifted line is on the right.

The more the scattering coefficients vary across the illumination pupil, the more plane waves must be simulated with TEMPEST. As part of work toward this dissertation, Pistor *et al.* investigate these effects in [68] where they define a quantity called the “shadow ratio” that indicates how dependent a feature’s scattering coefficients might be on the angle of incidence (see Figure 4-19). The shadow ratio is clearly a function of both the photomask and the imaging system. Table 4-1 presents the shadow ratios for various photomasks and imaging systems. One expects situations where the shadow ratio is high, such as the dual-trench phase-shift mask and inspection systems with high- σ , 1X optics to exhibit non-constant scattering coefficient behavior.

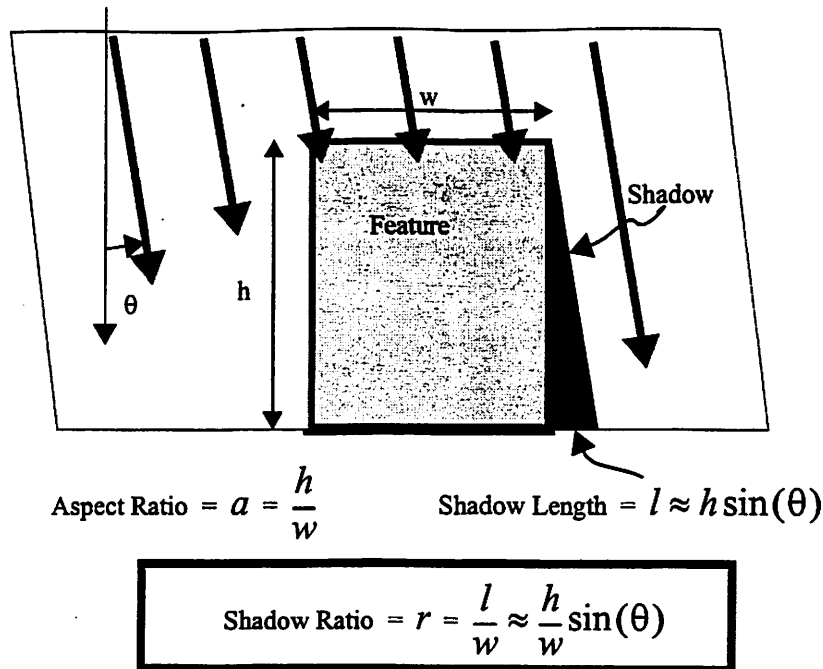


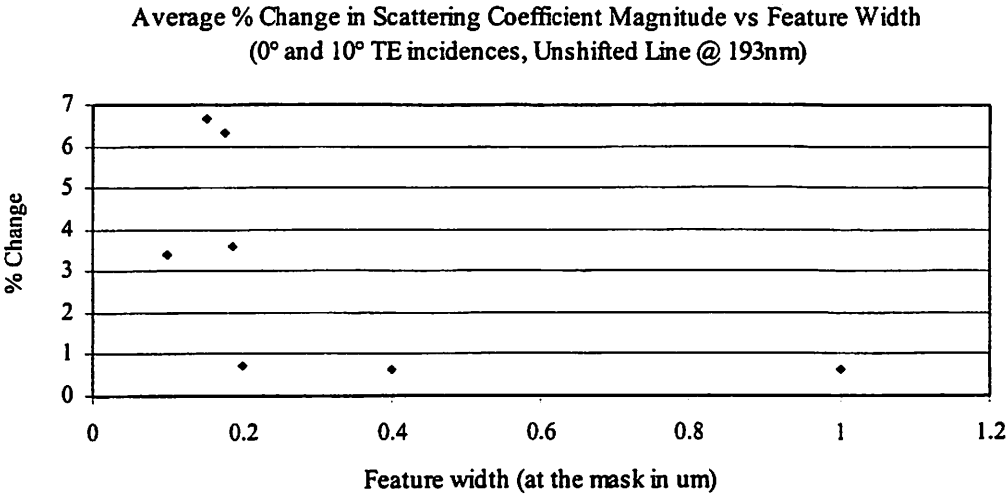
Figure 4-19. Defining the “Shadow Ratio”

The “Shadow Ratio” is the product of the aspect ratio and the sine of the angle of incidence. It is numerically equivalent to the fraction of the feature width which is in shadow. Its value represents the overall susceptibility to oblique incidence effects.

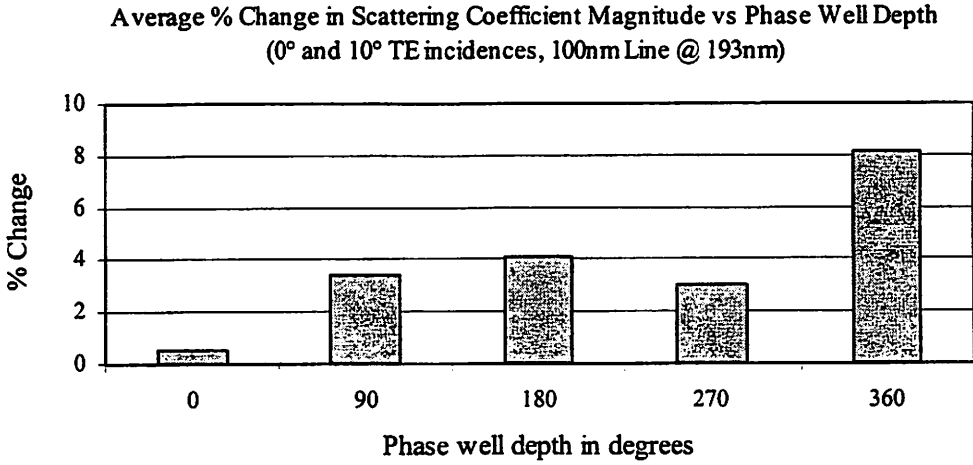
System	Reticle	NA	σ	$\theta_{air}, \theta_{glass}$	Feature Height/Width	Aspect Ratio	Shadow Ratio (S.R.)
193nm	binary with OPC	0.63	0.8	7.2,4.8	120/400	0.30	0.038
193nm	alternating PSM	0.63	0.5	4.5,3.0	313/400	0.78	0.061
193nm	Dual Trench PSM (90/270)	0.85	0.55	6.7,4.5	410/400	1.03	0.120
248nm	attenuating PSM (MoSi) 18%	0.63	0.8	7.2,4.8	284/560	0.51	0.064
EUV	Binary with Al absorber	0.25	0.6	2.1	100/200	0.5	0.018
Inspection (1X)	alternating PSM	0.6	1.0	58,34	313/400	0.78	0.468

Table 4-1. The Shadow Ratios for Various Systems

It is seen in Figure 4-20 that the scattering coefficients become dependent on the angle of incidence once a feature's aspect ratio gets high. When this happens the previous mask models begin to break down.



(a)



(b)

Figure 4-20. Scattering Coefficient Dependence on Feature Size

In (a), the width of a chrome opening is varied and the average percentage change in scattering coefficient magnitude (averaged over the -2, -1, 0, +1 and +2 orders) is calculated, while in (b) the same calculation is made for a 100nm wide (wafer dimension) line having different phase shifts. The scattering coefficients are seen to become dependent on angle of incidence as the feature aspect ratio becomes higher.

The same equations used in the previous mask model (Equation 4-42 and Equation 4-43) are used to extract the scattering coefficients from the electric field output by TEMPEST

and the weighted average interpolation scheme (Equation 4-28, Equation 4-29 and Equation 4-30) is used to approximate scattering coefficients for plane waves not simulated using TEMPEST.

One possible choice for the interpolation scheme would be to have the weights proportional to the inverse power of the k-space distance between the w_i and $w_{sim,pq}$ waves.

$$w_i = \frac{1}{|\vec{k}_i - \vec{k}_{sim,pq}|^\alpha} \quad \text{Eq. 4-44.}$$

Choosing $\alpha = 0$ would weigh all scattering coefficients equally, regardless of their location in k-space, while $\alpha = \infty$ would yield a zero weight for all scattering coefficients except the closest set. Finally, choosing $1 < \alpha < \infty$ yields a weighting where the scattering coefficients with reference waves close the input wave are weighted strongly, and scattering coefficients with reference waves far from the input wave are weighted weakly. Figure 4-21 shows an example of this sort of interpolation for various values of α .

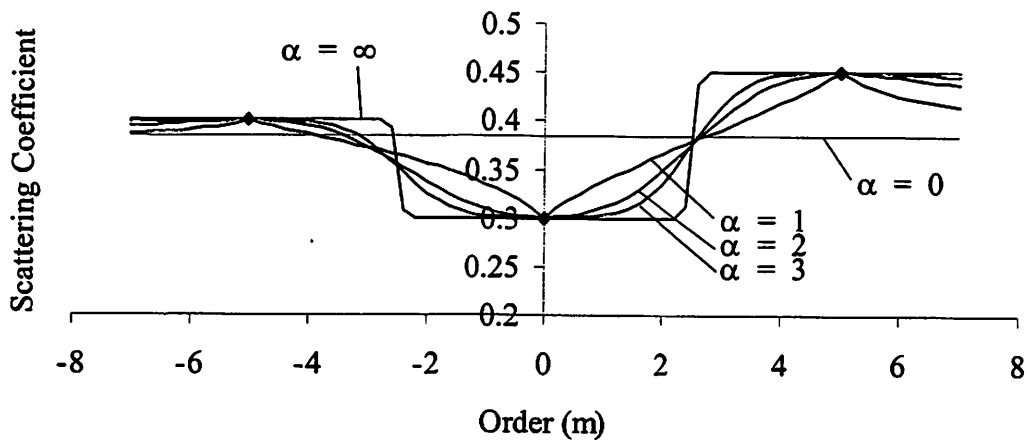


Figure 4-21. Inverse Power Law Weightings for Scattering Coefficient Interpolation

The different values for α yield different types of interpolated scattering coefficient values. An α values between 1 and 3 seems to be a reasonable choice.

Another interpolation scheme, called Planar Segment Linear Interpolation, sets the weights of all points to zero except for the closest three to the input wave. A plane is constructed

with the three vertices and used for interpolation. This interpolation scheme is illustrated in Figure 4-22.

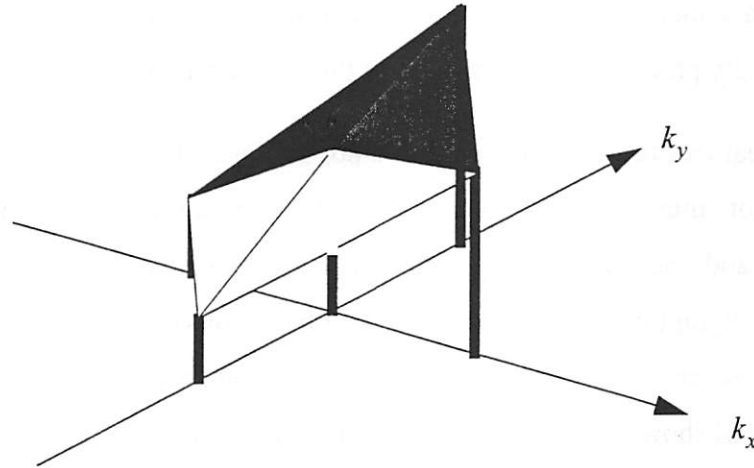


Figure 4-22. Planar Segment Linear Interpolation

Scattering coefficients are known at five points in k -space. Planar segments are created for each group of three neighboring k -space point for the purpose of interpolation. Planar segments could be extended for points outside of the triangle formed by the planar segment's projection onto the k_x - k_y plane.

Other interpolations schemes, such as low-order polynomial fitting may also be appropriate. The choice of which scheme to use really depends on how the scattering coefficients vary in k -space.

4.7.3. Choosing the Appropriate Mask Model

The choice of mask model for a particular mask depends on the mask topography and the behavior of the scattering coefficients for input waves across the illumination pupil. The thin mask approximation has been used extensively for simple binary (chrome-on-glass) masks where the relatively thin chrome (80nm to 200nm thick) and wide features (400nm and wider) make the feature aspect ratio small and 4X reduction optics limit plane wave angle of incidence to less than 15 degrees¹. The transmission function used by the thin mask model is a binary function (zero or one) and corresponds to the pattern of chrome on the mask.

1. The numerical aperture of the collection optics, as seen by the mask is NA/M , and for 4X reduction optics, a numerical aperture of $NA = 1.0$ and a partial coherence factor and $\sigma = 1.0$, the maximum angle of incidence to the mask is approximately 15 degrees.

OPC features (serifs and scatter bars), however, may have much smaller widths and introduce coupling between the electric field components. Adam has studied the limits of the thin mask model for OPC features[5] and found that rigorous simulation was necessary to accurately predict the performance of the smallest features.

It is clear that the thin mask model is not sufficient for phase shift masks which are inherently not “thin”. Wong[94] was the first to point out the lack of intensity balance between etched and unetched openings. This intensity imbalance is a direct result of the mask vertical topography and must be modeled with rigorous electromagnetic simulation. This does not, however, imply that scattering coefficients are a strong function of angle of incidence. Pistor[68] showed that scattering coefficients remain relatively constant for typical phase shift masks in printing situations.

Masks inspection systems, however, illuminate the mask with a much wider angular spectrum. One commonly used technique for inspection, scanning beam microscopy, for example, scans a focused beam across a wafer. The focused beam is made small in order to achieve a high resolution and thus contains very highly oblique plane waves - perhaps as high as 50 or 60 degrees. There can be no doubt that scattering coefficients will vary for incident waves at opposite extremes of the illumination pupil. Simulating only the normally incident TE and TM waves will not be sufficient.

A summary of the three mask models is given in Table 4-2..

4.8. Discussion

An imaging system is modeled as a collection of components that operate on plane waves. The source and illumination optic are considered as a source of mutually incoherent plane waves with different polarizations and angles of incidence. The object, typically a photo-mask in lithography, scatters an incident plane wave into many plane waves. The projection optic takes a single plane wave as input and produces a single output plane wave with the same polarization and accounts for the imaging pupil, aberrations, defocus, and optical magnification. Finally, the film stack at the image plane can be incorporated into the projection optic as a correction factor.

Approximation	Comment	Situations
Thin Mask	-completely defined by complex transmission function -constant scattering coefficients -scalar theory (one field component)	-binary masks -binary masks with OPC -EUV (no defects multilayer mirror defects)
Thick Polar Mask	-need two REMS (same angle of incidence, but different polarizations) -constant scattering coefficients (w.r.t. AOI, but not w.r.t. polarization) -vector theory	-Phase Shift Masks -Advanced OPC -EUV with defects (both pattern and multilayer mirror)
General 3D Mask	-need multiple REMS at different angles and polarizations -non-constant scattering coefficients -vector theory	-Advanced PSM (such as dual trench with ultra-small features, high NA & sigma) -Inspection (1X) Systems -Wild schemes (such as dark field imaging, $\sigma > 1$)

Table 4-2. Summary of Photomask Simulation Models

The imaging equations presented in this chapter take the vector nature of light fully into account and can accommodate various mask model complexities ranging from simple transmission function to complicated non-constant scattering coefficient models where information from the rigorous simulation of the scattering of several plane waves at different polarizations and angles of incidence is used together to model the mask.

With regards to efficiency, Hopkins' equations have the advantage that once the transmission cross coefficients are calculated, they need not be recalculated for different mask topographies. However, they must be recalculated for different imaging situations, such as through-focus. The equations presented in this chapter offer no efficiencies for different mask topographies, but do offer efficiencies for different imaging systems since once scattering coefficients are approximated for one mask topography, they can be used over and over again for different projection optic and film stack conditions.

The object or photomask is considered as a "black-box" that takes a single plane wave as input and outputs several plane waves that are related to the input plane wave by the scattering coefficients. Three mask models are presented, each differing from the other by how the scattering coefficients are calculated, and how many sets of scattering coefficients are calculated for different plane waves within the illumination pupil.

5 Simulation of Extreme Ultraviolet Lithography

5.1. Introduction

The smallest feature that can be printed on a wafer is directly related to the wavelength of light used by the lithographic imaging system. A formula often used by lithographers expresses minimum “Critical Dimension” (CD) or feature width as:

Equation 5-1.
$$CD = K_1 \frac{\lambda}{NA}$$

Present day state-of-the-art lithographic imaging systems use light emitted from a ArF laser with a wavelength of 193nm (Deep Ultraviolet or DUV) and have numerical apertures approaching 0.8. The use of advanced imaging techniques (phase shift masks, annular illumination, top-surface-imaging etc.) push the K_1 factor down to 0.3 to 0.4. This means that the smallest features that can be printed with 193nm lithography will be in the 80nm to 100nm range. To print smaller features, with smaller pitches, a smaller wavelength of light must be used.

The choice of wavelengths smaller than 193nm is far from an arbitrary choice. A suitable source, optical imaging system, and resist must exist. One wavelength for which all these requirements are met is 13.4nm and corresponds to a light that is on the border between ultraviolet and x-ray radiation. This region of the electromagnetic spectrum is called Extreme Ultraviolet (or EUV) or soft-x-ray. Lithography performed with EUV light is called Extreme Ultraviolet Lithography (EUVL) [9][82][77].

At EUV wavelengths, all materials are highly absorbing and have optical indices of refraction (n) very close to unity [7] meaning that refractive optics would be impractical (due to

the lack of light-refracting power). An alternative to refractive optics is reflective optics which implies the use of curved mirrors to reflect the EUV light. Again, due to the near unity refractive index of all materials at EUV wavelengths, a single material interface will not provide significant reflectivity. However, small reflections from many material interfaces could be made to add together to form a large reflection. This is the principle behind the multilayer mirror.

A multilayer mirror is a thin film stack of alternating layers of two different materials. The bilayer thickness is carefully chosen so that reflections from the layers add in phase.[8] With careful control of the deposition processes, multilayer mirrors made from alternating layers of Silicon and Molybdenum that yield power reflectivities in the 70% range have been built[54] for use in EUVL.

An extremely simplified model of an EUVL optical system is shown in Figure 5-1. The light emitted by the EUV source is collected by the collection optic (a curved multilayer mirror) and is incident onto the mask. The mask (Figure 5-2) is a multilayer mirror patterned with an absorbing material, such as chromium. The chromium absorber will absorb the incident EUV light with very little reflection while the uncovered areas of the multilayer mirror will reflect light. A projection optic collects the reflected light and forms an image of the mask at the wafer.

Simulation plays a critical role in the development of EUVL for several reasons - the primary one being the nonexistence of hardware. Very few experimental results are available and those that are available are expensive to obtain. Simulation provides guidance to the designers of the hardware by pointing out trends and dependencies. Mask designers need to know how important parameters such as feature dimensions and multilayer mirror defects are, while system designers need to understand the effects of parameters such as off-axis incidence, partial coherence and defocus. Simulation also provides results with a much higher degree of measurability. Simulation will continue to be a valuable tool even once hardware exists and experimental results are achievable.

Extreme Ultraviolet Lithography (EUVL) presents several challenges for rigorous electromagnetic simulation. The single most important hurdle to overcome is the memory require-

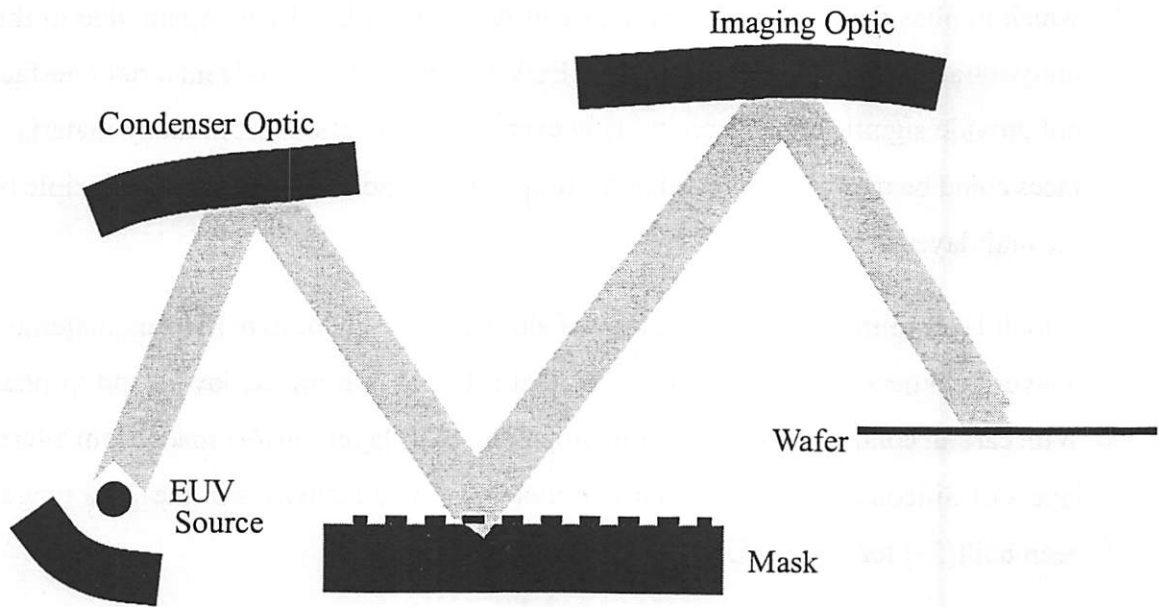


Figure 5-1. Simple Model For an Extreme Ultraviolet Lithography System

The source and condenser optic illuminate the mask with off-axis light. The light reflected from the mask is collected by the imaging optic and is directed to the wafer where the pattern at the mask is reproduced.

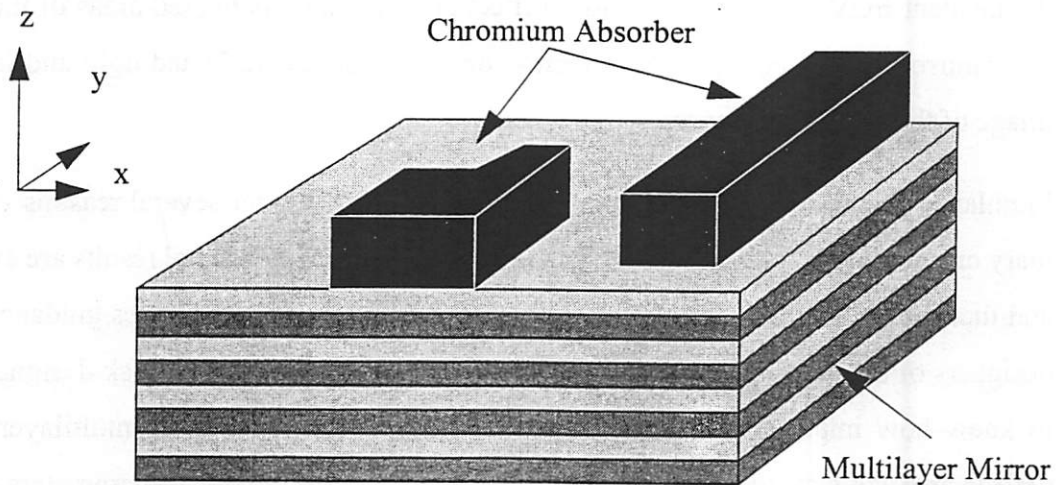


Figure 5-2. An EUVL mask

An EUVL mask is a multilayer mirror (typically 80 quarter-wavelength layers of alternating Si and Mo) that is patterned with an absorbing material (typically chromium). The chromium must be thick enough to attenuate the incident light in order for sufficient contrast to exist in the reflected field.

ment for EUV mask simulation. Because the mask feature size is so much larger than the wavelength (typically 13.4nm), very large simulation domains are required. Table 5-1 compares the feature size and memory required by TEMPEST for various wavelengths used in lithography.

Table 5-1. Wavelengths Features and Memory Required for Simulation for Various Photolithographies

Wave-length	Feature Width at Mask (4X)	Feature-To-Wave-length Ratio	Feature Height at Mask	Simulation Domain Size for 4X mask (2 by 2 contact holes)
248nm	180nm x 4 = 720nm	2.9	Chrome + Phase Well = 100nm+248nm=348nm (1.4 λ)	(using 22.5 cells/ λ) 65 MBytes
193nm	130nm x 4 = 520nm	2.7	Chrome + Phase Well = 100nm + 193nm = 293nm (1.5 λ)	(using 22.5 cells/ λ) 61 MBytes
13.4nm	100nm x 4 = 400nm	30	40 bilayer Mirror + 100nm Absorber = 368nm (27 λ)	(using 20 cells/ λ) 95000 MByte

Clearly, three dimensional simulation of EUVL photomasks is impractical with present day computer technology - unless new mathematical models are used to somehow reduce the amount of memory required.

In this thesis the use of parallel processing and the Fourier Boundary Condition (FBC) (Chapter 2) are used to overcome the computational barriers imposed by EUVL. Simulation work is divided into two categories: mask feature simulation and multilayer mirror defect simulation. Simulations presented in section 5.2 use the FBC in place of a perfect multilayer mirror to save memory. Effects of angle of incidence, absorber thickness, sidewall angle and corner rounding are investigated. Section 5.3 discusses how defects in the multilayer mirror structure are simulated for the purpose of assessing their printability.

5.2. Mask Feature Simulations

The EUV multilayer mirror is difficult to simulate with the finite-difference time-domain approach. The very thin (approximately $1/4 \lambda$) layers are difficult to discretize, the very small reflection coefficients of materials at EUV wavelengths are difficult to reproduce numerically, the many layers (typically 40 bilayers) require large amounts of memory to

be stored, the multiple reflections between layers cause the time to simulate to increase and last, but not least, there is the task of entering the multilayer mirror structure into the simulator input file.

Nguyen et al.[57] were the first to use TEMPEST to investigate (two-dimensional) absorber topography effects in EUVL. Bollepalli et al.[13] used a technique that stores the complex electric field at each layer and tracks the multiple reflections throughout the stack to investigate angle of incidence effects. Recently Schiavone et al.[69] have used rigorous coupled wave analysis (RCWA) to investigate the influence of absorber properties.

In this section, the Fourier Boundary Condition (FBC) (Chapter 2) is used to model the defect-free multilayer mirror used in the EUV photomask. This saves a tremendous amount of memory and simulation time because the entire mirror structure doesn't have to be programmed into the simulation domain. The mirror used for all feature simulations was a 40 bilayer Si/Mo mirror with reflection coefficients plotted in Figure 5-3.

Table 5-2 lists the optical properties of several materials commonly used in EUVL masks.

Table 5-2. Complex Index of Refraction for Various Materials at 13.4nm

Material	Use	$\delta (= 1 - n)$	$\beta (=k)$
Si	Multilayer Mirror	6.929e-5	1.821e-3
Mo	Multilayer Mirror	7.726e-2	6.220e-3
TiN	Absorber	6.340e-2	2.188e-2
Al	Absorber	-2.531e-3	2.957e-2
Cr	Absorber	6.667e-2	3.819e-2
SiO2	Buffer Layer	2.129e-2	1.057e-2

5.2.1. 1D pattern, 2D TEMPEST Domain

Several two-dimensional TEMPEST simulations of line/space patterns are used to investigate the effects of angle-of-incidence, mask focus, absorber thickness and side wall angle. The two-dimensional TEMPEST simulations of EUV mask features typically run in less than one minute and require less than 2 Megabytes of memory.

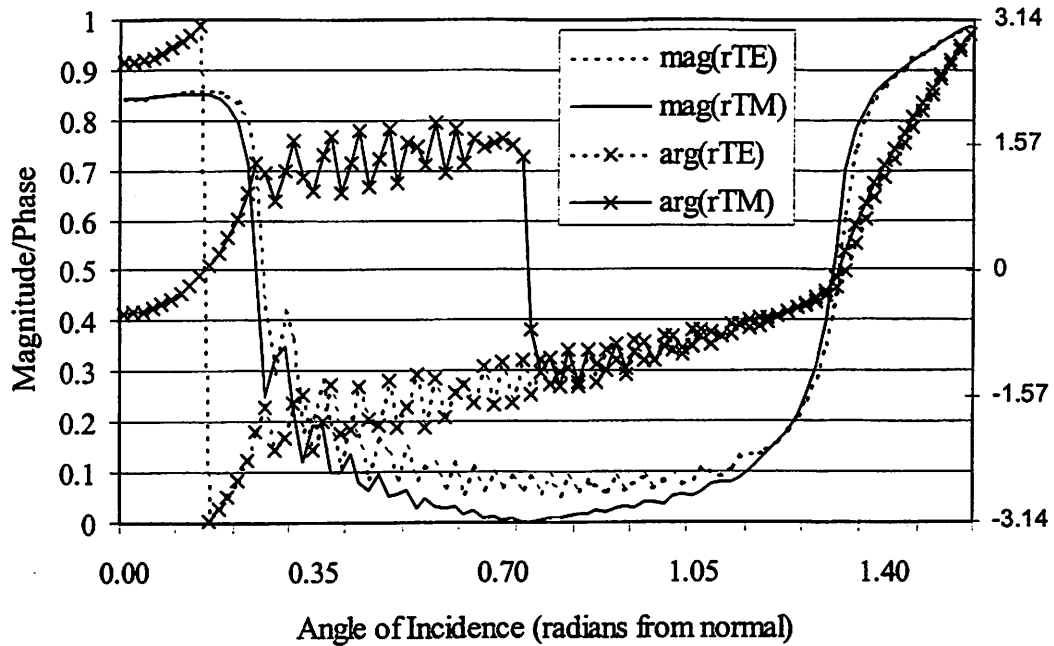


Figure 5-3. Reflection coefficients for 40 Bilayer Si/Mo Multilayer Mirror for EUVL at 13.4nm.

The reflection coefficient is calculated for a 40 bilayer Si/Mo multilayer mirror with $\Gamma = 0.4$, $d=6.938\text{nm}$, and for a wavelength of $\lambda = 13.4\text{nm}$.

5.2.1.1. Line/Space Pattern - 2D Topography

Figure 5-4 and Table 5-3 describe the line/space pattern topography. The multilayer mirror is replaced by a FBC that has been programmed with the reflectivity plotted in Figure 5-3.

Table 5-3. Simulation Parameters for EUV Line/Space Topography

Parameter	Description	Values(s)
CD	Line and Space Width at the Wafer	50nm
t_{Cr}	Thickness of chrome absorber	nominally 70nm, varied from 20nm to 70nm
t_{SiO_2}	Thickness of SiO2 buffer layer	20nm
θ_{sw}	Side wall angle	nominally 90 degrees, varied from 70 to 90 degrees
θ_i	Angle of incidence	nominally 3.8 degrees, varied from 0 to 8 degrees
NA	Numerical Aperture	0.25
σ	Partial Coherence Factor	0.60

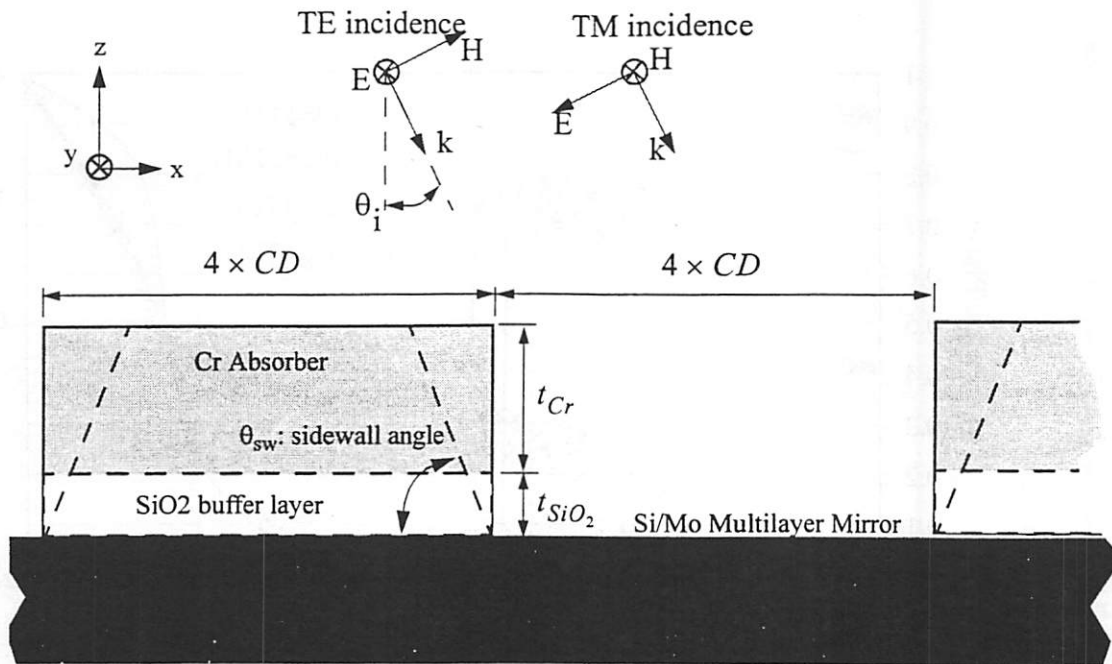


Figure 5-4. EUV Line/Space Topography - 2D TEMPEST

The basic topography of a line space pattern consists of a rectangle of chromium atop a multilayer mirror. The periodic boundary conditions (in the x-direction) imply that the physical situation represented by this topography is periodic.

Table 5-3. Simulation Parameters for EUV Line/Space Topography

Parameter	Description	Values(s)
M	Optical Demagnification	4X
z_{obj}	Object plane location - similar to mask plane of best focus	Nominally at the multilayer mirror surface, but varied from -120nm to +120nm

5.2.1.2. Near Field Intensity and Aerial Image

Figure 5-5 has two plots of the near field intensity and one plot of the aerial image for a nominal case (20nm SiO_2 buffer layer, 70nm chromium, vertical side walls and 3.8 degree incidence). In figure (a), the near field intensity in the zx -plane cross-section is shown. The attenuation of the incident field is observed inside the absorber material, and a standing wave pattern is observed over the bare mirror surface. A plane wave is excited unidirectionally and downward, at the “excitation plane” $z_{exc} = 120nm$. Above this excitation plane, only the reflected field exists. The reflected field is observed at the “observation plane” $z_{obs} = 125nm$. The intensity at the observation plane for both the TE and TM incidence are plotted in figure (b). The TE and TM waves are observed to scatter in a very sim-

ilar manner as evidenced by their reflected field intensities almost matching in figure (b). This does not imply that rigorous is not important, only that the TE and TM waves scatter in a similar fashion. In 3D, there could still be (and is) scattering from one polarization to another. Finally, the aerial image is plotted in figure (c). The “critical dimension” or “CD” measurement is defined to be the width of the bright line at the aerial image.

5.2.1.3. CD and position vs. Angle-Of-Incidence (AOI)

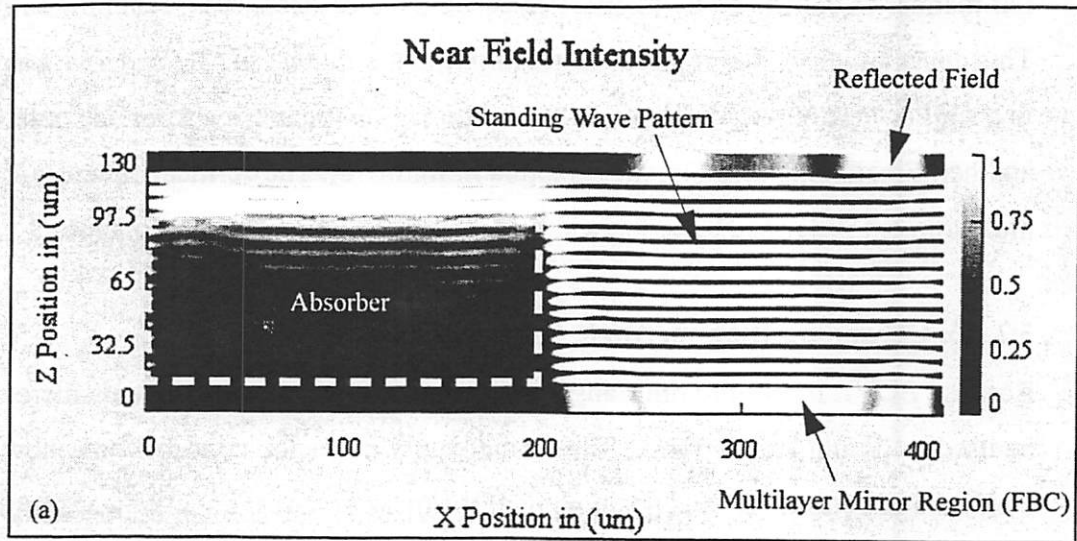
Because EUVL masks are not transmissive, but rather reflective, off axis incidence must be used to illuminate the mask. This immediately raises the concern about how angle of incidence affects the CD and positioning of the mask features. To investigate angle of incidence effects, aerial images were calculated for the nominal mask topography for several angles of incidence for different locations of the “object” plane (z_{obj}). The CD (width of the bright line) and the center position of the bright line were measured and plotted in Figure 5-6. The exposure level (intensity level at which the line width was measured) was chosen to yield a 50nm CD at an angle of incidence of 3.8 degrees.

The CD shrinks as angle of incidence increases but appears to be independent of the object plane location (z_{obj}). The position of the line changes with angle of incidence and also with the object plane location. The shift in line position with respect to angle-of-incidence is not a concern as the angle of incidence will be fixed. However, the dependence of line position on object plane location is a concern since the object plane is essentially the mask defocus.

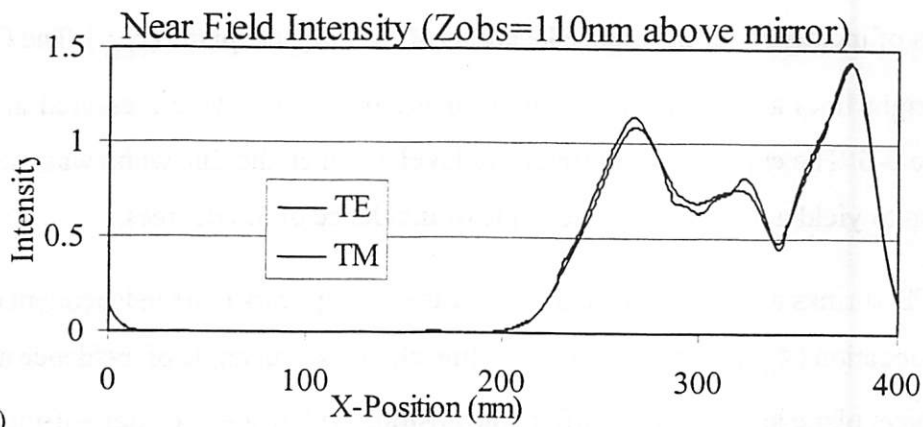
5.2.1.4. Absorber Material Thickness

Aerial images for three different absorber material thicknesses are plotted in Figure 5-7. For the thinnest case (30nm thickness), the absorber does not attenuate the incident field sufficiently and the DC level of the entire aerial image increases, lowering its contrast and increasing the CD of the line. But for a given mask, the chrome thickness is a set parameter and is not expected to vary by such a large degree.

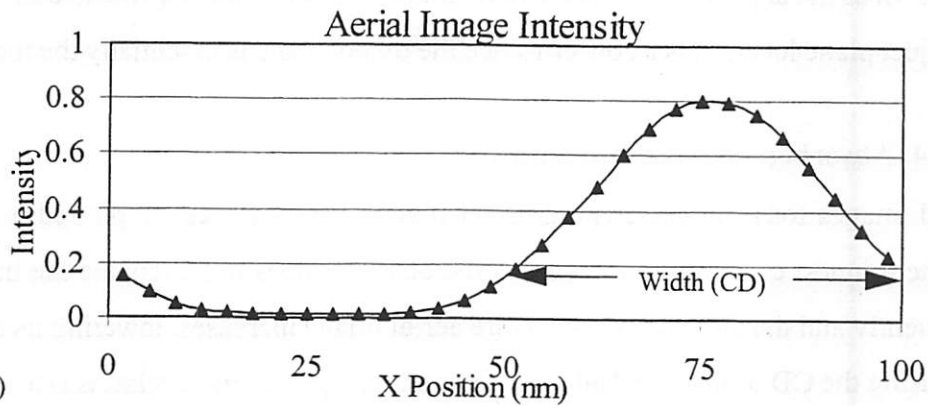
However, even for a set thickness, some small amount of thickness variation may be expected and the effect of this on aerial image is investigated in Figure 5-8 where the CD



(a)



(b)



(c)

Figure 5-5. 50nm Line/Space Pattern Near Fields and Aerial Image

(a) The near field in the zx -plane shows the field decaying inside the absorber and a standing wave pattern over the unpatterned mirror. (b) the reflected field observed at $Z_{obs} = 125 \text{ nm}$ (a cutline near the top of the first plot). (c) Aerial image intensity (4X reduction optic, $NA=0.25$ and $\sigma = 0.6$)

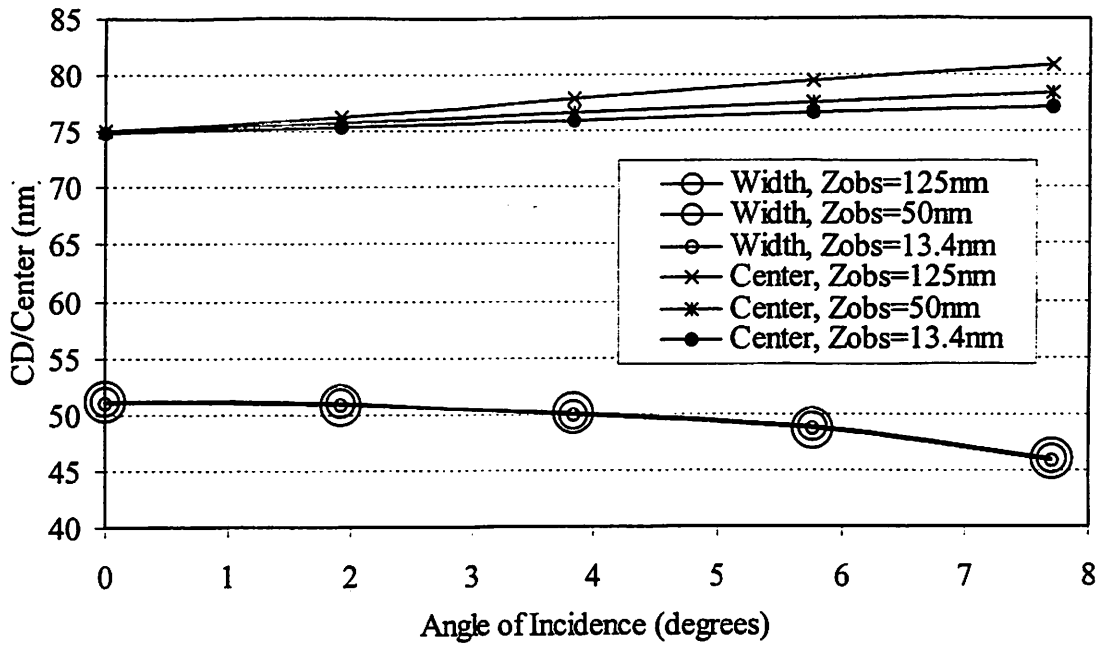


Figure 5-6. Line Width (CD) and Position for Various Object Plane Locations

The line width (nominally 50nm) shrinks as angle of incidence increases but appears to be independent of the object plane location (Z_{obj}). The position of the line changes with angle of incidence and also with the object plane location.

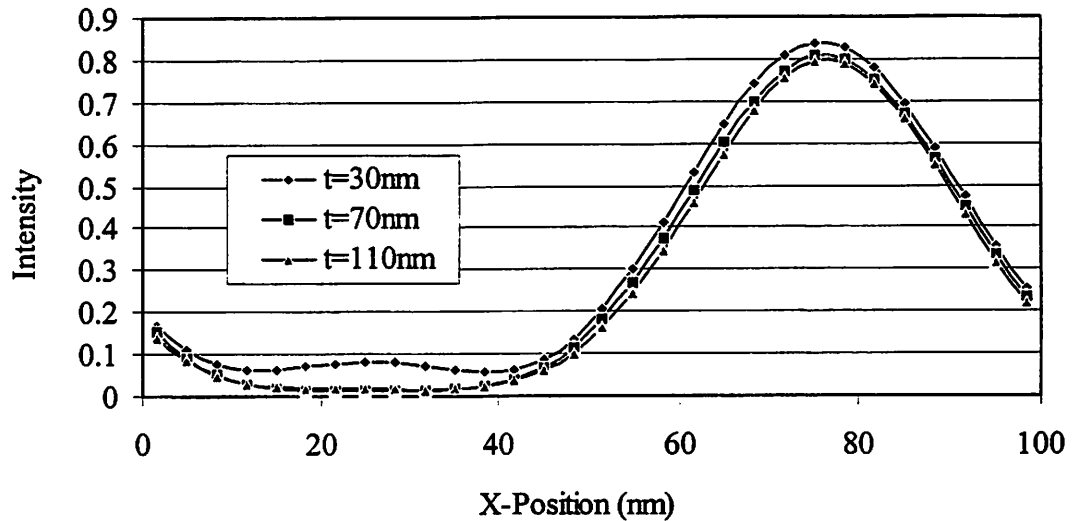


Figure 5-7. Aerial Image Intensity for Various Chrome Thicknesses

The thinner chrome provides less attenuation of the light impinging onto the absorber feature and leads to a higher DC level and a lower contrast.

is plotted over a small range of chrome thickness variation. A rather strong, periodic dependence of CD on absorber thickness is observed. The period, approximately 6.5nm is very close to a half-wavelength and indicates that this is clearly an interference effect between the light reflected off the top of the absorber and that penetrating down to the bottom of the absorber and reflecting back up. This effect was observed earlier by Toh and Davids[84] who also noted that “the CD variation due to mask height variation can be reduced by appropriate selection of the mask absorber material, as well as by increasing the illumination spectrum of the stepper.”

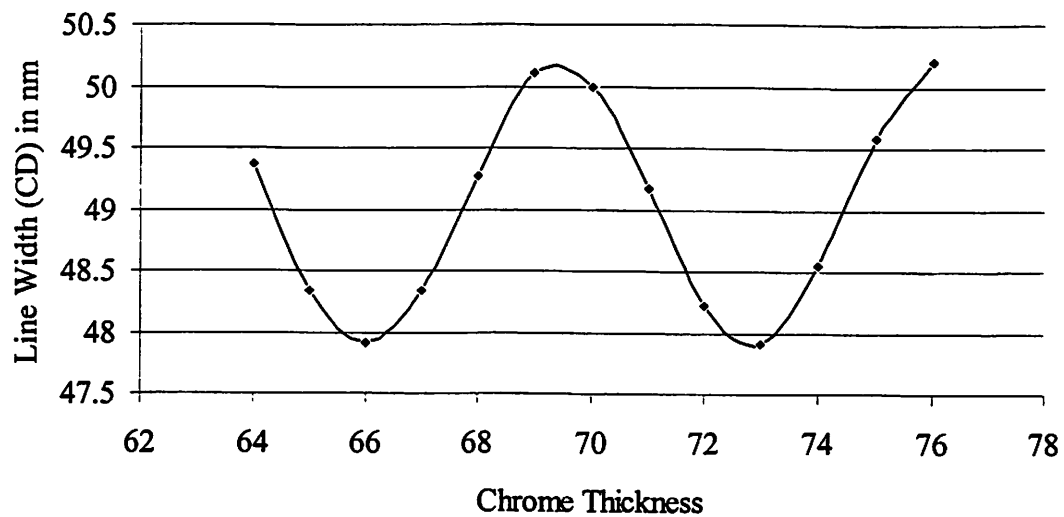


Figure 5-8. Line Width vs. Chrome Thickness

Even small changes in absorber material thickness can significantly affect the line width. This is because there is an interference effect between the small field reflecting off the top of the absorber and the small field which penetrates down through the absorber and reflects off the multilayer mirror. (hence the half-wavelength period of the above curve)

5.2.1.5. Absorber side wall angle

Decreasing the absorber feature’s vertical side wall slope decreases its effective horizontal width and thus reduces the amount of light that it “blocks”, increasing the effective width of the clear area and increasing the linewidth of the bright line. Figure 5-9 shows that a 10% increase in CD occurs for a decrease of 15 degrees in side wall angle.

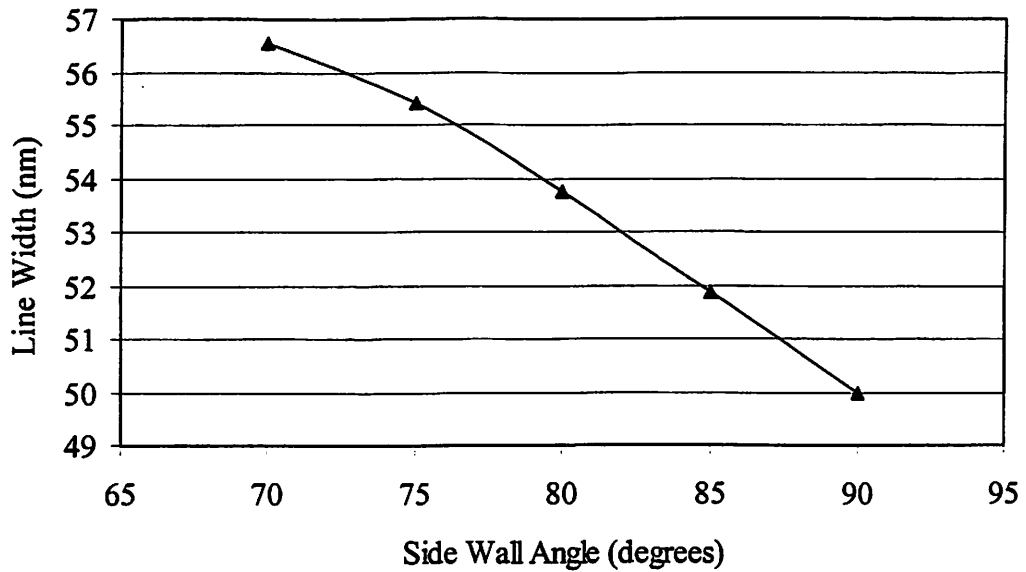


Figure 5-9. CD vs. Side Wall Angle

As the side wall angle decreases from vertical (90 degrees), the width of the absorber becomes smaller at the top (but remains constant at the bottom) and provides less absorption making the width of the bright line wider.

5.2.2. 2D pattern, 3D TEMPEST Domain

Two dimensional mask patterns, such as an array of contacts holes or line-ends require 3D TEMPEST simulations which require much more computation time and memory than do 2D simulations.

5.2.2.1. Square Features, 3D Topography

The topography of an exterior post is illustrated in Figure 5-10. The “interior” case has the chrome-covered and clear areas reversed. The simulation parameters used are presented in Table 5-4. Each TEMPEST run required less than 200 MByte of memory and ran in less than three hours on a 500 MHz Pentium processor.

Table 5-4. Simulation Parameters for EUV Line/Space Topography

Parameter	Description	Values(s)
CD	Line and Space Width at the Wafer	30nm
t_{Cr}	Thickness of chrome absorber	90nm (no buffer layer)
θ_{sw}	Side wall angle	90 degrees

3D Mask Topography - an Exterior Post

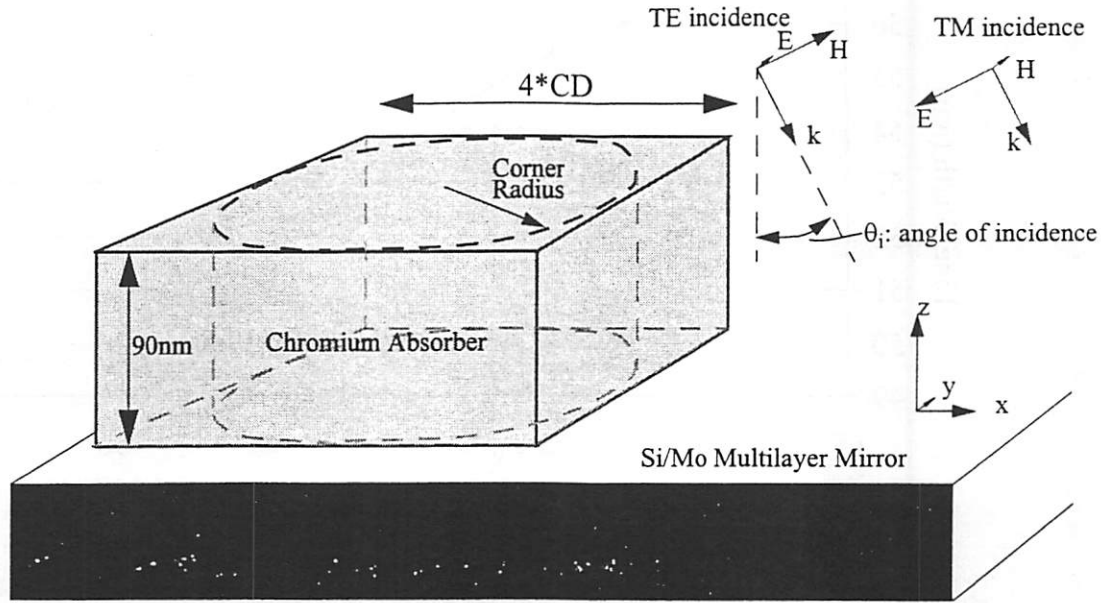


Figure 5-10. 3D Mask Topography

The 3D topography has a rectangular block of chromium atop a multilayer mirror. The feature depicted is an “exterior” post. The simulation domain contains one period of a periodic two dimensional array of posts.

Table 5-4. Simulation Parameters for EUV Line/Space Topography

Parameter	Description	Values(s)
r	Corner rounding radius	0, 20nm, 40nm
θ_i	Angle of incidence	3.2 degrees
NA	Numerical Aperture	0.25 and 0.35
σ	Partial Coherence Factor	0.60
M	Optical Demagnification	4X
z_{obj}	Object plane location - similar to mask plane of best focus	at multilayer surface

5.2.2.2. The near field

The near field intensity is shown in Figure 5-11 and exhibits a nonuniform behavior similar to the 2D case, especially in $y=60\text{nm}$ cutline. The field is symmetric in the y-direction as the illumination and topography have y-symmetry. The symmetry is broken in the x-direction by the angled incidence.

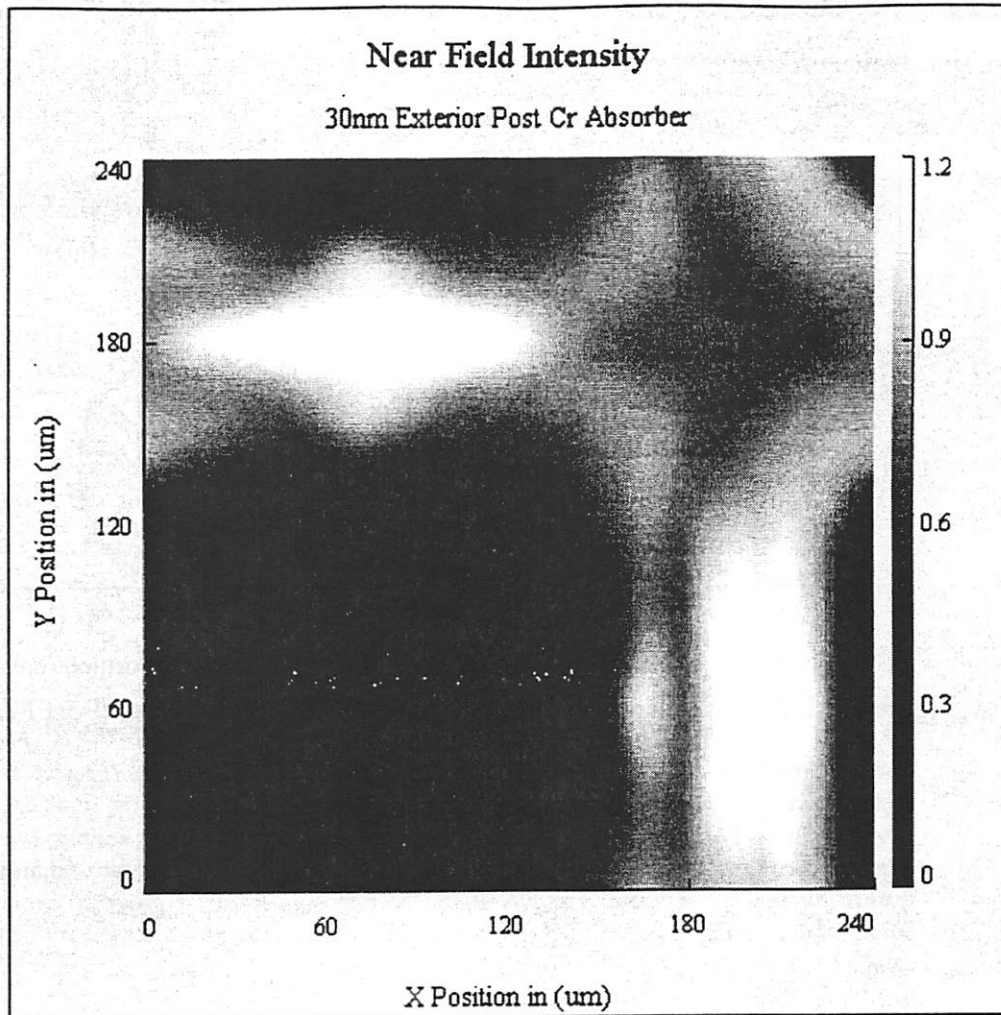


Figure 5-11. Near Field Intensity for 30nm Square Exterior Post

The reflected near field intensity is observed near the top of the simulation domain at an observation plane above the excitation plane. The dark square area corresponds to the area on the mirror covered by the absorber feature (hence very little reflected energy in that region).

5.2.2.3. Interior vs. Exterior Topographies

Aerial images for interior and exterior topographies are shown in Figure 5-12 for two different NA's. In both the NA=0.25 and NA=0.35 cases, the exposures (the level curves) were set so that the exterior topography's CD (width of the circular level curve in the x-direction) were 30nm. For the NA=0.25 case, there is a drastic difference in feature size. Both the exterior and interior features will not print simultaneously without severe mask

biasing. For the $NA=0.35$ case however, both the interior and exterior topographies yield similar feature sizes.

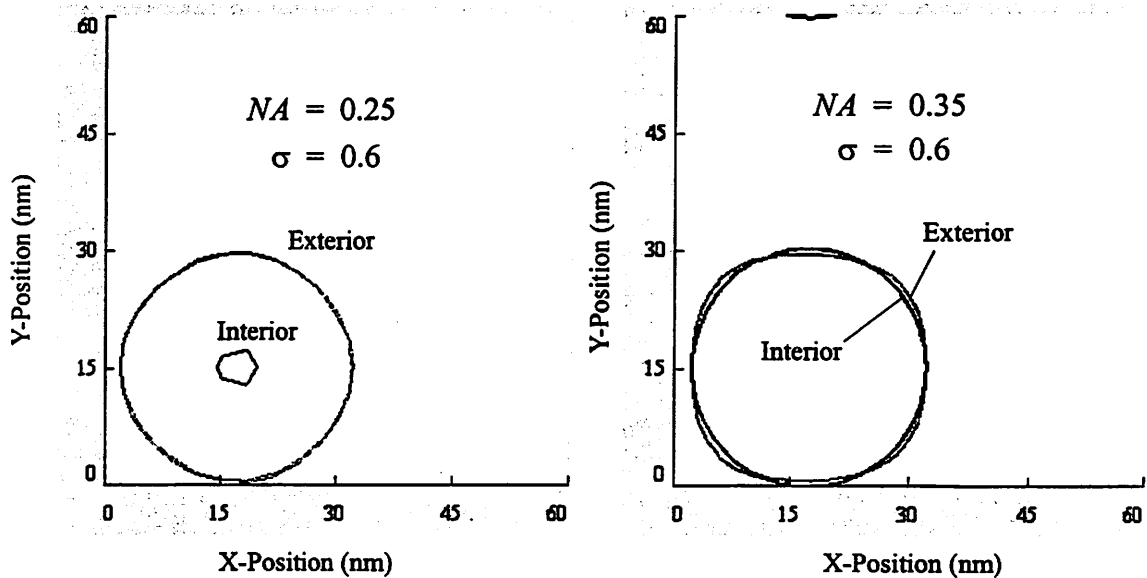


Figure 5-12. Aerial Images for Interior and Exterior 30nm Square Post Features

The “exterior” case has a 120nm by 120nm (mask dim.) chrome square absorber feature on the mirror. The “interior” case has a 120nm by 120nm clear square area in a chrome covered mirror. For the $NA=0.25$ case, the exposure level that produces a 30nm (wafer dim.) diameter feature for the exterior case produces only a 5nm (wafer dim.) diameter feature for the interior case. For $NA=0.35$, the exposure levels required to produce 30nm (wafer dim.) diameter features for both the interior and exterior cases are nearly equal.

5.2.2.4. Corner rounding on an Exterior Post

Figure 5-13 shows the effects of rounding the corners of an exterior absorber post. The three contours are for corner radii or 0nm, 20nm and 40nm. For a corner rounding of 40nm, only a 3.6% change in CD is observed. Corner rounding effects can be easily compensated for by mask bias.

5.2.2.5. Arbitrary Mask Pattern at two Angles of Incidence

The aerial image of a somewhat arbitrary mask pattern is presented in Figure 5-14. The pattern has 30nm features and is imaged with a camera having numerical aperture of 0.25. Plot (a) shows the aerial image when a 6.4° angle of incidence is used while plot (b) is for a 3.2° angle of incidence. To compare the two cases, equal intensity contours of the aerial images

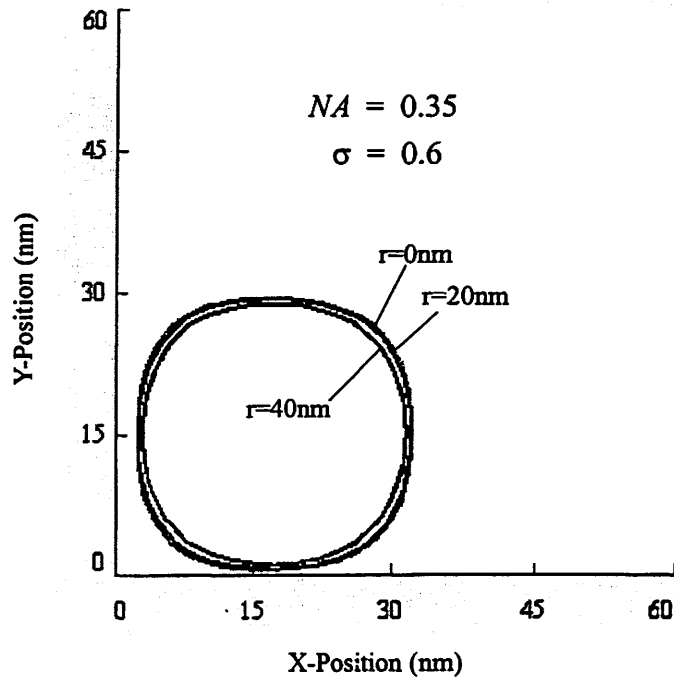


Figure 5-13. Aerial Images for Exterior 30nm Post with Various Corner Radii

The diameter of the feature for corner roundings of 0nm, 20nm and 40nm (mask dims.) are 29.43nm, 29.28nm, 28.35nm (wafer dims.) respectively.

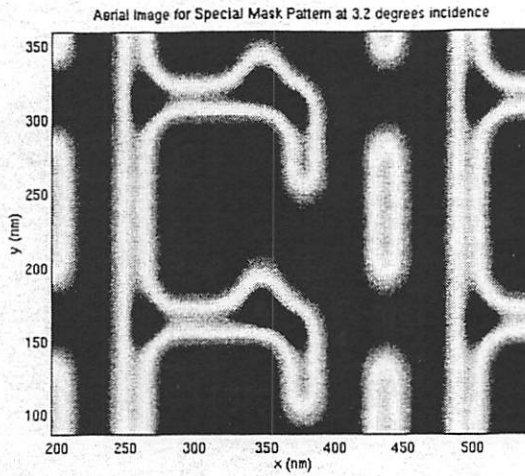
are superposed and compared in figure (c). The doses were adjusted so that the line widths at a particular place (indicated on figure (c)) match for the two cases. The contour lines show an improvement in proximity effects, line end shortening and overall CD uniformity as the angle of incidence decreases.

5.3. Defect Simulations

The previous section investigated the effects various topographical feature parameters such as corner rounding and side wall angle, but in all cases, the mirror was assumed to be the same defect-free mirror. The absence of multilayer mirror defects enabled the use of the Fourier Boundary Condition as an efficient way to model the mirror that avoids programming the entire mirror structure into the FDTD simulation grid.

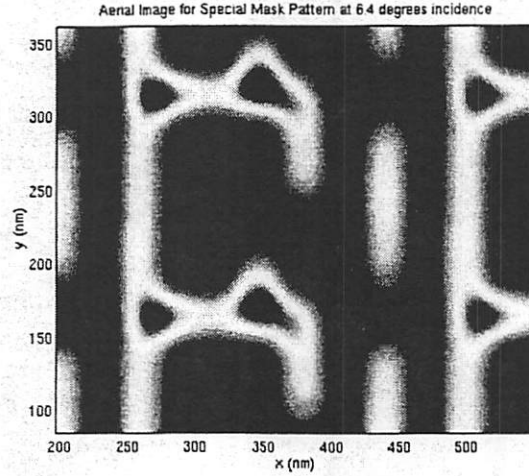
When the multilayer mirror has defects that break the uniform structure in the horizontal dimensions then the mirror is no longer a one-dimensional structure and can not be char-

Aerial Image at 3.2° Incidence



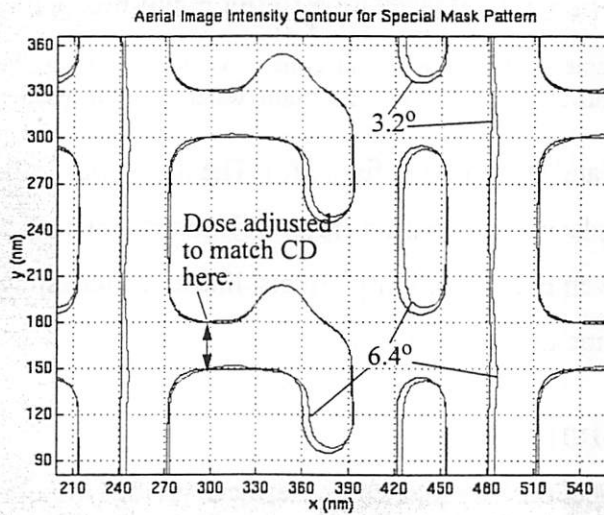
(b)

Aerial Image at 6.4° Incidence



(a)

Contour Curve Comparison



(c)

Figure 5-14. . 2D Pattern with 30nm Features at different angles of incidence

Figure (a): an arbitrary mask pattern's aerial image for 6.4° angle of incidence. Note the regions of high intensity at places where lines intersect. Figure (b) is the aerial image for the same pattern with 3.2° angle of incidence. The benefits of a smaller angles of incidence are illustrated by the contour comparison in figure (c). NA=0.25 for both cases.

acterized by its reflection coefficient vs. angle incidence and the Fourier Boundary Condition can not be used. Alternative models must be used to model the defective mirror.

The defects of primary concern are substrate defects that are present on the bare substrate before the multilayer mirror is deposited. These defects are troublesome not because they scatter EUV light, but because they distort the multilayer mirror structure deposited on top of them. This is illustrated in Figure 5-15 where defects are classified as either “point” defects or “line” defects. “Line” defect require only 2D TEMPEST simulation whereas “Point” defects require large 3D TEMPEST simulations.

To combat mirror defect issues, schemes for detecting the presence of substrate defects have been investigated[45]. Additionally, recent research[53] has shown that there exist mirror deposition parameters that can be varied to “smooth out” the defect profile as the subsequent mirror layers are deposited in an attempt to minimize mirror distortion at the top-most (and most important) mirror layers. But even with the substrate defect detection schemes and the defect smoothing, an understanding of how a distorted mirror affects the aerial image is needed because one needs to know how much to smooth out the defects and what the dimensions of the smallest “killer” defect are for the purposes of detection.

Nguyen et al.[59] were the first to investigate substrate defects and mirror distortion using TEMPEST. However, their work was limited to “line” type defects (see Figure 5-15 (c)) and for CD’s of 100nm. Bollepalli et al.[14], also investigated defect printability using rigorous simulation but was also limited to “line” type defects. In research connected to this thesis, Pistor and Neureuther [64] obtained 3D rigorous simulations of point defects using a parallelized TEMPEST (Chapter 3), considering only the top 10 bilayers of a multilayer mirror and assuming a constant Gaussian-shaped mirror profile for all bilayers. It was later realized that the discretization scheme used in [64] was insufficient for modeling very low profile defects. Pistor, Deng and Neureuther, in research connected to this thesis, developed a “graded material index” scheme[65] to reduce discretization error for low-profile defects (illustrated in Figure 5-16) and performed further simulations of point defects and point-defect-feature interactions, the major results of which are presented in the remainder of this section.

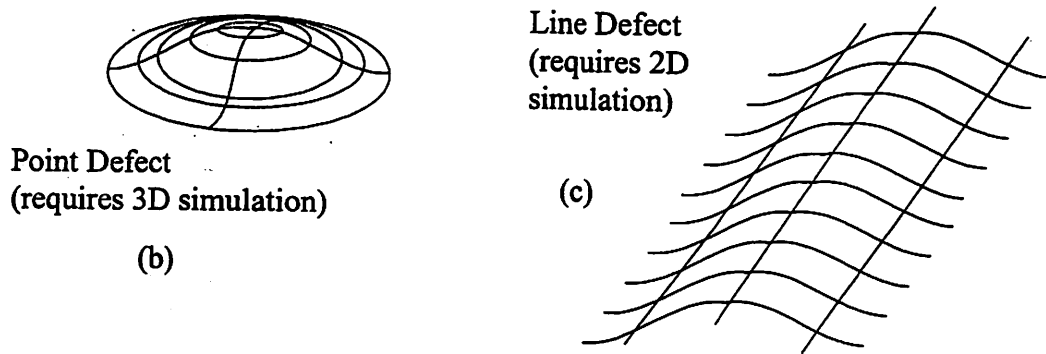
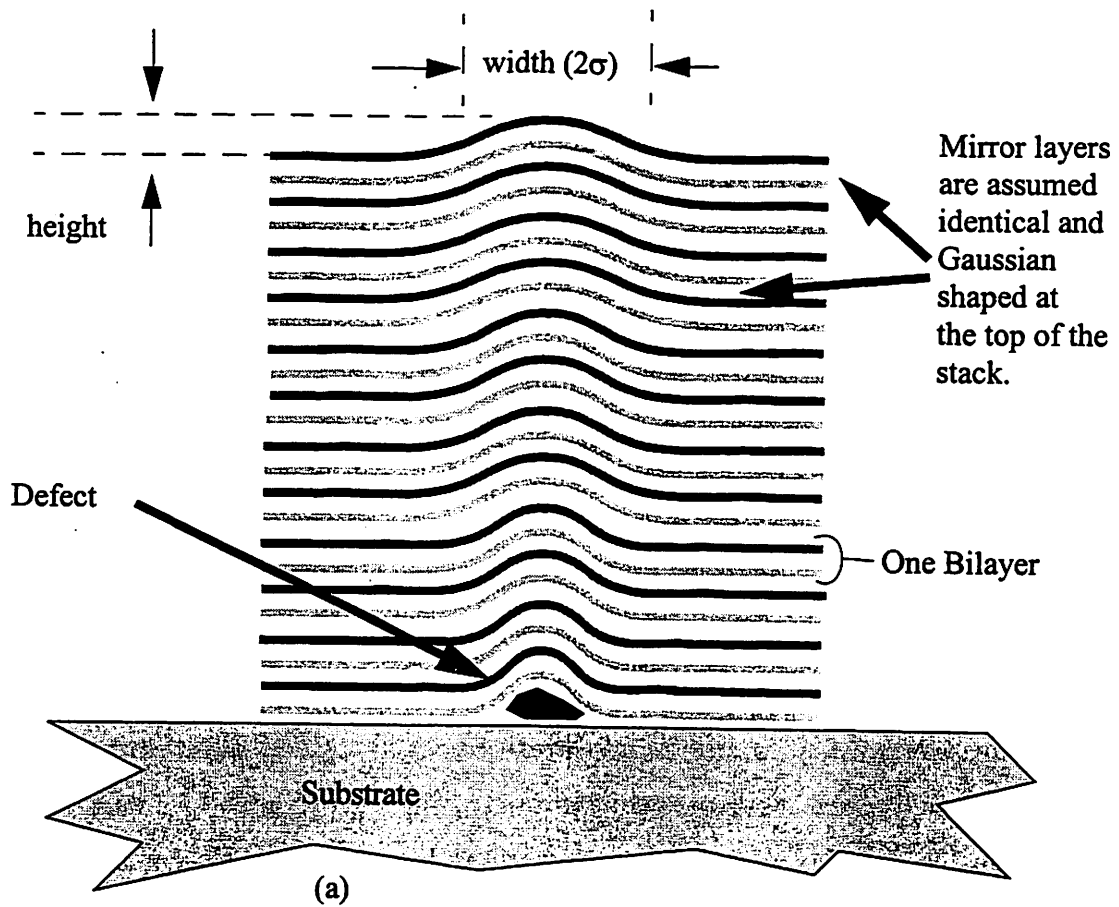


Figure 5-15. EUV multilayer defect topography

As the multilayer mirror layers are deposited, a particle on the substrate can cause distortion in the growth. For the purposes of simulation, defects are classified as either "Line defects" or "Point Defects". Although line defects are generally not seen in practice, they are useful because from a simulation point-of-view they require very little memory to simulate and much can be learned about how mirror distortions scatter.

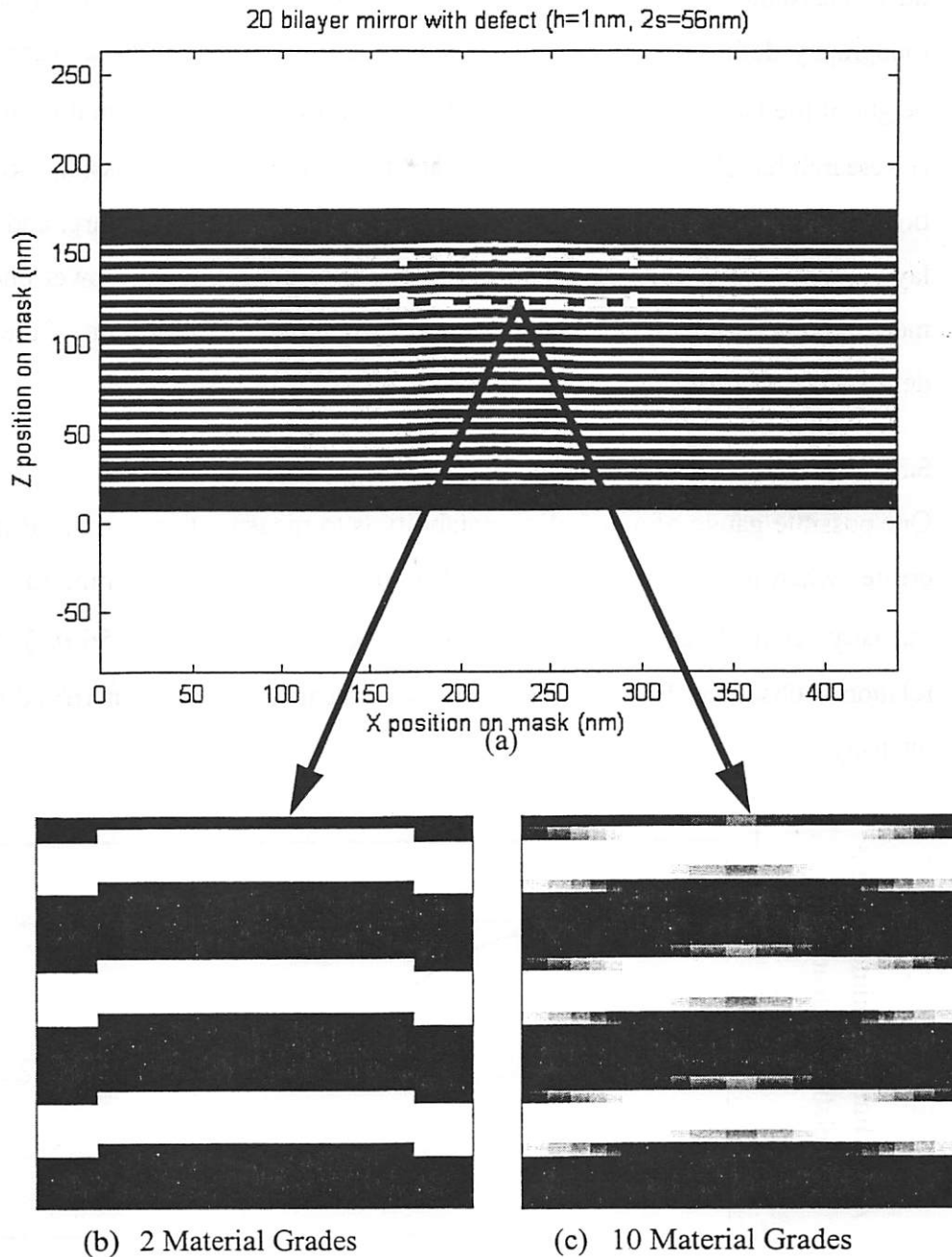


Figure 5-16. Averaging Material Properties to reduce Discretization Error

The Average Material Properties technique is used to reduce gridding error which is important for low-profile defects. In (a) a cross section of the topography is shown for twenty bilayers. The defect has a height of 1nm and is barely visible. When only two materials (Si and Mo) are used to discretize the defect, significant discretization error is introduced as shown in (b). Using a graded set of ten materials with optical properties ranging from Mo to Si helps to reduce the discretization error by “smoothing out” the step discontinuity and is illustrated in (c).

All simulations assumed that the substrate defect at the bottom of the multilayer mirror produce Gaussian-shaped mirror distortions in the top layers of the mirror. This simplifies the topography definition and provides a convenient way to describe a defect's size (by the height of the Gaussian and the 2σ width). This is a good approximation for two reasons: i) Research has shown that small substrate defect do produce Gaussian-like mirror distortions that are nearly the same in the top layers of the mirror structure, and ii) it is the top layers of the mirror substrate that provide most of the reflecting power and are therefore most important. The details of the mirror profile down a the bottom of the stack near the defect are not important.

5.3.1. Constant Width, Varying Height

One possible gauge of a defect's printability is to measure the amount of intensity loss it creates when printing in the clear field. Figure 5-17 plots the minimum of aerial image intensity versus defect height for a particular defect width ($2\sigma = 56nm$). A nearly linear relation is observed. Defects as shallow as 1nm cause a more than 16% dip in clear field intensity.

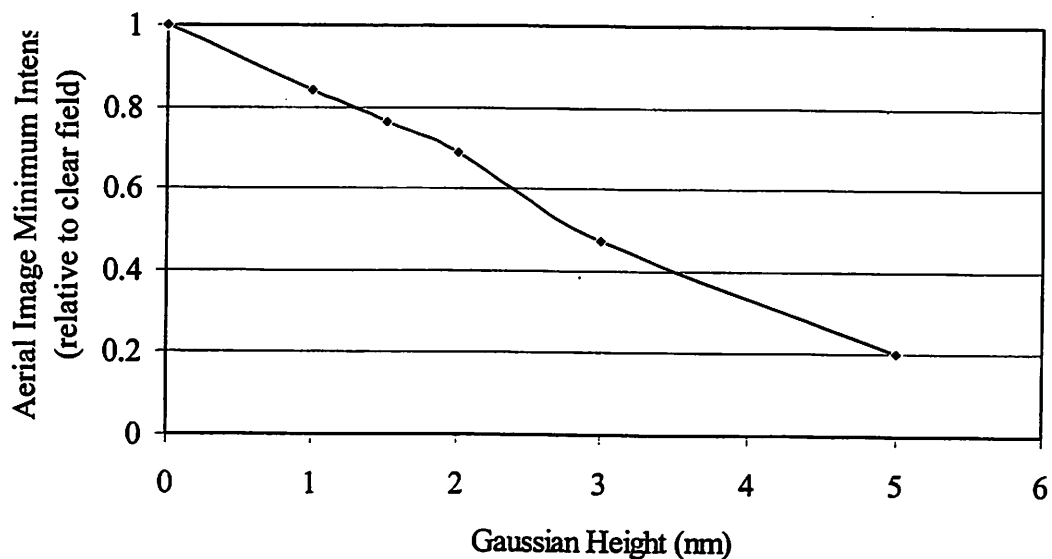


Figure 5-17. Aerial Image Minimum vs. Defect Height (for 56nm wide Gaussian point defect)

5.3.2. Constant Heights, Varying Widths

The minimum of the aerial image for several defects is graphed in Figure 5-18. The first and most obvious observation is that taller defects are stronger (i.e. they create larger dips in the clear field intensity) than shorter defects. The second observation concerns the effect of changing the defect width, while keeping the height constant. At first, the defect becomes stronger as the width increases. A worst case width exists at which the defect is most printable. Beyond this worst-case width the defect becomes weaker. One possible reason for this is that as the defect becomes wider, and flatter, its slope becomes closer to that of a perfect mirror and it begins to behave somewhat like a perfect mirror. In the limit as the defect becomes extremely wide, it will truly approximate a perfect mirror and the dip in aerial image intensity will approach zero.

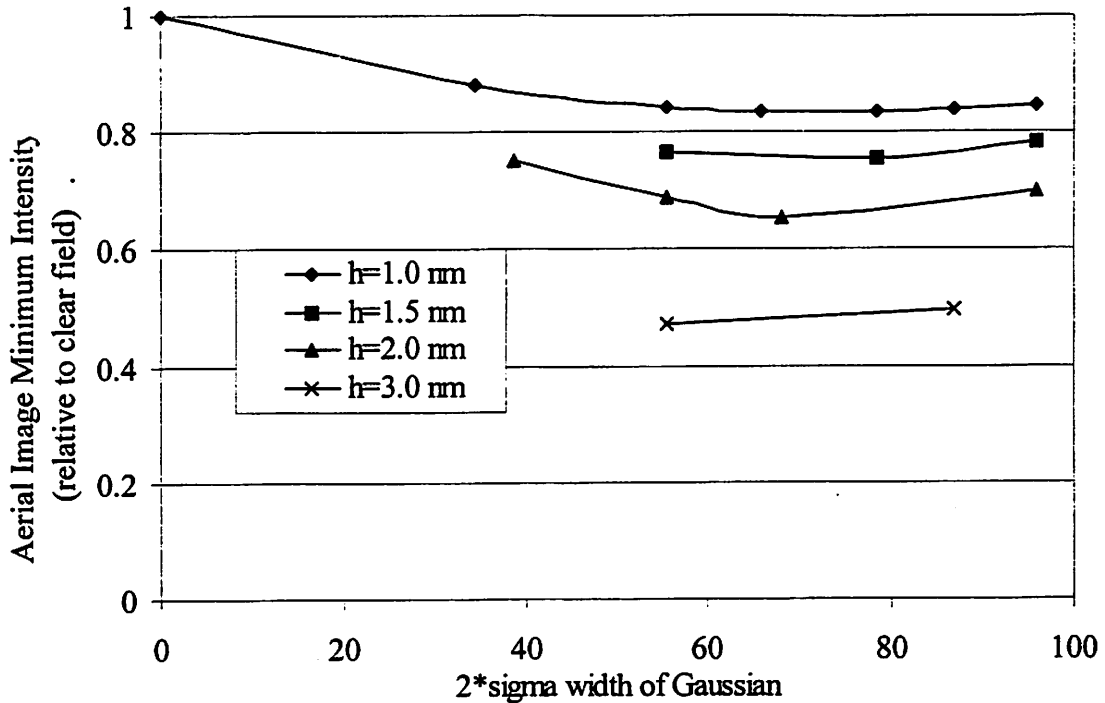


Figure 5-18. Clear field Intensity Minimum vs. Defect Width (2σ) for Various Defect Heights

Taller defects print more strongly than shorter ones. There appears to be a worst-case width at which the defects for a particular height print most strongly.

5.3.3. Point Defect Interaction with Line Feature

A better test of a defect's printability is to see how it interacts with mask features rather than just observing its effect on the clear field intensity. Figure 5-19 illustrates a simulation study in which a point defect's interaction with a line feature is investigated. In an attempt to better understand proximity effects, aerial images were calculated for various positions of the defect relative to the line feature. The defect had dimensions $h=1\text{nm}$ and $2\sigma = 56\text{nm}$. When the defect's center is at the line edge, a CD change of 8.5% is observed. As the defect moves away from the line, the percentage change in CD first increases as more of the defect moves out from under the line and gets exposed. Once the defect is about 22nm away from the line, a maximum change in CD is observed (about 12%). As the defect is moved further from the line, the change in CD begins to decrease because the defect becomes more and more isolated. Eventually, as the defect moves far enough away from the line, no change in line width would be expected.

5.4. Summary and Discussion

The development of Extreme Ultraviolet Lithography (EUVL) is critically dependent on simulation primarily because the hardware is not yet fully developed. Simulating EUVL masks is difficult because of their large size. The Fourier Boundary Condition (Chapter 2) has been used to save memory when modeling defect-free multilayer mirrors and a parallelized version of TEMPEST (Chapter 3) has been used to enable the multi-gigabyte 3D simulation domains required for rigorous 3D simulation of multilayer mirror defects.

A degradation in object-side depth of focus due to the off-axis imaging was observed. Minute changes in absorber thickness and side wall angle were seen to significantly affect CD. 3D TEMPEST simulations showed differences between "exterior" and "interior" square features and CD dependence on corner rounding.

Gaussian-shaped mirror profiles caused by deposition on top of substrate defects were seen to cause intensity reduction in the clear field. For a given defect height, a worse-case defect width was observed. A 1nm high, 56nm wide gaussian defect was seen to cause a line's width to change as much as 12% depending on where the defect was positioned in relation to the line.

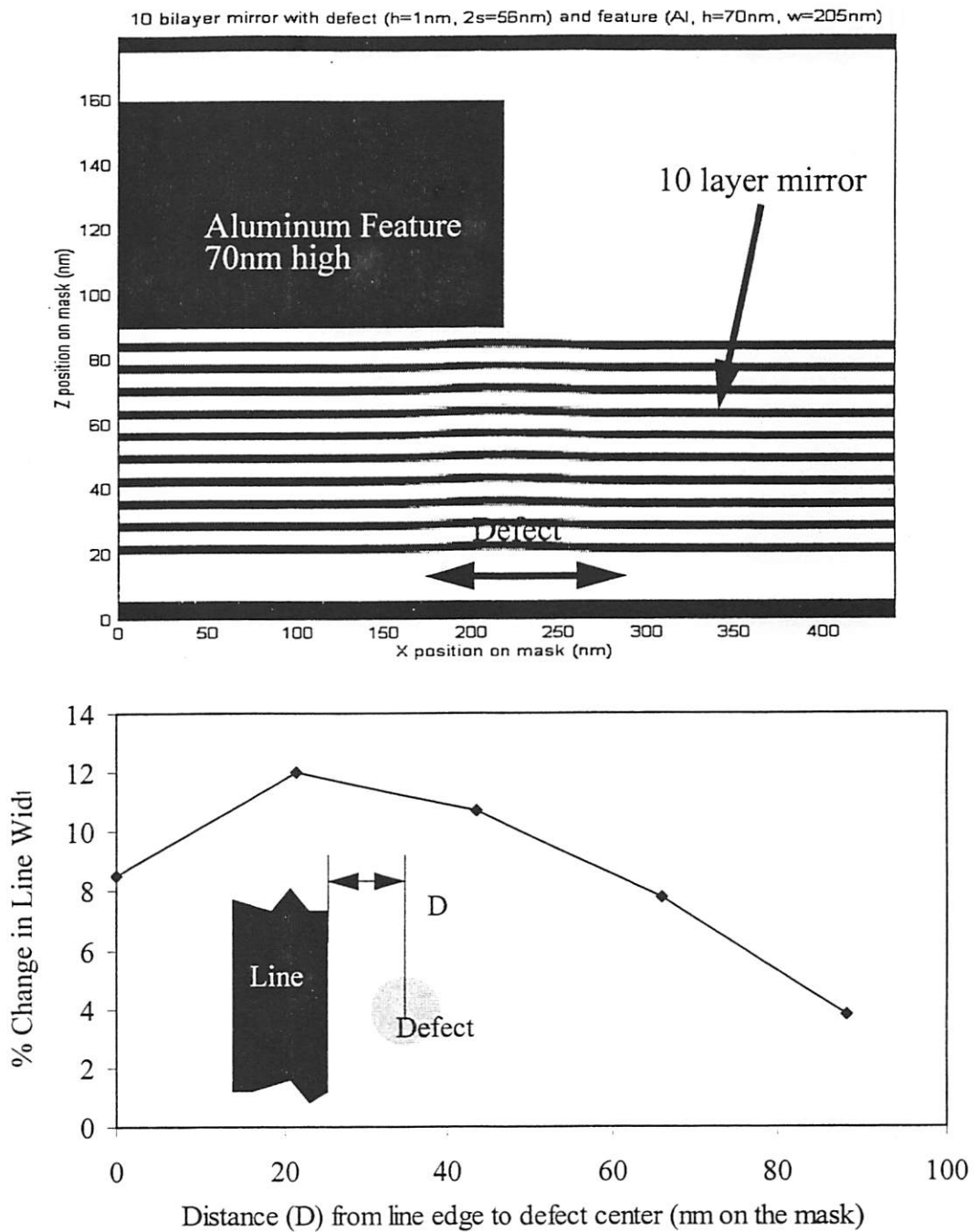


Figure 5-19. Line Width Change vs. Defect Proximity for 1nm x 56nm Defect

(a) The defect/feature topography has only a ten bilayer mirror and an aluminum absorber feature. The defect is quite shallow and difficult to see. The defect has $h=1$ and $2\sigma = 56\text{nm}$. (b) As the distance between the center of the defect and the line edge increases, the change in the CD increases to a maximum value near 12% and then decreases as the defect moves further and further from the line. This particular defect ($h=1\text{nm}$, $2\sigma=56\text{nm}$) is only a killer defect when it is in close proximity to a line edge.

Simulation has been shown to be a valuable tool for finding and understanding trends in EUVL.

6 Phase Shift Mask Inspection

6.1. Introduction

Rigorous Electromagnetic Simulation (REMS) has become a well established tool for modeling the photomask in reduction printing situations. It is, relatively speaking, much less expensive to calculate an aerial image than to actually generate and observe a real one. REMS has been used to predict defect printability[46], phase-shifter error effects[3], OPC effects[2], corner rounding effects[63], phase-shifter profile effects [85] and much more. REMS will continue to be a useful tool for aerial image calculation for the next several years.

The use of REMS of photomasks under inspection situations (as opposed to printing situations), however, is not so well established because it is complicated by a broader angular spectrum of plane waves incident onto the photomask. This broader angular spectrum of incident light leads to the requirement of more REMS in order to determine how the different plane waves scatter.[68]

Section 6.2 discusses and proposes a model for optical scanning microscopy - a commonly used technique in mask inspection tools. Section 6.3 presents a simulation study of a phase defect in an alternating phase-shift mask. Certain plane waves in the illumination pupil are shown to “see” the defect better than others. Annular illumination is shown to be better than circular illumination for defect detection.

6.2. Inspection System Overview and Theory

Optical mask inspection systems are essentially microscopes that magnify an observed area of a photomask and form an image on a CCD camera. The image is analyzed to determine if there are any defects in the observed region of the mask.

Inspection systems have been built based on both conventional microscopy and scanning optical microscopy. Conventional microscopy is very similar to the optics of a printing tool in that Köhler illumination is used to illuminate the mask and a projection optic forms an image of the mask at an image plane. Scanning microscopy involves the scanning of a focused beam across a region of the mask while collecting the scattered light. A simplified model for a scanning optical microscope is presented in Figure 6-1.

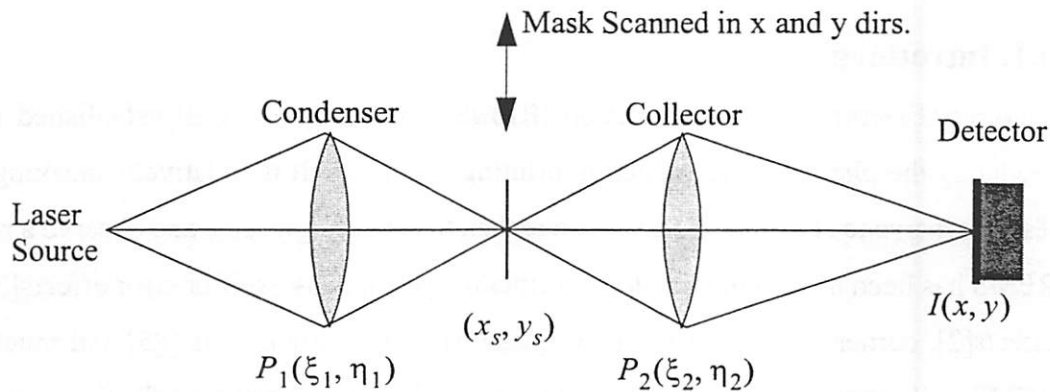


Figure 6-1. Simple Model for a Scanning Inspection System

A condenser optic focuses the laser to an Airy beam at the mask. The mask is scanned in the x and y directions. The scattered light is collected by the collector optic and detected. The output signal $I(x_s, y_s)$ from the detector is a function of the mask scan position. This scheme can be proved equivalent to conventional microscope imaging under the Hopkins approximation.

As explained in [86], the (non-confocal) scanning optical microscope is equivalent to a conventional optical microscope if the roles of the objective and condenser optics are reversed. In other words, the lens that focuses the laser light to a spot incident onto the mask plays the role of the projection optic in a conventional imaging system as described in Chapter 4, while the optic that collects the scattered light from the mask plays the role of the illumination optic, setting the degree of coherence in the system. This can be considered a duality. In the conventional microscope, the relative phases of the plane waves incident upon the mask are unimportant, while the relative phases of the scattered field (for a particular incident plane wave) are important. In the scanning optical microscope, the relative phases of the scattered plane waves are ignored by the detector but a specific phase relationship between the incident plane waves must exist in order to form the spot.

The proof of the above equivalence assumes a scalar theory, the paraxial approximation, and constant scattering coefficients (Hopkins' analysis [41][42]). It is a difficult task to prove the equivalence (or inequivalence) of conventional and scanning microscopy when a vector, non-paraxial, non-constant scattering coefficient model is assumed. Such a proof would be useful because it would allow the model developed in Chapter 4 to be applied to scanning optical microscopy. However, the proof is beyond the scope of this thesis. In place of such a proof, an efficient mathematical model for an optical scanning microscope is proposed in the next section.

6.2.1. A Proposed Model for Scanning Beam Optical Microscopy

At first glance, the simulation of the scanning beam appears to be a daunting task. One might attempt to run a TEMPEST simulation for each possible beam position as it scans over a small region of the mask. But, upon further consideration, one realizes that it is not necessary to run a TEMPEST simulation for each possible beam position. This is true for the same reason that it is not necessary to run a TEMPEST simulation for each plane wave in the illumination pupil when imaging: *scattering coefficients typically vary slowly over angle of incidence.*

The field incident onto the mask for a scan position of (x_s, y_s) is a coherent superposition of plane waves and is written:

Equation 6-1.
$$\tilde{F}_{inc}(x_s, y_s) = \sum_i \tilde{w}_i(x_s, y_s)$$

The magnitudes and phases of w_i are chosen in such a way that $\tilde{F}_{inc}(x_s, y_s)$ is a focused beam centered at (x_s, y_s) (i.e. for an Airy beam, a *circ* function is used). The scattered field from the mask, whether reflected or transmitted, (from Chapter 4) is written:

Equation 6-2.
$$\tilde{F}_{scat}(x_s, y_s) = \sum_i \sum_{m, n} \left[\begin{array}{c} SC_{TE, mn}(\tilde{w}_i(x_s, y_s)) \\ SC_{TM, mn}(\tilde{w}_i(x_s, y_s)) \end{array} \right]_{\tilde{k}_{scat, mn, i}}$$

where the coherent summation over the source points is contrasted to the incoherent summation of over the source integration points in the conventional imaging model of Chapter

4. The scattered field is then imaged by the collection optic (similar to the projection optic in Chapter 4):

$$\begin{aligned} \vec{F}_{img}(x_s, y_s) &= h \left(\sum_i \sum_{m, n} \begin{bmatrix} SC_{TE, mn}(\vec{w}_i(x_s, y_s)) \\ SC_{TM, mn}(\vec{w}_i(x_s, y_s)) \end{bmatrix} \right)_{\vec{k}_{scat, mn, i}} \\ &= \sum_i \sum_{m, n} h \left(\begin{bmatrix} SC_{TE, mn}(\vec{w}_i(x_s, y_s)) \\ SC_{TM, mn}(\vec{w}_i(x_s, y_s)) \end{bmatrix} \right)_{\vec{k}_{scat, mn, i}} \end{aligned}$$

Equation 6-3.

where $\vec{F}_{img}(x_s, y_s)$ is the superposition of plane waves at the detector that occurs when the scan position is (x_s, y_s) . The actual electric field at the image (light sensor or CCD detector) is:

$$\begin{aligned} \vec{E}_{img}(x, y; x_s, y_s) \\ = Re \left\{ \sum_i \sum_{m, n} e^{j(-k_{img, mn, i, x}x - k_{img, mn, i, y}y)} M_{\vec{k}_{img, mn, i}} h \left(\begin{bmatrix} SC_{TE, mn}(\vec{w}_i(x_s, y_s)) \\ SC_{TM, mn}(\vec{w}_i(x_s, y_s)) \end{bmatrix} \right)_{\vec{k}_{scat, mn, i}} \right\} \end{aligned}$$

Equation 6-4.

Finally, the signal coming out of the light sensor or CCD detector is the total energy deposited across its imaging surface and is:

$$I_{img}(x_s, y_s) = \int_{-\infty}^{\infty} \int_{-\infty}^{\infty} \frac{1}{2} |\vec{E}_{img}(x, y; x_s, y_s)|^2 dx dy$$

The same technique for estimating scattering coefficients outlined in Chapter 4 can be used for this optical scanning microscopy model. (i.e. calculate scattering coefficients for a few plane waves and then use these known scattering coefficients to approximate the scattering coefficients for other plane waves). Even if the equivalence described above could be proved, it is not necessary since the use of the conventional microscopy imaging equations in Chapter 4 are not more efficient than the equations presented here. The number of TEM-PEST simulations necessary (in both cases) is only a function of how the scattering coefficients vary across the illumination pupil.

6.3. A Simulation Study of Defect Printability and Inspection

Recent research by Tejnil et al.[81] investigates the printability, inspectability and repairability of phase defects in a dual-trench alternating phase shift mask. This chapter presents a simulation study of a similar topography.

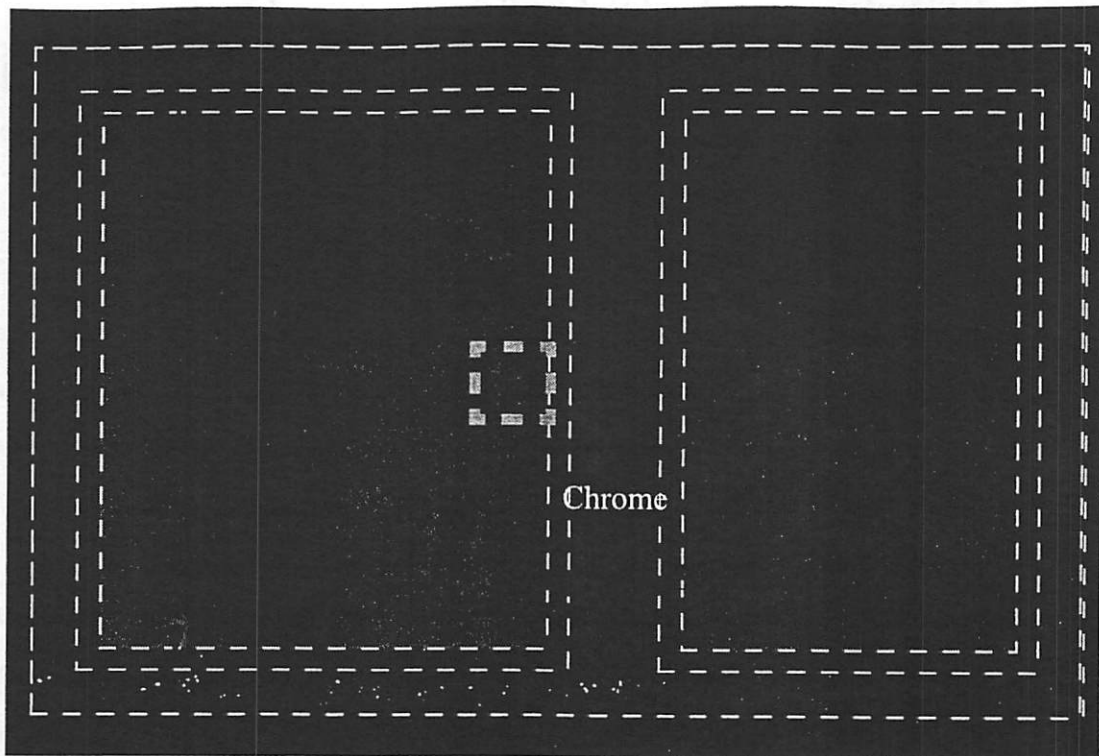
6.3.1. Topography

The mask topography consists of two rectangular openings in the chrome. The quartz behind one of the openings is etched back to a depth that yields a 180 degree relative phase shift (at 248nm) between the fields exiting each of the openings. A quartz bump defect is added adjacent to one of the vertical side walls of the phase-shifted opening. Figure 6-2(a) shows a cross section through the chrome and the relative location of the quartz defect. Figure 6-2(b) shows a cross section through the phase well. As in [81], simulations are performed both before and after an 80nm wet etch to determine the effect of wet-etch on defect printability. The wet-etched topography is shown in Figure 6-2(c). Note that the defect is etched isotropically just as the quartz side walls and thus the defect retains its full dimensions in the x and z directions and remains butted up against the side wall, but decreases its size in the y-direction by twice the wet-etch distance (160nm) as both faces normal to the y-axis are etched.

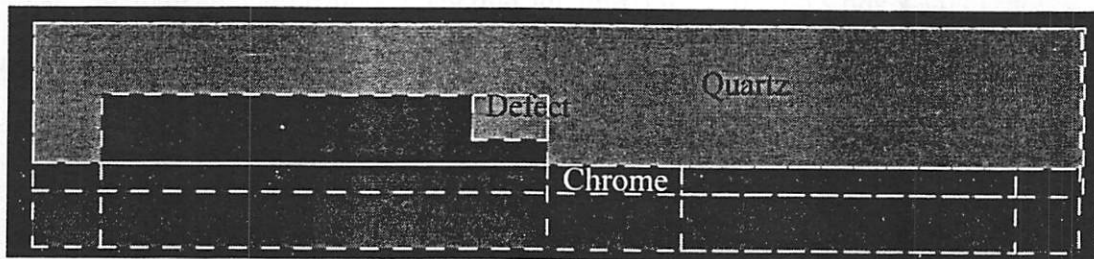
6.3.2. Printability

Before simulation of defect inspection is undertaken, the printability of the defect is established through simulation. The parameters for the printability simulations are taken from [81] and given in Table 6-1. The z dimension of the defect is 117 degrees at the printing wavelength of 248nm. The x and y dimensions are equal (before wet etch) and take the following values: 0nm (i.e. no defect), 115nm, 270nm and 405nm. After the 80nm wet etch, the y dimension is reduced by $2 \times 80\text{nm} = 160\text{nm}$.

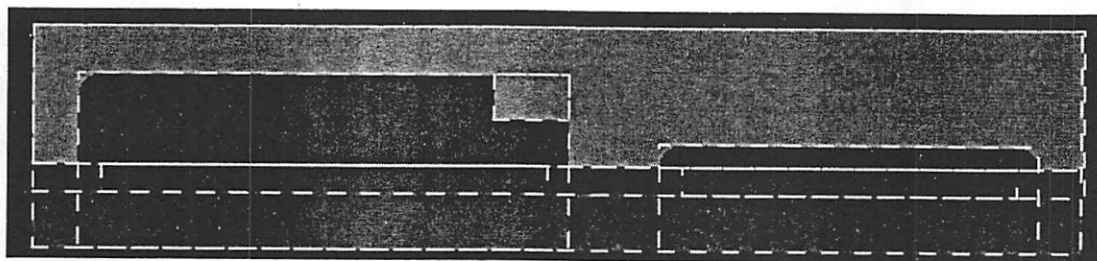
The near field intensity (output from TEMPEST taken just after the chrome) is plotted in Figure 6-3. Although the near field can not be directly measured by the inspection system, it is an intermediate value that is available in simulation. It is interesting to note that the defect is quite visible in the near field.



(a)



(b)



(c)

Figure 6-2. Alternating Phase Shift Mask with Defect Topography

(a) A cross section through the chrome shows two openings, a shifted opening and an unshifted opening. A “bump” defect is situated at the sidewall edge, its location in the xy-plane indicated by the dotted outline. (b) A zx-plane cross-section through the defect before wet etch. Note the vertical side walls on the phase shifter. (c) The same cross-section as (b), but after 80nm wet etch. Note the quartz undercut and corner rounding.

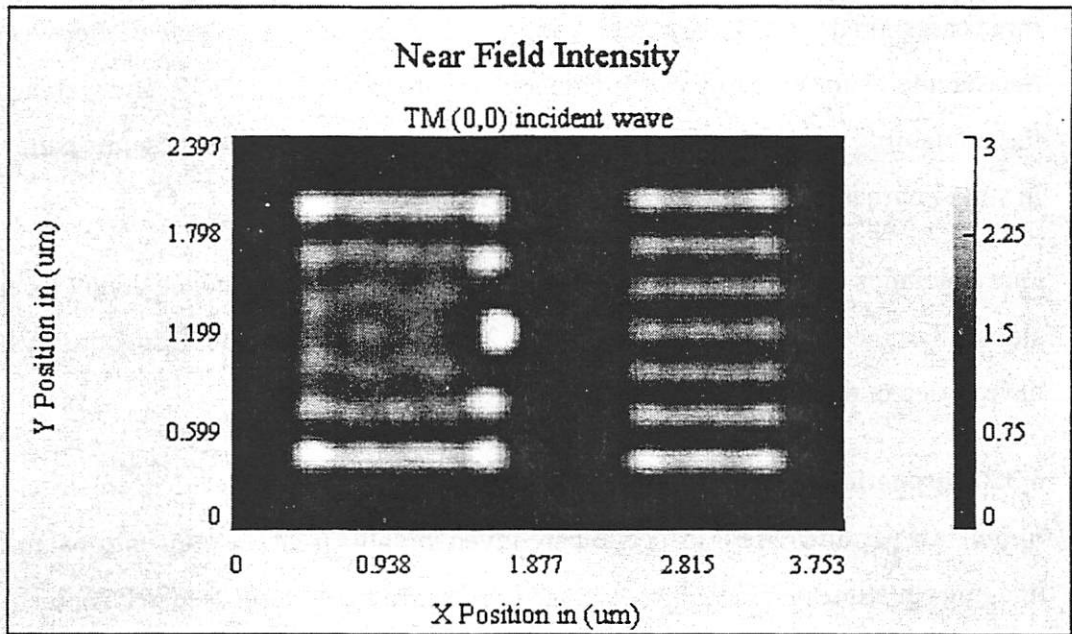
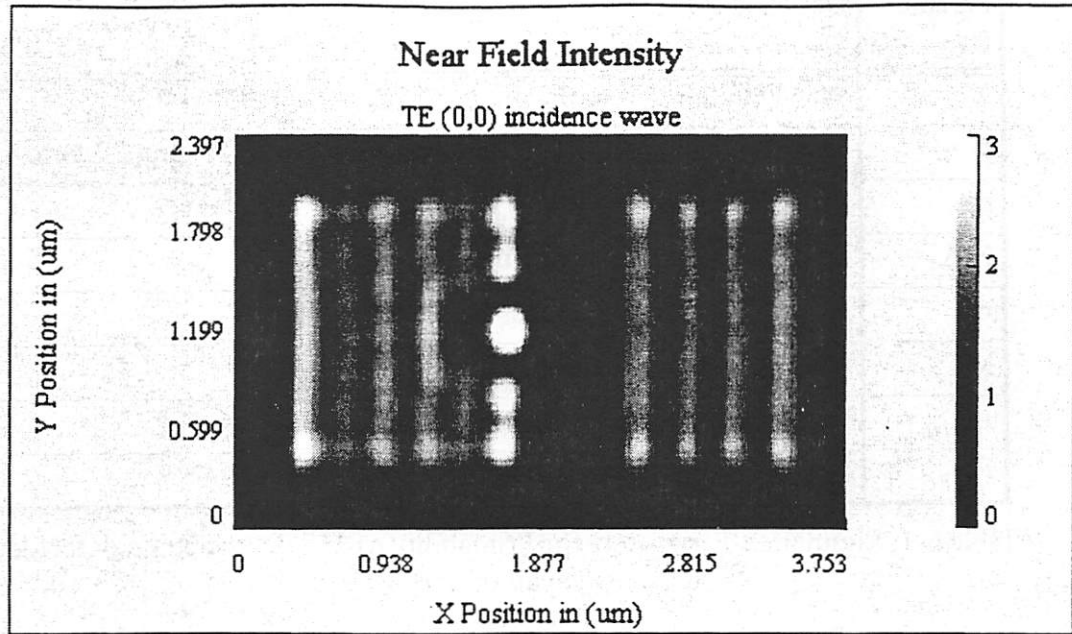


Figure 6-3. Near Field Intensity

The near field is observed just after scattering from the mask. The incident field is a normally incident plane wave. The defect is clearly visible for both y and x polarized light.

Parameter	Description	Value(s)
λ	Wavelength used for printing	248nm
s	Length of side of defect before wet etch	0nm, 115nm, 270nm, 405nm
p	Phase of defect at printing wavelength	117 degrees
N.A.	Numerical Aperture of printing tool	0.68
σ	Partial Coherence Factor	0.40
M	Optical Demagnification	4X
t_{resist}	Resist thickness (n=1.76, k=0.0166)	0.4um
t_{BARC}	B.A.R.C. thickness (n=1.45, k=0.3)	0.066um

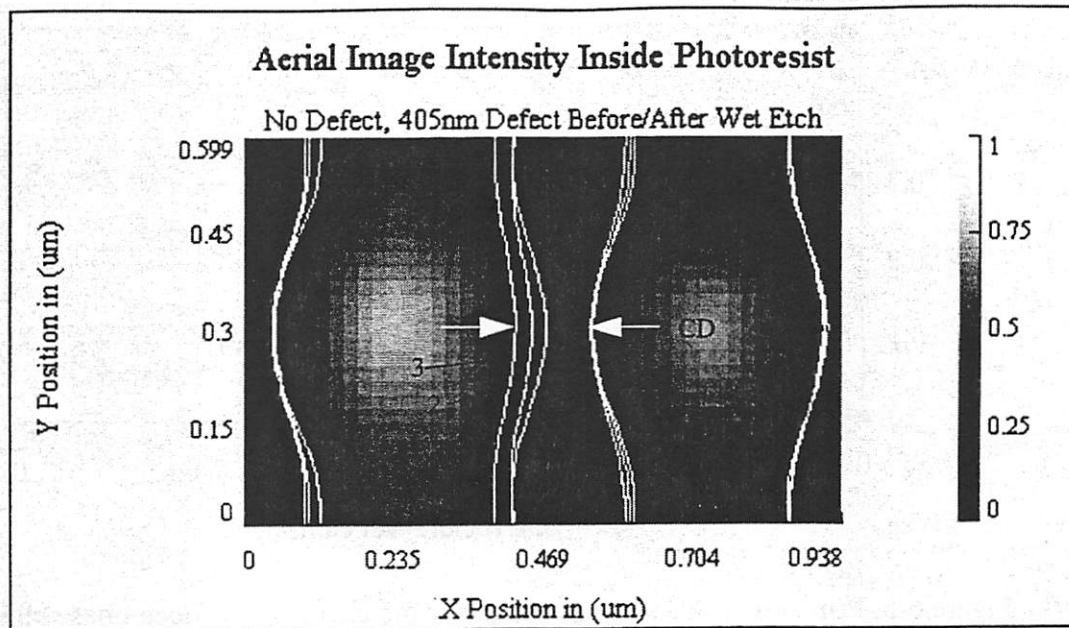
Table 6-1. Simulation Parameters for Printability of 117 degree bump defect located at sidewall of deep-shifter

The final assessment of the printability is based on measurements of intensity of the aerial image inside the thin layer of photoresist at the wafer. This field is shown in Figure 6-4 for three cases: no defect, 405nm defect before wet etch and 405nm defect after wet etch. CD measurements for all cases were made and are plotted in Figure 6-5. The wet etch reduces the printability of the defect because it reduces the defects size. These measurements are in strong agreement with data presented in [81].

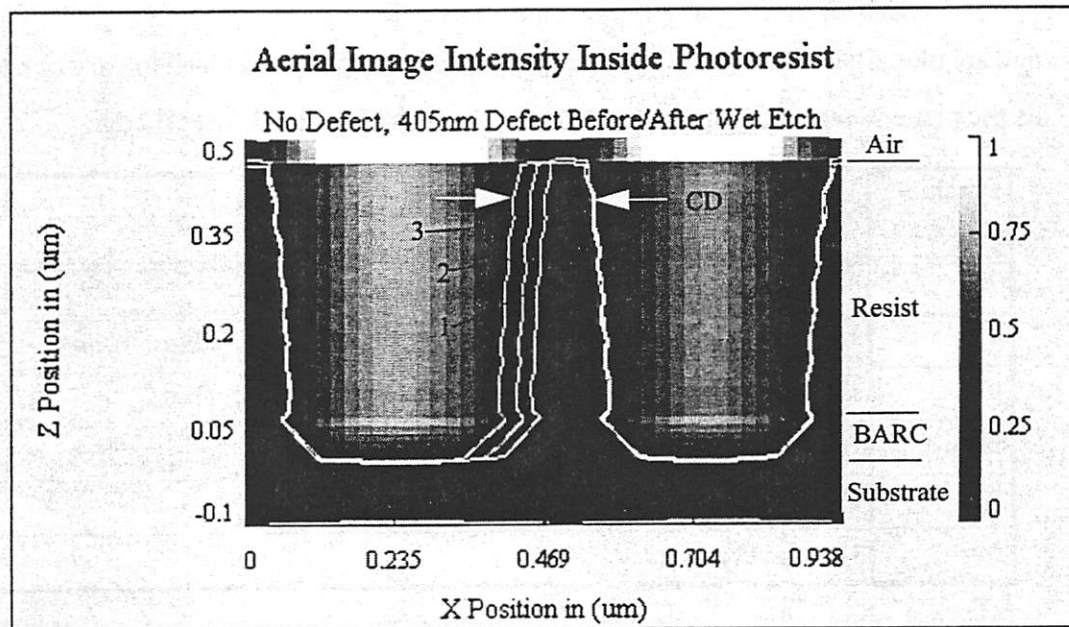
One concludes that the critical defect size for a 117 degree wet etched defect located at the side wall of the deep phase shifter is in the 200nm to 300nm range. Inspection systems will have to detect defect of this size.

6.3.3. Inspection

Simulation parameters for inspection are given in Table 6-2. The conventional microscopy imaging equations of Chapter 4 were used for the study. As discussed in Chapter 4, because inspection systems illuminate the mask with a wide angular spectrum of plane waves, the scattering coefficient dependence on angle of incidence must be accounted for. It is interesting to observe how much the scattering coefficients vary as the plane wave angle of incidence varies from normal to the pupil edge. Before proceeding with aerial image calculations, the scattering coefficients were measured as a function of angle of incidence



(a)



(b)

Figure 6-4. Aerial Image Inside Photoresist

(a) An xy-plane cross-section inside the resist, near the top surface of the resist. The bright areas correspond to the opening in the chrome. (b) A zx-plane cross-section through the film stack. (#1: No Defect, #2: 405nm, 117 deg. after wet-etch, #3: 405nm, 117 deg. before wet-etch.)

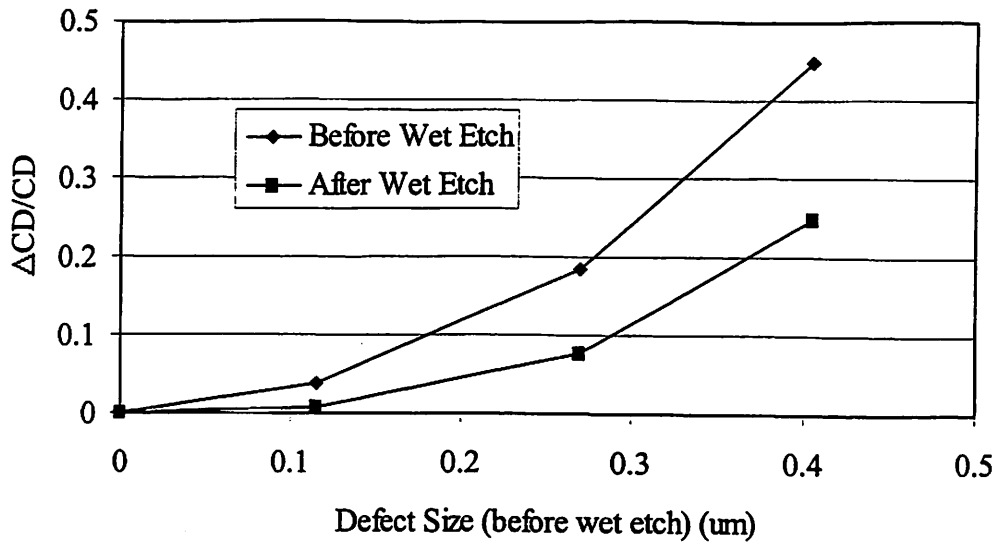


Figure 6-5. Printability of 117 degree phase bump defect in the deep phase-shifter vs. defect size before and after 80nm wet-etch

The wet etch reduces the size of the defect and moves it into the underetched region behind the chrome making the defect less printable.

and are plotted in Figure 6-6. The scattering coefficients are observed to vary by about 20% as the plane wave angle of incidence varies from normal, to the pupil edge.

Parameter	Description	Value(s)
λ	Wavelength used for inspection	365nm
s	Length of side of defect before wet etch	0nm, 270nm, 405nm
p	Phase of defect at printing wavelength	117 degrees
N.A.	Numerical Aperture of printing tool	0.65
σ	Partial Coherence Factor	1.0
M	Optical Demagnification	1X

Table 6-2. Simulation Parameters for Inspection of 117 degree bump defect located at sidewall of deep-shifter

To capture the scattering coefficient dependence on angle of incidence, TEMPEST simulations were run for the ten plane waves illustrated in Figure 6-7. A map of the interpolated (+1,+0)th scattered order magnitude is graphed in Figure 6-8. Each of the ten simulations

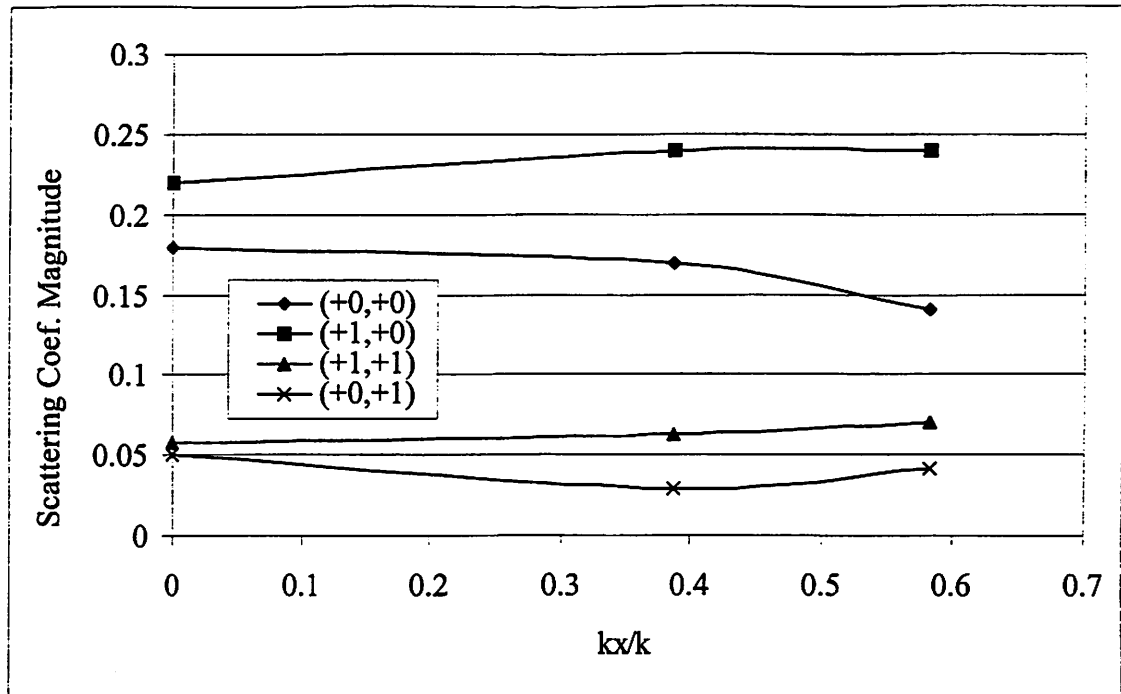


Figure 6-6. Scattered Order Dependence on Angle of Incidence

Four of the scattered orders are plotted for different angles of incidence along the $+k_x$ axis. Because the scattering coefficients are dependent on angle of incidence, multiple TEMPEST simulation must be used.

required approximately 100 MBytes and ran in less than two hours on a 600MHz Pentium III based laptop computer.

The first set of aerial images calculated were for a transmission mode inspection of a defect free mask and for a 405nm defect before wet etch. Both circular and annular illumination were used to discover the importance of the illumination pupil. The aerial images along with the difference signals (defined as the absolute value of the difference in intensity between an aerial image for a defect free mask and the aerial image for a mask with a defect) are plotted in Figure 6-9.

Defect visibility is quite poor with both types of illumination, however, the annular illumination yields a difference signal peak of 0.18 while the circular illumination difference signal peak is only 0.14. This suggests that annular illumination may be more effective in finding these sorts of defects. This can be explained by the fact that small features scatter light into wide angles. Annular illumination in conventional microscopy corresponds to an

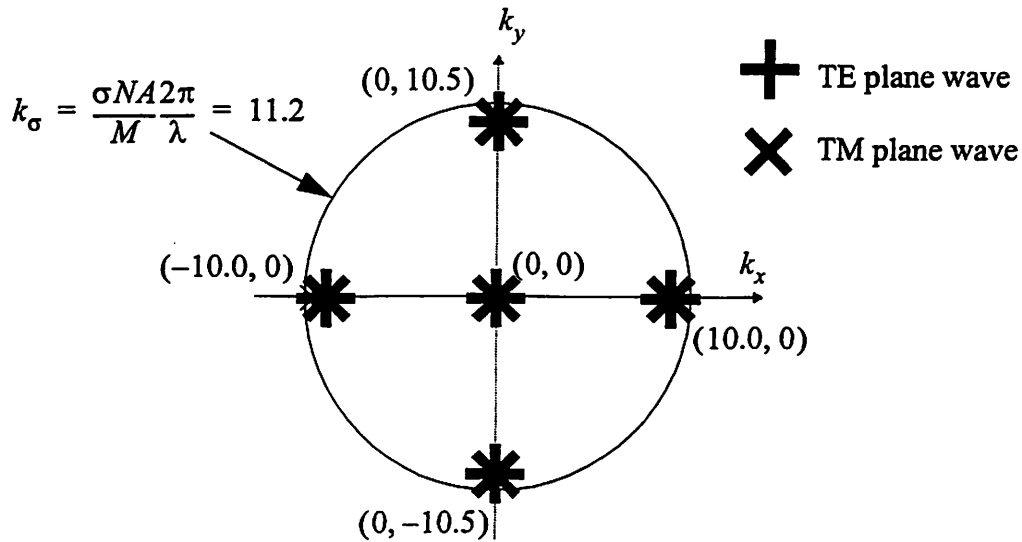


Figure 6-7. Locations in k-space of the 10 Plane Waves for Which Scattering Coefficients are Calculated With TEMPEST

Plane waves at normal incidence and near the edge of the illumination pupil are simulated with TEMPEST. For these plane waves, the scattering coefficients are known. For other plane waves inside the illumination pupil, the scattering coefficients are approximated (interpolated).

annular collection pupil in scanning beam microscopy and thus, the signal energy is due to the highly scattered orders. The energy scattered by the defect into the high orders is less “washed out” by the energy scattered into the high orders by the mask features.

To further investigate the effects of the illumination pupil (which physically corresponds to the collection angle of the collector in a scanning beam inspection system) aerial images for single plane wave illumination at various angles were calculated and are shown in Figure 6-10. It is evident that some angles of incidence are much better at seeing the defect than others. This type of information can be used to help inspection system designers improve phase defect visibility.

Finally, Figure 6-11 graphs the difference signal (defect visibility) vs. defect size (as measured before wet etch) for the cases of before and after wet etch using circular and annular illumination. In both cases, annular illumination leads to higher defect visibility as compared to circular illumination - particularly for smaller, less printable defects.

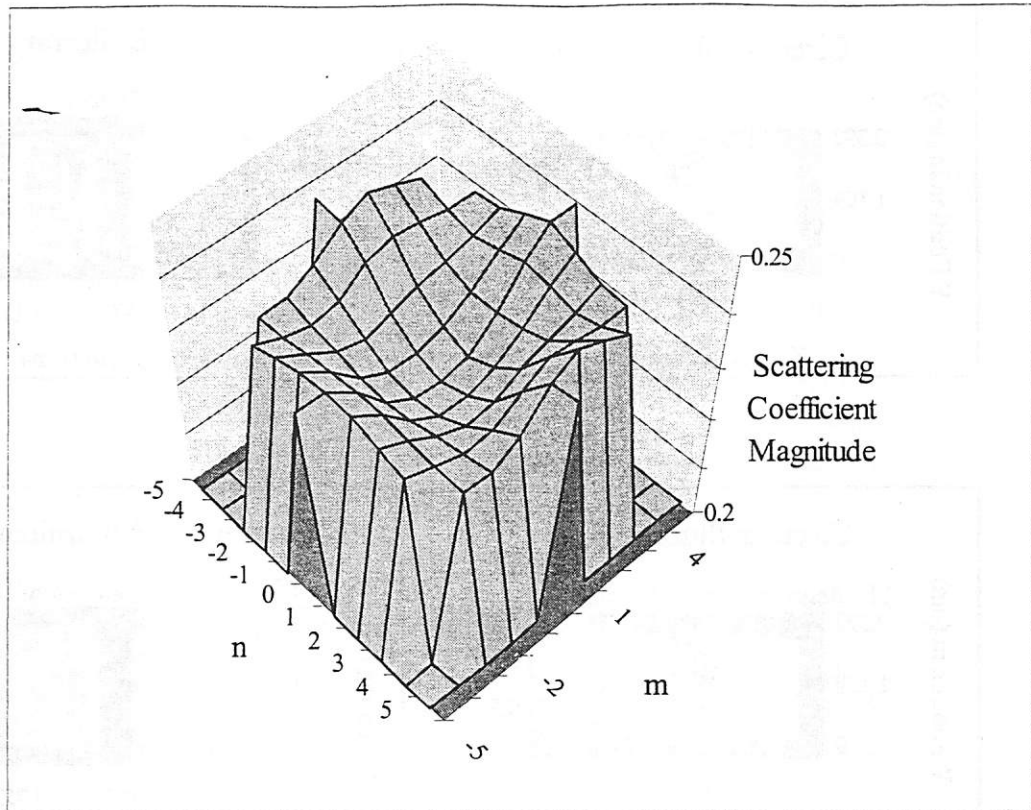


Figure 6-8. Plot of the magnitude of the scattering into the (+1,+0) scattered order vs. angle of incidence

6.4. Conclusions and Discussion

Scanning beam optical microscopy has been known to be equivalent to conventional microscopy under Hopkins' approximation (constant scattering coefficients and scalar theory). It is unclear whether the equivalence holds for a vector theory where the Hopkins' approximation is not made. However, an efficient model for scanning beam microscopy has been proposed.

The scattering coefficients for a typical phase-shift mask topography were seen to be dependent on angle of incidence and due to the high angular spectrum of plane waves incident upon the mask during inspection, multiple TEMPEST simulations for plane waves must be run to calculate scattering coefficients for highly oblique plane waves.

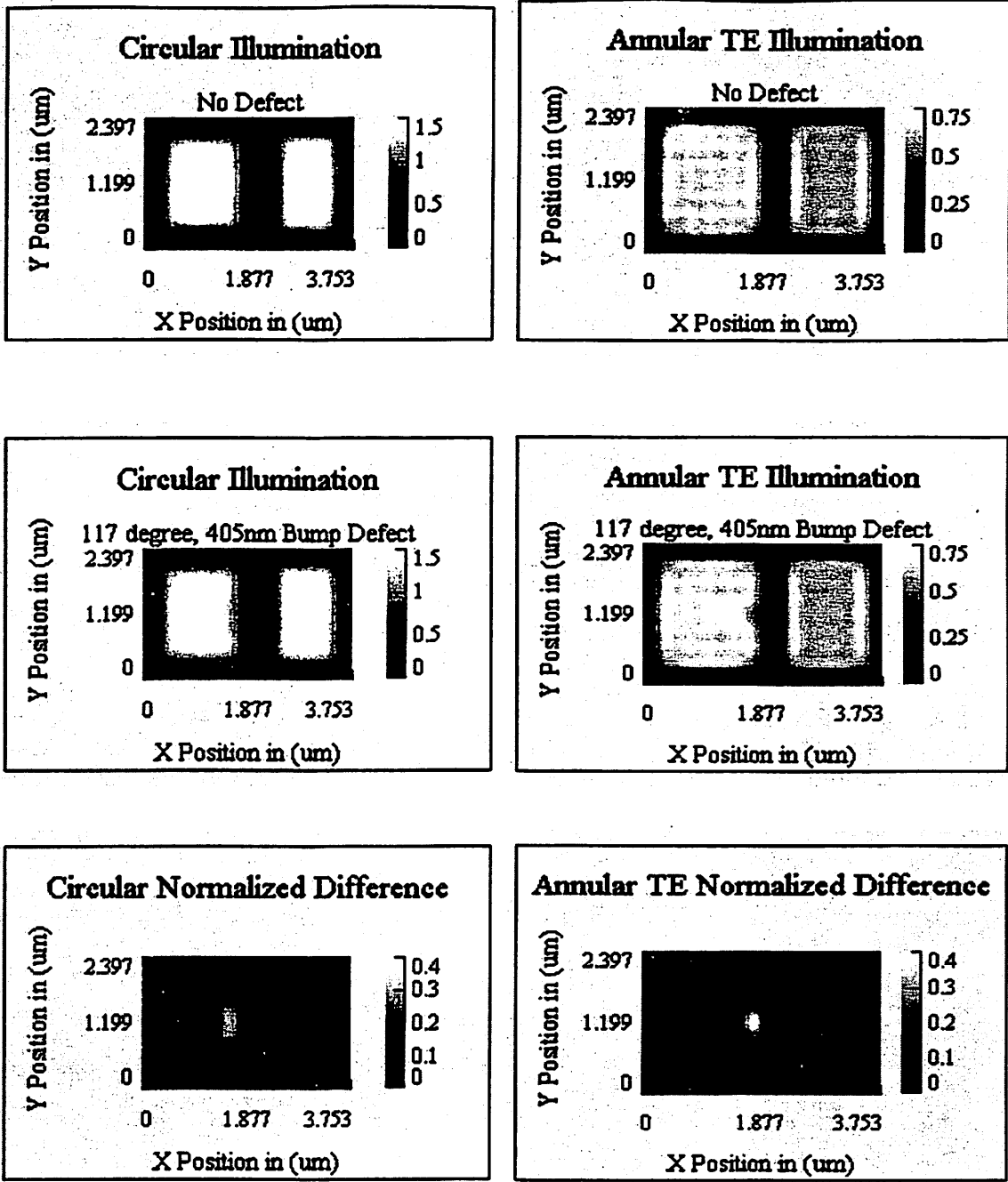


Figure 6-9. Annular Illumination Improves Phase Defect Visibility

The top figures show the aerial image intensity when no defect is present for circular and annular illumination. The middle pictures show the aerial image intensity when a 117 degree phase defect with $(405\text{nm})^2$ is present. The difference images (normalized to their defect-free total image energies) are plotted in the lower figures. The peak normalized intensity of the annular difference image is 0.18 while for the circular case it is 0.14. Annular illumination is better at "seeing" the defect.

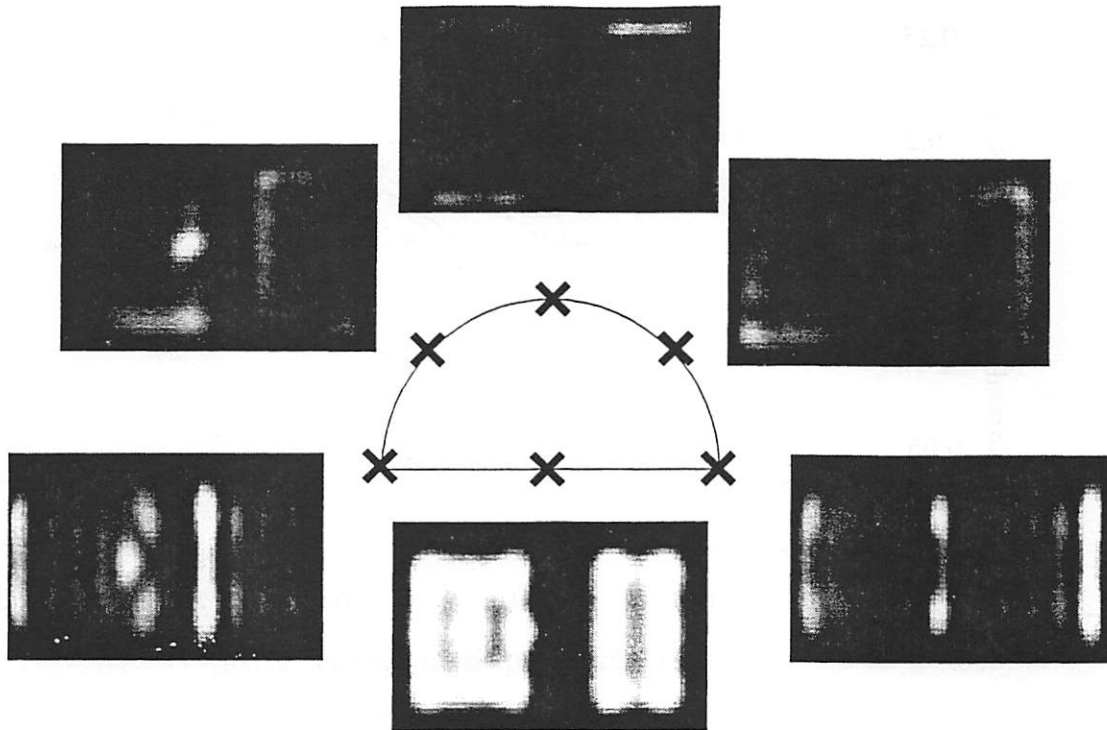


Figure 6-10. Aerial Images for Individual TE Plane Waves at Different Locations

Some angles of incidence are better at interacting with the defect than others. Only the top half of k-space is shown since the topography is symmetric in the y-direction. Plane waves with negative k_x appear to interact with the defect better than those with positive k_x values.

The printability of a 117 degree, bump defect located at the phase-shifter side wall was investigated through simulation. Isotropic wet etching was seen to decrease defect printability. Defects with a pre-wet-etch size larger than 200nm were seen to cause greater than 10% CD variation.

A simulation study of defect inspectability was undertaken. Both circular and annular illumination schemes were compared. Annular illumination was found to yield stronger normalized difference signals. This is explained by the fact that defects are efficient scatterers into high orders.

Simulation can allow a lithographer to understand how effective particular plane waves in the illumination pupil are at seeing defects. This capability may ultimately lead to new designs for mask defect inspection systems that are optimized for detection of phase defects in advanced phase-shift masks.

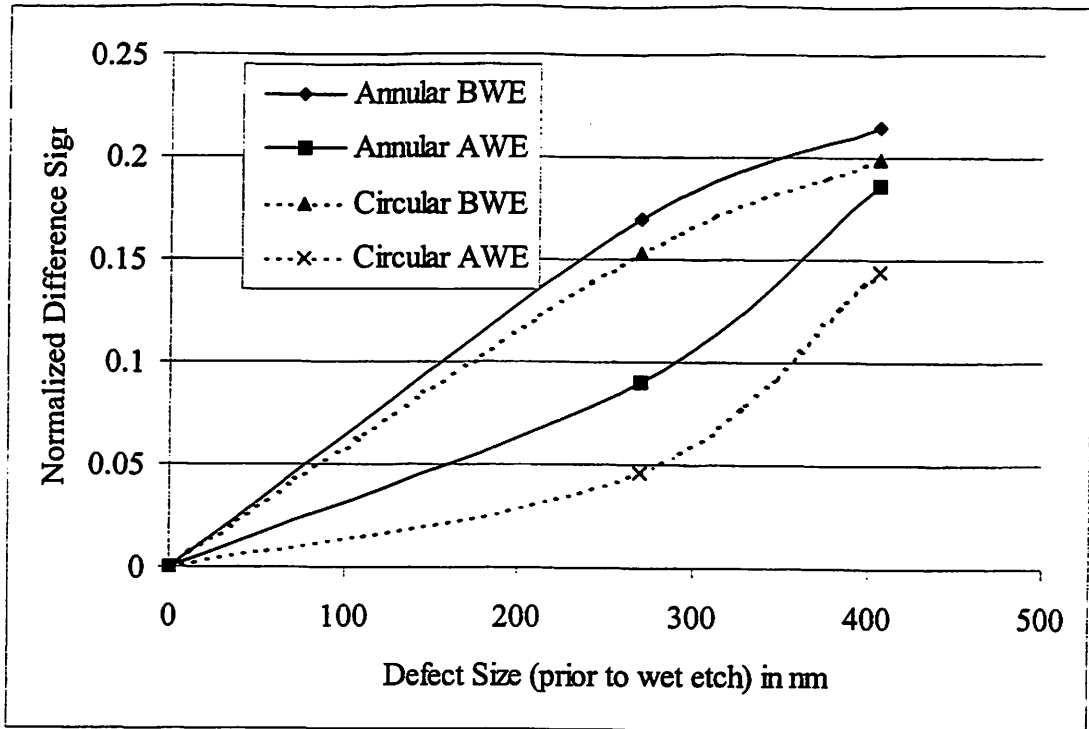


Figure 6-11. Defect Visibility Before/After Wet Etch, for Circular and Annular Illumination

The defects are less visible after wet etch because they are smaller. The difference signal for the annular illumination is stronger in all cases.

7 Other Simulations related to Lithography

There many applications of TEMPEST that are related to lithography. Thus far, this thesis has only touched upon two areas (EUV features and defects in Chapter 5 and phase defects in alternating phase shift masks in Chapter 6). This chapter is dedicated to a number of other lithography-related simulations.

7.1. Pinholes for EUV Point Diffraction Interferometry

Researchers [34][80][48] have been using point-diffraction interferometry for the characterization of EUV optical systems. Point-diffraction interferometry relies on the generation of a spherical reference wavefront by pinhole diffraction.

Goldberg[34] used rigorous FDTD simulation with TEMPEST to understand pinhole diffraction for the purposes of determining a pinhole size appropriate for the generation of a reference wave with sufficient quality for the metrology of EUV optics. An illustration of a topography similar to that investigated by Goldberg is shown in Figure 7-1.

Plots of the electric field intensity for the tapered pinhole topography are shown in Figure 7-2. Goldberg analyzed the complex field in the xy -plane (the intensity of which is shown in figure (b)) by propagating it to the far field and determining its deviation from a perfect spherical wave.

7.2. Alignment Mark Simulation

The ability to accurately align the wafer during printing (i.e. while inside a stepper or a scanner) is critically important to lithography. As feature dimensions continue to down-scale, the alignment signal tolerances become tighter. Further complicating the matter is

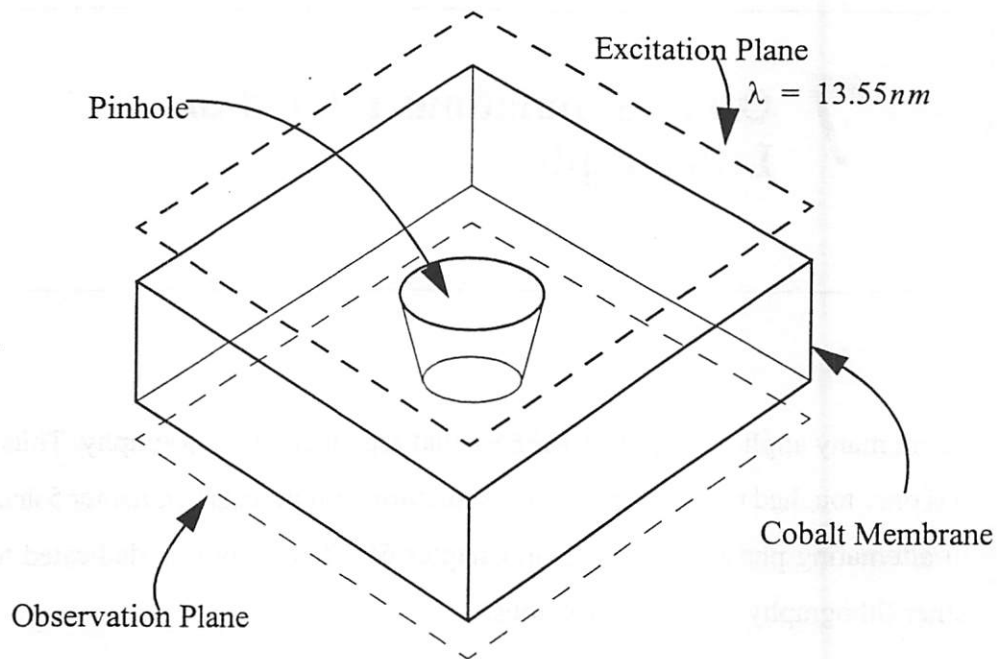


Figure 7-1. Topography for Pinhole used for Reference Wave Generation

The membrane is 90nm thick, with a (possibly tapered or flared) pinhole with diameter on the order of 50nm to 150nm. A polarized normally incident plane wave is incident from above, and the field is observed just below the membrane.

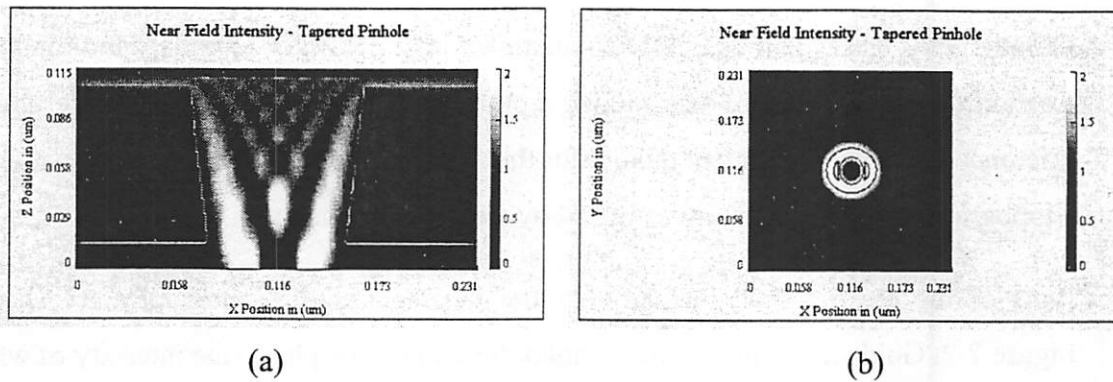


Figure 7-2. Near Field Intensity for Tapered Pinhole

The entrance diameter of the pinhole is 100nm and the exit diameter is 80nm. The field is clearly nonuniform and slightly asymmetric in the azimuthal direction due to polarization effects.

the fact that most wafer processing steps tend to degrade the alignment mark topography and signal. A detailed understanding of alignment marks and a method to predict alignment performance is needed.

Recent research by Yin[101] and Wu[97] has used TEMPEST to simulate the scattering from alignment mark topographies, to discover what are the critical parameters affecting signal contrast and to optimize the topography for performance.

A typical alignment mark topography is shown in Figure 7-3. Unlike the imaging systems discussed so far, alignment mark imaging involves the use of broadband illumination (500nm to 800nm wavelengths) and so several wavelengths within the band must be simulated. Table 7-1 lists the optical properties for the materials used in alignment mark simulation at various wavelengths. The final aerial image is a weighted summation of the aerial image intensities of the separate wavelengths.

Table 7-1. Complex Indices of Refraction for Various Wavelengths

Material	550 nm	600 nm	650 nm	700 nm	750 nm
Si	4.088 - j0.042	3.947 - j0.026	3.85 - j0.0165	3.783 - j0.0122	3.733 - j0.0092
Poly	3.915 - j0.105	3.774 - j0.0682	3.672 - j0.045	3.596 - j0.023	3.537 - j0.0212
Nitride	2.033	2.023	2.014	2.008	2.002
Oxide	1.474	1.473	1.472	1.471	1.47
Resist	1.68	1.68	1.68	1.68	1.68

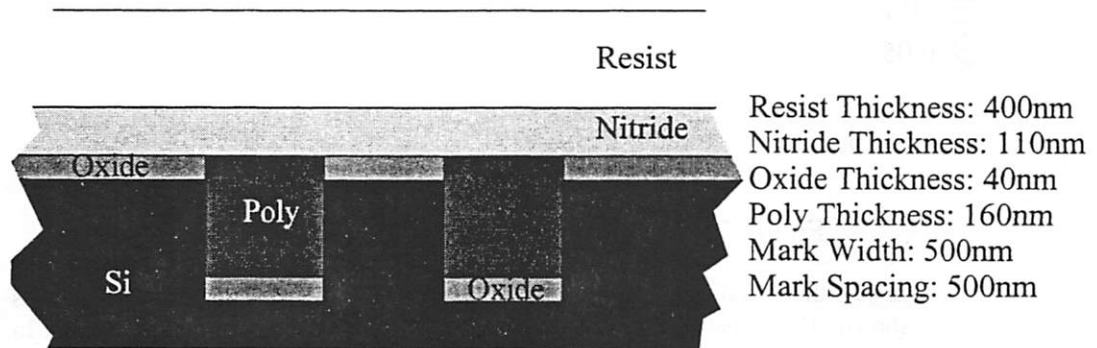


Figure 7-3. Alignment Mark Topography

A plane wave is incident from above and the reflected field is observed. The mark depth is chosen so that light reflected from the bottom of the mark and the top are out of phase.

The aerial image intensities for the individual wavelengths are plotted Figure 7-4 (a). Some wavelengths are able to see the alignment mark better than others. The total signal is shown in Figure 7-4 (b).

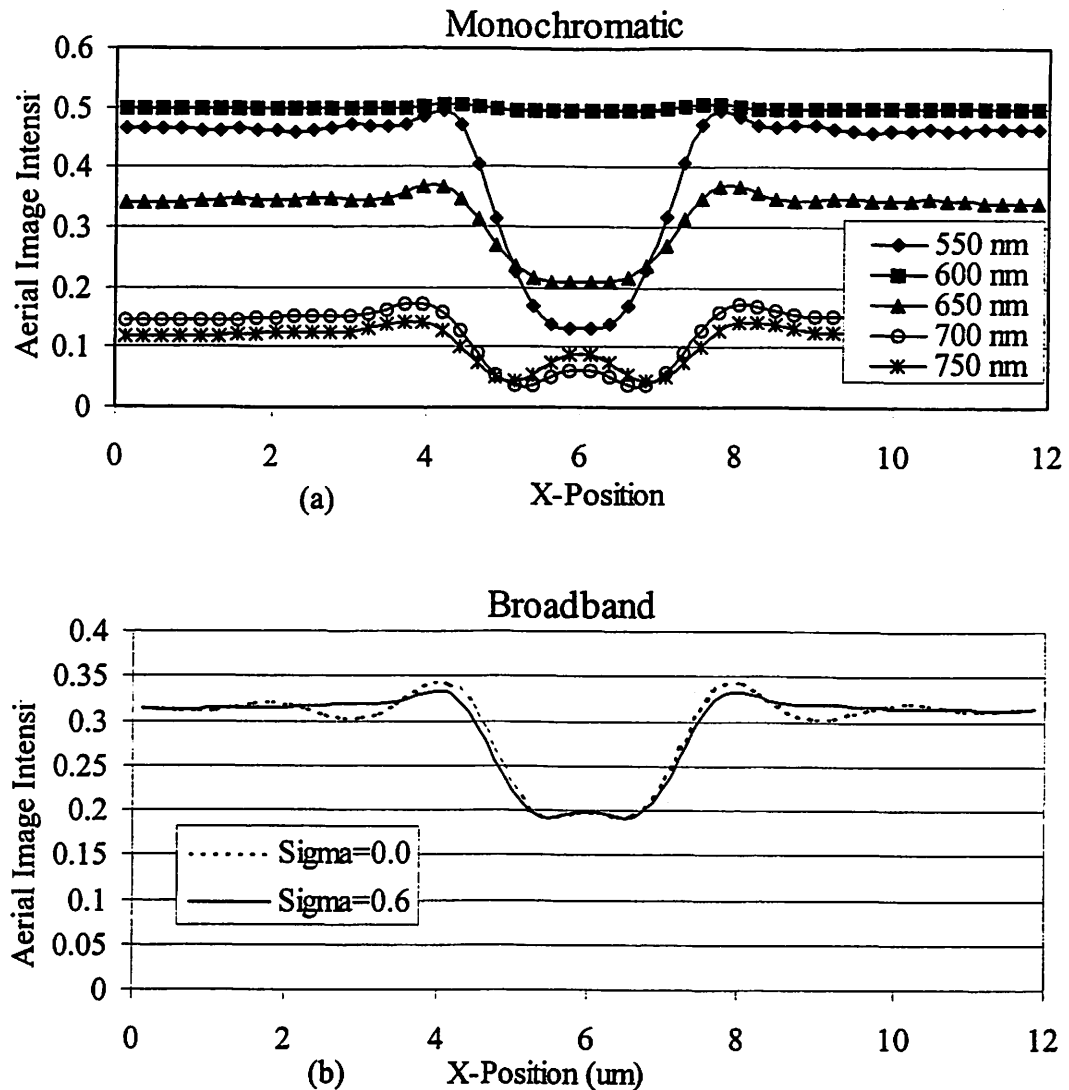


Figure 7-4. Aerial Image Intensities for Alignment Mark

In (a), the aerial image intensity for each of the five wavelengths simulated is shown. The signal quality varies significantly from wavelength to wavelength. In (b) the average intensity is shown under two different partial coherence conditions.

7.3. The Aberration Ring Test

Dirkson et al. [25][26] have recently introduced a technique for measuring aberrations in optical imaging systems. The Aberration Ring Test (ART) uses a circular phase shifting well with a 180 degree phase depth and a λ/NA diameter (wafer dimension) that, in the absence of aberrations, prints as a ring in the resist (see Figure 7-5). When aberrations are

present, the contours of the ring become distorted. The distorted contours can be mathematically analyzed to extract information about the aberrations in the optics.

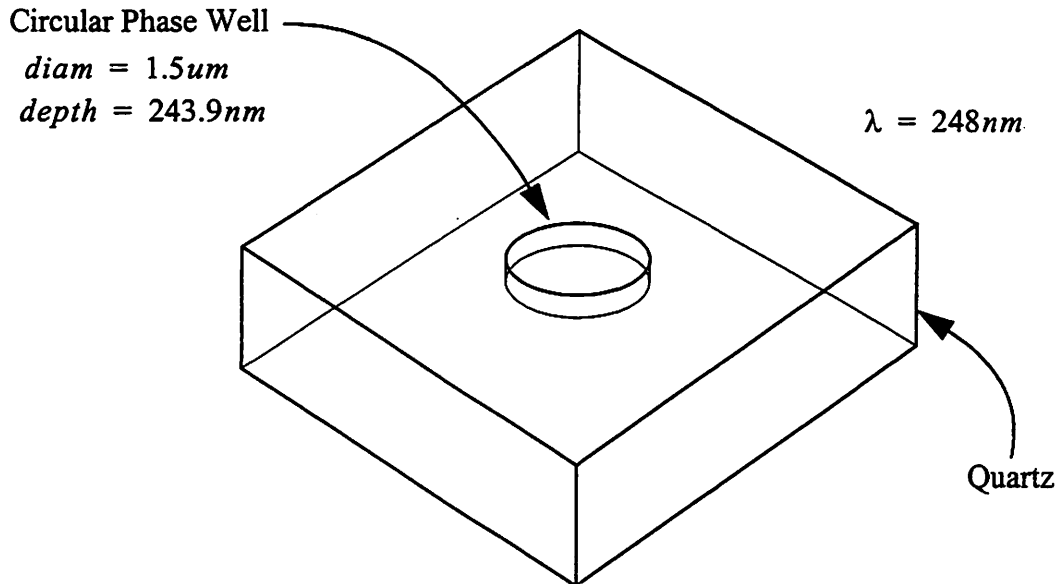


Figure 7-5. Mask Topography for Aberration Monitor

The mask topography for the aberration ring test (ART) is simply a circular phase well with diameter $\cong \lambda/NA$ (wafer dimension) and a depth of 180 degrees.

Scalar mask theory (i.e. thin mask with binary transmission) combined with thin-film stack theory (Chapter 4) has been used to demonstrate the effects of aberrations on the ring image. Figure 7-6 shows the aerial image intensity in a vertical cross-section that shows the ring through the depth of the resist. The inner radius of the ring is larger at the top of the resist than at the bottom due to absorption in the resist, while both radii oscillate slightly due to a small standing wave effect (from the small reflection off the BARC). Subsequent aerial images were observed in the xy -plane half way up the resist (i.e. at $z = 0.201 \mu m$).

Individual aberrations were introduced and their effects are seen in Figure 7-7.

To investigate the consequences of assuming a scalar, thin-mask model for ART simulation, full 3D TEMPEST simulations were run and aerial images were calculated and compared to those obtained using the thin scalar mask approximation.

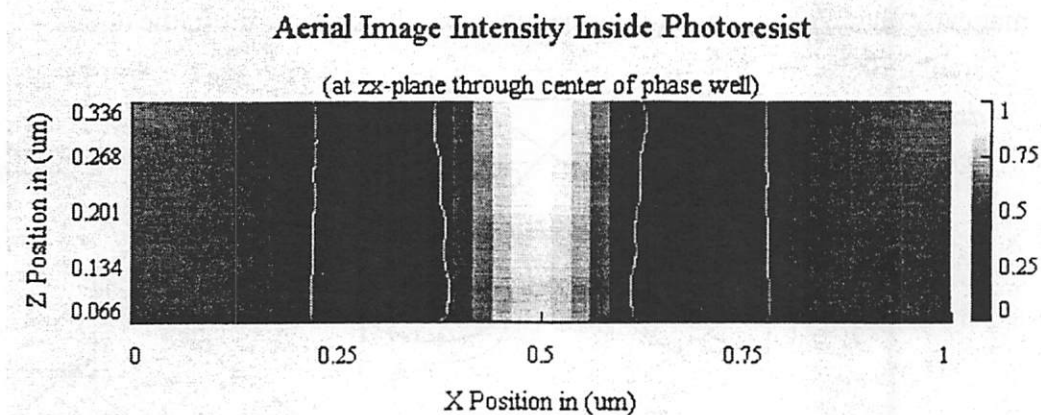


Figure 7-6. ART: Aerial Image Intensity Inside Photoresist

The resist is 270nm thick with a BARC at the bottom. The effects of attenuation, reflection from the bottom surface (BARC) and simple depth of focus make the ring profile non-uniform through the depth of the resist.

The complex electric field near the mask (the near field) is plotted in Figure 7-8. Where the scalar theory predicts a uniform and unity magnitude, the rigorous mask model shows that diffraction causes ringing. As a result, one can expect that some energy is scattered out of the range of the numerical aperture of the projection optic and thus the aerial image obtained using rigorous mask simulation will have less energy. The near field phase is seen to deviate significantly from the perfect (binary) phase assumed by the thin, scalar mask model.

Of course, the main concern is regarding how the aerial images obtained by using the scalar and rigorous mask models differ. This is illustrated in Figure 7-9 where one quadrant of the ring contours is analyzed.

From observation of only the “scalar” curves for the unaberrated and spherically aberrated cases, it is evident that positive spherical aberration causes the inner radius to drastically increase and the outer radius to slightly increase. When one inspects the contours for the “TEMPEST” curves, it is evident that the increase in inner radius due to the addition of spherical aberration is slightly larger than observed for the “scalar” curves. This indicates that diffraction from the sidewalls of the circular phase well introduces positive spherical aberration.

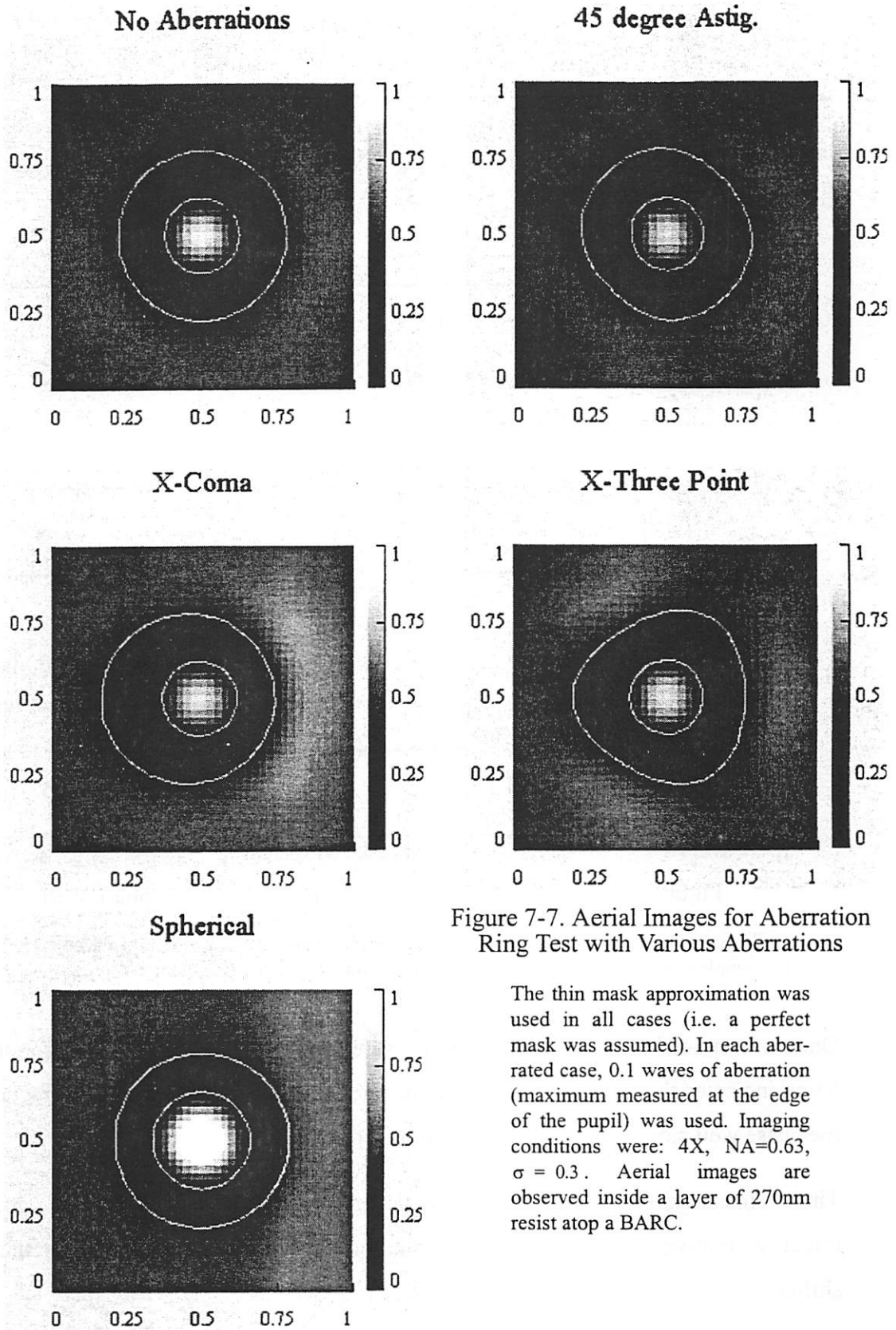
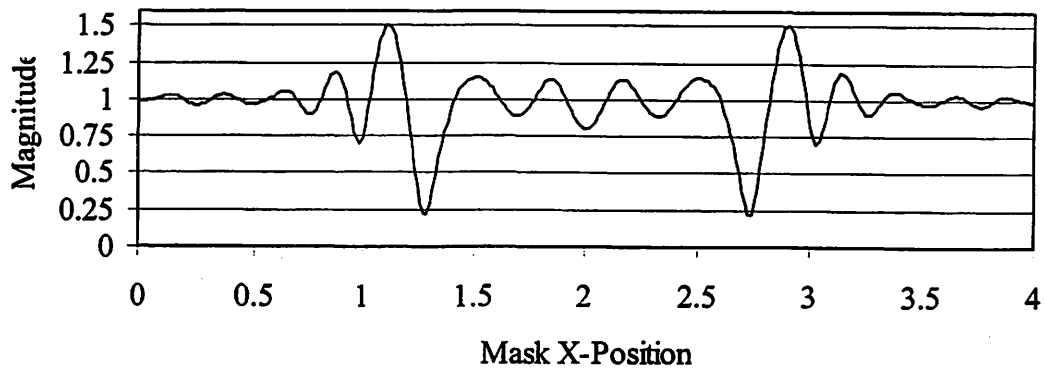


Figure 7-7. Aerial Images for Aberration Ring Test with Various Aberrations

The thin mask approximation was used in all cases (i.e. a perfect mask was assumed). In each aberrated case, 0.1 waves of aberration (maximum measured at the edge of the pupil) was used. Imaging conditions were: 4X, NA=0.63, $\sigma = 0.3$. Aerial images are observed inside a layer of 270nm resist atop a BARC.

Near Field Magnitude



Near Field Phase

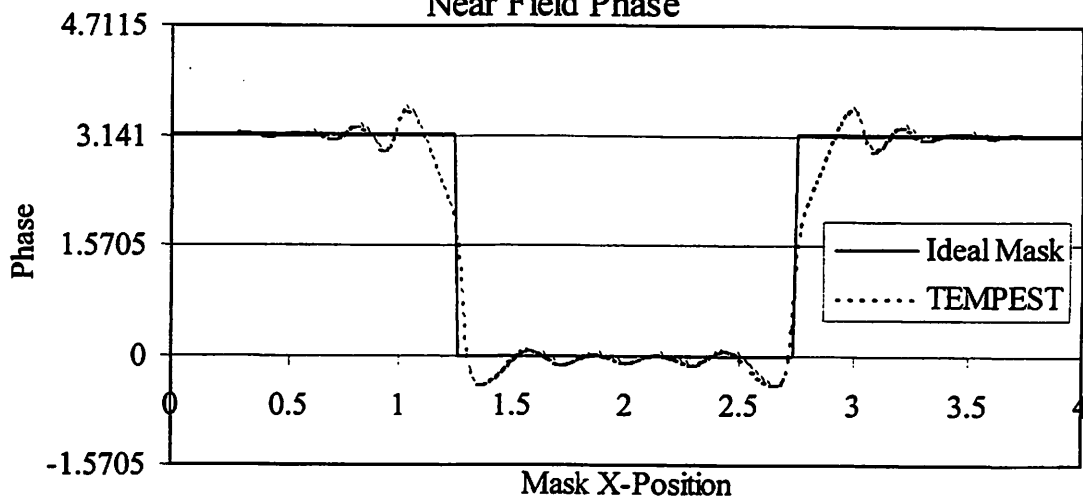


Figure 7-8. Near Fields across the diameter of the ART phase well

The complex electric field is observed very near to the mask, just after transmission. This complex field can be interpreted as a complex transmission function for a Kirchhoff-type mask.

One can conclude that the scalar model is useful for simulating the ART. Rigorous simulation indicates that some of the measured spherical aberration is due to diffraction from the phase well side walls. This can be calibrated out.

Three dimensional rigorous simulation will be necessary in future work to understand the effects of non-vertical sidewalls and nonuniformities in the depth of the circular phase shifter.

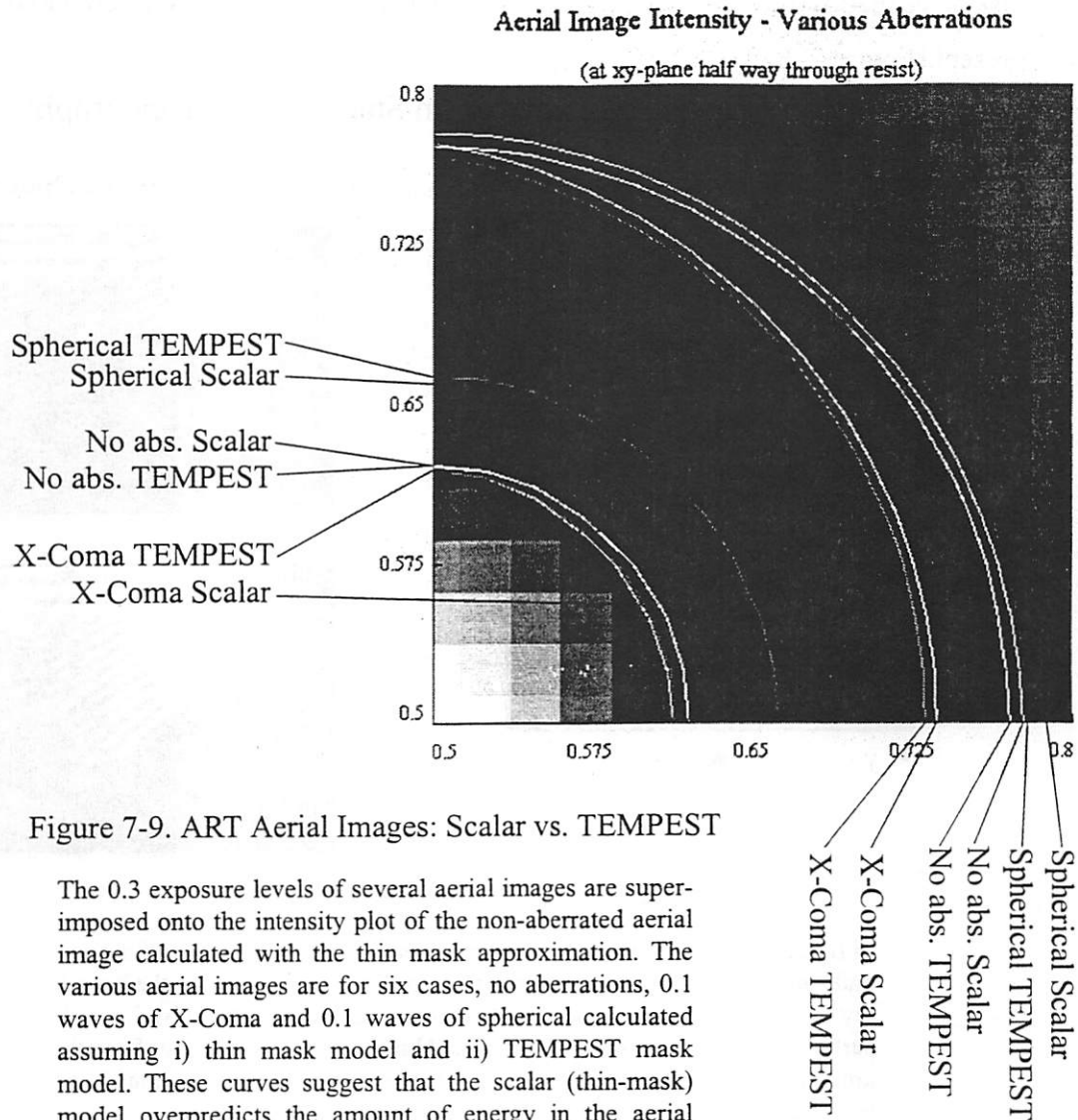


Figure 7-9. ART Aerial Images: Scalar vs. TEMPEST

The 0.3 exposure levels of several aerial images are superimposed onto the intensity plot of the non-aberrated aerial image calculated with the thin mask approximation. The various aerial images are for six cases, no aberrations, 0.1 waves of X-Coma and 0.1 waves of spherical calculated assuming i) thin mask model and ii) TEMPEST mask model. These curves suggest that the scalar (thin-mask) model overpredicts the amount of energy in the aerial image, and the amount of spherical aberration present.

7.4. Reflective Notching

When the aerial image is being formed inside a flat film stack, simple analytical methods (thin film theory) can be used to calculate the latent image. When the layer of photoresist is atop topography then the translational symmetry of the film stack is broken and other methods must be used to find the latent image.

Wong[95] and Socha[70] each used TEMPEST to investigate reflective notching in the patterning of a gate over non-planar, reflective topography. Pistor[67] used 3D TEMPEST simulation to investigate reflective notching that occurs during the projection printing of

disk drive read/write heads where highly non-planar topography and thick photoresist were present.(Figure 7-10)

Reflective Notching from Stacked Coil Topography

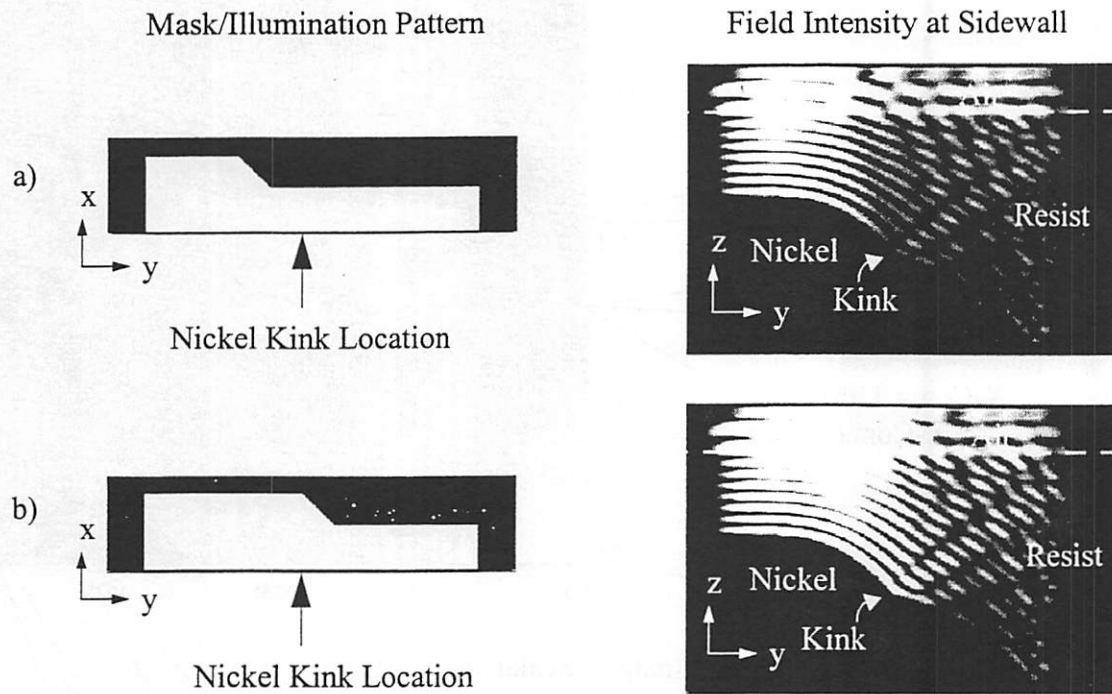


Figure 7-10. Reflective Notching

In figure (a) the wide portion of the bright feature will print on top of the second coil hump. The field plot shows a sharp vertical line defining the boundary between the wide and narrow feature sections. In figure 10b) the wide part of the trench now sits over the nickel kink. A ripple shoots out from the kink and the boundary between the wide and narrow trench sections is no longer a sharp vertical line.

7.5. Phase Shift Mask Topography Effects

The earliest use of FDTD simulation and TEMPEST for phase shifting masks was by Wong[87] who observed in simulation the imbalance in intensity transmission through shifted and unshifted openings in the chrome[47][61]. Since then it has become rather commonplace to use FDTD simulation for the analysis of phase shift mask topography effects: Adam studied phase shift mask defects[3], Socha studied high transmission attenuated phase shift mask topography effects[75][76], Todd for nonuniformities in phase shifter

depth[85], Hotta for shifter edge profile and the residual transmittance through the chrome[43], and other authors for general topographical effects [27][38].

A considerable amount of insight can be gained from 2D TEMPEST simulation (corresponding to 1D mask patterns, i.e. lines and spaces) which typically require less than one megabyte of memory and less than one minute to run. Figure 7-11 and Table 7-2 show a typical parameterized phase shift mask topography. It is a line/space pattern and requires 2D TEMPEST simulation.

Table 7-2. Variable Parameters for 2D Alt. PSM Topography

Parameter Name	Description	Values (nominal in parentheses)
l_c	Line width	(150nm)
l_s	Space Width	(150nm)
p	Pitch (=Line Width + Space Width)	(300nm)
d	Phase Difference between shifted and unshifted spaces	(180 degrees), 174 degrees, 186 degrees
r	Corner Rounding Radius caused by isotropic wet etch	(80nm), 0nm, 20nm, 40nm, 60nm, 80nm, 100nm, 120nm, 140nm
t	Chrome Thickness (pure chrome, no oxide)	(100nm), 40nm, 60nm, 80nm, 100nm, 120nm, 140nm
h	Micro-trenching caused during isotropic dry etch	(0nm), 0nm, 8nm, 16nm, 24nm, 32nm, 40nm, 48nm
NA	Numerical Aperture	0.7
σ	Partial Coherence Factor	0.3
defocus	Wafer Side Defocus	(0um), -0.4um to 0.4um in 0.1um steps
t_{resist}	Thickness of Resist as Wafer ($n=1.76$, $k=0.0166$)	300nm
t_{BARC}	Thickness of BARC under resist at Wafer ($n=1.45$, $k=0.3$)	66nm
z_{img}	Location of image focal plane above poly-Si substrate in the wafer stack	300nm (from bottom of stack)
$z_{measure}$	Location at the aerial image where measurements are made (inside the resist)	166nm (from bottom of stack, 1/3rd the way up the resist)

Figure 7-12, Figure 7-13, Figure 7-14 and Figure 7-15 show the results obtained when various mask parameters are varied.

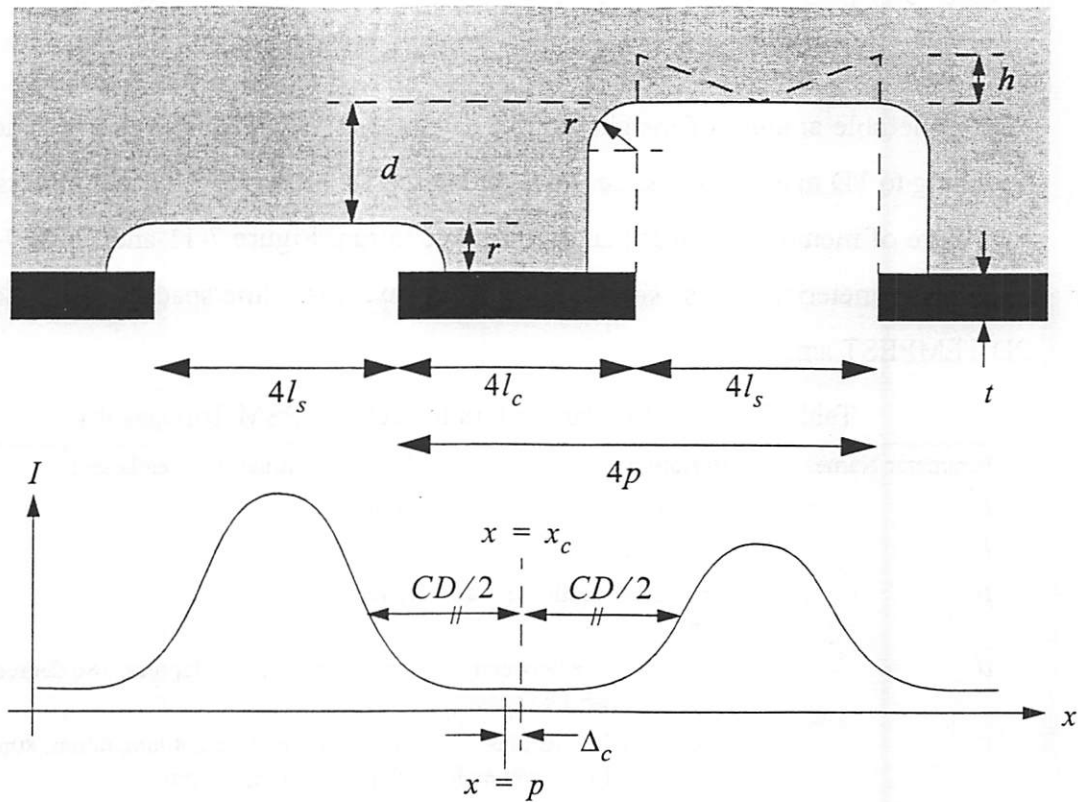


Figure 7-11. Two-dimensional Alternating Phase Shift Mask Topography

7.6. Conclusions

There are many widely varying applications of FDTD simulation and imaging system modeling in optical lithography. Even more applications will surface in the near future as wafer alignment systems and mask and wafer metrology systems become more complicated and as 157nm and EUV lithographies come on-line.

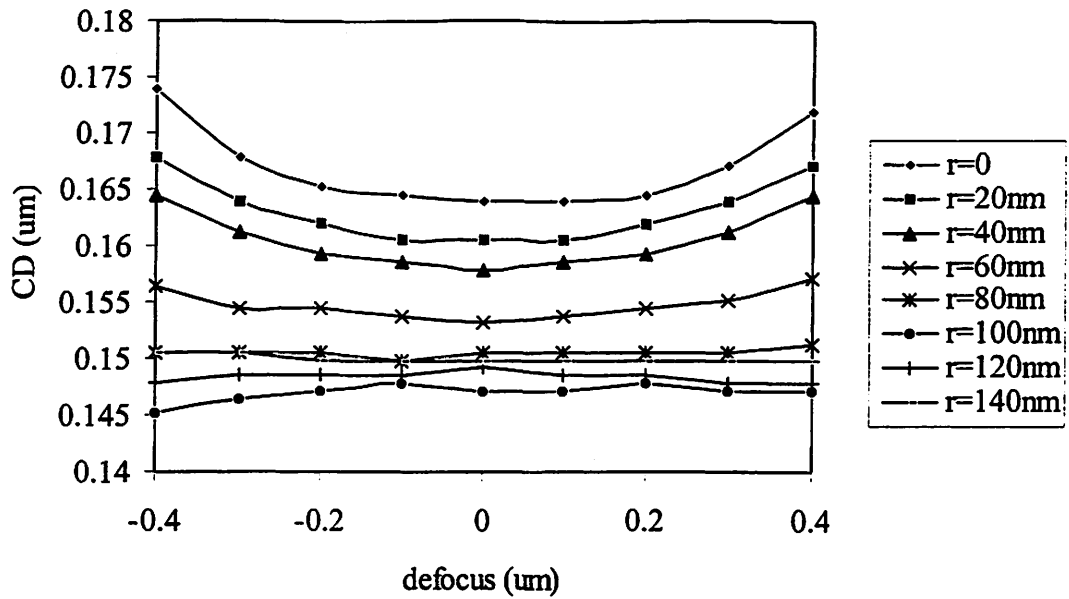


Figure 7-12. Effect of Isotropic Wet Etch

To achieve an intensity balance between the shifted and unshifted spaces, an isotropic (wet) etch is often applied. The corner radius (amount of wet etch) affects both the CD and the process window.

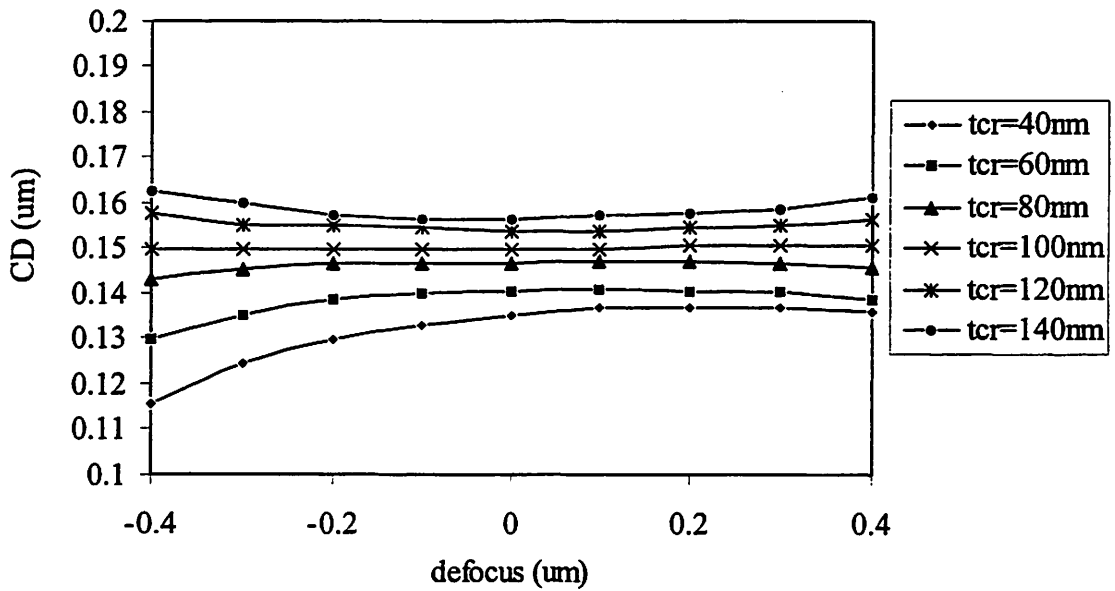


Figure 7-13. Effect of Chrome Thickness

Partial transmission through the chrome can play a role in CD accuracy[43].

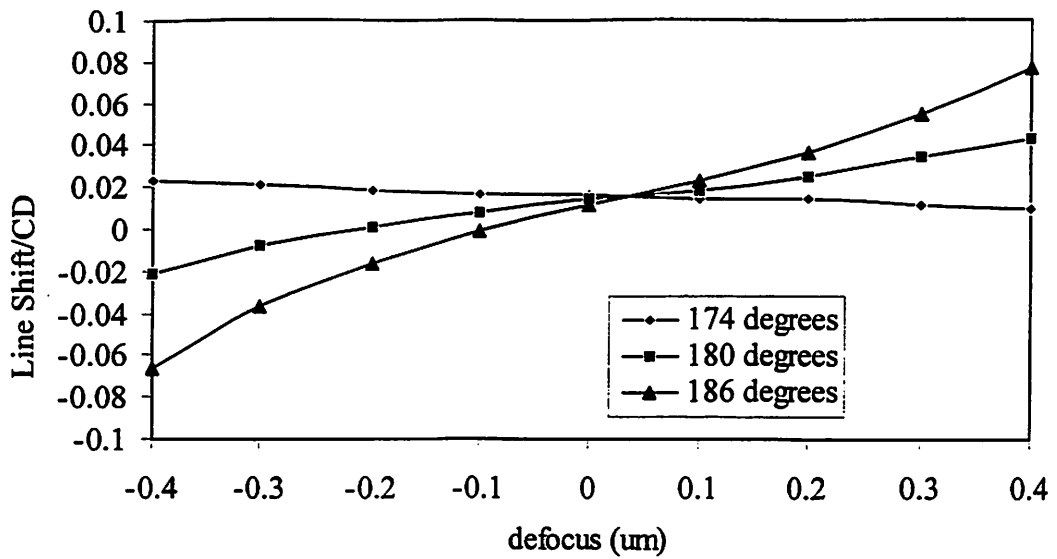


Figure 7-14. Effect of Phase Difference

The CD remains relatively constant through focus for small amounts of phase error between the shifted and unshifted spaces. The line position however will shift with focus when phase error is present.

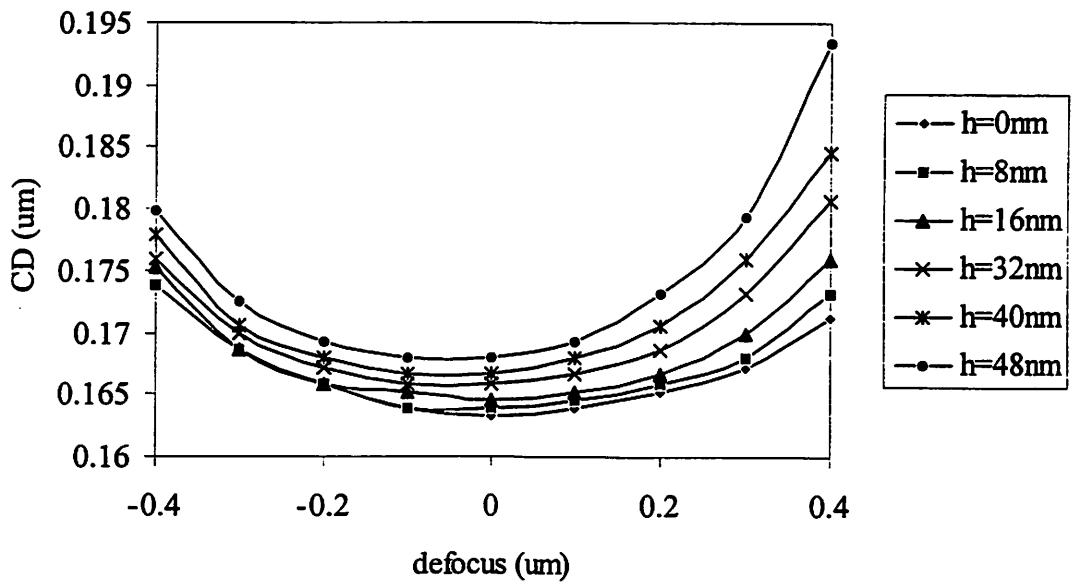


Figure 7-15. Effect of Microtrenching during Plasma Etch

Microtrenching [85] causes a nonuniform profile at the bottom of the phase well.

8 Conclusions

This thesis has discussed several issues related to electromagnetic simulation and modeling in lithography.

The computer program TEMPEST, developed at U.C. Berkeley, is an implementation of the Finite-Difference Time-Domain algorithm used for solving the Maxwell equations. This thesis has documented many of the recent improvements to TEMPEST including the re-parallelization of the code for running on a Network of Workstations, the implementation of the Perfectly Matched Layers boundary condition and the introduction of a novel boundary condition, the Fourier Boundary Condition that can be used to efficiently model EUV multilayer mirrors.

A model for optical imaging that is valid when highly oblique angles of incidence are present was developed and used to calculate aerial images from EUV masks, alternating phase shift masks with defects and several other situations related to lithography.

The theory has been presented in the early chapters while the applications were dealt with in later chapters.

8.1. Theory

The Fourier Boundary Condition (FBC) was developed as an efficient model for an EUVL multilayer mirror. It operates on the Fourier components (plane) waves of the incident field and can be programmed to yield an arbitrary reflectivity versus angle-of-incidence. The FBC was demonstrated to be both an accurate and efficient model for a multilayer mirror.

A parallelized version of TEMPEST using the Message Passing Interface to run across a Network of Workstations (NOW) was developed and benchmarked. It was observed that

the performance depended strongly on the inter-process communications overhead. The performance across several processors in the same box approximated the ideal linear speed-up curve, while the performance when all communications were over a network showed a maximum speed-up factor of only 2.5 for 6 processes.

An imaging system is modeled as a collection of components that operate on plane waves. The source and illumination optic are considered as a source of mutually incoherent plane waves with different polarizations and angles of incidence. The photomask scatters an incident plane wave into many plane waves. The projection optic takes a single plane wave as input and produces a single output plane wave with the same polarization and accounts for the imaging pupil, aberrations, defocus, and optical magnification. Finally, the film stack at the image plane can be incorporated into the projection optic as a correction factor.

The imaging equations presented take the vector nature of light fully into account and can accommodate various mask model complexities ranging from simple transmission function to complicated non-constant scattering coefficient models where information from the rigorous simulation of the scattering of several plane waves at different polarizations and angles of incidence is used together to model the mask.

Three mask models were presented, each differing from the other by how the scattering coefficients are calculated, and how many sets of scattering coefficients are calculated for different plane waves within the illumination pupil.

8.2. The Applications

8.2.1. EUVL

The development of Extreme Ultraviolet Lithography (EUVL) is critically dependent on simulation primarily because the hardware is not yet fully developed. The Fourier Boundary Condition was used to save memory when modeling defect-free multilayer mirrors and the parallelized version of TEMPEST was used to enable the multi-gigabyte 3D simulation domains required for rigorous 3D simulation of multilayer mirror defects.

A degradation in object-side depth of focus due to the off-axis imaging was observed. Minute changes in absorber thickness and side wall angle were seen to significantly affect

CD. 3D TEMPEST simulations showed differences between “exterior” and “interior” square features and CD dependence on corner rounding.

Gaussian-shaped mirror profiles caused by deposition on top of substrate defects were seen to cause intensity reduction in the clear field. For a given defect height, a worse-case defect width was observed. A 1nm high, 56nm wide gaussian defect was seen to cause a line’s width to change as much as 12% depending on where the defect was positioned in relation to the line.

8.2.2. Phase Shifting Masks: Defect Printability and Inspection

The scattering coefficients for a typical phase-shift mask topography were seen to be dependent on angle of incidence and due to the high angular spectrum of plane waves incident upon the mask during inspection, multiple TEMPEST simulations for plane waves must be run to calculate scattering coefficients for highly oblique plane waves.

The printability of a 117 degree, bump defect located at the phase-shifter side wall was investigated through simulation. Isotropic wet etching was seen to decrease defect printability. Defects with a pre-wet-etch size larger than 200nm were seen to cause greater than 10% CD variation.

A simulation study of defect inspectability was undertaken. Both circular and annular illumination schemes were compared. Annular illumination was found to yield stronger normalized difference signals. This is explained by the fact that defects are efficient scatterers into high orders.

Simulation can allow a lithographer to understand how effective particular plane waves in the illumination pupil are at seeing defects. This capability may ultimately lead to new designs for mask defect inspection systems that are optimized for detection of phase defects in advanced phase-shift masks.

8.2.3. Other uses of simulation in lithography

There are many widely varying applications of FDTD simulation and imaging system modeling in optical lithography as evidenced by the simulations presented in Chapter 7. Pinholes, alignment marks, reflective notching and aberration monitors can be investigated

with the techniques discussed in this thesis. Even more applications will surface in the near future as wafer alignment systems and mask and wafer metrology systems become more complicated and as 157nm and EUV lithographies come on-line.

8.3. Future

There is no doubt that feature sizes will continue to shrink while the complexity and cost of the associated lithographies will heighten. Simultaneously, the computational power available to lithographers will increase. Therefore, the utility of simulation in lithography will continue to grow.

New algorithms and approximations may one day reduce the simulation times for large 3D domains from hours to seconds. It may soon be possible for a defect inspection/repair system to instantly assess the printability of a particular defect, or for an OPC engineer to rigorously verify the performance of a serif or scatter bar, or for a mask designer to run a massive optimization of some topographical feature.

A Plane Waves

A.1. Uniform Plane Waves in Free Space

A uniform plane wave propagating in free space can be fully characterized by specifying its wavelength, direction of propagation, polarization, magnitude and phase. In this thesis, polarization will be specified as TE or TM relative to the xy -plane. TE polarization has the electric field in the xy -plane while the TM field has the magnetic field lying in the xy -plane. Circular and elliptical polarizations are linear combinations of the TE and TM polarizations.

The complex electric field for a single uniform plane wave of a particular polarization and with a particular direction of propagation is written:

Equation A-1.
$$\vec{E}(\vec{x}, t) = \vec{E}_0 e^{j(\omega t - \vec{k} \cdot \vec{x})}$$

where the wave's complex amplitude \vec{E}_0 is the a complex vector representing the wave's magnitude and phase and polarization and \vec{k} is the "k-vector" for the plane wave and specifies the wave's direction of propagation. The following other relations apply:

Equation A-2.
$$\omega = \frac{2\pi c}{\lambda}$$

Equation A-3.
$$\vec{k} = k_x \hat{i}_k + k_y \hat{j}_k + k_z \hat{k}_k$$

Equation A-4.
$$k = \frac{2\pi}{\lambda} = \sqrt{k_x^2 + k_y^2 + k_z^2}$$

Equation A-5.
$$k_{xy} = \sqrt{k_x^2 + k_y^2}$$

Equation A-6.
$$k_z = \text{dir}_z \sqrt{k^2 - k_{xy}^2}$$

Equation A-7.

$$dir_z \in \{-1, 1\}$$

ω is the radian frequency, \vec{k} is the “k-vector” with cartesian components k_x , k_y and k_z , k is the wave number, k_{xy} is the magnitude of the k-vector’s projection onto the xy-plane, dir_z is -1 if the wave travels “downwards” (in the negative z-direction) and +1 if the wave travels “upwards” (in the positive z-direction).

The wave’s complex amplitude \vec{E}_0 can be represented with two different component forms. The first form is the usual “Cartesian component” form:

Equation A-8.

$$\vec{E}_0 = E_x \hat{i} + E_y \hat{j} + E_z \hat{k}$$

where \hat{i} , \hat{j} and \hat{k} are the usual cartesian unit vectors. The second component form is called the “polar component” form¹:

Equation A-9.

$$\vec{E}_0 = A_{TE} \hat{e}_{TE} + A_{TM} \hat{e}_{TM}$$

where \hat{e}_{TE} and \hat{e}_{TM} are unit vectors in the direction of the TE mode’s electric field and the TM mode’s electric field respectively. \hat{e}_{TE} and \hat{e}_{TM} depend on the direction of propagation \vec{k} as illustrated in Figure A-1.

For a given direction of propagation, plane wave propagation in lossless media requires that the electric field be perpendicular to the direction of propagation. This means that there are only two degrees of freedom for the direction of the electric field. This highlights an advantage that the polar component form has over the Cartesian component form: it has only two coefficients corresponding to two degrees of freedom avoiding any confusion there may be regarding the electric field direction. Additionally, it is a convenient basis for the consideration of polarized waves because the basis vectors, \hat{e}_{TE} and \hat{e}_{TM} , are always purely TE and purely TM respectively.

The following notation for plane waves is introduced:

1. The term “polar component” as opposed to “polar” is used to avoid confusion with polar coordinates.

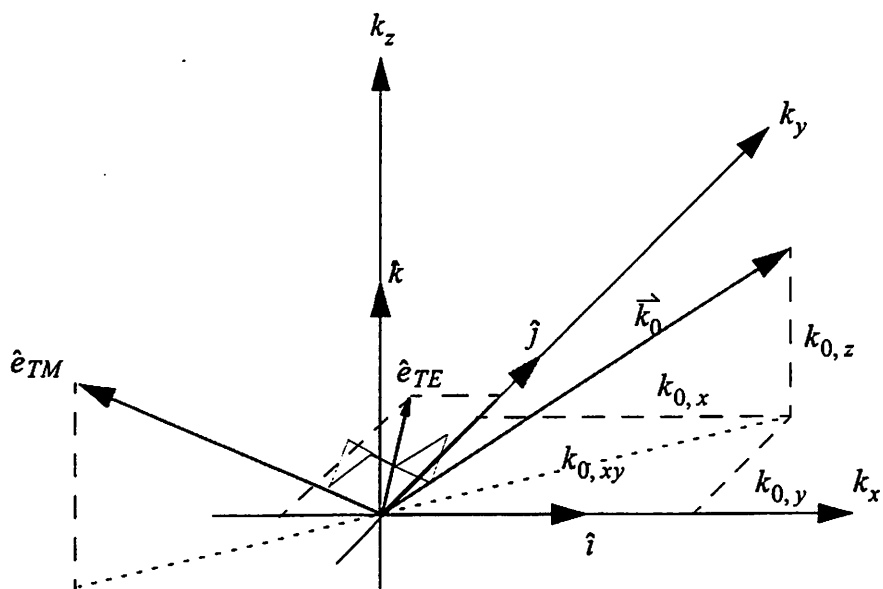


Figure A-1. \hat{e}_{TE} and \hat{e}_{TM} depend on the direction of propagation \vec{k} .

The unit basis vector \hat{e}_{TE} always remains normal to the direction of propagation and tangential to the xy -plane while \hat{e}_{TM} is always normal to the direction of propagation and normal to \hat{e}_{TE} .

Equation A-10.

$$\tilde{w} = \begin{bmatrix} A_{TE} \\ A_{TM} \end{bmatrix}_{\vec{k}}$$

Where the tilde (\sim) below the variable indicates that the variable is a placeholder for a plane wave. The two-element subscripted vector holds the TE and TM coefficients of the plane wave (with reference to the polar component form described above) and the subscript

denotes the direction of propagation of the plane wave. For $\tilde{w}_1 = \begin{bmatrix} A_{1,TE} \\ A_{1,TM} \end{bmatrix}_{\vec{k}_1}$ and

$\tilde{w}_2 = \begin{bmatrix} A_{2,TE} \\ A_{2,TM} \end{bmatrix}_{\vec{k}_2}$ with $\vec{k}_1 \neq \vec{k}_2$, the quantity $\tilde{w}_1 + \tilde{w}_2$ is a coherent¹ superposition of two

1. "Coherent" because a definite phase relationship is assumed to exist between all plane waves in the sum

plane waves with different directions of propagation. Similarly, the quantity $\sum_i \tilde{w}_i$ is coherent a superposition of many plane waves.¹

The relation between the two sets of coefficients is as follows:

$$\text{Equation A-11.} \quad \begin{bmatrix} \tilde{E}_x \\ \tilde{E}_y \\ \tilde{E}_z \end{bmatrix}_{\tilde{k}} = \begin{bmatrix} \frac{k_y}{k_{xy}} & \frac{k_z k_x}{k k_{xy}} \\ \frac{k_x}{k_{xy}} & \frac{k_z k_y}{k k_{xy}} \\ 0 & \frac{k_{xy}}{k} \end{bmatrix} \begin{bmatrix} \tilde{A}_{TE} \\ \tilde{A}_{TM} \end{bmatrix}_{\tilde{k}}, \quad k_{xy} \neq 0$$

A similar relation exists for the magnetic field:

$$\text{Equation A-12.} \quad \begin{bmatrix} \tilde{H}_x \\ \tilde{H}_y \\ \tilde{H}_z \end{bmatrix}_{\tilde{k}} = \frac{1}{\eta} \begin{bmatrix} \frac{k_z k_x}{k k_{xy}} & \frac{k_y}{k_{xy}} \\ \frac{k_z k_y}{k k_{xy}} & \frac{k_x}{k_{xy}} \\ \frac{k_{xy}}{k} & 0 \end{bmatrix} \begin{bmatrix} \tilde{A}_{TE} \\ \tilde{A}_{TM} \end{bmatrix}_{\tilde{k}}, \quad k_{xy} \neq 0$$

When $k_{xy} = 0$, the plane wave will be propagating in a direction normal to the xy-plane (either the +z or -z direction) in which case the TE and TM polarizations are arbitrarily defined with the following formulae:

$$\text{Equation A-13.} \quad \begin{bmatrix} \tilde{E}_x \\ \tilde{E}_y \\ \tilde{E}_z \end{bmatrix}_{(0, 0, \pm k)} = \begin{bmatrix} 0 & \text{dir}_z \\ 1 & 0 \\ 0 & 0 \end{bmatrix} \begin{bmatrix} \tilde{A}_{TE} \\ \tilde{A}_{TM} \end{bmatrix}_{(0, 0, \text{dir}_z k)}$$

$$\text{Equation A-14.} \quad \begin{bmatrix} \tilde{H}_x \\ \tilde{H}_y \\ \tilde{H}_z \end{bmatrix}_{(0, 0, \pm k)} = \frac{1}{\eta} \begin{bmatrix} -\text{dir}_z & 0 \\ 0 & 1 \\ 0 & 0 \end{bmatrix} \begin{bmatrix} \tilde{A}_{TE} \\ \tilde{A}_{TM} \end{bmatrix}_{(0, 0, \text{dir}_z k)}$$

1. Note that $\tilde{w}_1 + \tilde{w}_2 \neq \begin{bmatrix} \tilde{A}_{1, TE} + \tilde{A}_{2, TE} \\ \tilde{A}_{1, TM} + \tilde{A}_{2, TM} \end{bmatrix}_{\tilde{k}_1}$. The quantity must be carried around as $\tilde{w}_1 + \tilde{w}_2$.

The three cartesian components are not independent, but polar components are. The polar component form is useful when a separation between the polarizations is needed such as when applying a reflection coefficient to a plane wave. (as in the Fourier Boundary Condition in Chapter 2 and the thin-film stack analysis in Chapter 4). The cartesian component decomposition is useful when dealing with a scalar diffraction theory.

Because there are only two degrees of freedom for the electric field direction, any two of the three Cartesian components of the electric field will suffice to completely describe the polarization. Taking the x and y components one can write:

$$\begin{aligned} \begin{bmatrix} E_x \\ E_y \end{bmatrix}_{\vec{k}} &= \begin{bmatrix} k_y & k_z k_x \\ k_{xy} & k k_{xy} \\ k_x & k_z k_y \\ k_{xy} & k k_{xy} \end{bmatrix} \begin{bmatrix} A_{TE} \\ A_{TM} \end{bmatrix}_{\vec{k}} \\ &= M_{\vec{k}} \begin{bmatrix} A_{TE} \\ A_{TM} \end{bmatrix}_{\vec{k}} \end{aligned}$$

Equation A-15.

where the transformation matrix $M_{\vec{k}}$ is implicitly defined. Now an inverse relation can be written:

$$\begin{bmatrix} A_{TE} \\ A_{TM} \end{bmatrix}_{\vec{k}} = M_{\vec{k}}^{-1} \begin{bmatrix} E_x \\ E_y \end{bmatrix}_{\vec{k}}$$

This transformation between bases will be useful in plane wave decomposition (Appendix B) and plane wave translation (Appendix C).

A.2. K-Space Representation of Plane Waves

A plane wave's direction of propagation and polarization can be represented graphically on a k-space plot. A "+" symbol is used to indicate TE polarization and a "X" symbol is used to indicate TM polarization. The symbol is located at the coordinates (k_x, k_y) , and thus, the symbol's location denotes the direction of propagation of the plane wave. Figure A-2 illustrates this graphical representation by showing several plane waves plotted

in k-space. Arrows are used to indicate the direction of the electric field for each of the plane waves (as projected onto the xy-plane). The arrows are not necessary since the electric field direction can be deduced from the polarization (TE or TM) and the location.

The k-space plot does not give information of about the magnitude and phase of a plane wave, nor the sign of the k_z component (i.e. dir_z in Equation A-6), nor the wavelength. It is assumed that the sign of k_z component and the wavelength are the same for all plane waves represented on a k-space plot.

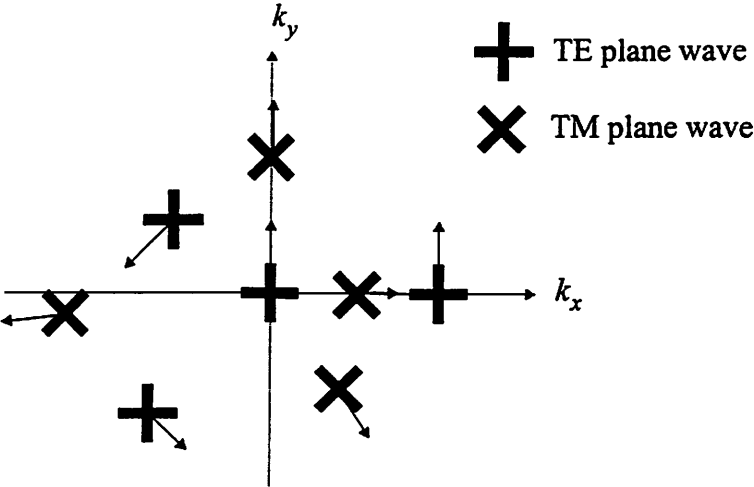


Figure A-2. K-Space Representation of plane waves

The arrows are drawn for illustrative purposes only and represent the electric field direction for the various plane waves.

B TE and TM Plane Wave Decomposition of the Discretized Electric Field

B.1. Decomposition of the Continuous Electric Field

In the continuum, for a periodic mask

Equation B-1.
$$\underline{\vec{E}}(\hat{x}, t) = \underline{E}_x(\hat{x}, t)\hat{i} + \underline{E}_y(\hat{x}, t)\hat{j} + \underline{E}_z(\hat{x}, t)\hat{k}$$

where $\underline{\vec{E}}(\hat{x}, t)$ is a periodic function in x and in y with period L_x and L_y respectively. The underbar indicates the complex field.

The coefficients for a particular Fourier component $(k_x, k_y) = \left(\frac{2\pi m}{L_x}, \frac{2\pi n}{L_y}\right)$ (with m and n integers) for the x and y components of the electric field are written:

Equation B-2.
$$\begin{bmatrix} \underline{E}_{x, mn}(z_0) \\ \underline{E}_{y, mn}(z_0) \end{bmatrix} = \int_0^{L_y} \int_0^{L_x} \begin{bmatrix} \underline{E}_x(x, y, z_0, t) \\ \underline{E}_y(x, y, z_0, t) \end{bmatrix} e^{j(k_x x + k_y y)} dx dy$$

Not all Fourier components correspond to propagating plane waves. Only those values of m and n for which

Equation B-3.
$$k_x^2 + k_y^2 < k^2 = \left(\frac{2\pi}{\lambda}\right)^2$$

correspond to propagating plane waves. This is equivalent to the condition:

Equation B-4.
$$\left(\frac{m}{M}\right)^2 + \left(\frac{n}{N}\right)^2 \leq 1$$

where M and N are the number of propagating order on the positive half axes give by:

Equation B-5.
$$M = \text{floor}\left(\frac{L_x}{\lambda}\right) \text{ and } N = \text{floor}\left(\frac{L_y}{\lambda}\right).$$

For the purposes of imaging, only the propagating fields are of interest, for they are the only components that propagate away from the mask and enter the imaging optics. The propagating component of the electric field consists of only the propagating plane waves and is written:

Equation B-6.
$$\begin{bmatrix} \underline{E}_{prop,x}(\hat{x}, t) \\ \underline{E}_{prop,y}(\hat{x}, t) \end{bmatrix} = \sum_{\left(\frac{m}{M}\right)^2 + \left(\frac{n}{N}\right)^2 \leq 1} e^{j(\omega t - (k_x x + k_y y))} \begin{bmatrix} \underline{E}_{x,mn}(z_0) \\ \underline{E}_{y,mn}(z_0) \end{bmatrix}$$

It is this propagating component of the electric field which is to be expressed as a summation of TE and TM plane waves:

Equation B-7.
$$\begin{bmatrix} \underline{E}_{prop,x}(\hat{x}, t) \\ \underline{E}_{prop,y}(\hat{x}, t) \end{bmatrix} = \sum_{\left(\frac{m}{M}\right)^2 + \left(\frac{n}{N}\right)^2 \leq 1} e^{j(\omega t - (k_x x + k_y y))} \begin{bmatrix} \frac{k_y}{k_{xy}} & \frac{k_z k_x}{k k_{xy}} \\ \frac{k_x}{k_{xy}} & \frac{k_z k_y}{k k_{xy}} \end{bmatrix} \begin{bmatrix} A_{TE}(z_0) \\ A_{TM}(z_0) \end{bmatrix}_{\hat{k}}$$

Comparing Equation B-6 and Equation B-7 immediately yields a relationship between the TE and TM plane wave coefficients and the Cartesian component Fourier coefficients:

Equation B-8.
$$\begin{bmatrix} \underline{E}_{x,mn} \\ \underline{E}_{y,mn} \end{bmatrix} = \begin{bmatrix} \frac{k_y}{k_{xy}} & \frac{k_z k_x}{k k_{xy}} \\ \frac{k_x}{k_{xy}} & \frac{k_z k_y}{k k_{xy}} \end{bmatrix} \begin{bmatrix} A_{TE} \\ A_{TM} \end{bmatrix}_{\hat{k}_{mn}} = [M]_{\hat{k}_{mn}} \begin{bmatrix} A_{TE} \\ A_{TM} \end{bmatrix}_{\hat{k}}$$

and inverting the system yields

Equation B-9.
$$\begin{bmatrix} A_{TE} \\ A_{TM} \end{bmatrix}_{\hat{k}_{mn}} = [M]_{\hat{k}_{mn}}^{-1} \begin{bmatrix} \underline{E}_{x,mn} \\ \underline{E}_{y,mn} \end{bmatrix}$$

Now a method of determining the Cartesian Fourier components $\begin{bmatrix} \underline{E}_{x,mn} \\ \underline{E}_{y,mn} \end{bmatrix}$ from the discretized time/space fields stored by the FDTD method is required.

B.2. Decomposition of the Discretized Electric Field

For monochromatic radiation,

$$\begin{aligned}\underline{\vec{E}}(\vec{x}, t) &= \underline{\vec{E}}_0(\vec{x})e^{j\omega t} = \underline{\vec{E}}_0(\vec{x})(\cos(\omega t) + j\sin(\omega t)) = \underline{\vec{E}}_0(\vec{x})\left(\cos(\omega t) + j\cos\left(\omega t - \frac{\pi}{2}\right)\right) \\ &= \text{Re}\{\underline{\vec{E}}(\vec{x}, t)\} + j\text{Re}\{\underline{\vec{E}}(\vec{x}, t - T/4)\} = \underline{\vec{E}}(\vec{x}, t) + j\underline{\vec{E}}(\vec{x}, t - T/4)\end{aligned}$$

where $T = \frac{1}{f} = \frac{2\pi}{\omega}$ is the cycle (the period) of the time harmonic radiation. The expression expresses the complex field in terms of the real field at two points in time separated by a quarter-cycle. This also applies to the y-component of the electric field and so:

$$\text{Equation B-10.} \quad \begin{bmatrix} \underline{E}_x(\vec{x}, t) \\ \underline{E}_y(\vec{x}, t) \end{bmatrix} = \begin{bmatrix} E_x(\vec{x}, t) \\ E_y(\vec{x}, t) \end{bmatrix} + j \begin{bmatrix} E_x(\vec{x}, t - T/4) \\ E_y(\vec{x}, t - T/4) \end{bmatrix}$$

and similarly for the discretized fields:

$$\text{Equation B-11.} \quad \begin{bmatrix} \underline{E}_x^n[i, j, k] \\ \underline{E}_y^n[i, j, k] \end{bmatrix} = \begin{bmatrix} E_x^n[i, j, k] \\ E_y^n[i, j, k] \end{bmatrix} + j \begin{bmatrix} E_x^{n-N_T/4}[i, j, k] \\ E_y^{n-N_T/4}[i, j, k] \end{bmatrix}$$

where it assumed that N_T is a multiple of 4.

The relation between the discretized and continuous fields is as follows:

$$\text{Equation B-12.} \quad E_x(i\Delta x\hat{i} + j\Delta y\hat{j} + k\Delta z\hat{k} + \Delta\vec{r}_{ex}, (n + 0.5)\Delta t) \cong E_x[i, j, k]$$

$$\text{Equation B-13.} \quad E_y(i\Delta x\hat{i} + j\Delta y\hat{j} + k\Delta z\hat{k} + \Delta\vec{r}_{ey}, (n + 0.5)\Delta t) \cong E_y[i, j, k]$$

Where the $\Delta\vec{r}_{ex}$ and $\Delta\vec{r}_{ey}$ are the displacements of the x and y electric field components from the center of the Yee cell.

The staggered grid arrangement (fortuitously?) has the z-coordinates of the x and y components of the electric field withing the Yee cell equal (i.e. $r_{ex,z} = r_{ey,z}$). The xy-plane containing the the x and y components of the electric field at the position $k = k_0$ is

Equation B-14.

$$z_0 = k_0 \Delta z + r_{ex,z} = k_0 \Delta z + r_{ey,z}.$$

For convenience, it is assumed that the xy-plane in continuous space for which the fields are decomposed into TE and TM waves is aligned with the xy-plane at k_0 that contains the x and y components of the electric field. (i.e. $z = z_0$). So, at $z = z_0$, Equation B-2 gives

$$\begin{aligned} \begin{bmatrix} \underline{E}_{x,mn}(z_0) \\ \underline{E}_{y,mn}(z_0) \end{bmatrix} &= \int_0^{L_y} \int_0^{L_x} \begin{bmatrix} \underline{E}_x(x,y,z_0, (n+0.5)\Delta t) \\ \underline{E}_y(x,y,z_0, (n+0.5)\Delta t) \end{bmatrix} e^{j(k_x x + k_y y)} dx dy \\ &\equiv \sum_{i=0}^{N_x-1} \sum_{j=0}^{N_y-1} \begin{bmatrix} E_x^n[i,j,k_0] e^{j\left(\frac{2\pi m}{L_x}(i+r_{ex,x})\Delta x + \frac{2\pi n}{L_y}(j+r_{ex,y})\Delta y\right)} \\ E_y^n[i,j,k_0] e^{j\left(\frac{2\pi m}{L_x}(i+r_{ey,x})\Delta x + \frac{2\pi n}{L_y}(j+r_{ey,y})\Delta y\right)} \end{bmatrix} \Delta x \Delta y \end{aligned}$$

Equation B-15.

where the right-most expression is a discrete sum approximation to the integrals and is immediately recognized as Discrete Fourier Transform and thus

$$\begin{aligned} &= \Delta x \Delta y \begin{bmatrix} e^{j\left(\frac{2\pi m}{L_x} r_{ex,x} \Delta x + \frac{2\pi n}{L_y} r_{ex,y} \Delta y\right)} \sum_{i=0}^{N_x-1} \sum_{j=0}^{N_y-1} E_x[i,j,k] e^{j\left(\frac{2\pi m}{L_x} i \Delta x + \frac{2\pi n}{L_y} j \Delta y\right)} \\ e^{j\left(\frac{2\pi m}{L_x} r_{ey,x} \Delta x + \frac{2\pi n}{L_y} r_{ey,y} \Delta y\right)} \sum_{i=0}^{N_x-1} \sum_{j=0}^{N_y-1} E_y[i,j,k] e^{j\left(\frac{2\pi m}{L_x} i \Delta x + \frac{2\pi n}{L_y} j \Delta y\right)} \end{bmatrix} \\ &= \Delta x \Delta y \begin{bmatrix} e^{j\left(\frac{2\pi m}{L_x} r_{ex,x} \Delta x + \frac{2\pi n}{L_y} r_{ex,y} \Delta y\right)} \underline{E}_x[-m, -n] \\ e^{j\left(\frac{2\pi m}{L_x} r_{ey,x} \Delta x + \frac{2\pi n}{L_y} r_{ey,y} \Delta y\right)} \underline{E}_y[-m, -n] \end{bmatrix} \end{aligned}$$

Equation B-16.

The factors $e^{j\left(\frac{2\pi m}{L_x} r_{ex,x} \Delta x + \frac{2\pi n}{L_y} r_{ex,y} \Delta y\right)}$ and $e^{j\left(\frac{2\pi m}{L_x} r_{ey,x} \Delta x + \frac{2\pi n}{L_y} r_{ey,y} \Delta y\right)}$ are the staggered grid correction factors which correct for the fact that discretized field components approximate the continuous field components at different places within a Yee cell.

Finally the coefficients for the TE and TM plane waves are calculated:

$$\begin{aligned}
\begin{bmatrix} A_{TE, mn} \\ A_{TM, mn} \end{bmatrix}_{k_{mn}} &= [M]_{k_{mn}}^{-1} \begin{bmatrix} E_{x, mn} \\ E_{y, mn} \end{bmatrix} \\
&= \Delta x \Delta y [M]_{k_{mn}}^{-1} \begin{bmatrix} e^{j\left(\frac{2\pi m}{L_x} r_{ex,x} \Delta x + \frac{2\pi n}{L_y} r_{ex,y} \Delta y\right)} E_x[-m, -n] \\ e^{j\left(\frac{2\pi m}{L_x} r_{ey,x} \Delta x + \frac{2\pi n}{L_y} r_{ey,y} \Delta y\right)} E_y[-m, -n] \end{bmatrix}
\end{aligned}$$

Equation B-17.

C Plane Wave Translation in K-Space

Consider a plane wave $w = \begin{bmatrix} A_{TE} \\ A_{TM} \end{bmatrix}_k$ travelling with k-vector k . This appendix finds the

plane wave $w' = \begin{bmatrix} A'_{TE} \\ A'_{TM} \end{bmatrix}_k$ travelling with a direction $k' = k + \Delta k$ that has a polarization

that is “most similar” to the polarization of w and that has an energy the same as the energy of w .

By “most similar” polarization it is meant that the electric fields of the two waves point in the same general direction.¹ Geometrically, this “most similar” polarization condition is defined as:

The wave w' will have a polarization that is “most similar” to the polarization of the wave w when the projections of electric fields in the plane transverse to the propagation direction of the original plane wave w , are equal.

From Appendix A, all three Cartesian components of the electric field for w can be determined:

1. It may not be possible for the electric field of w' to point in the exact same direction as that of w because of the requirement that the electric field be perpendicular to the direction of propagation.

Equation C-1.
$$\vec{E} = \begin{bmatrix} E_x \\ E_y \\ E_z \end{bmatrix}_{\vec{k}} = \begin{bmatrix} \frac{k_y}{k_{xy}} & \frac{k_z k_x}{k k_{xy}} \\ \frac{k_x}{k_{xy}} & \frac{k_z k_y}{k k_{xy}} \\ 0 & -\frac{k_{xy}}{k} \end{bmatrix} \begin{bmatrix} A_{TE} \\ A_{TM} \end{bmatrix}_{\vec{k}}, \quad k_{xy} \neq 0$$

The projection of this electric field vector onto the plane P that is transverse to the direction of propagation, \vec{k} , of the original wave, w , (i.e. P has normal \vec{k}) is:

Equation C-2.
$$\vec{E}_{proj} = \vec{E} - \frac{(\vec{E} \cdot \vec{k})\vec{k}}{|\vec{k}|^2}$$

Now, an intermediate plane wave, w'' , with the direction of propagation \vec{k}' , is defined by applying Equation A-16 to the x and y components of the projected electric field.

Equation C-3.
$$\vec{w}'' = [M]_{\vec{k}'}^{-1} \left(\begin{bmatrix} E_{proj,x} \\ E_{proj,y} \end{bmatrix} \right)$$

The plane wave w'' satisfies the “most similar” polarization condition but not necessarily the energy condition and must be adjusted to do so:

Equation C-4.
$$\vec{w}' = \begin{bmatrix} A'_{TE} \\ A'_{TM} \end{bmatrix}_{\vec{k}'} = |\vec{w}|_{\vec{k}'} \frac{\vec{w}''}{|\vec{w}''|_{\vec{k}'}}$$

The functional notation is introduced to represent this plane wave translation algorithm:

Equation C-5.
$$w' = \text{translate}(w, \vec{k}')$$

Bibliography

- [1] E. Abbe, "Beitrage zur Theorie des Mikroskops und der mikroskopischen Wahrnehmung," *Archiv f. Mikroskopische Anat.*, vol. 9, pp. 413-468 (1873).
- [2] K. Adam *et al.*, "Analysis of OPC features in binary masks at 193nm", *Proc. SPIE Vol. 4000*, pp. 711-722, 2000.
- [3] K. Adam *et al.*, "Characterization of phase defects in phase shift masks", *J. Vac. Sci. Technol. B 18(6)*, Nov/Dec 2000, pp. 3227-3231.
- [4] K. Adam *et al.* "Simplified Models for Edge Transitions in Rigorous Mask Modeling", *Proc. SPIE Vol. 4346*, 2001. (to be published)
- [5] Adam, K. *et al.*, "Analysis of OPC features in binary masks at 193 nm", *Proc. SPIE Vol. 4000*, (2000) pp. 711-722.
- [6] T. E. Anderson, D. E. Culler, D. A. Patterson, and the NOW team, "A case for Networks of Workstations: NOW," *IEEE Micro*, Feb, 1995.
- [7] Attwood, D., *Soft x-rays and extreme ultraviolet radiation: principles and applications*, (Cambridge University Press, 1999), pp. 56-61.
- [8] *ibid.*, pp.98-122.
- [9] *ibid.*, pp.395-416.
- [10] Berenger, J., "A Perfectly Matched Layer for the Absorption of Electromagnetic Waves", *Journal of Computational Physics*, 114, pp185-200, 1994.
- [11] P. H. Berning, "Theory and Calculations of Optical Thin Films," *Physics of Thin Films*, ed. George Hass (Academic Press, New York, 1963), pp. 931-934.
- [12] F. Bloch, "On the Quantum Mechanics of Electrons in Crystal Lattices," *Z. Phys.*, 52, 555, 1928.

- [13] B. S. Bollepalli *et al.*, "Imaging properties of the extreme ultraviolet mask," *J. Vac. Sci. Technol. B* 16(6), Nov/Dec 1998, pp. 3444-3448.
- [14] Bollepalli, B. S., *et al.*, "Computation of reflected images from extreme ultraviolet masks," *Proc. SPIE Vol. 3676*, pp. 587-597, 1999.
- [15] M. Born and E. Wolf, *Principles of Optics, 7th (Expanded) Edition*, (Cambridge University Press, 1999)
- [16] *ibid.*, pp. 595-599.
- [17] *ibid.*, pp. 572-577.
- [18] *ibid.*, pp. 135-136.
- [19] *ibid.*, pp. 54-74.
- [20] L. Capodici *et al.*, "Effects of advanced illumination schemes on design manufacturability and interactions with optical proximity corrections," *Proc. SPIE Vol. 4181*, pp. 58-67, 2000.
- [21] D. C. Cole *et al.*, "Derivation and Simulation of Higher Numerical Aperture Scalar Aerial Images", *Jpn. J. Appl. Phys. Vol. 31* (1992) pp. 4110-4119.
- [22] D. Cole *et al.*, "Extending scalar aerial image calculations to higher numerical apertures," *Journal of Vacuum Science and Technology B*, vol. 10, No. 6, pp. 3037-3041 (1992).
- [23] Y. Deng, *et al.* "Models for Characterizing the Printability of Buried EUV Defects", *Proc. SPIE Vol. 4343*, 2001. (to be published)
- [24] Y. Deng, *et al.* "Rigorous Electromagnetic Simulation Applied in Alignment Systems", *Proc. SPIE Vol 4346*, 2001. (to be published)
- [25] P. Dirksen *et al.*, "Novel aberration monitor for optical lithography", *Proc. SPIE Vol. 3679*, pp. 79-86, 1999.
- [26] P. Dirksen *et al.*, "Impact of high order aberrations on the performance of the aberration monitor", *Proc. SPIE Vol. 4000*, pp. 9-17, 2000.
- [27] A. Erdmann *et al.*, "Rigorous diffraction for future mask technology", *Proc. SPIE Vol. 4000*, pp. 684-694, 2000.
- [28] D. G. Flagello *et al.*, "Understanding High Numerical Aperture Optical Lithography," *Microelectronic Engineering, Vol 17* (1992) pp. 105-108.
- [29] P.D. Flanner III *et al.*, "Two-Dimensional Optical Proximity Effects," *Proc. SPIE, vol. 633*, pp. 239-244, 1986.

- [30] P.D. Flanner III, *Two-dimensional Optical Imaging for Photolithography Simulation*, University of California, Berkeley, May 12, 1986. M.S. Thesis.
- [31] J. Gamelin, *Simulation of Topography Scattering for Optical Lithography with the Connection Machine*, M.S. Thesis, Memorandum No. UCB/ERL M89/71, University of California, Berkeley, May 1989.
- [32] J. Gamelin, R. Guerrieri, and A. R. Neureuther, "Exploration of Scattering from Topography with Massively Parallel Computers," *J. Vac. Sci. Technol. B*, vol. 7, no. 6, pp. 1984-1990 (1989).
- [33] Gedney, S. D., "An anisotropic PML Absorbing Media For the FDTD Simulation of Fields in Lossy and Dispersive Media", *Electromagnetics*, vol. 16, No. 14, pp. 399-415, July-August, 1996.
- [34] K. A. Goldberg, *Extreme Ultraviolet Interferometry*, Ph. D. Thesis, LBNL-41283, 1997.
- [35] J. W. Goodman, *Introduction to Fourier Optics, 2nd Edition*, (McGraw-Hill, 1996)
- [36] *ibid.*, pg. 44.
- [37] *ibid.*, pg. 113.
- [38] R. Gordon *et al.* "Design and analysis of manufacturable alternating phase-shifting masks", *Proc. SPIE Vol. 3546*, pp. 606-616, 1998.
- [39] R. Guerrieri, K. Tadros, J. Gamelin, and A. Neureuther, "Massively Parallel Algorithms for Scattering in Optical Lithography," *IEEE Trans. CAD*, vol. 10, no. 9, pp. 1091-1100 (1991).
- [40] R. L. Higdon, "Numerical Absorbing Boundary Conditions for the Wave Equation," *Mathematics of Computation*, vol. 49, no. 179, pp. 65-90, Jul. 1987.
- [41] H. H. Hopkins, "The concept of partial coherence in optics," *Proc. Roy. Soc. A*, vol. 208, p. 263 (1951).
- [42] H. H. Hopkins, "On the diffraction theory of optical images," *Proc. Roy. Soc. A*, vol. 217, p. 408 (1953).
- [43] S. Hotta *et al.*, "Effects of shifter edge topography on through focus performance", *Proc. SPIE Vol. 4186* (to be published), 2000.
- [44] J.D. Jackson, *Classical Electrodynamics*, pp. 739-742, John Wiley & Sons, 1975.
- [45] S. Jeong *et al.*, "At-wavelength detection of extreme ultraviolet lithography mask blank defects", *J. Vac. Sci. Technol. B* 16(6), Nov/Dec 1998, pp. 3430-3434.

- [46] Kim *et al.*, "Alternating PSM Phase Defect Printability for 100nm KrF Lithography", *Proc. SPIE*, Vol. 3998, pp. 308-320 (2000).
- [47] R. Kostelak, C. Pierrat, J. Garofalo, and S. Vaidya, "Exposure Characteristics of Alternate Aperture Phase-Shifting Masks Fabricated Using a Subtractive Process," *J. Vac. Sci. Technol. B*, vol. 10, no. 6, pp. 3055-3061, Nov. 1992.
- [48] S. H. Lee, *Extreme Ultraviolet (EUV) Holographic Metrology for Lithography Applications*, Electronics Research Laboratory, University of California, Berkeley, Memorandum No. UCB/ERL M00/63, Dec. 2000.
- [49] P. Lorrain, D. R. Corson, F. Lorrain, *Electromagnetic Fields and Waves, 3rd Edition*, pp. 554-561, (W. H. Freeman and Company), 1988.
- [50] C. A. Mack, *Inside Prolith*, (Finle Technologies, 1997), pg. 27.
- [51] K. K. Mei, and J. Fang, "Superabsorption - A Method to improve Absorbing Boundary Conditions," *IEEE Trans. Antennas Propagation*, vol. 40, no. 9, pp. 1001-1010, Sept. 1992.
- [52] "Message Passing Interface Forum. MPI: A message-passing interface standard." *International Journal of Supercomputer Applications*, 8(3/4), 1994.
- [53] P. B. Mirkarimi, D. G. Stearns, "Investigating the growth of localized defects in thin films using gold nanospheres," *Applied Physics Letters Vol. 77*, pp. 2243-2245, Oct. 2000.
- [54] C. Montcalm *et al.*, "Multilayer reflective coatings for extreme-ultraviolet lithography," *Proc. SPIE Vol. 3331*, pp. 42-51, 1998.
- [55] G. Mur, "Absorbing Boundary Conditions for the Finite-Difference Approximations of the Time-Domain Electromagnetic-Field Equations," *IEEE trans. on Electromagnetic Comp.*, vol. EMC-23, no. 4, pp. 377-382, Nov., 1981.
- [56] A. R. Neureuther *et al.*, "Coherence of Defect Interactions with Features in Optical Imaging," *J. Vac. Sci. Technol. B*, pp. 308-312, Jan/Feb 1987.
- [57] K. B. Nguyen, *et al.*, "Effects of absorber topography and multilayer coating defects on reflective masks for soft x-ray/EUV projection lithography," *Proc. SPIE Vol. 1924*, pp. 418-434, 1993.
- [58] Nguyen, K. B., *et al.*, "Printability of substrate and absorber defects on extreme ultraviolet lithographic masks", *J. Vac. Sci. Technol. B* 13(6), Nov/Dec 1995, pp. 3082-3088.

- [59] Nguyen, K. B., Wong, A. K., Neureuther, A. R., Attwood, D. T., Nguyen, T. D., "Aerial Images of EUV Projection Lithography Masks with Defects in Reflective Coatings: Electromagnetic Simulation", pp. 47-53, *OSA Proceedings on Soft X-Ray Projection Lithography, 1993, Vol 18*.
- [60] W. Partlo *et al.*, "Depth of focus and resolution enhancement of i-line and deep-UV lithography using annular illumination", *Proc. SPIE Vol. 1927*, pp. 137-157, 1993.
- [61] C. Pierrat, A. Wong, and S. Vaidya, "Phase-Shifting Mask Topography Effects on Lithographic Image Quality," in *Technical Digest---International Electron Devices Meeting*, pp. 53-56, Dec. 1992.
- [62] Pistor, T., *Expanding the Simulation Capability of TEMPEST*, Electronics Research Laboratory, University of California, Berkeley, 1997.
- [63] T. V. Pistor *et al.* "Rigorous simulation of mask corner effects in extreme ultraviolet lithography," *J. Vac. Sci. Technol. B* 16(6), Nov/Dec 1998, pp. 3449-3455.
- [64] T. V. Pistor *et al.* "Extreme ultraviolet defect simulation," *J. Vac. Sci. Technol. B* 17(6), Nov/Dec 1999, pp. 3019-3023.
- [65] T. V. Pistor *et al.* "Extreme ultraviolet mask defect simulation: Low profile defects," *J. Vac. Sci. Technol. B* 18(6), Nov/Dec 2000.
- [66] T. V. Pistor *et al.* "Calculating aerial images from EUV masks", *Proc. SPIE Vol. 3676*, pp. 679-696, 1999.
- [67] T. Pistor *et al.*, "Simulation of Reflective Notching with TEMPEST", *Proc. SPIE Vol. 3051*, pp. 595-605, 1997.
- [68] T.V. Pistor, A.R. Neureuther, R. J. Socha, "Modeling Oblique Incidence Effects in Photomasks", *Proc. of SPIE, Vol. 4000*, pp. 228-237 (2000).
- [69] P. Schiavone *et al.*, "Rigorous electromagnetic simulation of EUV masks: influence of the absorber properties," *Proceedings of MNE 2000*, paper # AM 13B, 2000.
- [70] R. Socha *et al.*, "The Effect of the Partial Coherence on Reflective Notching", *Proc. SPIE Vol. 3051*, pg. 479, 1997.
- [71] R. Socha, *Propagation Effects of Partially Coherent Light in Optical Lithography and Inspection*, Ph.D. Thesis, Memorandum No. UCB/ERL M97/55, Electronics Research Laboratory, College of Engineering, University of California, Berkeley, August, 1997.
- [72] *ibid.*, pp. 31-34.
- [73] R. Socha and A. Neureuther, "Propagation effects of partial coherence in optical lithography," *J. Vac. Sci. Technol. B, vol. 14*, p. 3724 (1996).

- [74] R. Socha, C. Progler, and A. Neureuther, "The Effect of Partial Coherence on Reflective Notching," *Proc. of SPIE*, vol. 3051 (1997).
- [75] R. J. Socha *et al.*, "Design of 200nm, 170nm, 140nm DUV Contact Sweeper High Transmission Attenuating Phase Shift Mask through Simulation Part 1," *Proc. SPIE Vol. 3546*, pp. 617-641, 1998.
- [76] R. J. Socha *et al.*, "Design of 200nm, 170nm, 140nm DUV Contact Sweeper High Transmission Attenuating Phase Shift Mask: Experimental Results Part 2," *Proc. SPIE Vol. 3679*, pp. 38-54, 1999.
- [77] Sweeney, D. W., *et al.*, "EUV Optical Design for a 100nm CD Imaging System," *Proc. SPIE Vol. 3331*, pp. 2-10, 1998.
- [78] A. Taflove, *Computational Electrodynamics The Finite-Difference Time-Domain Method* (Artech House, 1995), pp. 59-78.
- [79] *ibid.*, pp. 545-583.
- [80] E. Tejnil, *Characterization of Extreme Ultraviolet Imaging Systems*, Ph. D. Thesis, Electronics Research Laboratory, University of California, Berkeley, Memorandum No. UCB/ERL M97/81, Nov. 1997.
- [81] E. Tejnil *et al.*, "Evaluation of printability and inspection of phase defects on hidden-shifter alternating phase-shift masks", *Proc. SPIE Vol. 4066*(2000), pg. 376.
- [82] D. A. Tichenor *et al.* "EUV engineering test stand", *Proc. SPIE Vol. 3997*, pp. 48-69, 2000.
- [83] K. Toh, *Two Dimensional Images with Effects of Lens Aberrations in Optical Lithography*, M.S. Thesis, Memorandum #UCB/ERL M88/30, University of California at Berkeley, May 1988.
- [84] K. Toh *et al.*, "EUV Stepper Characterization using Lithography Modeling", *2nd International Workshop on Extreme Ultraviolet Lithography*, October 16-19, 1999.
- [85] B. Todd *et al.*, "AFM Metrology and 3-D Modeling of Short Range Anomalies in Etched Photomask Features", *Proc. SPIE Vol. 4344* (to be published), 2001.
- [86] T. Wilson and C. Sheppard, *Theory and Practice of Scanning Optical Microscopy*, Academic Press, Chapter 3.
- [87] A. Wong and A. Neureuther, "Mask Topography Effects in Projection Printing of Phase-shifting Masks," in *IEEE Transactions on Electron Devices*, vol. 41, no. 6, pp. 895-902, June 1994.

- [88] A. Wong, *Rigorous Three-Dimensional Time-Domain Finite-Difference Electromagnetic Simulation*, Ph.D. Dissertation, University of California at Berkeley (1994)
- [89] *ibid.*, pp. 11-15.
- [90] *ibid.*, pp. 21-25.
- [91] *ibid.*, pp. 32-36.
- [92] *ibid.*, pp. 43-59.
- [93] *ibid.*, pp. 71-72.
- [94] *ibid.*, pp. 78-82.
- [95] *ibid.*, pp. 118-120.
- [96] A. Wong, *Tempest Users' Guide*, Memorandum No. UCB/ERL M95/14, University of California, Berkeley, March 1995.
- [97] Q. Wu *et al.*, "Optimization of Segmented Alignment Marks for Advanced Semiconductor Fabrication Processes", *Proc. SPIE. Vol. 4344* (to be published) (2001)
- [98] K. S. Yee, "Numerical Solution of Initial Boundary Value Problems Involving Maxwell's Equations in Isotropic Media," *IEEE Trans. Ant. Prop. vol. 14*, pp. 302-307 (1966).
- [99] M. Yeung, "Modeling high numerical aperture optical lithography," *Proc. SPIE, vol. 922*, pp. 149-167 (1988).
- [100] M. Yeung, D. Lee, R. Lee, and A. Neureuther, "Extension of the Hopkin's theory of partially coherent imaging to include thin-film interference effects," *Proc. SPIE, vol. 1927*, pp. 452-462 (1993).
- [101] X. Yin *et al.* "Subwavelength alignment mark signal analysis of advance memory products", *Proc. SPIE. Vol. 3998*, pp. 449-459 (2000)
- [102] L. Zhao and A. C. Cangellaris, "GT-PML: Generalized theory of perfectly matched layers and its application to the reflectionless truncation of finite-difference time-domain grids," *IEEE Trans. Microwave Theory Tech., vol. 44, no. 12*, pp. 2555-2563, December 1996.